

LOAN DOCUMENT

PHOTOGRAPH THIS SHEET

①

INVENTORY

AD-A261 972



DTIC ACCESSION NUMBER

LEVEL

AFDSR-TR-93-0118

DOCUMENT IDENTIFICATION

Dec 92

DISTRIBUTION STATEMENT A

Approved for public release
Distribution Unlimited

DISTRIBUTION STATEMENT

DTIC
ELECTE
MAR 10 1993
S C D

DATE ACCESSIONED

| | |
|--------------------|-----------------------------|
| ACCESSION FOR | |
| NTIS | GRA&I |
| DTIC | TRAC |
| UNANNOUNCED | |
| JUSTIFICATION | |
| BY | |
| DISTRIBUTION/ | |
| AVAILABILITY CODES | |
| DISTRIBUTION | AVAILABILITY AND/OR SPECIAL |
| A-1 | |

DISTRIBUTION STAMP

DTIC QUALITY INSPECTED 1

DATE RETURNED

98 3 10 012
~~98 3 4 070~~

DATE RECEIVED IN DTIC

93-04698



REGISTERED OR CERTIFIED NUMBER

PHOTOGRAPH THIS SHEET AND RETURN TO DTIC-FDAC

H
A
N
D
L
E

W
I
T
H

C
A
R
E

UNITED STATES AIR FORCE
SUMMER RESEARCH PROGRAM -- 1992
GRADUATE STUDENT RESEARCH PROGRAM (GSRP) REPORTS

VOLUME 8

PHILLIPS LABORATORY

RESEARCH & DEVELOPMENT LABORATORIES

5800 Uplander Way

Culver City, CA 90230-6608

Program Director, RDL
Gary Moore

Program Manager, AFOSR
Lt. Col. Claude Cavender

Program Manager, RDL
Billy Kelley

Program Administrator, RDL
Gwendolyn Smith

Submitted to:

AIR FORCE OFFICE OF SCIENTIFIC RESEARCH

Bolling Air Force Base

Washington, D.C.

December 1992

REPORT DOCUMENTATION PAGE

1. AGENCY USE ONLY (Leave blank)

2. REPORT DATE
28 Dec 92

3. REPORT TYPE AND DATES COVERED
Annual 1 Sep 91 - 31 Aug 92

4. TITLE AND SUBTITLE

1992 Summer Faculty Research Program (SFRP)
Volumes 1 - 16

F49620-90-C-0076

5. AUTHOR

Mr Gary Moore

6. PERFORMING ORGANIZATION NAME(S) AND ADDRESS(ES)

Research & Development Laboratories (EDL)
5800 Uplander Way
Culver City CA 90230-6600

AFOSR-TR- 93 0118

7. FUNDING NUMBERS

AFOSR/NI
110 Duncan Ave., Suite B115
Bldg 410
Bolling AFB DC 20332-0001
Lt Col Claude Cavender

8. SUPPLEMENTARY NOTES

9. DISTRIBUTION STATEMENT

UNLIMITED

10. ABSTRACT (Maximum 200 words)

The purpose of this program is to develop the basis for continuing research of interest to the Air Force at the institution of the faculty member; to stimulate continuing relations among faculty members and professional peers in the Air Force to enhance the research interests and capabilities of scientific and engineering educators; and to provide follow-on funding for research of particular promise that was started at an Air Force laboratory under the Summer Faculty Research Program.

During the summer of 1992 185 university faculty conducted research at Air Force laboratories for a period of 10 weeks. Each participant provided a report of their research, and these reports are consolidated into this annual report.

11. SUBJECT TERMS

12. SECURITY CLASSIFICATION
OF REPORT

UNCLASSIFIED

13. SECURITY CLASSIFICATION
OF THIS PAGE

UNCLASSIFIED

14. SECURITY CLASSIFICATION
OF ABSTRACT

UNCLASSIFIED

UL

15. AVAILABILITY STATEMENT

PREFACE

This volume is part of a 16-volume set that summarizes the research accomplishments of faculty, graduate student, and high school participants in the 1992 Air Force Office of Scientific Research (AFOSR) Summer Research Program. The current volume, Volume 8 of 16, presents the final research reports of graduate student (GSRP) participants at Phillips Laboratory.

Reports presented herein are arranged alphabetically by author and are numbered consecutively -- e.g., 1-1, 1-2, 1-3; 2-1, 2-2, 2-3.

Research reports in the 16-volume set are organized as follows:

| VOLUME | TITLE |
|---------------|--|
| 1 | Program Management Report |
| 2 | Summer Faculty Research Program Reports: Armstrong Laboratory |
| 3 | Summer Faculty Research Program Reports: Phillips Laboratory |
| 4 | Summer Faculty Research Program Reports: Rome Laboratory |
| 5A | Summer Faculty Research Program Reports: Wright Laboratory (part one) |
| 5B | Summer Faculty Research Program Reports: Wright Laboratory (part two) |
| 6 | Summer Faculty Research Program Reports: Arnold Engineering Development Center; Civil Engineering Laboratory; Frank J. Seiler Research Laboratory; Wilford Hall Medical Center |
| 7 | Graduate Student Research Program Reports: Armstrong Laboratory |
| 8 | Graduate Student Research Program Reports: Phillips Laboratory |
| 9 | Graduate Student Research Program Reports: Rome Laboratory |
| 10 | Graduate Student Research Program Reports: Wright Laboratory |
| 11 | Graduate Student Research Program Reports: Arnold Engineering Development Center; Civil Engineering Laboratory; Frank J. Seiler Research Laboratory; Wilford Hall Medical Center |
| 12 | High School Apprenticeship Program Reports: Armstrong Laboratory |
| 13 | High School Apprenticeship Program Reports: Phillips Laboratory |
| 14 | High School Apprenticeship Program Reports: Rome Laboratory |
| 15 | High School Apprenticeship Program Reports: Wright Laboratory |
| 16 | High School Apprenticeship Program Reports: Arnold Engineering Development Center; Civil Engineering Laboratory |

1992 GRADUATE RESEARCH REPORTS

Phillips Laboratory

| <u>Report Number</u> | <u>Report Title</u> | <u>Author</u> |
|----------------------|--|-------------------------|
| 1 | Experimental Investigation of Homogeneous and Heterogeneous Nucleation/Condensation Processes and Products in Coil | W. Mark Barnett |
| 2 | Ion-Molecule Reactions at High Temperatures | Melani Menendez-Barreto |
| 3 | Some Models of Thermal Blankets on Satellites | Rodney L. Bates |
| 4 | Optical and Atmospheric Turbulence | Mary Agnes Beals |
| 5 | A Method to Solve Near-Minimum Time Maneuvers of Flexible Spacecraft Using Parameter Optimization | Michael T. Carter |
| 6 | High Temperature Absorption Spectroscopy of Na/Li Mixtures for Application to Solar Plasma Propulsion | Paul S. Erdman |
| 7 | Lagrangian Formulation of Lageos's Spin Dynamics | Christopher Fuchs |
| 8 | (Report not received) | |
| 9 | Large-Scale Methods in Computational Electromagnetics using Synchronous Out-of-Core Techniques | Michael C. Governale |
| 10 | A Study of Coupled Oscillatory Neural Network Models | John A. Greenfield |
| 11 | High Temperature Heat Pipe Modeling Under Low Power Heat Loads and Cryogenic Phase Change Material Devices in Space Applications | Steven E. Griffin |
| 12 | Design and Characterization of a Magnetoplasma-Dynamic Thruster and Optical Diagnosis System | Mohanjit S. Jolly |
| 13 | Design of a Digital Loop Compensation Filter of an Adaptive Optics System for Atmospheric Turbulence Compensation | Kurt W. Kunzler |
| 14 | Compact Toroid Mass Entrainment Sensitivity to Initial Density Distributions using Numerical Simulation | Robert John Leiweke |
| 15 | Fidelity of Polarization Recovery using a Double Fiber-Coupled Phase-Conjugate Mirror | Darron D. Lockett |
| 16 | (Report not received) | |
| 17 | Simulation of Fluid Flow in Two Dimensions using a Hexagonal Lattice Gas | Francis H. Maurais |
| 18 | Progress on the Working Fluid Experiment: Formation of a Plasma Working Fluid for Compression by Liner Implosion | Jane Messerschmitt |

Phillips Laboratory (cont'd)

| <u>Report Number</u> | <u>Report Title</u> | <u>Author</u> |
|--------------------------|---|--------------------|
| 19 | Correlating Injector Performance for Use as Engineering Design Criteria | Michael P. Moses |
| 20 | Analysis of ONYNEX and MSRP Seismic Refraction Data in New England | Andrew Paulson |
| 21 | Establishment of an Arcjet Optical Diagnostics Facility at Phillips Lab | Jeffrey Pobst |
| 22 | A Computational Model of the Magnetospheric Boundary Layer | David W. Rose |
| 23 | Establishment of an Arcjet Optical Diagnostics Facility at Phillips Lab | John Schilling |
| 24 | A Study of Aero-Optics | Brian Staveley |
| 25 | (Report not received) | |
| 26 | A Brief Study of Passive Viscous Damping for the SPICE Bulkhead Structure | Thomas J. Thompson |
| 27 | Vibration and Compression Testing of Composite Isogrid Panels | Sean A. Webb |

EXPERIMENTAL INVESTIGATION OF HOMOGENEOUS AND HETEROGENEOUS
NUCLEATION/CONDENSATION PROCESSES AND PRODUCTS IN COIL.

Philip D. Whitefield
Research Associate Professor
Department of Chemistry

and

W. Mark Barnett
Graduate Student
Department of Chemistry

Cloud and Aerosol Sciences Laboratory,
University of Missouri - Rolla. (UMR/CASL).
Norwood Hall G11
Rolla, MO 65401

Final Report for:
Summer Research Program
Phillips Laboratory

Sponsored by:
Air Force Office of Scientific Research
Bolling Air Force Base, Washington, D.C.

August 1992.

**EXPERIMENTAL INVESTIGATION OF HOMOGENEOUS AND HETEROGENEOUS
NUCLEATION/CONDENSATION PROCESSES AND PRODUCTS IN COIL.**

Philip D. Whitefield
Research Associate Professor
and

W. Mark Barnett
Graduate Student

Department of Chemistry Cloud and Aerosol Sciences Laboratory,
University of Missouri - Rolla.

Abstract

This paper describes the preliminary results of an ongoing study to characterize the nature and sources of sub-micron aerosols in the Phillips Laboratory small scale supersonic COIL device and other COIL devices. Aerosols from both sub- and supersonic flow regimes were sampled and characterized using the University of Missouri-Rolla, Mobile Aerosol Sampling System (MASS). Under all operating conditions where the oxygen generator discs were rotating, significant concentrations of aerosols were detected. Typically these aerosols had peak dry diameters of <0.05 microns and nascent wet diameters of <0.08 microns. Their total number density increased with increasing rotating disc velocity and with the addition of chlorine. A maximum number density of $<3000/\text{cc}$ was observed at maximum chlorine flow rates when the initial generator mixture had been heavily depleted (i.e. neutralized with chlorine). Experiments to observe homogeneous nucleation of aerosols in simulated supersonic laser gas flows were unsuccessful. The critical supersaturation spectra for a KOH, KCl, I_2 have been measured and compared to theoretical calculations.

ION-MOLECULE REACTIONS AT HIGH TEMPERATURES

Melani Menendez-Barreto
Graduate Student
Department of Physics
University of Puerto Rico at Mayaguez
Mayaguez, PR 00680

Jeffrey F. Friedman
Assistant Professor
Department of Physics
University of Puerto Rico at Mayaguez
Mayaguez, PR 00680

Thomas M. Miller
Professor
Department of Physics and Astronomy
University of Oklahoma
Norman, OK 73019

Final Report for:
Summer Research Program
Phillips Laboratory, Geophysics Directorate

Sponsored by:
Air Force Office of Scientific Research
Bolling Air Force Base, Washington, DC

August 1992

ION-MOLECULE REACTIONS AT HIGH TEMPERATURES

Melani Menéndez-Barreto
Graduate Student
Department of Physics
University of Puerto Rico at Mayaguez

Jeffrey F. Friedman
Assistant Professor
Department of Physics
University of Puerto Rico at Mayaguez

Thomas M. Miller
Professor
Department of Physics and Astronomy
University of Oklahoma

Abstract

A flowing afterglow apparatus designed for the measurement of ion-molecule reaction rate coefficients at temperatures higher than any previous work was debugged and put into operation during the summer of 1992. Ion-molecule reaction rate coefficients were measured for a variety of systems in the temperature range 300-1200 K: $O^- + H_2, D_2, N_2, CO, NO,$ and CH_4 ; $Ar^+ + H_2, O_2, CO, NO,$ and CH_4 ; $O_2^+ + CH_4$; and $Cl^- + CH_3Br$ and CH_3I .

**SOME MODELS OF
THERMAL BLANKETS ON SATELLITES**

**RODNEY L. BATES
DEPARTMENT OF MATHEMATICS
UNIVERSITY OF MISSISSIPPI
UNIVERSITY, MS 38677**

**FINAL REPORT FOR:
AFOSR SUMMER RESEARCH PROGRAM
PHILLIPS LABORATORY**

**SPONSORED BY:
AIR FORCE OFFICE OF SCIENTIFIC RESEARCH
BOLLING AIR FORCE BASE, WASHINGTON, D.C.**

AUGUST 1992

SOME MODELS OF
THERMAL BLANKETS ON SATELLITES

RODNEY L. BATES
DEPARTMENT OF MATHEMATICS
UNIVERSITY OF MISSISSIPPI

ABSTRACT

For a variety of reasons, satellites often have a thermal blanket placed on their exterior. This causes the surface of the satellite to be rough, which has a definite impact on the imaging of the satellite. The goal of this project was to model this behavior, so that the reflectance properties of the surface could be determined. Beginning with a surface with a random height distribution, several surfaces were developed using discrete Fourier transform filtering design techniques. In this report, these techniques are discussed; and the filters are given explicitly. In addition, computer generated 3-D plots of some of the resulting surfaces are included.

SOME MODELS OF THERMAL BLANKETS ON SATELLITES

RODNEY L. BATES

INTRODUCTION

For a variety of reasons, a satellite may be covered with a "thermal blanket", a material which resembles metal foil. This thermal blanket is a significant factor with respect to the imaging of the satellite. Therefore an accurate model of the rough surface created by placing the blanket on the satellite is necessary to generate an optimal image. This report gives some such models and describes how each model was developed.

METHODOLOGY

To begin, a surface was generated with a Gaussian height distribution. (see Figure 1) This was done by producing a two-dimensional array of Gaussian distributed random numbers, in this case the size of the array was 64x64. Thus each point in the grid is associated with a number, which is the height of the surface at that particular point. In order to simulate the "wrinkles" of the surface, the Fourier transform of the array was calculated using a two-dimensional Fast Fourier Transform (FFT), then a variety of filters was applied, each generating a different surface, and then the inverse FFT was applied.

The bulk of this paper is devoted to the description of the various filters used and the various surfaces that resulted from the different filters. A method was employed to generate computer images of the surfaces; and these images are included in Figures 1-4.

The first filter used was a modification of the zonal low pass filter which will be discussed later. The main idea is to take a rectangle of predetermined dimensions from the transformed

array and set all values not in the rectangle to zero. A precise formula is given as follows:

$$F(u, v) = 1 \text{ whenever } a \leq u \leq b \text{ and } c \leq v \leq d \\ 0 \text{ otherwise}$$

where a,b,c,d are the parameters of the rectangle. Interesting results which arise from adjusting these parameters will be discussed later. In the sequel, this filter will be referred to as first.filter.

The remaining filters were taken directly from [1]. The first of these are the zonal low pass and zonal high pass filters. Here N is the size of the array and C is the filter cutoff frequency for $0 \leq C \leq 1 + \frac{N}{2}$.

Zonal Low Pass Filter

$$F(u, v) = 1 \text{ whenever } 0 \leq u \leq C-1 \text{ and } 0 \leq v \leq C-1$$

$$0 \leq u \leq C-1 \text{ and } N+1-C \leq v \leq N-1$$

$$N+1-C \leq u \leq N-1 \text{ and } 0 \leq v \leq C-1$$

$$N+1-C \leq u \leq N-1 \text{ and } N+1-C \leq v \leq N-1$$

$$F(u, v) = 0 \text{ otherwise}$$

Zonal High Pass Filter

$$F(0, 0) = 1$$

$$F(u, v) = 0 \text{ whenever } 0 \leq u \leq C-1 \text{ and } 0 \leq v \leq C-1$$

$$0 \leq u \leq C-1 \text{ and } N+1-C \leq v \leq N-1$$

$$N+1-C \leq u \leq N-1 \text{ and } 0 \leq v \leq C-1$$

$$N+1-C \leq u \leq N-1 \text{ and } N+1-C \leq v \leq N-1$$

$$F(u, v) = 1 \text{ otherwise}$$

Next are the Butterworth low pass and Butterworth high pass filters. These differ from the zonal filters in that they involve a factor other than 0 or 1. Here n is the order of the filter and C and N are as before:

Butterworth Low Pass Filter:

$$F(u, v) = \frac{1}{1 + \left(\frac{(u^2 + v^2)^{1/2}}{C} \right)^{2n}} \text{ whenever } \begin{aligned} &0 \leq u \leq \frac{N}{2} \text{ and } 0 \leq v \leq \frac{N}{2} \\ &0 \leq u \leq \frac{N}{2} \text{ and } 1 + \frac{N}{2} \leq v \leq N-1 \\ &1 + \frac{N}{2} \leq u \leq N-1 \text{ and } 0 \leq v \leq N-1 \\ &1 + \frac{N}{2} \leq u \leq N-1 \text{ and } 1 + \frac{N}{2} \leq v \leq N-1 \end{aligned}$$

$F(u, v) = 0$ otherwise

Butterworth High Pass Filter

$$F(u, v) = \frac{1}{1 + \left(\frac{C}{(u^2 + v^2)^{1/2}} \right)^{2n}} \text{ whenever } \begin{aligned} &0 \leq u \leq \frac{N}{2} \text{ and } 0 \leq v \leq \frac{N}{2} \\ &0 \leq u \leq \frac{N}{2} \text{ and } 1 + \frac{N}{2} \leq v \leq N-1 \\ &1 + \frac{N}{2} \leq u \leq N-1 \text{ and } 0 \leq v \leq \frac{N}{2} \\ &1 + \frac{N}{2} \leq u \leq N-1 \text{ and } 1 + \frac{N}{2} \leq v \leq N-1 \end{aligned}$$

$F(u, v) = 0$ otherwise

The parameters of each of these transfer filter functions were experimented with to obtain different surfaces. Adjusting the parameters of first filter gave the most interesting results, which will be discussed in the following.

RESULTS

Computer generated plots of the various surfaces are shown in Figures 1-4. Shown first is the surface with a Gaussian height distribution and no filtering. This particular distribution

has a mean of 0 and a standard deviation of .5. Next is the surface resulting from using first-order filter with $a = 32$, $b = 48$, $c = 32$, and $d = 48$. The direction of the "wrinkles" on this surface can be controlled by changing the height and width of the rectangle. This is illustrated in Figure 2. To cause almost all of the wrinkles to go in the x direction, the rectangle is given the parameters $a = 20$, $b = 50$, $c = 43$, $d = 45$. These parameters correspond to taking a rectangle of small height and large width. Similarly, to create wrinkles in the y direction, the parameters are $a = 43$, $b = 45$, $c = 20$, and $d = 50$. Here the rectangle has large height and small width.

In Figure 3, the surface resulting from using the Butterworth filters are shown; and in Figure 4 we have the surfaces given from the zonal filters. Here $C = 25$ and $n = 10$. It seems that the Butterworth low pass filter may come closest to simulating the material of interest; however each of the surfaces can be modified by changing their parameters and by changing the parameters of the original Gaussian surface.

CONCLUSION

The goal of this project was to develop a model of the rough surface created by placing a thermal blanket on a satellite. This model would allow others to determine the reflectance properties needed for imaging purposes. The end result of this work has given several surfaces to choose from; and the ability to modify these surfaces to suit a more particular need.

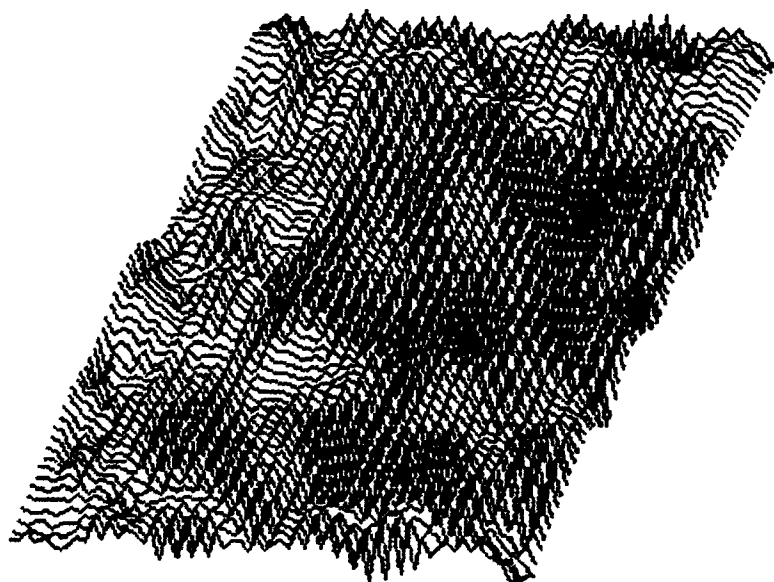
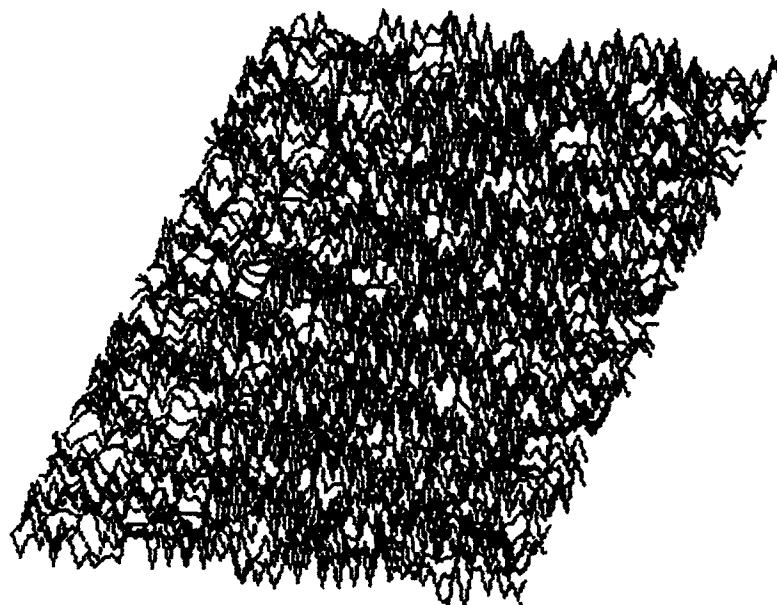


Figure 1
Top: Gaussian surface with no filtering
Bottom: surface created using first.filter

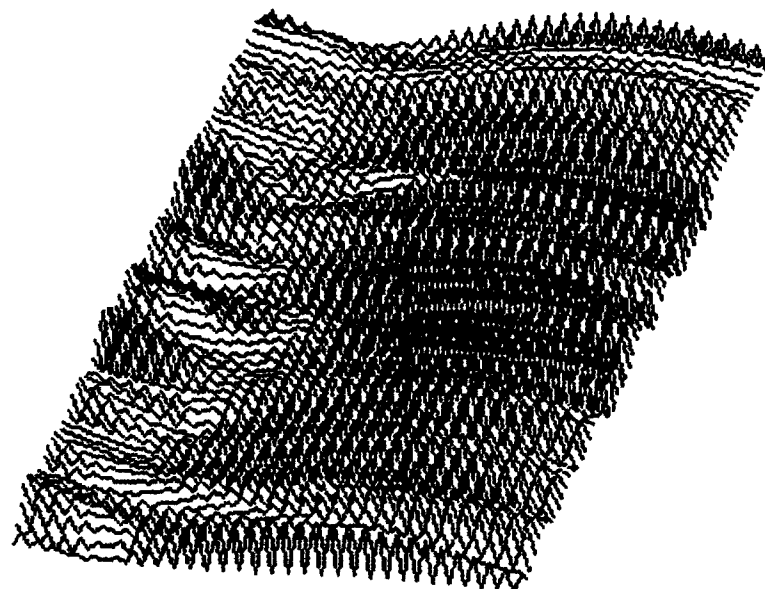
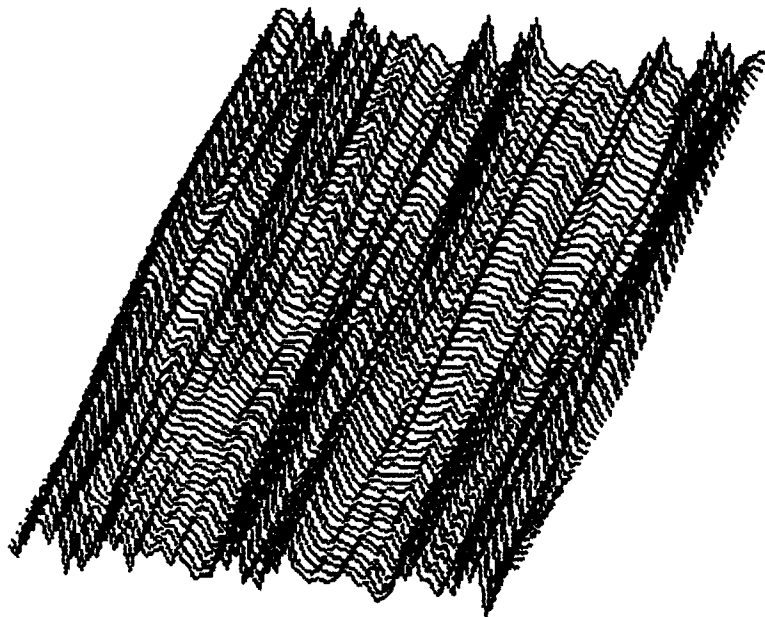


Figure 2
Top: surface created using first.filter with adjusted parameters
Bottom: surface created using first.filter with adjusted parameters

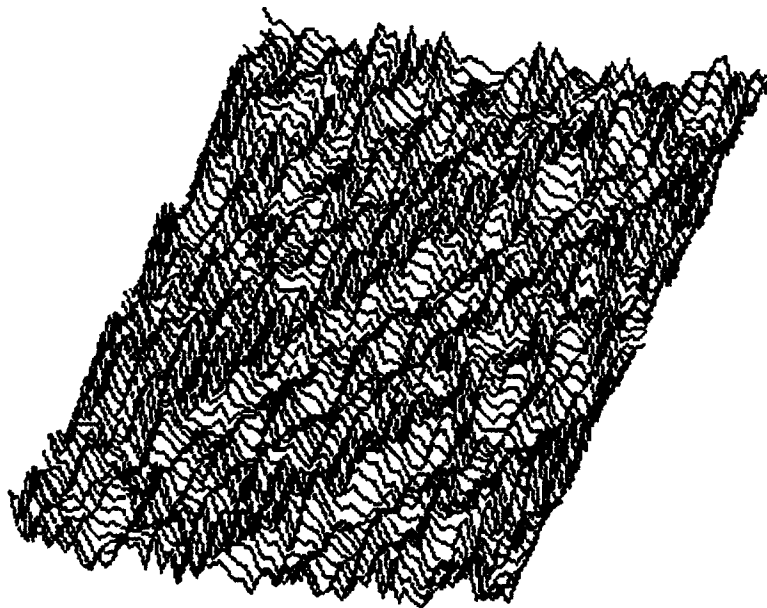
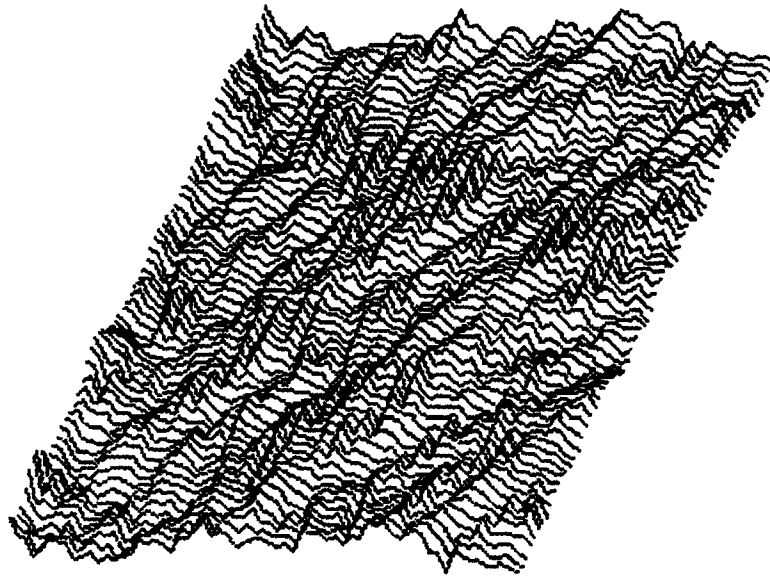


Figure 3
Top: surface created using Butterworth low pass filter
Bottom: surface created using Butterworth high pass filter

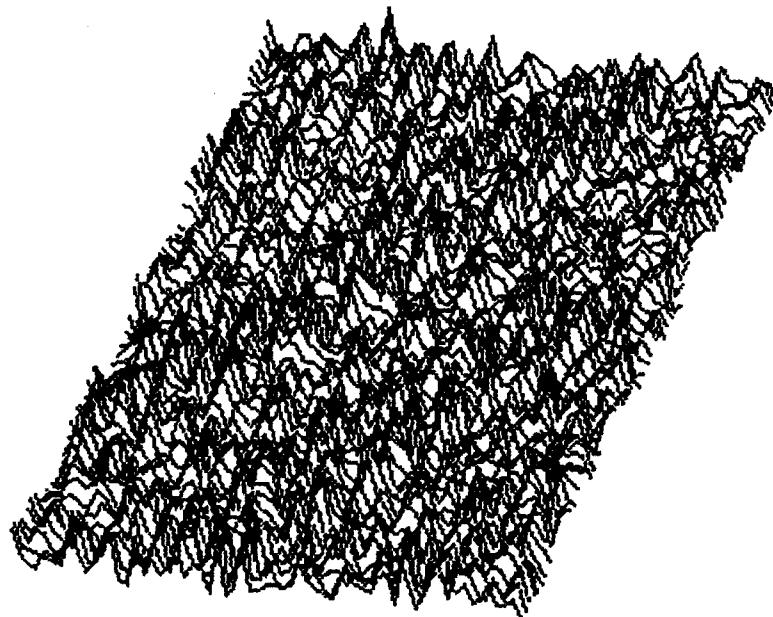
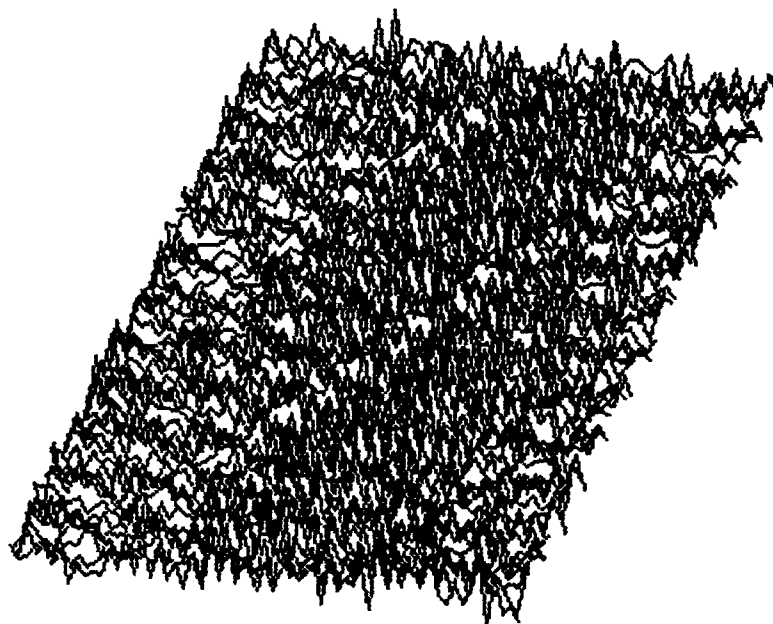


Figure 4
Top: surface created using zonal low pass filter
Bottom: surface created using zonal high pass filter

REFERENCES

1. Pratt, William K., Digital Image Processing, Wiley-Interscience, New York, 1991, 245-250

OPTICAL AND ATMOSPHERIC TURBULENCE

submitted by

MAYER HUMI, Professor
DEPARTMENT OF MATHEMATICAL SCIENCES
Worcester Polytechnic Institute
Worcester, MA 01609-2280

with

MARY AGNES BEALS
DEPARTMENT OF MATHEMATICS
Virginia Polytechnic Institute
Blacksburg, VA 24061-0123

Final Report for
Summer Research Program
Phillips Laboratory

Sponsored by
AFOSR, Bolling Air Force Base
Washington, D.C.

September 1992.

OPTICAL AND ATMOSPHERIC TURBULENCE

MAYER HUMI, Professor
DEPARTMENT OF MATHEMATICAL SCIENCES
Worcester Polytechnic Institute

Abstract

For many important applications it is imperative to estimate correctly the spectral density of atmospheric turbulence. To this end one must collect meteorological data and "detrend" it to obtain the turbulent residual. The objective of this project was to experiment with different detrending (= filtering) strategies and gauge their impact on the computed spectral densities of the flow variables. To help accomplish this objective a general purpose software package was written and used.

**A METHOD TO SOLVE NEAR-MINIMUM TIME MANEUVERS
OF FLEXIBLE SPACECRAFT USING PARAMETER OPTIMIZATION**

**Michael T. Carter
Graduate Student
Department of Aerospace Engineering**

**Texas A&M University
College Station, TX 77843**

**Final Report for:
AFOSR Summer Research Program
Phillips Laboratory
Edwards Air Force Base, CA**

**Sponsored by:
Air Force Office of Scientific Research
Bolling Air Force Base, Washington, D.C.**

August 1992

A METHOD TO SOLVE NEAR-MINIMUM TIME MANEUVERS OF FLEXIBLE SPACECRAFT USING PARAMETER OPTIMIZATION

Michael T. Carter
Graduate Student
Department of Aerospace Engineering
Texas A&M University

Abstract

Determining the control to maneuver a large flexible space structure in minimum time is investigated using *Sequential Quadratic Programming* (SQP), which calculates the near-minimum time maneuver by optimizing a parameter set. The researcher chooses parameters which adequately describe the control profile predicted by the optimal control from calculus of variations theory. Control shaping is added to the profile to prevent discontinuous control jumps from exciting vibrations in the flexible structure; the parameter optimization method can use the shaped profile in its solution process. The SQP algorithm is tested on the ASTREX (Advanced Structure Technology Research Experiment) test article at Phillips Laboratory, Edwards AFB, CA.; the ASTREX structure is modeled with a complex rigid body motion which includes gyroscopic and gravitational effects as well as damping from attached cabling. Since the ASTREX test article has a limited volume of pressurized air to generate thrust, a maximum fuel constraint must be imposed on the problem; however, the SQP algorithm can include inequality as well as equality constraints. Using this algorithm, numerical analyses showed that the optimal control for large angle rotations of the ASTREX structure is closer to the optimal minimum fuel solution than the optimal minimum time solution due to the fuel constraint. Parameter optimization has obvious computational speed advantages by solving for the near-minimum time control rather than the exact optimal control; however, the researcher should carefully choose the control profile to be parametrized to ensure a near-minimum time solution if parameter optimization is used when control or state constraints are added to the problem.

A METHOD TO SOLVE NEAR-MINIMUM TIME MANEUVERS OF FLEXIBLE SPACECRAFT USING PARAMETER OPTIMIZATION

Michael T. Carter

Introduction

Optimal large angle spacecraft maneuvers have been studied by many researchers in the past decade. During this period, most work is separated into two areas: three-dimensional rigid-body maneuvers and single-axis flexible structure maneuvers.

For rigid-body maneuvers, the optimal maneuver problem, whose optimality is based on an energy or time criterion, is usually reduced to a Two-Point Boundary Value Problem (TPBVP) using Pontryagin's principle. Gradient or shooting methods can then be employed to converge on a control solution iteratively. However, this method depends on a good initial guess for the initial costates to converge due to the increased dimensions of the state-costate space. Li and Bainum¹ developed a method to estimate the initial costates for the shooting method using a quasilinearization technique for the near-minimum time problem combined with appropriate scaling of the magnitudes. The TPBVP method offers a capable method to solve for the attitude maneuvers of real-world unsymmetrical structures, but each maneuver, even for the same body, requires an unrelated initial guess for the costates and therefore, little insight about the optimal control solution is gained.

Considering a simplified spherical body with equal orthogonal external thrust components, Bilimoria and Wie² demonstrated computationally that the Euler-axis rotation is not time optimal for three-dimensional maneuvers. Solving for time-optimal controls, they discovered a distinct number of switches in the bang-bang maneuvers for a sphere: five switches for greater than 73° rotations and seven switches below this critical rotational angle. Testing also displayed a switching sequence where each axis would wait for the other axes to switch before switching a second time. From the Li and Bainum paper above, a rest-to-rest maneuver for a body with only principal axis inertias corresponds with these conclusions; however, a second example for a highly unsymmetrical body matched neither the predicted number of switches or switching sequence. Continuing this research, Byers and Vadali³ compared the numerical results for Euler-axis, five-switch and seven-switch rotations and determined the time differential is not significant for actual control implementation.

While significant contributions were being made in minimum-time rigid-body maneuvers, Thompson, Junkins and Vadali⁴ cautioned against the use of bang-bang controls in real structures, due to the impossibility of a torque-generating device closely approximating a discontinuous control jump, the excitation of poorly modeled higher modes when applied to a flexible structure, and the switch time sensitivity to modeling errors. Control shaping was developed to counteract each of these problems with a very successful albeit simple solution of exchanging the bang-bang control with a approximate sign function and multiplier combination. Recent work in single-axis flexible body maneuvers has verified the effectiveness of this technique.^{5,6}

This paper addresses the three-dimensional rigid-body large-angle maneuvers of an unsymmetrical flexible structure, the ASTREX test article at Phillips Laboratory, Edwards AFB, CA. Using a parameter optimization method which optimizes the maneuver parameter set associated with an optimal control profile from the calculus of variations solution, the near-minimum time solution can be computed quickly and easily compared to the exact optimal control from a TPBVP solution. Other advantages of parameter optimization is its acceptance of included control shaping techniques and maximum fuel limits for the maneuver. This computational speed in finding a solution and the ease with which equality and inequality constraints can be added to the problem formulation will make parameter optimization invaluable for designing controls quickly to test on the actual ASTREX structure. However, the main role of the computed near-minimum time control is to provide a standard against which future real-time controllers will be matched to determine their relative performance.

The ASTREX Test Article

The ASTREX (Advanced Space Structures Technology Research Experiment) test article at Phillips Laboratory, Edwards AFB, CA, is a 5155 kg (11,356 lb.) dynamically-scaled structural model of a 3-mirror Space-Based Laser beam expander. The test article is balanced at the hub on an airbearing system that applies a 210 psi compressed airflow cushion under a hemispherical ball mounted at the top of a 5-meter vertical pedestal. The test article itself consists of three major sections:

1. The *Primary Structure* is a 5.5-meter diameter truss constructed of over 100-7.5 cm diameter graphite epoxy tubes with aluminum end fittings that are attached to star node connections. The primary structure includes six sets of steel plates mounted on its face to simulate the primary mirror and two cylindrical masses mounted on its sides to simulate tracker telescopes. A pair of

30 gallon air tanks are attached inside the hub directly above the air-bearing system.

2. The *Secondary Structure* is a triangular structure which houses the reaction wheel actuator and the mass designed to simulate the secondary mirror. It is connected to the primary truss by a tripod arrangement of three 5.1-meter graphite-epoxy tubes manufactured with embedded sensors and actuators.

3. The *Tertiary Structure* is a structure designed to hold the electronics and power supply for the data acquisition and control (DAC) system and other masses to balance the secondary mirror.

Figure 1 shows a diagram of the trusses and their major components.⁷

The large-angle retargeting capability is provided with the Cold Gas Reaction Control system, which consists of four pairs of 900 N (200 lbf) thrusters and six pairs of 36 N (8 lbf) thrusters mounted on the edges of the hexagonal primary truss. Pressurized air (up to 500 psi) from the two 30 gallon tanks inside the hub is fed to the thrusters through a series of air hoses, ball valves and air filters. An external compressor on the ground can require approximately fifteen minutes after each maneuver to repressurize the air tanks. Using these thrusters, the ASTREX structure can safely slew at a maximum safe rotation speed and acceleration of $10^\circ/\text{sec.}$ and $10^\circ/\text{sec.}^2$ respectively.

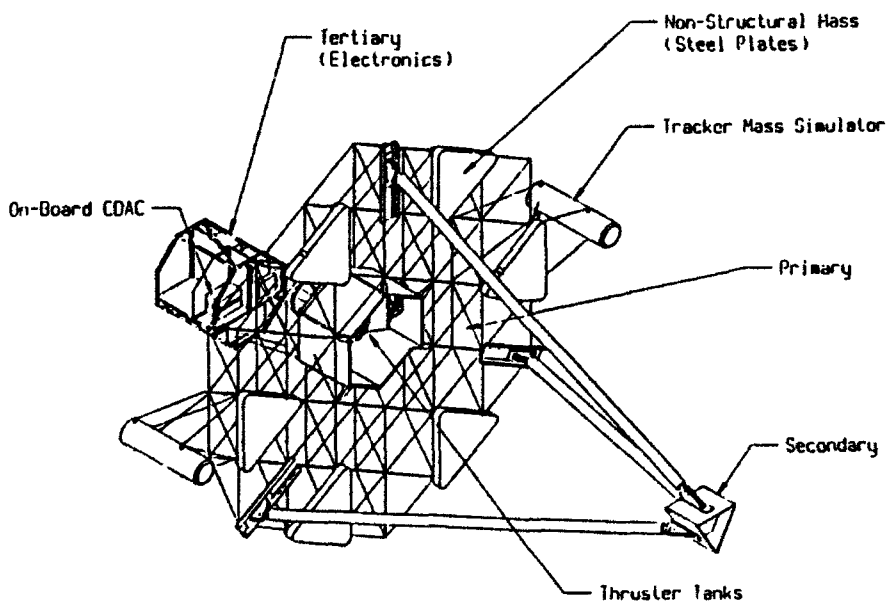


Figure 1. Components of the ASTREX Test Article

The real-time Control and Data Acquisition Computer (CDAC), which includes a VAXstation 3100 workstation as a front end, an INTEL 80386/Weitek 3167-based parallel processor unit, and an input/output unit having 32 input and 32 output channels for analog data as well as 64 bits of digital I/O, acquires data from the position encoder, the rate sensors and linear accelerometers. In addition, the CDAC system can compute a real-time control (if the algorithm is provided by the user) and command the actuators using the MatrixX/Autocode software on the VAXstation 3100 workstation. A high speed data link connects the CDAC input/output unit mounted on the tertiary with the parallel processor unit on the ground.

Three optical position encoders, which are mounted on an actively-controlled, double-gimbal 3-axis cable follower that follows the test article rotation, record the position counts during the rotation; each encoder is sensitive to 3 μ rad. From the position counts, the cable follower computer calculates the test article attitude in quaternions and sends the data to the parallel processor unit through SCSI cabling. More than a simple mount for the position encoder, the cable follower also allows external electrical, pneumatic, and communication lines to be connected to the test article without introducing dominating disturbance moments to the system.⁸

Mathematical Model

In the rigid-body motion model, two reference frames are employed:

1. the *pedestal axis* is an inertially-fixed reference frame which points in the true vertical and true horizon plane; the ASTREX rest position is pitch down 30° in this coordinate system
2. the *test article axis* is the body-fixed reference frame

As shown in Figure 2, the origin for both systems is the pivot point, the location where the test article is attached to the pedestal at the air bearing.

In this paper, maneuvers are described with Euler angles (1-2-3 set) for an intuitive understanding of the motion. However, quaternions are employed in the computer model to avoid singularities and more importantly, to have a simpler equation for integration. The differential equation for the Euler parameters is given as:

$$\dot{\underline{\beta}} = \frac{1}{2}G(\omega)\underline{\beta} \quad (1)$$

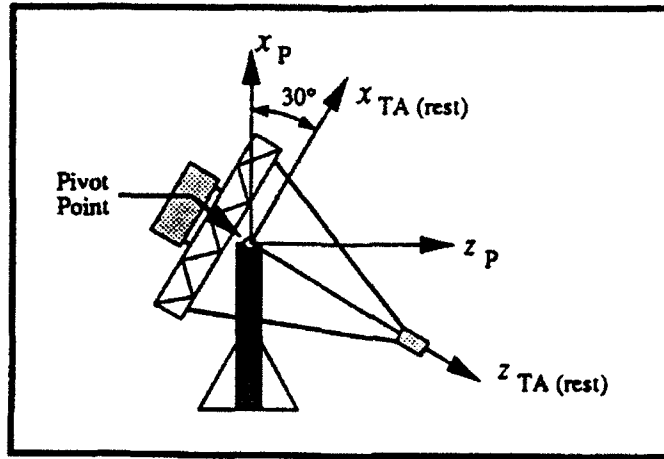


Figure 2. Reference Frames for Rigid-Body Rotational Motion

where the quaternions β are in the pedestal axis and the matrix $G(\omega)$ is given by:

$$G(\omega) = \begin{bmatrix} 0 & -\omega_1 & -\omega_2 & -\omega_3 \\ \omega_1 & 0 & \omega_3 & -\omega_2 \\ \omega_2 & -\omega_3 & 0 & \omega_1 \\ \omega_3 & \omega_2 & -\omega_1 & 0 \end{bmatrix} \quad (2)$$

The ω 's represent the angular velocity components in the body axis.⁹

The moment for a basic rotation of a body in three-dimensions is given as:

$$\underline{M} = I \underline{\dot{\omega}} + \tilde{\omega} I \underline{\omega} \quad (3)$$

I designates the inertia matrix in body axis and the tilde over a vector in this paper (such as ω above) represents the cross-product matrix of that vector. The control \underline{u} is a non-dimensional vector with values in the range of $[-1, +1]$. The location of each thruster and its relationship to the \underline{u} vector is given in Table 1. The control matrix B is calculated from entering that information in the following moment equation.

$$\underline{M} = \underline{r} \times \underline{F} \quad (4)$$

Since this equation is valid for any force acting on a rotating body, the moment caused by a center of gravity which does not coincide with the pivot point can also be determined with this formula.

$$\underline{M}_{cg} = \tilde{r}_{cg} C(\theta_1, \theta_2, \theta_3) \begin{Bmatrix} -mg \\ 0 \\ 0 \end{Bmatrix} \quad (5)$$

Table 1. Individual Thruster Position and Control Relationship

| Thruster # | Node # | X _{ta} (m) | Y _{ta} (m) | Z _{ta} (m) | Thr. Magn. (lb) & Dir. | Relation to u |
|------------|--------|---------------------|---------------------|---------------------|---------------------------|------------------|
| 1 | 327 | -1.35 | -2.7116 | -0.374655 | -8 | u ₁ |
| 2 | 325 | 1.35 | -2.7116 | -0.374655 | +8 | -u ₂ |
| 3 | 321 | 1.35 | 2.7116 | -0.374655 | -8 | -u ₁ |
| 4 | 323 | -1.35 | 2.7116 | -0.374655 | +8 | u ₂ |
| 5 | 427 | -2.82649 | 0.0 | -0.172850 | +8 | -u ₃ |
| 6 | 437 | 2.82649 | 0.0 | -0.172850 | -8 | -u ₃ |
| 7 (1-2) | 324 | -1.35 | 2.5465 | -0.374655 | +200 | u ₂ |
| 8 (3-4) | 328 | -1.35 | -2.5465 | -0.374655 | -200 | u ₁ |
| 9 (5-6) | 322 | 1.35 | 2.5465 | -0.374655 | -200 | -u ₁ |
| 10 (7-8) | 326 | 1.35 | -2.5465 | -0.374655 | +200 | -u ₂ |

A moment is also included to model the effect of hanging cables on the rotation of the ASTREX structure. The cable follower is designed to prevent the attached cabling from causing disturbances which will significantly affect the test article rotation; currently, many cables are not attached and simply hang down from the primary and tertiary trusses. The reasons behind this anomaly is the complexity in removing and reattaching the cables while subsystems continue to be added, as well as unexpected cable follower motion from the tracking controller of the cable follower assuming the pull of intertwined cables meant the test article was in motion. To model this significant disturbance of the cables, a spring-like damping moment is added when the ASTREX structure moves away from its rest position.

$$\underline{M}_{cable} = -D_{\theta_3}(\theta_3) K_{\theta} d\theta_{rest} \quad (6)$$

D_{θ_3} is a coordinate transformation of θ_3 degrees about the roll axis, while K_{θ} is a diagonal matrix of the spring constants for the yaw, pitch, and roll respectively. The difference between the current Euler angles and the rest position for the structure is given in the vector $d\theta_{rest}$. The total external moment applied to the ASTREX structure is given by the following summation.

$$\underline{M} = \underline{B}\underline{u} + \underline{M}_{cg} + \underline{M}_{cable} \quad (7)$$

The maximum pressure in the air tanks that supply the pressurized air to the thrusters is 500 psi. Readings from the ASTREX pressure system during an actual maneuver indicate only 430 psi is available at the beginning of the maneuver due to pressure losses at the ball valve, etc. From this information, the average pressure drop is assumed to be about 300 psi. The following equation uses this assumed pressure drop to determine the volume of pressurized air available for each maneuver.

$$V_{Available} = 2 V_{Tank} \frac{\Delta p}{p_{atm}} \quad (8)$$

The multiple of two in this equation indicates the two air tanks. The computed volume for the available pressurized air is 163.33 ft³. To verify the final pressure drop is less than this amount, the rate at which the volume of pressurized air in the tanks is depleted must be integrated. The differential equation for this depletion is given by:

$$\dot{V}_{air} = 2 K_{air} \sum |u_i| \quad (9)$$

where K_{air} is a thruster calibration constant of 0.2334 ft³/lb.

The equations of motion for ASTREX and the depletion rate of the pressurized air volume in the air tanks are combined to form the state equations for the model.

$$\dot{\underline{x}} = \begin{Bmatrix} \dot{\underline{\beta}} \\ \dot{\underline{\omega}} \\ \dot{V}_{air} \end{Bmatrix} = \begin{Bmatrix} \frac{1}{2} G(\omega) \underline{\beta} \\ I^{-1} [B \underline{u} - \tilde{\omega} I \underline{\omega} - m g \tilde{r}_{cg} C(\theta_1, \theta_2, \theta_3)(:,1) - D_{\theta}(\theta_3) K_{\theta} \underline{d\theta}_{ran}] \\ 2 K_{air} \sum |u_i| \end{Bmatrix} \quad (10)$$

Problem Formulation

The basic problem is to move the ASTREX test article from one state (position and velocity) to a second state in minimum time. Since a fuel constraint is imposed on this problem, the optimal control is no longer the unconstrained optimal minimum-time control predicted from calculus of variations. Calculus of variations can solve for the optimal control for a minimum time maneuver with an imposed fuel constraint; unfortunately, the form of that control cannot be parametrized. Therefore, the researcher must choose an optimal control profile which can be parametrized, apply the fuel constraint in the parameter optimization problem, and hope that the determined near-minimum time solution is close to the exact optimal control with the applied constraint.

Two optimal control profiles which can be parametrized are the minimum time problem and the minimum fuel problem. Since it is unknown how the fuel constraint will affect the problem, both profiles will be tested in the numerical studies using the SQP algorithm. The following section develops the calculus of variations origin for the unconstrained optimal minimum time and minimum fuel control profile.

Optimal Minimum Time Control

Using calculus of variations, the minimum-time control is formulated as:

$$\text{Minimize } J = p_0 \text{ subject to: } \dot{\underline{x}}' = p_0 \dot{\underline{x}} \quad (11)$$

p_0 designates the final time of the maneuver; the state equations from the previous section are normalized in time such that the maneuver time will vary from 0 to 1. Since each thruster has a maximum saturation limit (of 8lb. or 200 lb.), a control constraint must be placed on the problem to ensure the control solution does not go outside of this range. Using Pontryagin's principle, the control constraint is applied.

$$H(\underline{x}^*, \underline{\lambda}^*, \underline{u}, t) \geq H(\underline{x}^*, \underline{\lambda}^*, \underline{u}^*, t) \quad (12)$$

This equation simply states that the Hamiltonian of the optimal control (denoted by the asterisk) will be less than the Hamiltonian for any other applied control. By looking at the terms that are multiplied by \underline{u} in the Hamiltonian, the researcher can decide the value of \underline{u} which will minimize the product of those terms and the \underline{u} vector. Recall that the non-dimensional control vector \underline{u} was previously limited to $[-1, +1]$. Therefore, the optimal control is divided into three regions:

$$S_i = \underline{\lambda}^T \frac{\partial \dot{\underline{x}}}{\partial \underline{u}'} \begin{cases} < 0, & u_i = +1 \\ > 0, & u_i = -1 \\ = 0, & u_i \text{ is Singular} \end{cases} \quad (13)$$

S_i is defined as the switching function; it defines the control for each instant of time during the maneuver. In the case where the switching function is zero, the control is singular (undefined by Pontryagin's principle). As long as the switching function does not remain zero for a finite time interval, the control will be bang-bang; in other words, the control will alternate between fully saturated controls in opposing directions. For nonlinear systems, the exact number of switches between these saturated controls in opposite directions can not be determined.^{10,11}

Optimal Minimum Fuel Control

In the same manner as above, the minimum fuel control problem is stated.

$$\text{Minimize } J = \int_0^1 |\underline{u}(t)| dt \text{ subject to: } \dot{\underline{x}}' = p_0 \dot{\underline{x}} \quad (14)$$

Using Pontryagin's principle to apply the control constraint, the following control values are determined to be possible depending on the switching function value.

$$S_i = \underline{\lambda}^T \frac{\partial \dot{\underline{x}}}{\partial \underline{u}'} \begin{cases} < -1, u_i = +1 \\ > -1 \text{ \& } < +1, u_i = 0 \\ > 1, u_i = -1 \\ = +1 \\ = -1 \end{cases} \left. \vphantom{\begin{matrix} < -1, u_i = +1 \\ > -1 \text{ \& } < +1, u_i = 0 \\ > 1, u_i = -1 \\ = +1 \\ = -1 \end{matrix}} \right\} u_i \text{ is Singular} \quad (15)$$

Assuming the singular region is not finite, this control will be bang-off-bang; the control will fully saturate, shut off (during this time, the structure will coast), and then fully saturate in the opposite direction. Again, in this case, the number of switches between these regions can not be determined in advance of the simulation.^{10,11}

Parameter Optimization

Both the optimal minimum time and optimal minimum fuel problems act in the state-costate space. Due to the difficulty of this solution process, parameter optimization is considered instead, as an easier method to solve the minimum time problem. The bang-bang (optimal minimum time) control and the bang-off-bang (optimal minimum fuel) control are parametrized, so that a parameter set can define the shape of each control. For example, the bang-bang control can be parametrized by:

- Initial Saturation Control, p_{init}
- Switch Times, p_{sw}

while the bang-off-bang control can be defined by:

- Individual Saturation Control, p_{sat}
- Smoothing Multiplier Rise Time, p_{rise}

These parameters are optimized for the performance index and the given boundary conditions by using the *Sequential Quadratic Programming* (SQP) algorithm, which solves non-linear programming problems.

The problem is constructed by first defining the performance index, the equality and inequality constraints, and the inclusive upper and lower parameter limits.

$$\text{Minimize } J = f(p) \text{ subject to: } \begin{cases} g_j(p) = 0 \\ g_i(p) \geq 0 \\ p_{lower} \leq p \leq p_{upper} \end{cases} \quad (16)$$

To solve for the parameter change at each iteration, a quadratic programming subproblem must also be solved.

$$\begin{aligned} & \text{Minimize } \frac{1}{2} \underline{\Delta p}^T B_k \underline{\Delta p} + \nabla f(p)^T \underline{\Delta p} \\ & \text{subject to: } \begin{cases} \nabla g_j(p)^T \underline{\Delta p} + g_j(p) = 0 \\ \nabla g_i(p)^T \underline{\Delta p} + g_i(p) \geq 0 \\ p_{\text{lower}} - p_k \leq \underline{\Delta p} \leq p_{\text{upper}} - p_k \end{cases} \end{aligned} \quad (17)$$

B_k is the positive definite approximation to the Hessian; it will be modified using the modified BFGS or David-Fletcher-Powell method, if the subproblem constraints are not satisfied in each iteration. Note that infeasible points are then possible during the solution process. The gradients of the performance index, the equality constraints and the inequality constraints can either be solved analytically or using finite difference methods. To find the best update for the parameters at each iteration, a one-dimension search solves for the appropriate multiplier ϵ to determine the next set of parameters which minimizes the augmented Lagrangian function.¹²

$$p_{k+1} = p_k + \epsilon \underline{\Delta p}, \quad \text{where } \epsilon \in (0,1) \quad (18)$$

The one-dimensional search multiplier is constrained between 0 and 1.

Applying this method to the bang-bang parameters, the problem is formulated as:

$$\text{Minimize } J = \frac{1}{2} p_0^2 \text{ subject to: } \begin{cases} \underline{x}_f - \frac{\partial \underline{x}_{bc}(1)}{\partial \underline{p}} \underline{p} = 0 \\ V_{\text{Available}} - \int_0^1 \dot{V}_{\text{air}} d\tau \geq 0 \\ 1^* \leq p_0 \leq 60^* \\ -1 \leq \underline{p}_{\text{init}} \leq +1 \\ 0 \leq \underline{p}_{\text{rev}} \leq 1 \end{cases} \quad (19)$$

\underline{x}_f defines the final desired boundary condition states, while the integrated states are given by:

$$\underline{x}_{bc}^T = [\beta_1 \quad \beta_2 \quad \beta_3 \quad \omega_1 \quad \omega_2 \quad \omega_3] \quad (20)$$

The asterisks in the above equation represent numbers which are arbitrarily chosen to satisfy the form for the SQP problem. The formulation for the bang-off-bang problem using the SQP method is given below.

$$\text{Minimize } J = \frac{1}{2} p_0^2 \text{ subject to: } \begin{cases} \underline{x}_f - \frac{\partial \underline{x}_{bc}(1)}{\partial \underline{p}} \underline{p} = 0 \\ V_{\text{Available}} - \int_0^1 \dot{V}_{\text{air}} d\tau \geq 0 \\ 1^* \leq p_0 \leq 60^* \\ -1 \leq \underline{p}_{\text{sat}} \leq +1 \\ 0.05^* \leq \underline{p}_{\text{rise}} \leq 0.25 \end{cases} \quad (21)$$

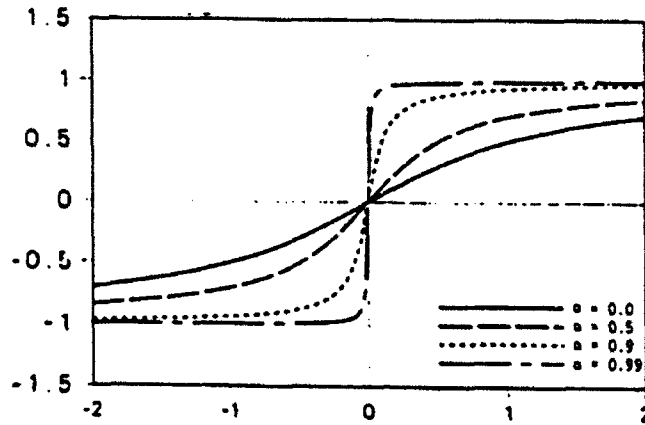


Figure 3. Effect of Smoothing Parameter on Sign Function Approximation

With the problem in this form, a commercial SQP algorithm such as the one included in the IMSL Math Libraries can be used to optimize the parameters with little programming effort by the researcher.

Control Shaping

As mentioned in the introduction, control shaping is necessary to alleviate many real-world problems in applying an optimal minimum time or minimum fuel control. The bang-bang control can be represented as:

$$u_i = -p_{init} \text{sign}(S_i) \quad (22)$$

where p_{init} is the initial saturation control and S_i represents the switching function. The switching function can also be designated as a function of the parameters by setting it equal to the non-dimensional time differences between the current maneuver time and the switch times. For example, for a single axis, the switching function for a six-switch control might be:

$$S_i = (\tau - p_{sw1})(\tau - p_{sw2}) \quad (23)$$

By finding an approximate function to replace the discontinuity of the sign function, the bang-bang control can be smoothed. Thompson, Junkins and Vadali chose an inverse tangent function.⁴

$$\text{sign}(S_i) = \frac{2}{\pi} \tan^{-1} \left(\frac{S_i}{1 - \alpha_{sm}} \right), \quad \alpha_{sm} \in [0, 1) \quad (24)$$

Figure 3 shows how the smoothing parameter α_{sm} in this equation alters the function shape from a sine wave to a bang-bang control.

With the sign function approximation, smoothing is applied at each switch but the beginning and end of the maneuver still have discontinuous control jumps as the control is turned on and off respectively. A multiplier function can apply a smooth third-order polynomial control transition as the control is turned on or off.

$$m(\eta) = \eta^2(3 - 2\eta), \quad \eta \in [0, 1] \quad (25)$$

In this equation, η defines whether the control is off, saturated, or undergoing a smooth transition between two control levels.

$$\eta(\tau) = \begin{cases} 0, & \text{No Control} \\ 1, & \text{Saturated Control} \\ y_2 + (y_2 - y_1) \frac{\tau - \tau_{sat}}{\tau_{rise}}, & \text{Smooth Start} \\ y_1 + (y_2 - y_1) \frac{\tau - \tau_{sat}}{\tau_{rise}}, & \text{Smooth Stop} \end{cases} \quad (26)$$

The researcher defines the non-dimensional rise time τ_{rise} and the non-dimensional time that the saturated control occurs τ_{sat} . The initial control magnitude y_1 and the final control magnitude after the rise time y_2 are also needed. Using this user-supplied information, the normalized maneuver time τ determines the function value.

The bang-off-bang does not directly switch from a saturation control in one direction to a saturation control in the other. Therefore, the approximation for the sign function is not needed to smooth this control; the control can be defined simply by using the multiplier function $m(\eta)$. Considering each saturated control as an impulse, the impulse is formed by a smooth start immediately followed by a smooth stop using the η function.

Numerical Results

The current mass of the ASTREX structure is 5155 kg. From the finite element model, the following ASTREX moment of inertia matrix in the test article axis has been determined.

$$I = \begin{bmatrix} 22,205. & -14.63 & -225.06 \\ -14.63 & 15,705. & -8.16 \\ -225.06 & -8.16 & 22,395. \end{bmatrix} \text{ kg} \cdot \text{m}^2$$

For the following tests, each control combination is defined as the maximum saturated control for the thrusters in the yaw, pitch, and roll (test article axis) directions respectively. [Thrusters with different maximum saturated controls will not be applied together about an individual body axis.] Using this convention, the control combinations and their control matrices that are used in the following analyses are presented.

1. 8-8-8 Combination

$$B = \begin{bmatrix} 167.14 & 167.14 & 0. \\ -83.21 & 83.21 & 0. \\ -96.49 & -96.49 & 201.17 \end{bmatrix} N-m$$

2. 200-200-8 Combination

$$B = \begin{bmatrix} 3924.1 & 3924.1 & 0. \\ -2080.3 & 2080.3 & 0. \\ -2265.6 & -2265.6 & 201.2 \end{bmatrix} N-m$$

Each of the following tests includes all components of the rigid-body motion simulation : the gyroscopic motion, the gravity gradient, and the cable damping. The center of gravity location in the test article axis is:

$$L_{cg} = [-3.5019 \quad 0.2491 \quad -5.5206] 10^{-4} m$$

The matrix for the cable damping spring constants has been experimentally determined as:

$$K_{\theta} = \text{diag}([5 \quad 2000 \quad 500]) \frac{N-m}{rad}$$

With this structural information, the state equations can be integrated.

To define each maneuver, the researcher must specify: the control profile, the thruster combination, the smoothing parameter for the sign approximation, the non-dimensional rise time for the multiplier function, and the fuel constraint. The smoothing parameter α_{sm} in the following analyses is 0.99; remember that $\alpha_{sm} = 1$ is the best approximation for the bang-bang control. All of the following SQP solutions are for slewing the ASTREX test article 150° about the yaw maneuver in minimum time. Table 2 displays the effect of the user-supplied maneuver criteria given in the list above.

Table 2. Comparison of SQP Solutions for an ASTREX 150° Yaw Maneuver

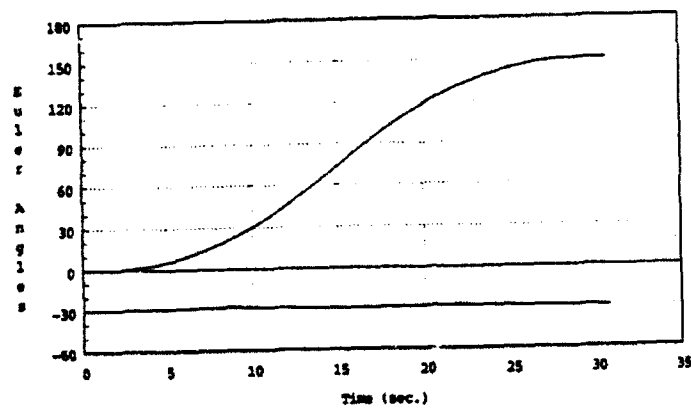
| Test No. | Control Profile | Thruster Combination | Non-Dimensional Rise Time | Needed Volume of Pressurized Air (ft ³) | Maneuver Time (sec) |
|----------|--------------------|----------------------|---------------------------|---|---------------------|
| 1 | 3-Switch Bang-Bang | 8-8-8 | 0.10 | 166.45* | 28.56 |
| 2 | 6-Switch Bang-Bang | 8-8-8 | 0.10 | 163.33 | 29.32 |
| 3 | 6-Switch Bang-Bang | 200-200-8 | 0.10 | 863.14* | 5.92 |
| 4 | 6-Switch Bang-Bang | 200-200-8 | 0.10 | 163.33 | 30.63 |
| 5 | Bang-Off-Bang | 200-200-8 | 0.10 | 163.32 | 18.43 |
| 6 | Bang-Off-Bang | 200-200-8 | 0.05 | 163.33 | 16.43 |

The asterisks in the needed pressurized air volume denote the numerical studies where the fuel constraint is not applied. For a bang-bang control using the 8-8-8 thruster combination, the fuel constraint does not change the maneuver time or the volume of pressurized air. However, the fuel constraint on the 200-200-8 thruster combination makes the maneuver time five times longer than the unconstrained bang-bang case. Of course, the unconstrained bang-bang maneuver in Test 3 is using a similar five times increase in the needed pressurized air volume. An important observation is that the maneuver time for the constrained 8-8-8 thruster combination and the constrained 200-200-8 combination is very similar; this suggests the fuel constraint for the bang-bang control is unable to utilize additional thrust capabilities greater than the 8-8-8 thruster combination. Therefore, the bang-off-bang control in Test 5 is investigated to determine if the coast maneuver between the saturated bang-bang controls will permit a faster maneuver time. Fortunately, the bang-off-bang maneuver time is only 0.6 times that of the bang-bang control with the fuel constraint.

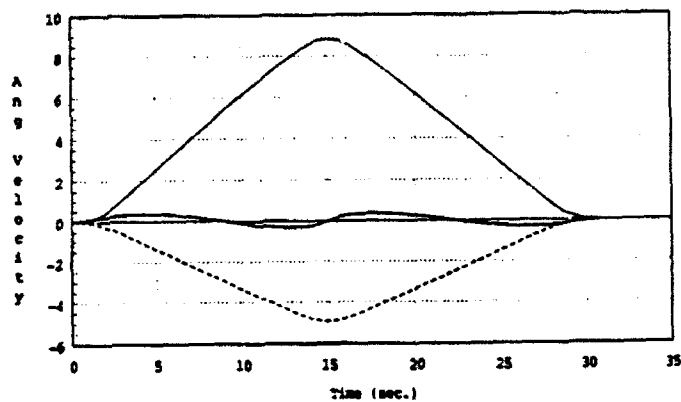
The importance of the smoothing multiplier non-dimensional rise time on the maneuver time is also investigated. The non-dimensional rise time can be arbitrarily defined in the range (0.0, 0.25); obviously, the greater rise time will produce less excitation to the flexible structure. In the previous tests, the non-dimensional rise time is set at 0.1; for Test 6, the rise time is decreased to 0.05 to observe how the maneuver time is affected. Since the control in each axis for a bang-off-bang control includes four rise times, the time decrease is expected to be between 0 and 0.2 of the non-dimensional maneuver time. The maneuver time actually decreased by two seconds or 0.1 of the non-dimensional maneuver time for Test 5.

Figures 4 and 5 show the Euler angles and angular velocity of the ASTREX structure for the given control history from Test 4 and Test 5 respectively. In both cases, the maneuver is primarily a smoothed third-order polynomial slew only in the yaw axis. Despite the faster maneuver time, the bang-off-bang control only reaches the same maximum maneuver velocity in the yaw and pitch axis of the body axis as the bang-bang control. Notice the bang-off-bang control in Figure 5 (c) uses about seven times the thrust of the bang-bang control in Figure 4 (c). The maneuver time reduction of the bang-off-bang control results from this ability to harness the higher thruster forces with the given fuel constraint.

(a) Euler Angles (deg)



(b) Angular Velocity (deg/sec)



(c) Thrust Control Profile (lb.)

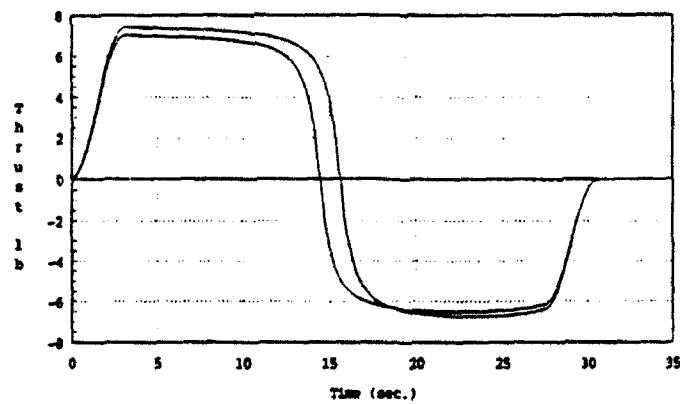
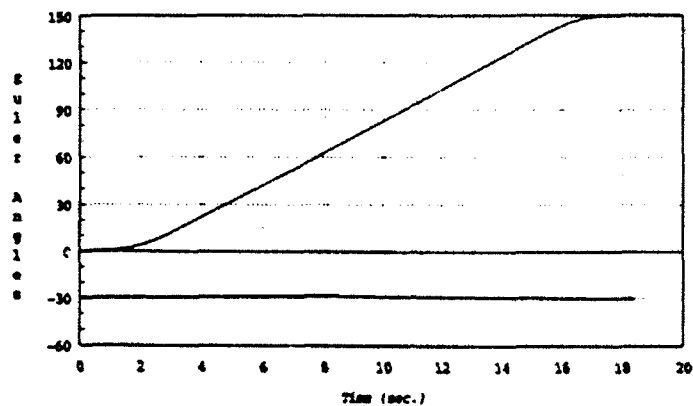
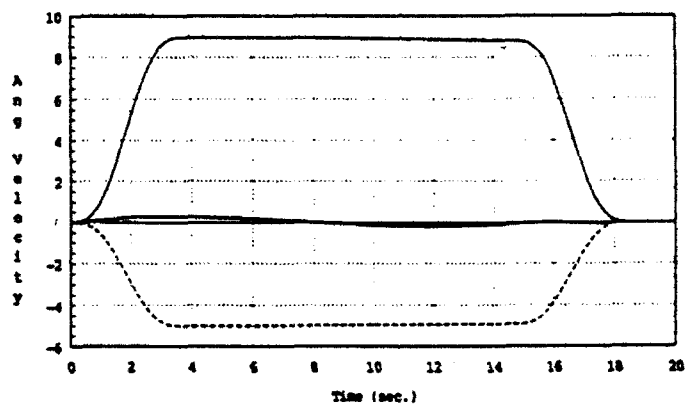


Figure 4. Bang-Bang Control for an ASTREX 150° Yaw Maneuver (Test 4)

(a) Euler Angles (deg)



(b) Angular Velocity (deg/sec)



(c) Thrust Control Profile (lb.)

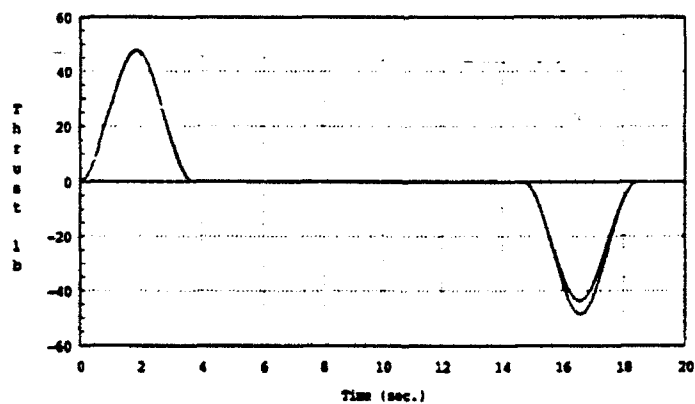


Figure 5. Bang-Off-Bang Control for an ASTREX 150° Yaw Maneuver (Test 5)

Conclusions

Parameter optimization has obvious computational speed advantages by solving for the near-minimum time control rather than the exact optimal control from the traditional TPBVP; however, the researcher should carefully choose the control profile to be parametrized to ensure the minimum time solution if parameter optimization is used when control or state constraints are added to the problem. The numerical results for the ASTREX large-angle maneuver show that the SQP solution based on the bang-bang control is unable to utilize the higher thrust potential of the 200 lb. thrusters with the imposed fuel constraints; in this situation, the bang-off-bang control solution generates higher torques to complete the maneuver in less time. On the other hand, at a certain rotation angle for small-angle rotations, the bang-bang control rather than the bang-off-bang control is the time-optimal control when the fuel limitation is no longer the dominating factor.

Although most flexible spacecraft will not be limited to the harsh fuel constraints imposed on the ASTREX test article, fuel constraints are still present. Future research needs to develop methods to predict the transition point (rotation angle) where bang-off-bang profiles should replace the bang-bang profile to determine the near-minimum time control. On the ASTREX structure, numerical studies will determine if the reduction in maneuver time for small-angle rotations is sufficient to use a different control profile for that region. At the same time, after the position encoder and angular rate sensors are operational on the test article, the controls generated by the SQP algorithm will be tested in experimental maneuvers to verify the rigid-body model accuracy and to analyze how successful the control shaping is suppressing vibrations.

Acknowledgments

I would like to thank the staff at Research & Development Laboratories who provided me with essential information about the AFOSR requirements and procedures. Dr. Alok Das and Lt. Derek Cossey of Phillips Laboratory assisted me throughout the summer in making my stay at the ASTREX facility both friendly and productive. My deep appreciation goes to Dr. N.S. Abhyankar of Dynacs, Inc. whose knowledge of the ASTREX test article prevented many errors in my work. Finally, I would like to thank my advisor Dr. S.R. Vadali of Texas A&M University for his patience and long-distance guidance in this research.

References

- ¹Li, F. and Bainum, P.M. "An Improved Shooting Method for Solving Minimum-Time Maneuver Problems", Paper presented at ASME Winter Annual Meeting, Dallas, November 1990.
- ²Billimoria, K.D. and Wie, B. "Minimum Time Large Angle Reorientation of a Rigid Spacecraft". AIAA Paper 90-3486, AIAA Guidance, Navigation, and Control Conference, Portland, Oregon, August 1990.
- ³Byers, R.M., Vadali, S.R. and Pollock, T.C. "Feedforward/Feedback Control for Near Time-Optimal Spacecraft Reorientation", Paper AAS 91-406 presented at the AAS/AIAA Astrodynamics Specialist Conference, Durango, CO, August 1991.
- ⁴Thompson, R.C., Junkins, J.L. and Vadali, S.R. "Near-Minimum Time Open-Loop Slewing of Flexible Vehicles," *Journal of Guidance, Navigation & Control* Vol. 12, No. 1, Jan-Feb 1989, pp. 82-88.
- ⁵Byers, R.M., Vadali, S.R., and Junkins, J.L. "Near-Minimum Time Closed-Loop Slewing of Flexible Spacecraft" *Journal of Guidance, Control & Dynamics*, Vol.13, No.1, Jan.-Feb. 1990, pp.57-65.
- ⁶Junkins, J.L., Rahman, Z., Bang, H., "Near-Minimum-Time Control of Distributed Parameter Systems: Analytical and Experimental Results" *Journal of Guidance, Control & Dynamics*, Vol.14, No.2, Mar.-Apr. 1991, pp. 406-415.
- ⁷Abhyankar, N.S., Ramakrishnan, J., et al. "Modeling, System Identification and Control of ASTREX", Paper presented at the NASA/DOD Controls-Structures Interaction Technology Conference, Lake Tahoe, NV, March 1992.
- ⁸Das, A., Berg J.L., et al. *ASTREX - A Unique Test Bed for CSI Research*, Paper presented at the 29th IEEE Conference on Decision and Control, December 1990.
- ⁹Junkins, J.L. and Turner, J.D. *Optimal Spacecraft Rotational Maneuvers*, Elsevier Scientific, Amsterdam, Holland, 1985.
- ¹⁰Kirk, D.E. *Optimal Control Theory*, Prentice-Hall, Inc., Englewood Cliffs, NJ, 1970.
- ¹¹Bryson, A.E. and Ho, Y.-C. *Applied Optimal Control*, Hemisphere Publishing Corporation, Washington, D.C., 1975.
- ¹²IMSL Math/Library, Edition 1.1, IMSL Inc., Houston, December 1989.

HIGH TEMPERATURE ABSORPTION SPECTROSCOPY
OF Na/LI MIXTURES
FOR APPLICATION TO SOLAR PLASMA PROPULSION

Paul S. Erdman
Candidate
Doctor of Philosophy
Department of Physics and Astronomy
University of Iowa
Iowa City, IA 52242

Final Report for:
Summer Research Program
Phillips Laboratory

Sponsored by:
Air Force Office of Scientific Research
Edwards Air Force Base, CA

September 1992

HIGH TEMPERATURE ABSORPTION SPECTROSCOPY
OF NA/LI MIXTURES
FOR APPLICATION TO SOLAR PLASMA PROPULSION

Paul S. Erdman
Candidate
Doctor of Philosophy
Department of Physics and Astronomy
University of Iowa

Abstract

The solar plasma propulsion concept involves absorbing solar energy directly into the propellant of the rocket. Materials which would work well as solar absorbers and high specific impulse propellants would be high pressure hydrogen gas seeded with alkali metals such as lithium and sodium. To study the absorption characteristics of the various alkali metal candidates under high temperature and pressure the Plasma Spectroscopy Cell (PSC) has been constructed. The PSC has been operated up to 2100 Kelvin at one atmosphere to study the optical absorption of sodium/lithium mixtures in the range of 330 to 900 nm. Strong absorption features have been observed and have tentatively been assigned to various atomic and molecular transitions.

HIGH TEMPERATURE ABSORPTION SPECTROSCOPY OF Na/Li MIXTURES FOR APPLICATION TO SOLAR PLASMA PROPULSION

Paul S. Erdman

INTRODUCTION

A proposed method of propelling spacecraft is to directly energize the rocket propellant to high temperature using concentrated solar energy [1]. Since the energy output of the sun is mostly in the visible to one micron range, the propellant should be chosen to absorb well at these wavelengths. Hydrogen is typically chosen as a propellant in many propulsion schemes because its low mass gives it a high specific impulse, but hydrogen lacks the ability to absorb in the visible and near visible wavelengths. A seedant which absorbs well in the visible region could be added to the hydrogen propellant. The question then becomes how well the seedant and possible hydrides formed in the high temperature and pressure environment of the rocket engine would be able to absorb the solar energy. To answer that question, the Plasma Spectroscopy Cell (PSC) has been constructed to enable researchers to study the spectroscopy of potential seedant elements and the possible hydrides under the conditions of extreme temperature and pressure.

PROBLEM

Alkali metal vapors are already known to be strong absorbers in the visible and near infrared region of the spectrum [2]. The ideal choice for a seedant would then be lithium, the lightest of the alkali metals, since it offers high optical absorption and high specific impulse.

Last year work on this project showed that atomic lithium and diatomic lithium at temperatures up to 1793 Kelvin and one atmosphere of pressure would absorb well in the wavelength regions of 450 to 570 nm (the B-X transition of Li_2) and 610 to 750

nm (the A-X transition and triplet absorption of Li_2 as well as the 2s-2p atomic transition). The spectroscopic range of these experiments was limited to 450 to 750 nm.

The weak area of absorption in the above lithium data was the 570 to 610 nm region. However, the broadening of the 2s-2p atomic line and the presence of the sodium (an impurity in our Li sample) D line at 589 nm suggested that the addition of sodium to the absorption region would be one possible way of absorbing in the 570 to 610 nm gap. The next set of experiments to be performed with the PSC would then have to be with the addition of sodium into the lithium sample. This also meant the possibility of creating the NaLi molecule which may also produce absorption in the desired wavelength range.

METHODOLOGY

The sodium/lithium sample was mixed in a zirconium crucible on a hot plate in an argon hood to prevent contamination of the sample. The sample was covered with octane to again prevent atmospheric contamination as the sample was placed into the evaporator region of the PSC and loaded into the cell.

Operation of the PSC went to maximum temperatures of 1340 C in the evaporator and 2100 K in the hot zone. Pressures were kept near 1 atmosphere.

A Princeton Instruments model TE/CCD-576T-UV spectrometer was used to collect data along one of the optical axes of the hot zone. A Xenon lamp was used as a light source to obtain absorption spectra in the wavelength range of 330 to 665 nm.

RESULTS

It would not be possible to fit the abundance of gathered data into this one report. However, a typical sample is shown in Figure 1. The spectrum shows negative absorbance as calculated by

$$A = -\ln [(\text{transmission} - \text{background}) / (I_0 - \text{background})].$$

The spectrum was taken when the evaporator was operating at 940 C and the hot zone at 1850 K. The spectrum has been scaled to emphasize the absorption features of the B-X transition of the sodium dimer peaking at 470 nm. Visible atomic lines are the 3s - 4p transition at 330 nm (the doublet is not resolved) and the broadened sodium D lines at 589 nm (also not resolved) for the 3s - 3p transition. Just to the left of the broad D lines is a feature peaked at 551 nm resulting from the triplet transition of sodium.

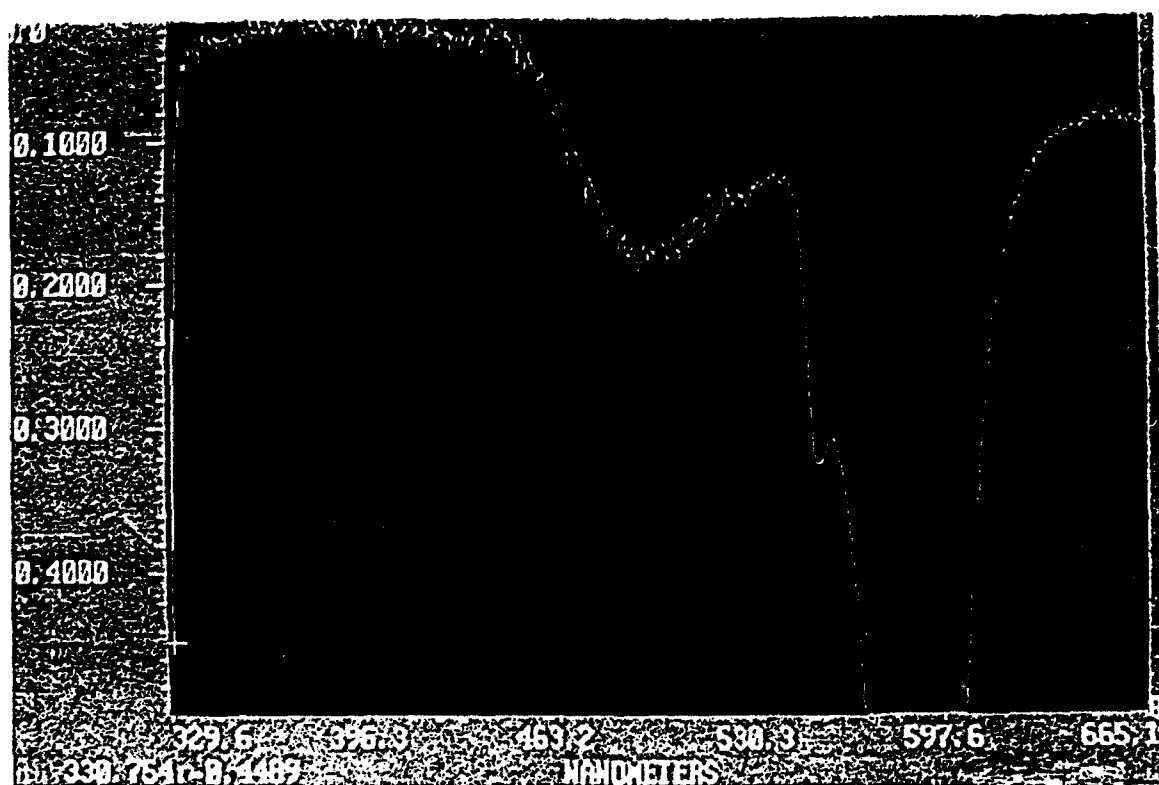


Figure 1. Negative absorbance spectrum of Na and Na₂ in the PSC. At a pressure of one atmosphere, the cell was operating at temperatures of 1340 C in the evaporator and 2100 K in the hot zone.

CONCLUSIONS

Sodium shows promise of filling the absorption gap in the 570 to 610 nm region where lithium does not absorb well. The drawback with using sodium as a propellant as compared to lithium is that sodium has a higher atomic mass and will therefore have a lower specific impulse. The tradeoff between the additional energy absorbed and the lower average specific impulse would have to be determined.

Additional work is needed in the analysis of the abundance of data collected, particularly in the positive identification of the various absorption features. The regions where Na_2 , Li_2 , and NaLi have absorption features all overlap. When the possibility exists that all molecules are present at the same time, it becomes necessary to calculate absorption profiles for the known molecules and subtract the information from the data to find out if additional features are left over which can be attributed to the unknown molecules.

Also, the temperatures given for the hot zone in this report are based upon power curves obtained with previous tests of the PSC correlated with thermocouple measurements. More accurate temperatures could be obtained using methods of calculating temperatures from spectral lines with known transition characteristics.

REFERENCES

1. Larson, C.W. (1987), "Solar Plasma Propulsion," Report AFRPL TR-85-096 of the Air Force Propulsion Laboratory, Edwards Air Force Base, California.
2. Stwalley, W.C. and Koch, M.E. (1980), "Alkali Metal Vapors: Laser Spectroscopy and Applications," *Optical Engineering*, Vol. 19, No. 1, Jan. /Feb., pp. 71-84.

LAGRANGIAN FORMULATION OF LAGEOS'S SPIN DYNAMICS

**Christopher Fuchs
Institute of Field Physics
Department of Physics and Astronomy
University of North Carolina
Chapel Hill, NC 27599-3255**

**Final Report for:
Summer Research Program
Phillips Laboratory**

**Sponsored by:
Air Force Office of Scientific Research
Bolling Air Force Base, Washington, D.C.**

September 1992

LAGRANGIAN FORMULATION OF LAGEOS'S SPIN DYNAMICS

Christopher Fuchs
Institute of Field Physics
Department of Physics and Astronomy
University of North Carolina at Chapel Hill

Abstract

The LAGEOS-III experiment is designed to verify the "magnetic components" of the earth's gravitational field predicted by General Relativity by precisely measuring the orbit and spin parameters of two satellites with complementary orbit inclination angles. In particular, the experiment will make use of a previously launched satellite (LAGEOS) and require the launching of another (LAGEOS-III, scheduled for 1993). This experiment is a component in the Air Force's effort to formulate and improve precise global timing and positioning requirements. One difficulty encountered in the project is the theoretical uncertainty in the late-time behavior of LAGEOS's spin dynamics due to the satellite's oblateness and interaction with the earth's magnetic field. Repercussions of this uncertainty surface when attempting to formulate recommendations for the LAGEOS-III orbital injection parameters. Thus a reevaluation of (at least a simple model of) LAGEOS's spin dynamics would appear advisable. Preliminary work in this direction and a more detailed discussion of the motivating issues can be found in the report of A. Kheifets¹ in this volume.

Here we carefully derive the Lagrangian governing the spin dynamics of a slightly oblate spheroidal conductor in an almost circular earth orbit. This Lagrangian takes into account both gravitational and magnetic effects and gives rise to equations of motion valid out to first time derivatives in the magnetic field. The term "slightly oblate" refers to the gravitational interaction only; as far as the magnetic interaction is concerned, the conductor is treated as perfectly spherical. We then use the resulting Lagrange equations of motion to ascertain information concerning certain time-asymptotic behaviors of LAGEOS. In particular, we show that the satellite's spin precession rate within its orbital plane is bounded even at late times. This contradicts the opposing result of Bertotti and Iess².

LAGRANGIAN FORMULATION OF LAGEOS'S SPIN DYNAMICS

Christopher Fuchs

I. INTRODUCTION

The LAGEOS-III experiment is designed to verify the "magnetic components" of the earth's gravitational field predicted by General Relativity by precisely measuring the orbit and spin parameters of two satellites with complementary orbit inclination angles. In particular, the experiment will make use of a previously launched satellite (LAGEOS) and require the launching of another (LAGEOS-III, scheduled for 1993). This experiment is a component in the Air Force's effort to formulate and improve precise global timing and positioning requirements. One difficulty encountered in the project is the theoretical uncertainty in the late-time behavior of LAGEOS's spin dynamics due to the satellite's oblateness and interaction with the earth's magnetic field. Repercussions of this uncertainty surface when attempting to formulate recommendations for the LAGEOS-III orbital injection parameters. Thus a reevaluation of (at least a simple model of) LAGEOS's spin dynamics would appear advisable. Preliminary work in this direction and a more detailed discussion of the motivating issues can be found in the report of A. Kheifets¹ in this volume.

Here we carefully derive the Lagrangian governing the spin dynamics of a slightly oblate spheroidal conductor in an almost circular earth orbit. This Lagrangian takes into account both gravitational and magnetic effects and gives rise to equations of motion valid out to first time derivatives in the magnetic field. The term "slightly oblate" refers to the gravitational interaction only; as far as the magnetic interaction is concerned, the conductor is treated as perfectly spherical. We then use the resulting Lagrange equations of motion to ascertain information concerning certain time-asymptotic behaviors of LAGEOS. This limiting behavior is effected in the equations of motion by taking the limit that the satellite's spin frequency go to zero. This connects explicitly to the time-limiting behavior through the fact this spin frequency should go to zero in time by way of Ohmic

heating due to the magnetically induced eddy currents. In particular, we show that the satellite's spin precession rate within its orbital plane is bounded even at late times. This contradicts the opposing result of Bertotti and Iess².

In actual description, as far as these considerations are concerned, the LAGEOS satellite is a fairly complex device and its spin dynamics a fairly complex problem. The bulk of its volume consists of two hollowed aluminum hemispheres bolted together along their axes of symmetry. The hollow area is filled by a more dense brass cylinder. Moreover the surface of the resulting sphere is inlaid with quite a number of cylindrical quartz retroreflectors each ~ 3 cm thick. In all the satellite forms a slightly oblate spheroid of radius ~ 30 cm. LAGEOS is in an approximately circular orbit 5900 km above the earth's surface. Its orbital inclination and period are approximately 110° and 3.75 hours respectively. As of 1989 the satellite's spin period was about 46 seconds. Note must also be made of the fact that the earth's magnetic dipole vector makes an angle of about 10° with the earth's axis and rotates about that with a period of a day. We state all this for completeness and to stress the simplifications made in the present model. Since our calculations will ultimately give only qualitative time-asymptotic behaviors, these simplifications appear reasonable.

The plan of this report is as follows. Section II below derives the model's Lagrangian. Along the way, an expression for the conductor's induced magnetic dipole moment is found. That part of the Lagrangian due to the gravitational interaction is derived in this volume by A. Kheyfets¹ and is thus taken as given here. Section III digresses from our actual problem and stresses the need for Lagrangian methods in situations such as this by means of a simple but unrelated example — the equation of motion for a neutrally charged magnetic dipole moving in the presence of an electric charge. Section IV finally exhibits the model's time-asymptotic behaviors from the consequent Lagrange equations of motion. From this the late-time boundedness of the satellite's spin precession rate can be clearly seen. Section V summarizes the results of the preceding sections, points out details requiring clarification, and avenues for further research.

II. Induced Dipole Moment and Spin Dependent Potential

By means of the nature of Lagrangian mechanics, the total Lagrangian governing the satellite's spin reduces to a simple sum:

$$L = L_g - U_m \quad (1)$$

where L_g is the Lagrangian governing the gravitational interaction and U_m is an effective potential due to the conductor's motion in a magnetic field. In this report, we take L_g as that given by Kheifets¹. The goal of this section is to derive an explicit expression for U_m . Before writing either L_g or U_m explicitly, however, we must first introduce some notation.

We take the satellite to be a slightly oblate spheroid of approximate radius a , mass m , and conductivity σ with a distance r between its and the earth's centers of mass. For the calculations we choose a body-fixed frame $\hat{1}, \hat{2}, \hat{3}$, with the axis defined by $\hat{3}$ being the axis of symmetry. Hence $I_1 = I_2 \neq I_3$ where I_k is the moment of inertia about the k 'th axis. For the actual LAGEOS satellite, $\Delta \equiv \frac{I_3 - I_1}{I_3} \approx .0335$. Finally, in order to use a Lagrangian formulation in the first place, we must introduce three independent parameters to describe the satellite's orientation. For this we use the standard eulerian angles θ, ϕ, ψ obtained from a space-fixed frame $\hat{1}, \hat{2}, \hat{3}$. We assume $\hat{3}$ orthogonal to the satellite's plane of orbit. With this choice, θ describes the angle between $\hat{3}$ and $\hat{3}$ and ϕ describes the satellite's precession about $\hat{3}$. And the components of the satellite's spin vector $\vec{\omega}$ in the body-fixed frame are³

$$\begin{aligned} \omega_1 &= \dot{\phi} \sin \theta \sin \psi + \dot{\theta} \cos \psi \\ \omega_2 &= \dot{\phi} \sin \theta \cos \psi - \dot{\theta} \sin \psi \\ \omega_3 &= \dot{\phi} \cos \theta + \dot{\psi}. \end{aligned} \quad (2)$$

With this notation we take as given

$$L_g = \frac{1}{2} I_1 (\dot{\theta}^2 + \dot{\phi}^2 \sin^2 \theta) + \frac{1}{2} I_3 (\dot{\psi} + \dot{\phi} \cos \theta)^2 + \frac{GM(I_3 - I_1)}{r^3} P_2(\cos \theta), \quad (3)$$

where G is Newton's constant, M is the earth's mass, $P_2(x) = \frac{1}{2}(3x^2 - 1)$ is a Legendre polynomial, and $\omega_0^2 = \frac{GM}{r^3}$ gives the satellite orbit frequency. Now we can move on to the problem of deriving U_m .

Heuristically our problem is quite simple. The conducting satellite spinning in the earth's magnetic field induces a time-changing magnetic flux within the frame fixed to the satellite. This time changing flux, by means of Faraday's law, in turn produces an electric field in the conductor. And this itself causes various electric currents — eddy currents. The currents, by means of Ampère's law, have an associated magnetic dipole moment and consequently interact with the given magnetic field. This interaction finally creates a torque changing the satellite's original spin vector. Technical details, however, quickly multiply. For the most part, the following calculation is an elaboration of the treatment found in Landau and Lifshitz⁴.

The most abstract form for U_m comes directly from the Lorentz force law. As shown in Goldstein³, for instance, a charged particle q with velocity \vec{v} in electric and magnetic potentials Φ and \vec{A} can be treated formally as maintaining a velocity dependent potential energy

$$U = q\Phi - \frac{q}{c} \vec{A} \cdot \vec{v}, \quad (4)$$

where c is the speed of light. The total potential energy for distributions ρ of charges and \vec{J} of currents would then be

$$U = \int \rho \Phi d^3x - \frac{1}{c} \int \vec{A} \cdot \vec{J} d^3x, \quad (5)$$

where d^3x is the volume element of integration. In the case that $\rho = 0$, writing $\vec{J} = c(\nabla \times \vec{\mathcal{M}})$ by means of Ampère's law where $\vec{\mathcal{M}}$ is a magnetic dipole density, this reduces to

$$\begin{aligned} U_m &= - \int \vec{A} \cdot (\nabla \times \vec{\mathcal{M}}) d^3x \\ &= - \int [\vec{\mathcal{M}} \cdot (\nabla \times \vec{A}) - \nabla \cdot (\vec{A} \times \vec{\mathcal{M}})] d^3x \\ &= - \left[\int \vec{B} \cdot \vec{\mathcal{M}} d^3x - \oint (\vec{A} \times \vec{\mathcal{M}}) \cdot d\vec{s} \right] \end{aligned} \quad (6)$$

where \vec{B} is the magnetic field and $d\vec{s}$ is a surface area element. Taking the surface of integration outside the conductor so that $\vec{\mathcal{M}} = 0$, assuming \vec{B} constant over the integration volume (as we most assuredly can in our case), and noting that $\vec{M} = \int \vec{\mathcal{M}} d^3x$ defines the total magnetic dipole moment,

this finally simplifies to

$$U_m = -\vec{M} \cdot \vec{B}. \quad (7)$$

Thus our problem reduces to finding an explicit expression for the induced magnetic dipole moment \vec{M} . Along with Landau and Lifshitz⁴, in the following calculation we explicitly assume:

- 1) $\omega \ll c/l$ where ω is the total satellite rotation frequency and l is the satellite dimension
- 2) $\mu = 1$ where μ is the satellite's magnetic permeability
- 3) $\omega \ll 1/T$ where T is the mean free time for electrons in the conductor.

To get a handle on where we should start, we note that with respect to the body-fixed frame the satellite encounters a time varying magnetic field. This time dependence can be seen explicitly by writing the components B_1, B_2, B_3 of \vec{B} in the body-fixed frame in terms of the analogous components $\tilde{B}_1, \tilde{B}_2, \tilde{B}_3$ in the space-fixed frame:

$$\begin{aligned} B_1 &= (\cos\psi \cos\phi - \cos\theta \sin\phi \sin\psi) \tilde{B}_1 + (\cos\psi \sin\phi + \cos\theta \cos\phi \sin\psi) \tilde{B}_2 + (\sin\psi \sin\theta) \tilde{B}_3 \\ B_2 &= (-\sin\psi \cos\phi - \cos\theta \sin\phi \cos\psi) \tilde{B}_1 + (-\sin\psi \sin\phi + \cos\theta \cos\phi \cos\psi) \tilde{B}_2 + (\cos\psi \sin\theta) \tilde{B}_3 \\ B_3 &= (\sin\theta \sin\phi) \tilde{B}_1 - (\sin\theta \cos\phi) \tilde{B}_2 + (\cos\theta) \tilde{B}_3. \end{aligned} \quad (8)$$

From this we would like to use Landau and Lifshitz as a starting point. The problem they solve is that of finding the induced magnetic moment for a conducting sphere in a uniform periodic external field. Writing the periodic field in complex form (i.e. $\vec{B} = \hat{b} B e^{-i\omega t}$, B is the maximum field magnitude and \hat{b} is the unit vector in the field's direction), the solution they find is

$$\vec{M} = V \operatorname{Re} [\alpha \vec{B}], \quad (9)$$

where $V = \frac{4}{3}\pi a^3$ is the sphere's volume, $\operatorname{Re}[\]$ signifies the operation of taking the real part, $\alpha = \alpha' + i\alpha''$ is the complex magnetic polarisability per unit volume,

$$\begin{aligned} \alpha' &= -\frac{3}{8\pi} \left[1 - \frac{3}{x} \frac{\sinh x - \sin x}{\cosh x - \cos x} \right] \\ \alpha'' &= -\frac{9}{4\pi} x^{-2} \left[1 - \frac{1}{2} x \frac{\sinh x + \sin x}{\cosh x - \cos x} \right], \end{aligned} \quad (10)$$

and $x = \frac{2a}{\delta} = \frac{2a}{c} \sqrt{2\pi\sigma\omega}$ for conductor skin depth δ .

With this given, we can simply use the following recipe. On time scales small with respect to the reciprocals of the angular velocities, the satellite motion should adequately model the uniform rotation of a sphere in a uniform magnetic field — just with three axes of rotation ($\hat{1}, \hat{2}, \hat{3}$) and three rotational frequencies ($\omega_1, \omega_2, \omega_3$). Rotation about $\hat{3}$, for instance, will cause a periodic variation in B_1 and B_2 (in the body-fixed frame) with frequency ω_3 and thus produce magnetic moments in the $\hat{1}$ and $\hat{2}$ directions. Similarly for rotations about $\hat{1}$ and $\hat{2}$. The total (instantaneous) magnetic moment for the sphere will then just be the sum of all these. That this is true can be seen from even the most rough outline of the derivation in Landau and Lifshitz. They find \vec{M} essentially by just first solving the Maxwell equations both in the conducting sphere and the vacuum outside the sphere and then matching the two solutions at the boundary. Because Maxwell's equations are linear, our statement follows.

It should be noted here that because of the satellite's orbital motion through the earth's magnetic dipole field

$$\vec{B} = \nabla \frac{\vec{d} \cdot \vec{r}}{r^3} = \frac{r^2 \vec{d} - 3 \vec{r} (\vec{r} \cdot \vec{d})}{r^5}, \quad (11)$$

where \vec{d} is the earth's dipole vector, the magnetic field's "true" instantaneous frequency in the body-fixed frame can't be just due to the spin components ω_k . There should be some further residual due to this neglected time rate of change. In the calculation for the induced moment \vec{M} this will be explicitly ignored. Interestingly enough, though, time derivatives due to this change will still crop up in the Lagrange equations of motion. This follows from the fact that the Lagrange equations of motion explicitly call for a total time derivative. Thus including the orbital variation of the field at the level of the spin-dependent potential would have the effect of making the equations of motion valid out to second time derivatives in the field. We proceed with the assumption that our approximation is adequate.

This recipe easily translates to the following technical description. Let $\alpha'_k, \alpha''_k, x_k$, etc. refer to

the polarisabilities, etc. based on the frequency ω_k . Because of a right-handed rotation $\omega_3 dt$ about $\hat{3}$,

$$\begin{aligned} B_1(t+dt) &= B_1(t) \cos \omega_3 dt + B_2(t) \sin \omega_3 dt = \operatorname{Re} \left[(B_1(t) + i B_2(t)) \exp(-i \omega_3 dt) \right] \\ B_2(t+dt) &= -B_1(t) \sin \omega_3 dt + B_2(t) \cos \omega_3 dt = \operatorname{Re} \left[(B_2(t) - i B_1(t)) \exp(-i \omega_3 dt) \right]. \end{aligned} \quad (12)$$

These variations in turn cause the induced magnetic moments

$$\begin{aligned} M_1(t+dt) &= V \operatorname{Re} [\alpha_3 B_1(t+dt)] \\ &= V \operatorname{Re} \left[(\alpha'_3 + i \alpha''_3) (B_1(t) + i B_2(t)) (\cos \omega_3 dt - i \sin \omega_3 dt) \right] \\ &= V \left[(\alpha'_3 B_1 - \alpha''_3 B_2) \cos \omega_3 dt + (\alpha''_3 B_1 + \alpha'_3 B_2) \sin \omega_3 dt \right] \end{aligned} \quad (13)$$

$$\begin{aligned} M_2(t+dt) &= V \operatorname{Re} [\alpha_3 B_2(t+dt)] \\ &= V \operatorname{Re} \left[(\alpha'_3 + i \alpha''_3) (B_2(t) - i B_1(t)) (\cos \omega_3 dt - i \sin \omega_3 dt) \right] \\ &= V \left[(\alpha'_3 B_2 + \alpha''_3 B_1) \cos \omega_3 dt + (\alpha''_3 B_2 - \alpha'_3 B_1) \sin \omega_3 dt \right]. \end{aligned}$$

In the limit $dt \rightarrow 0$ we recover from these expressions the instantaneous induced magnetic moment

$$\vec{M}^{(3)} = V \left\{ [\alpha'_3 B_1(t) - \alpha''_3 B_2(t)] \hat{1} + [\alpha''_3 B_1(t) + \alpha'_3 B_2(t)] \hat{2} \right\}. \quad (13)$$

The superscript in this expression is meant to signify that this is the dipole induced from rotations about $\hat{3}$ only; it is not meant to denote a component of a vector. The induced magnetic moments due to rotations about $\hat{1}$ and $\hat{2}$ can be written immediately by inspection. All that needs be performed is a cyclic permutation of indices.

$$\begin{aligned} \vec{M}^{(2)} &= V \left\{ [\alpha'_2 B_3(t) - \alpha''_2 B_1(t)] \hat{3} + [\alpha''_2 B_3(t) + \alpha'_2 B_1(t)] \hat{1} \right\} \\ \vec{M}^{(1)} &= V \left\{ [\alpha'_1 B_2(t) - \alpha''_1 B_3(t)] \hat{2} + [\alpha''_1 B_2(t) + \alpha'_1 B_3(t)] \hat{3} \right\} \end{aligned} \quad (14)$$

Summing these three pieces gives the full time-dependent induced magnetic moment

$$\begin{aligned} \vec{M} &= V \left\{ [(\alpha'_2 + \alpha'_3) B_1 - \alpha''_3 B_2 + \alpha''_2 B_3] \hat{1} + [\alpha''_3 B_1 + (\alpha'_1 + \alpha'_3) B_2 - \alpha''_1 B_3] \hat{2} \right. \\ &\quad \left. + [-\alpha''_2 B_1 + \alpha'_1 B_2 + (\alpha'_1 + \alpha'_2) B_3] \hat{3} \right\}. \end{aligned} \quad (15)$$

Now simply inserting this result into the formal expression we find

$$\begin{aligned} \vec{M} \cdot \vec{B} = V \{ & [(\alpha'_2 + \alpha'_3) B_1 - \alpha''_3 B_2 + \alpha''_2 B_3] B_1 + [\alpha''_3 B_1 + (\alpha'_1 + \alpha'_3) B_2 - \alpha''_1 B_3] B_2 \\ & + [-\alpha''_2 B_1 + \alpha''_1 B_2 + (\alpha'_1 + \alpha'_2) B_3] B_3 \}. \end{aligned} \quad (16)$$

Note that all the terms in this expression due to the imaginary part of α cancel. Consequently, using the definition $B^2 = B_1^2 + B_2^2 + B_3^2 = \tilde{B}_1^2 + \tilde{B}_2^2 + \tilde{B}_3^2$, this simplifies to

$$\vec{M} \cdot \vec{B} = V \left[\alpha'_1 (B^2 - B_1^2) + \alpha'_2 (B^2 - B_2^2) + \alpha'_3 (B^2 - B_3^2) \right], \quad (17)$$

our long sought after expression. Unfortunately, though, this doesn't seem to simplify any further. For instance, not even the term containing the B_k with the simplest functional form — namely B_3 — reduces; written out it assumes the unattractive form

$$\begin{aligned} B^2 - B_3^2 = & -\sin^2 \theta \sin^2 \phi \tilde{B}_1^2 - \sin^2 \theta \cos^2 \phi \tilde{B}_2^2 - \cos^2 \theta \tilde{B}_3^2 + 2 \sin^2 \theta \sin \phi \cos \phi \tilde{B}_1 \tilde{B}_2 \\ & - 2 \sin \theta \cos \theta \sin \phi \tilde{B}_1 \tilde{B}_3 + 2 \sin \theta \cos \theta \cos \phi \tilde{B}_2 \tilde{B}_3 + B^2. \end{aligned} \quad (18)$$

This completes the goal of this section and prepares us for actually writing out the Lagrange equations.

III. The Need for a Lagrangian Formulation

There is a standard sort of lore in the physics community that the force on a magnetic dipole \vec{M} in a general magnetic field \vec{B} is

$$\vec{F} = \nabla (\vec{M} \cdot \vec{B}) \quad (19)$$

and the torque is

$$\vec{N} = \vec{M} \times \vec{B}. \quad (20)$$

Consequently, by the Newton and Euler equations of motion³, one would have

$$m\vec{v} = \nabla (\vec{M} \cdot \vec{B}) \quad (21)$$

and

$$\begin{aligned}
I_1 \dot{\omega}_1 - \omega_2 \omega_3 (I_2 - I_3) &= M_2 B_3 - M_3 B_2 \\
I_2 \dot{\omega}_2 - \omega_3 \omega_1 (I_3 - I_1) &= M_3 B_1 - M_1 B_3 \\
I_3 \dot{\omega}_3 - \omega_1 \omega_2 (I_1 - I_2) &= M_1 B_2 - M_2 B_1,
\end{aligned} \tag{22}$$

where \vec{v} is the dipole's velocity and all other symbols are as defined in the last section. Given this, it seems that one would want to immediately apply these formulas to the problem at hand and skip the intermediate derivation by way of a Lagrangian formulation. There is a flaw in this reasoning, however, whenever either \vec{M} or \vec{B} is nonconstant in time. To illustrate this for the torques in our problem would be difficult; so instead we illustrate this for Eq. (21) with a simpler example from the literature^{5,6,7} that has received some attention.

Consider a magnetic dipole \vec{M} of mass m with velocity \vec{v} in a static electric field \vec{E} at time $t = 0$. Suppose $\vec{B} = 0$ in this same frame. We will study the dipole's kinematics from the point of view of an instantaneous co-moving reference frame of velocity \vec{u} (i.e. $\vec{v} = \vec{u}$ at $t = 0$, but \vec{u} is independent of time). In this frame the only interaction possible is a magnetic interaction and hence the proper Lagrangian for deriving the equations of motion is

$$L = \frac{1}{2} m (\vec{v} - \vec{u})^2 + \vec{M} \cdot \vec{B}, \tag{23}$$

where \vec{B} is the magnetic field created by the Lorentz transformation. To order u/c , \vec{B} is just given by⁸

$$\vec{B} = -\frac{1}{c} \vec{u} \times \vec{E} \tag{24}$$

where again \vec{E} is the electric field in the untransformed frame. Thus

$$\begin{aligned}
L &= \frac{1}{2} m (\vec{v} - \vec{u})^2 - \frac{1}{c} \vec{M} \cdot (\vec{u} \times \vec{E}) \\
&= \frac{1}{2} m (\vec{v} - \vec{u})^2 - \frac{1}{c} \vec{u} \cdot (\vec{E} \times \vec{M})
\end{aligned} \tag{25}$$

and so the Lagrange equations of motion at $t = 0$ will be

$$\frac{\partial L}{\partial \vec{x}} - \frac{d}{dt} \frac{\partial L}{\partial (\vec{v} - \vec{u})} = 0 \tag{26}$$

where $\vec{x} = \vec{v} - \vec{u}$. But this implies

$$-\frac{1}{c} \nabla [\vec{u} \cdot (\vec{E} \times \vec{M})] - \frac{d}{dt} \left\{ m(\vec{v} - \vec{u}) - \frac{1}{c} \left[\frac{\partial(\vec{v} - \vec{u})}{\partial \vec{u}} \right]^{-1} \frac{\partial}{\partial \vec{u}} [\vec{u} \cdot (\vec{E} \times \vec{M})] \right\} = 0 \quad (27)$$

and consequently

$$m\vec{v} = \nabla(\vec{M} \cdot \vec{B}) + \frac{1}{c} \frac{d}{dt} (\vec{E} \times \vec{M}). \quad (28)$$

The point is that this expression is not identical to Eq. (21) as one might have superficially expected. Moreover there are simple nonrelativistic situations in which the two terms $\nabla(\vec{M} \cdot \vec{B})$ and $\frac{1}{c} \frac{d}{dt} (\vec{E} \times \vec{M})$ can be of comparable magnitude⁹. Thus a Lagrangian formulation for our problem appears to be the safest strategy to take.

IV. Lagrange Equations and Asymptotics

The full set of Euler-Lagrange equations governing the spin dynamics of the satellite are

$$\frac{\partial L}{\partial \theta} - \frac{d}{dt} \frac{\partial L}{\partial \dot{\theta}} = 0, \quad \frac{\partial L}{\partial \phi} - \frac{d}{dt} \frac{\partial L}{\partial \dot{\phi}} = 0, \quad \frac{\partial L}{\partial \psi} - \frac{d}{dt} \frac{\partial L}{\partial \dot{\psi}} = 0. \quad (29)$$

From these a completely detailed picture of the satellite's motion could in principle be derived. We, however, are only interested in the time-asymptotic behavior of $\dot{\phi}$. Thus we may focus on just one of these equations if it reveals the appropriate information. This already greatly simplifies our task, but we can go even further. By means of kinetic energy dissipation due to Ohmic resistance of the eddy currents, we may uniquely couple the flow of time to the degradation of ω_3 . Hence we may focus on the simpler limit $\omega_3 \rightarrow 0$ instead of the more tedious $t \rightarrow \infty$. Finally we make one further simplifying (but standard^{1,2,3}) assumption, namely that $\dot{\theta} = \ddot{\theta} = 0$, and freeze these variables out at the level of the Lagrangian.

All this taken together suggests we study the reduced Lagrange equation

$$\frac{\partial L}{\partial \theta} = 0. \quad (30)$$

We turn to this task immediately. The first thing required, though, is that we introduce a bit of

notation by way of an intermediate step

$$\frac{\partial \alpha'_k}{\partial \theta} = \frac{\partial \alpha'_k}{\partial x_k} \frac{\partial x_k}{\partial \omega_k} \frac{\partial \omega_k}{\partial \theta} = \frac{a}{c} \sqrt{\frac{2\pi\sigma}{\omega_k}} \frac{\partial \alpha'_k}{\partial x_k} \frac{\partial \omega_k}{\partial \theta} = \frac{4\pi a^2}{c^2} \sigma \frac{1}{x_k} \frac{\partial \alpha'_k}{\partial x_k} \frac{\partial \omega_k}{\partial \theta} \equiv f(x_k) \frac{\partial \omega_k}{\partial \theta} \quad (31)$$

where

$$f(x) = \frac{4\pi a^2}{c^2} \sigma \frac{1}{x} \frac{\partial \alpha'}{\partial x} = \frac{9a^2\sigma}{c^2} \frac{1}{x^2} \left[2 \frac{1 - \cosh x \cos x}{(\cosh x - \cos x)^2} - \frac{1}{x} \frac{\sinh x - \sin x}{\cosh x - \cos x} \right]. \quad (32)$$

Note also, by means of the identities $\cos^2 x + \sin^2 x = 1$ and $\cosh^2 x - \sinh^2 x = 1$, the last expression can also be written in the form

$$f(x) = \frac{9a^2\sigma}{c^2} \frac{1}{x^2} \left[1 - \frac{(\sinh x - \sin x)(\sinh x + \sin x)}{(\cosh x - \cos x)^2} - \frac{1}{x^3} \frac{\sinh x - \sin x}{\cosh x - \cos x} \right]. \quad (33)$$

For later reference, we tabulate now that in the limit $\omega \rightarrow \infty$ (and consequently $x \rightarrow \infty$):

$$\alpha' \rightarrow -\frac{3}{8\pi}, \quad \alpha'' \rightarrow 0, \quad f(x) \rightarrow 0. \quad (34)$$

This follows from the fact that for large x

$$\frac{\sinh x \mp \sin x}{\cosh x - \cos x} \approx 1 \quad \text{and} \quad \frac{(\sinh x - \sin x)(\sinh x + \sin x)}{(\cosh x - \cos x)^2} \approx 1. \quad (35)$$

For studying the opposing limit $\omega \rightarrow 0$ it is convenient to first consider the following Taylor expansions found by means of *Mathematica*TM:

$$\begin{aligned} \alpha' &= -\frac{1}{1680\pi} x^4 + \frac{1}{665280\pi} x^8 + \dots \\ \frac{d\alpha'}{dx} &= -\frac{1}{420\pi} x^3 + \frac{1}{83160\pi} x^7 + \dots \\ \alpha'' &= \frac{1}{80\pi} x^2 - \frac{1}{33600\pi} x^6 + \dots \\ \frac{d\alpha''}{dx} &= \frac{1}{40\pi} x - \frac{1}{5600\pi} x^5 + \dots \end{aligned} \quad (36)$$

and

$$f(x) = \frac{4\pi a^2}{c^2} \sigma \left[-\frac{1}{420\pi} x^2 + \frac{1}{83160\pi} x^6 + \dots \right]. \quad (37)$$

Then it clearly follows that in the limit $\omega \rightarrow 0$:

$$\alpha' \rightarrow 0, \quad \alpha'' \rightarrow 0, \quad f(x) \rightarrow 0. \quad (38)$$

These points out of the way, Eq. (30) written out explicitly is

$$\dot{\phi}^2(I_1 \sin \theta \cos \theta) + \dot{\phi} \left\{ -I_3 \omega_3 \sin \theta + V(B^2 - B_1^2)f(x_1) \cos \theta \sin \psi + V(B^2 - B_2^2)f(x_2) \cos \theta \cos \psi - V(B^2 - B_3^2)f(x_3) \sin \theta \right\} + \left\{ -\frac{3}{2} \omega_0^2 (I_3 - I_1) \sin \theta \cos \theta - 2V \left(\alpha'_1 \frac{\partial B_1}{\partial \theta} + \alpha'_2 \frac{\partial B_2}{\partial \theta} + \alpha'_3 \frac{\partial B_3}{\partial \theta} \right) \right\} = 0, \quad (39)$$

just a simple quadratic equation in $\dot{\phi}$. Since we want to study the behavior of $\dot{\phi}$ with respect to ω_3 only while leaving ω_1 and ω_2 fixed, it is convenient to rewrite this equation with the fixable quantities grouped:

$$\dot{\phi}^2(I_1 \sin \theta \cos \theta) + \dot{\phi} \left\{ -I_3 \omega_3 \sin \theta - V(B^2 - B_3^2)f(x_3) \sin \theta + C'_1 \right\} + \left\{ -\frac{3}{2} \omega_0^2 (I_3 - I_1) \sin \theta \cos \theta - 2V \alpha'_3 \frac{\partial B_3}{\partial \theta} + C'_2 \right\} = 0 \quad (40)$$

where

$$C'_1 = V \left[(B^2 - B_1^2)f(x_1) \cos \theta \sin \psi + (B^2 - B_2^2)f(x_2) \cos \theta \cos \psi \right] \quad (41)$$

$$C'_2 = -2V \left(\alpha'_1 \frac{\partial B_1}{\partial \theta} + \alpha'_2 \frac{\partial B_2}{\partial \theta} \right)$$

Note that C'_1 and C'_2 represent bounded functions of θ , ϕ , and ψ (where the term "bounded" here is with reference to ω_1 and ω_2 being fixed). Note also that $\frac{\partial B_3}{\partial \theta}$ does not depend on ω_3 . Now we may easily study the asymptotics of $\dot{\phi}$.

For large ω_3 , Eq. (40) becomes

$$\dot{\phi}^2(I_1 \sin \theta \cos \theta) + \dot{\phi}(-I_3 \omega_3 \sin \theta) + \left\{ -\frac{3}{2} \omega_0^2 (I_3 - I_1) \sin \theta \cos \theta - \frac{3V}{4\pi} \alpha'_3 \frac{\partial B_3}{\partial \theta} + C'_2 \right\} = 0. \quad (42)$$

This has as solution

$$\dot{\phi} = \frac{1}{2I_1 \sin \theta \cos \theta} \left\{ I_3 \omega_3 \sin \theta - \sqrt{\left(I_3 \omega_3 \sin \theta \right)^2 - 4I_1 \sin \theta \cos \theta \left[-\frac{3}{2} \omega_0^2 (I_3 - I_1) \sin \theta \cos \theta - \frac{3V}{4\pi} \alpha'_3 \frac{\partial B_3}{\partial \theta} + C'_2 \right]} \right\}. \quad (43)$$

The minus sign in front of the root is fixed by simple physical considerations (no oblateness, no magnetic fields \Rightarrow no precession). Clearly then as $\omega_3 \rightarrow \infty$, $\dot{\phi} \rightarrow 0$ since the last term under the root is

independent of ω_3 . This is just as one would expect since fast spins should be resistant to torques.

Of more interest though is the opposing limit. To first order in ω_3 , Eq. (40) becomes

$$\dot{\phi}^2 + \dot{\phi} \left[-\frac{I_3}{I_1} \frac{\omega_3}{\cos \theta} + \frac{8}{105} \pi \left(\frac{a^2 \sigma}{c^2} \right)^2 \frac{V}{I_1 \sin \theta \cos \theta} (B^2 - B_3^2) \omega_3 + C_1 \right] + \left[-\frac{3}{2} \omega_0^2 \frac{I_3 - I_1}{I_1} + C_2 \right] = 0 \quad (44)$$

where

$$C_1 = \frac{V}{I_1 \sin \theta} \left[(B^2 - B_1^2) f(x_1) \sin \psi + (B^2 - B_2^2) f(x_2) \cos \psi \right] \quad (45)$$

$$C_2 = -\frac{2V}{I_1 \sin \theta \cos \theta} \left[\alpha'_1 \frac{\partial B_1}{\partial \theta} + \alpha'_2 \frac{\partial B_2}{\partial \theta} \right]$$

are also bounded functions since θ is assumed fixed by way of the condition $\dot{\theta} = \ddot{\theta} = 0$. Taking

$$\frac{I_3}{I_1} \approx 1, \quad \frac{I_3 - I_1}{I_1} \approx \Delta, \quad I_1 \approx \frac{2}{5} m a^2, \quad (46)$$

this equation becomes

$$\dot{\phi}^2 + \dot{\phi} \left[-\frac{\omega_3}{\cos \theta} + \frac{16}{63} \frac{a}{m} \left(\frac{\pi a^2 \sigma}{c^2} \right)^2 \frac{B^2 - B_3^2}{\sin \theta \cos \theta} \omega_3 + C_1 \right] + \left[-\frac{3}{2} \omega_0^2 \Delta + C_2 \right] = 0. \quad (47)$$

Now taking the limit $\omega_3 \rightarrow 0$ all the way (while, once again, keeping all other variables fixed) we get

$$\dot{\phi} = -\frac{1}{2} C_1 - \frac{1}{2} \sqrt{C_1^2 - 4C_2 + 6\omega_0^2 \Delta}. \quad (48)$$

Where again the minus sign in front of the root is fixed by the reasoning (no oblateness, no magnetic fields \Rightarrow no precession). The thing to be noted here is that $\dot{\phi}$ does not tend to a value constant in time (even as $\omega_3 \rightarrow 0$) since $\dot{\psi}$ will not generally be zero and since C_1 and C_2 are functions of $\phi = \int \dot{\phi} dt$ itself. $\dot{\phi}$ will however be bounded in magnitude by means of the boundedness of C_1 and C_2 . This completes the work of this section.

V. Conclusions

In this report we have derived an expression for the induced magnetic dipole moment of a spherical conductor with arbitrary spin in a uniform magnetic field. In that derivation a possible time-dependence for the external magnetic field was allowed but assumed small with respect to the (body-

fixed frame) change induced by the satellite spin itself. From this magnetic moment an expression for the satellite's spin dependent potential energy was easily constructed and an expression for the satellite's total Lagrangian finally written. This Lagrangian takes into account not only the magnetic interaction but also the coupling of the earth's gravitational field to the satellite's oblateness as first explored by A. Kheyfets¹. From there it was just a matter of writing down the Lagrange equations of motion in order to be able to study the satellite's precession rate asymptotics. Fortunately it turned out that only one of the three Lagrange equations need be considered in concluding that question. Under the assumption that the satellite will not be nutating ($\dot{\theta} = 0$) at late times headway was made and an asymptotic bound shown to exist for the precession rate. The asymptotics were explicitly in terms of the limit $\omega_3 \rightarrow 0$ rather than the limit $t \rightarrow \infty$. This was allowed by the unique correspondence between the flow of time and the degradation of ω_3 due to kinetic energy dissipation by means of Ohmic resistance to the induced eddy currents.

At least four difficulties exist for this treatment. First off time variations in the magnetic field due to the satellite's earth orbital motion were ignored. As stated this only leaves out a second magnetic time derivative in the equations of motion and can be conveniently overlooked as long as the satellite spin period is small in comparison to its orbital period. We are, however, studying the asymptotics of the precession as $\omega_3 \rightarrow 0$. Thus a more rigorous treatment must necessarily include those effects. Secondly, for late times, we allowed ourselves the assumption of no nutation. Although not demonstrated in this report, this assumption can be shown to be sound^{1,10} — for late times that is. What happens when the satellite evolution is not near asymptotia? This should be investigated in detail but will probably require numerical work. This leads to the third difficulty. How near is the satellite's present state of evolution to asymptotia? Nothing in the present analysis can reveal an answer to this. Finally, the model in this report as far as magnetic effects are concerned is a perfectly spherical conductor — quite different from the real thing. For qualitative asymptotic results, this appears to be entirely adequate. However if the satellite's evolution is sufficiently far from asymptotia

this may be as dangerous an assumption for even qualitative results as anything else.

Clearly the direction for future research is not a straight path. Both analytical and numerical methods will be required to settle the difficulties described above. On the analytical side a more full writing and decoupling of the Lagrange equations should be the first step. The "distance" of the present day spin dynamics from asymptotia would appear to be the first question tacklable by numerical methods. Both projects appear at this time to be of equal merit. However in the words of A. Kheifets¹, "But, whatever the means, it is clear that the efforts in studying LAGEOS's spin dynamics should continue until all the questions are answered."

VI. References

- ¹A. Kheyfets, Spin Dynamics of LAGEOS Satellite, p. 20-1 of this volume.
- ²B. Bertotti and L. Iess, *J. Geophys. Res.* **96**, 2431 (1991).
- ³H. Goldstein, *Classical Mechanics*, Addison-Wesley Publ. Co., Reading, MA (1981).
- ⁴L. Landau, E. Lifshitz, and L. Pitaevskii, *Electrodynamics of Continuous Media*, Pergamon Press, Oxford (1984).
- ⁵T. Boyer, *Phys. Rev. A* **36**, 5083 (1987).
- ⁶Y. Aharanov, P. Pearle, and L. Vaidman, *Phys. Rev. A* **37**, 4052 (1988).
- ⁷C. Fuchs, *Phys. Rev. D* **42**, 2940 (1990).
- ⁸J. Jackson, *Classical Electrodynamics*, John Wiley & Sons, New York (1975).
- ⁹S. Coleman and J. Van Vleck, *Phys. Rev.* **171**, 1370 (1968).
- ¹⁰C. Fuchs, unpublished notes.

THIS PAGE INTENTIONALLY LEFT BLANK

**LARGE-SCALE METHODS IN COMPUTATIONAL ELECTROMAGNETICS
USING SYNCHRONOUS OUT-OF-CORE TECHNIQUES**

Michael C. Governale
Research Associate
Department of Physics

Utah State University
Logan, Ut 84322

Final Report for:
Summer Research Program
Phillips Laboratory

Sponsored by:
Air Force Office of Scientific Research
Kirtland Air Force Base, Albuquerque, N.M.

September 1992

**LARGE-SCALE METHODS IN COMPUTATIONAL ELECTROMAGNETICS
USING SYNCHRONOUS OUT-OF-CORE TECHNIQUES**

Michael C. Governale
Research Associate
Department of Physics
Utah State University

Abstract

A Finite Difference Time Domain algorithm for computational electromagnetics was studied using synchronous out-of-core methods. The technique was developed for use on objects which are too large to be stored conventionally in the computer's RAM. Results showed a trade-off between increased sizes of problems that can be modeled and increased run-time from the technique's disk input and output. With today's massively parallel supercomputers the technique was found feasible on three dimensional objects gridded up to 10^{10} cells.

LARGE-SCALE METHODS IN COMPUTATIONAL ELECTROMAGNETICS USING SYNCHRONOUS OUT-OF-CORE TECHNIQUES

Michael C. Governale

INTRODUCTION

Recent improvements in computer design has prompted a new surge in the field of computational physics. Among the many problems not yet solved is the limitation of the memory available in RAM. This has posed great difficulty in the field of electromagnetics as the amount of memory required to study how electromagnetic fields interact with large objects generally exceeds the RAM. One way to overcome this problem is through the use of synchronous out-of-core techniques (e.g. paging). This method allows you to model objects of up to 10^7 cells on computer workstations such as the SUN SPARC-2. This technique has also proved useful on massive parallel machines like the CM-2 and CM-5. As a result, the ability to do objects as large as 10^{10} cells has been realized. This, as Dr. Allen Taflove has pointed out, truly reflects the "reinvention of Maxwell's equations" in the computer age.

METHODOLOGY

This paper illustrates the methods used in simulating the electric and magnetic fields induced by an outside source on a simulated aircraft pod using FD-TD [1] methods for large objects. The key to handling large objects relies on a paging method dubbed the "card shuffle", implemented in the Xcode computer program. Xcode uses a Scattered Field Formulation and a virtual source [1], with all calculations done in MKSA units. All materials are considered to have infinite conductivity and thus to be perfect conductors. The change to dispersive media and a total field formulation is straightforward [2][1].

For the sake of simplicity, the boundary conditions used are

first order Mur on all faces. Second order Mur boundary conditions can be readily implemented as required [3]. A strip of free space cells surrounds the object being modeled to allow for the scattering of the field. This "white space" taken around the object being illuminated is twenty cells and it is noted that more white space may become necessary as the number of time steps or the size of the object is increased.

THE MODEL

The model chosen to demonstrate the paging technique is a long cylindrical object with a hemisphere capping the front, and a flat plate covering the back. This approximates the size and shape of an Air Force pod or missile. There is a circular hole in the front of the pod centered about the axis of symmetry and a bulkhead has been inserted near the front, sixty-four cells from the hole. A wire is centered and mounted on the bulkhead directed toward

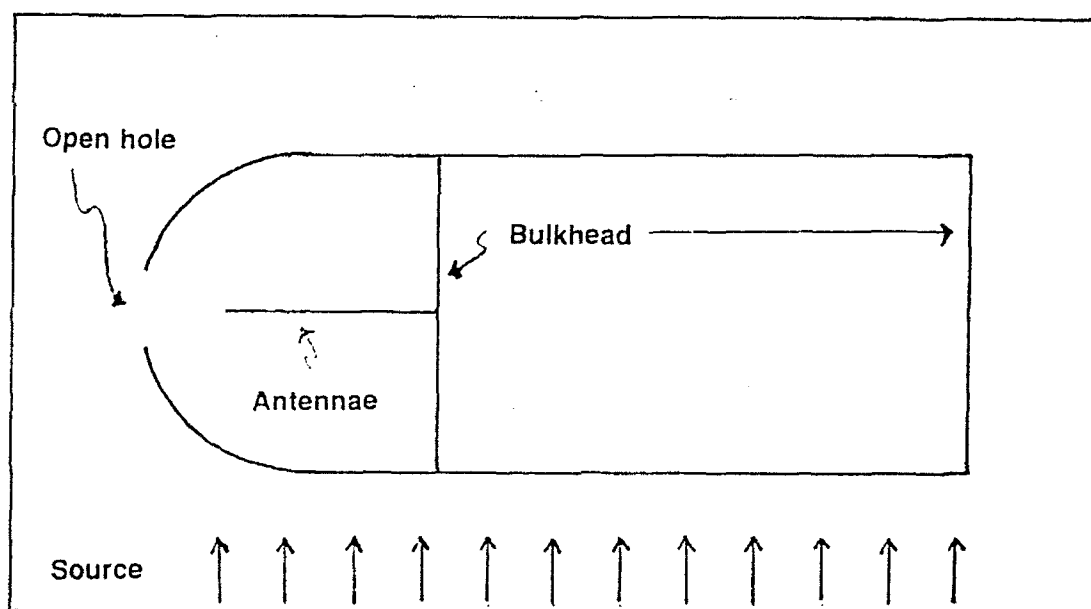


FIGURE 1: The basic geometry of the model.

the front (see fig. 1), serving as an antennae and allowing one to study the modes that are induced in the interior of the pod.

The dimensions of the pod, which we affectionately call the 'silver bullet', is 65 x 65 x 424 cells, or 39 x 39 x 254.4 cm. at 5 GHz. In english units this is 15.35" x 15.35" x 100.2". The "electrical size" of an object refers to the number of cells in the dimension of a volume. When the white space is included, this makes the overall grid size 105 x 105 x 464, or 5.12×10^6 cells.

The model is illuminated by a gaussian plane wave pulse, with frequency content of 5 GHz. The RAM required to treat this job using conventional FD-TD methods would be 375.2 Mbytes, whereas the paging method requires the use of only 8.8 Mbytes or a 97.6% reduction in RAM. The technique relies heavily on disk input and output, or multiple reads and writes to disk (i/o) and so depends entirely on i/o speed and disk storage space. A SUN workstation was used having 55 Mbytes of RAM and 1.2 Gbytes of disk storage space. The highlight and eventual goal of the algorithm is that it may be used on a parallel computer [4]. Early trials on the massively parallel CM-2 have resulted in single iteration run times that are five times faster than the SUN workstation. Future implementation of this method for parallel computers is expected to reduce this to thirty times faster than the SUN workstation. The time it takes for the Gaussian pulse to completely cross the sample space is defined as an illumination. As an example, a single illumination for this model requires 244 iterations of the time loop, which takes 61.6 hours on the SUN, 12.3 hours on the CM-2, and is expected to be 2.05 hours using multiple i/o channels on the CM-5 (available in early 1993).

A consequence of further increasing the size of the object is that the i/o time will become excessively long, making the SUN workstation an un-economical platform from the total run-time viewpoint. However, massive parallel computers using multiple i/o channels promise the ability to handle up to 10^{10} cells economically.

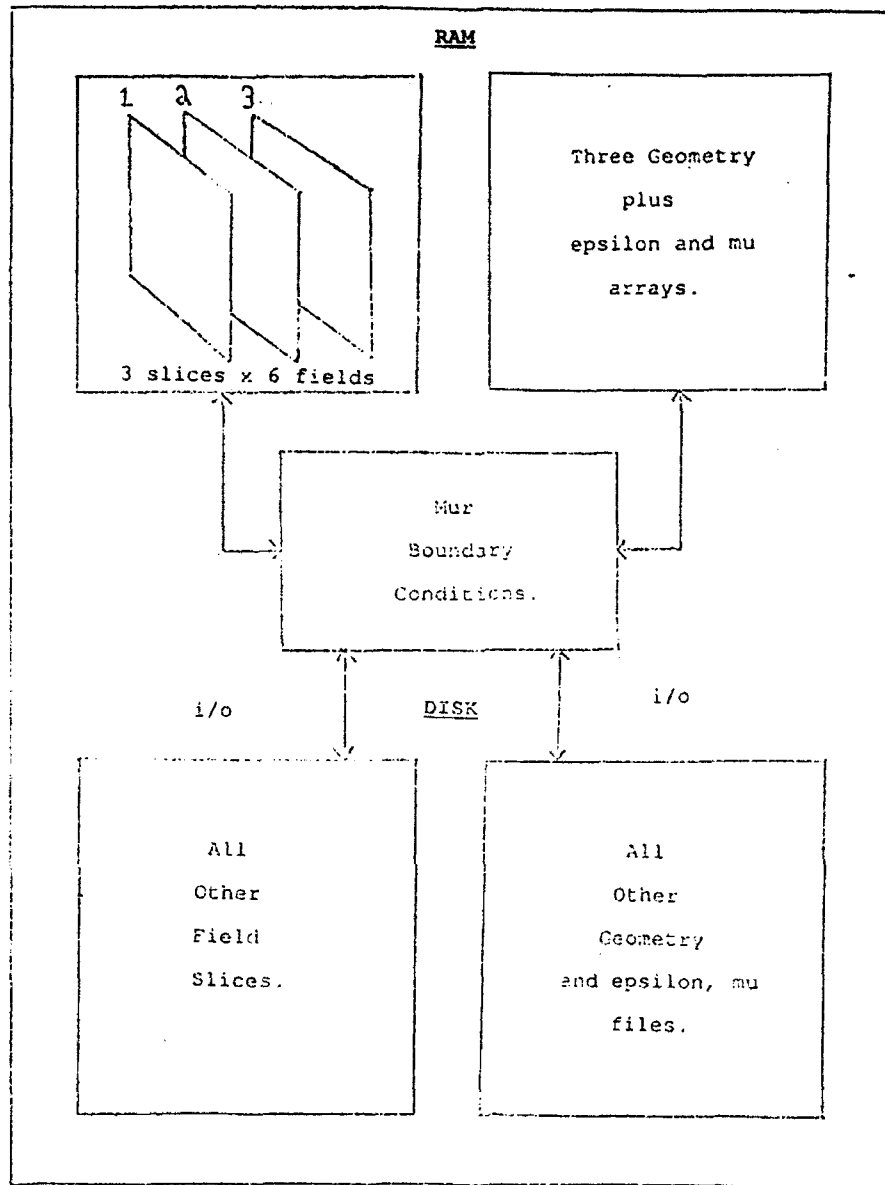


FIGURE 2: Schematic of the distribution of data in both the RAM, and on hard disk.

DATA

The basic idea for the paging method is to only operate on three slices of the entire object at a time. A slice refers to

the number of cells in a two dimensional piece which is one cell thick. You update the middle slice for the current time step based on data from the other two slices, the slice which is behind you and the slice which is ahead. You need three field components each for the electric and magnetic fields, or eighteen slices of field values in RAM per spatial increment. You also need the geometry specifiers, assuming no magnetic currents, to distribute the geometry information to the electric fields. Three components must be used to specify the geometry in each individual cell due to the offset of the location of each field component inside the Yee-cell [5]. This all boils down to a RAM requirement of six field values times the number of cells in a slice times three slices plus three geometry specifiers. The geometry specifier is required only for the middle slice so you have $((18+3)=21 \text{ slices}) \times n^2 \times 8 \text{ bytes}$, where n^2 is the number of cells squared assuming the dimensions are equal. Conventional FD-TD methods require 9 cubes $\times n^3 \times 8 \text{ bytes}$, or six matrices for the field components, and three geometry specifiers so that the paging method reduces the RAM by $7/3n$ on a square grid. If the grid is not square, the paging method still requires the same amount of RAM, but the conventional method uses 9 cubes $\times n^2 \times m \times 8 \text{ bytes}$, and you reduce the requirement by $7/3m$. Consideration of storage due to Radiation Boundary Conditions [6], for which you need four arrays for each face, or $((4 \times n \times m) + (2 \times n^2 \times 4))$ bytes, brings the total RAM of the paging method for both the FD-TD and Mur conditions to $((232 \times n^2) + (128 \times n \times m))$ bytes. The Mur term is the same using conventional methods, as is the use of the permittivity and permeability, so you still end up saving $3m/7$ times more RAM.

The basic overview of the algorithm is to initialize and store to disk an E_x , E_y , E_z , and H_x , H_y , H_z component for every value in the direction across the slices. The program then enters the time loop, where it opens the first three slices, operates on them, and writes the middle slices back to disk. The program then shuffles the mid and top files down to the bottom and mid, discarding the information in the previous bottom slice, and then reads in the new

TABLE 1: Outline of the computer algorithm.

1. Initialization
 - a) declarations.
 - b) zero all arrays.
 - c) calculate constants.
2. Input
 - a) wavelength.
 - b) number of iterations.
3. Create data files
 - a) initialize them to the array values (zero).
4. Enter the time loop
 - a) input data from disk for the first three slices.
5. Calculate the Magnetic Fields
 - a) enter the k-loop, for paging k=2.
 - b) read geometry file for k-value from disk.
 - c) do hx component.
 - d) do hy component.
 - e) do hz component.
6. Calculate the Electric Fields
 - a) do ex component (sources included here).
 - b) do ey component (sources included here).
 - c) do ez component (sources included here).
 - d) implement Mur boundary conditions.
 - i) if k=2, do Mur on left face.
 - ii) if k=last-1, do Mur on right face.
 - iii) otherwise use saved values of edges for updating the boundary values.
 - e) sample fields for time history.
 - f) write updated middle files to disk.
 - g) move middle file to bottom, top file to middle.
 - h) read new top file from disk.
 - i) increment k to k+1.
 - j) increment time loop, goto step 4a.

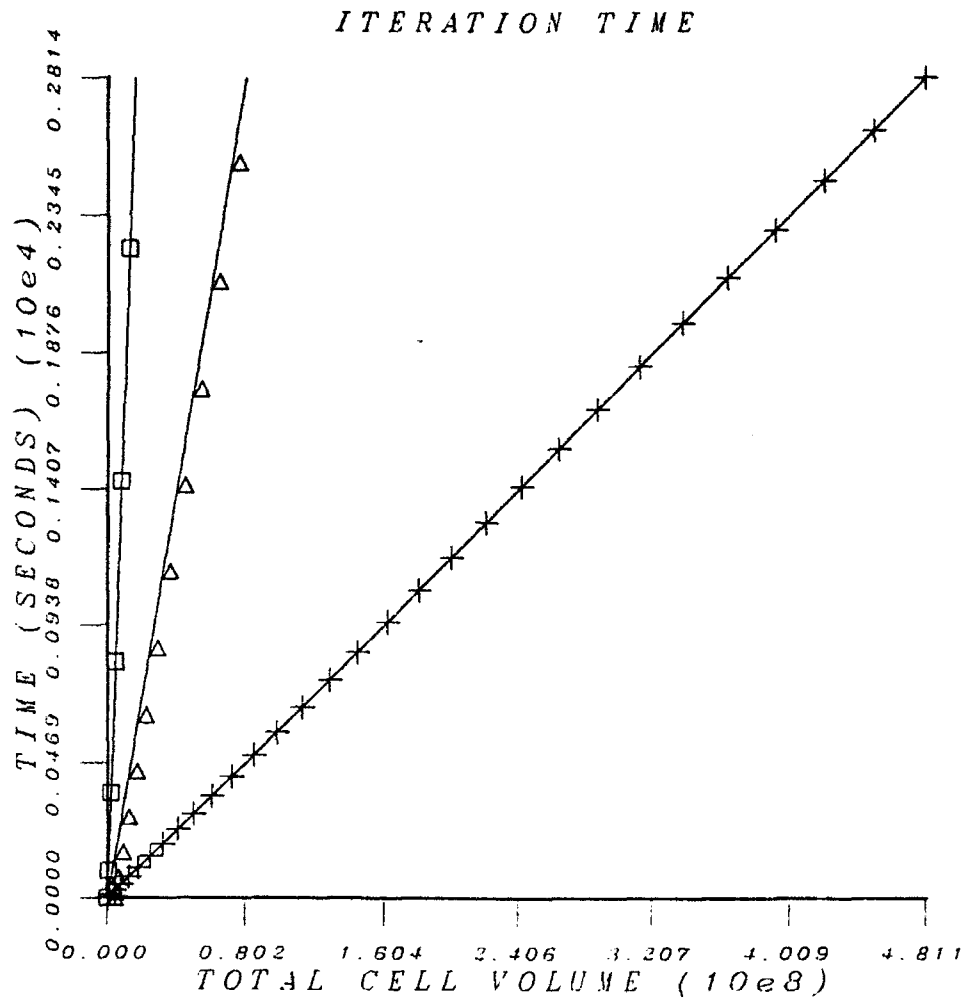
top slice from disk. This process is repeated until the end of the sequence of slices is reached, where the time loop is then incremented. The simplicity involved here is that only the eighteen slices and three boundary value arrays being operated on are required for use in RAM.

In order to understand how the technique depends on time, the algorithm must process $((6 \times n^2 \times 2 \text{ i/o}) + (3 \times n^2 \times 1 \text{ i/o})) \times 8$

bytes of information via reads and writes per step in the k-direction. The first term takes care of the update on the six middle slices, and the second term refers to reading in the geometry specifiers. The boundary conditions require $(2 \times 2 \text{ i/o}) \times 8$ bytes and two field samplers require $(2 \times 1 \text{ i/o}) \times 8$ bytes, after adding these terms and multiplying all except the boundary condition term by m for the number of slices in one time step, we obtain the amount of information processed totally by i/o. Next we must divide these terms by the i/o speed, which for the SUN is .97 Mbytes / second. The CPU term is found by taking the total number of operations in one time step, and then dividing by the number of operations per second that the particular computer can do. This may be done by taking the number of cells operated on for the boundary condition and adding on a core term which consists of the number of cells times the number of operations per cell, which I have found to be about 36. After adding on this smaller CPU term you arrive at:

$$t = \left(\frac{(136m+32)n^2}{.97 \times 10^6} \right) + \left(\frac{128nm+64n^2+36n^2m}{10^6} \right) .$$

Calculated values for electrical sizes of $81 \times 81 \times 71$, $105 \times 105 \times 71$, and $381 \times 381 \times 71$ on the SPARC-2 at 5 GHz., were 83.5, 139.5, and 1833 seconds respectively, actual values were 84, 140, and 1835 seconds. The equation shows how the i/o term can get very large and the CPU term depends on the number of calculations the computer can do per second. A vital point here is that the time optimization of the technique depends on the i/o speed which can be optimized by using multiple i/o channels, less i/o, and faster machines such as the CM-2 and CM-5. Figure Three summarizes this point. In the plot I have a length $m=200$, and allow the girth n^2 to vary from 1 to 1600. You can see the difference in iteration times with regards to the SUN, CM-2, and CM-5. A straightforward extrapolation reveals that a size of $733 \times 667 \times 200$ cells, or 9.78×10^7 cells would be done at about 572 seconds per iteration.



Used a fixed length of $m=200$.

□-□-□ SUN

△-△-△ CM-2

+--+ CM-5

FIGURE 3: Iteration time versus the electrical size for the SUN, CM-2, and CM-5.

A illumination of 500 time-steps would require a time of 3.31 days to complete. This size at a frequency of 1 GHz is $22 \times 20 \times 6$ meters, which would enclose an object about the size of a jet fighter.

The fields chosen for study were the electric field at slice 50 ($k=50$) and a magnetic loop centered about the wire at slice 83 ($k=83$) (three cells from the bulkhead where the wire originates). The electric field samples were taken primarily to provide a time history from which graphics could be generated. In figure Four, I

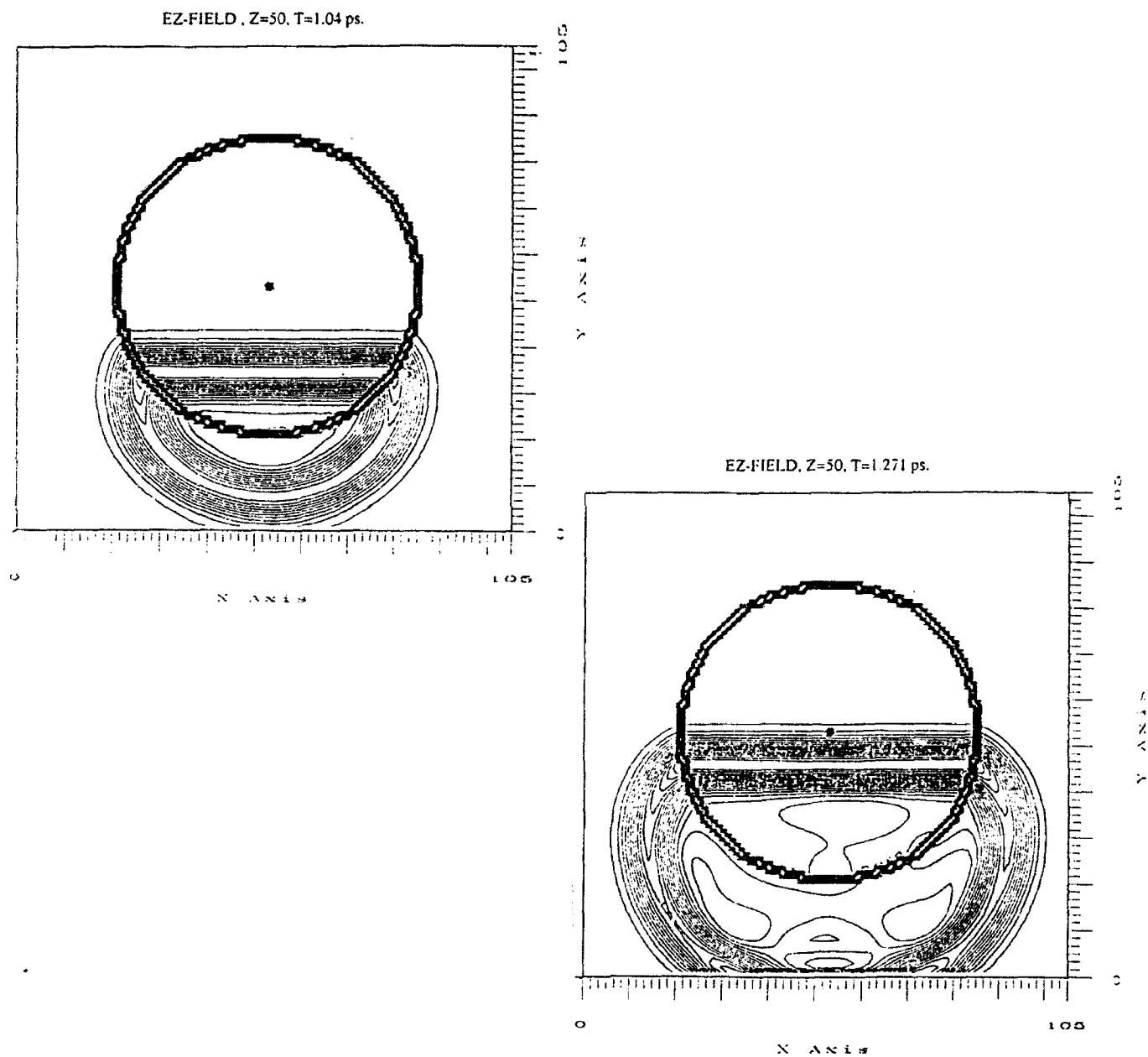


FIGURE 4: Scattering of the E_z component at $k=50$.

show the scattered component of E_z in a cross section of the pod taken at $k=50$. Notice the effect of using square cells to specify the geometry, which is the cause of the disfiguration near the wall area.

The magnetic loop was used to obtain data from currents that are induced into the wire as the Gaussian pulse passes by. The data for the loop is processed using an approximation for

$$\int \vec{H} \cdot d\vec{s} = I_{enc} .$$

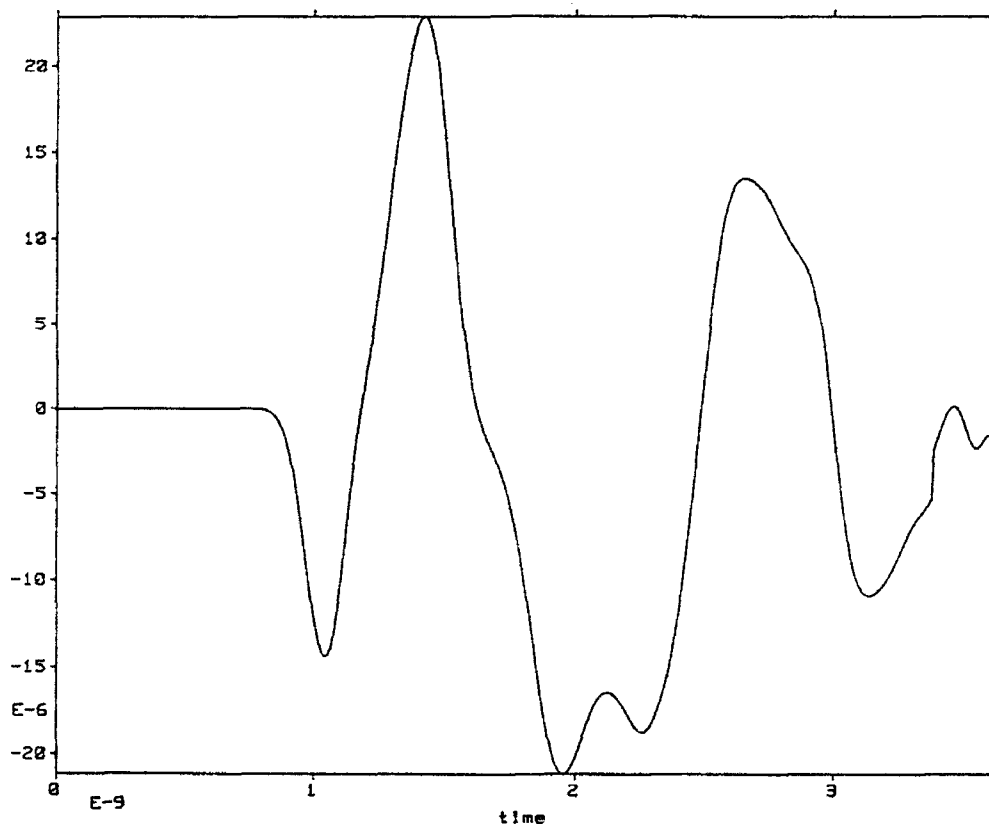


FIGURE 5: The time domain of the currents generated in the wire.

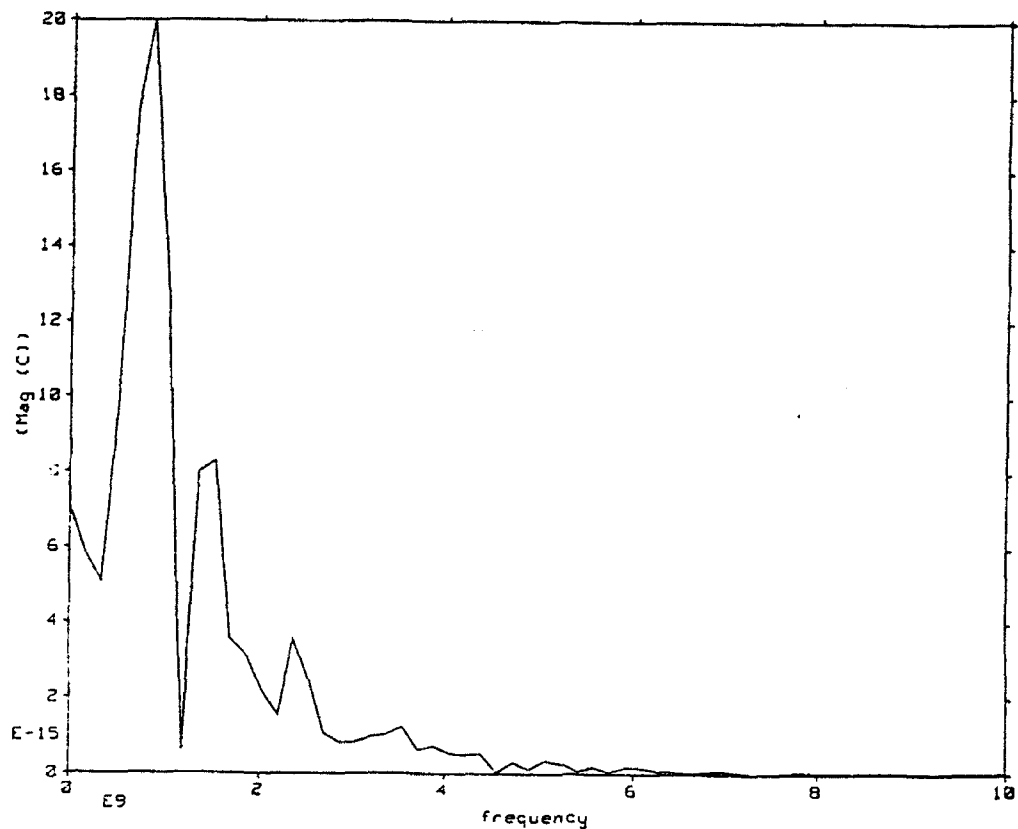


FIGURE 6: The frequency domain of the currents generated in the wire.

The approximation is made by taking the line integral to be equal to the step-size times four values of H which lie on a circular path of integration summed. These currents were recorded for a total of 315 iterations so that a Fourier transform of the time history into frequency space could be made. The gaussian pulse which generated these excitations lasted for 0.739 ps and the time history recorded was over 3.64 ps in order to allow time for the wire to ring down. Figures Five and Six show the current verses time and the Fourier transform of this data, respectively. In the time domain, the long flat line at the beginning represents the time taken for the pulse to excite the wire. The first dip and hump is the pulse exciting and inducing a current into the wire,

and the waves that follow are the oscillating currents in the wire induced by the reflections of decaying waves that are ringing down inside the cavity. The Fourier transform shows a primary peak which corresponds to the resonant frequency of the cavity and a corresponding standing frequency on the wire. The second peak is the second overtone. Treating the wire inside the pod as in free space it has cutoff frequency of .781 Ghz, and the frequency given by the pod data is .83 Ghz. Similarly the frequency domain data shows a second and third resonant frequency of 1.56 and 2.34 Ghz inside the pod which corresponds to the free space overtones at 1.55 and 2.41 Ghz (see figure Six).

CONCLUSION

A large object of electrical size 5.12×10^6 cells was successfully modeled with the synchronous out-of-core technique described above. The trade-off of total run-time vs. computational volume was found to be substantial, but objects as large as 10^7 cells were affordably modeled on a small SUN workstation. Further research and testing has shown that the method is suitable for implementation on massive parallel computers, and that model sizes of 10^9 cells are feasible using the CM-2 and Cray today. The new release of the CM-5 in 1993 will allow modeling of 10^{10} cell problems using multiple i/o channels. Ongoing research has been planned to further test this technique on the CM-5 as soon as it comes available. A parallelized version of this large scale FD-TD technique, including higher order boundary conditions and large geometry specifiers, is expected to be completed and tested on the CM-2 this coming year.

REFERENCES

- [1] Taflove, A.; Basis and Application of Finite-Difference Time-Domain Techniques for Modeling Electromagnetic Wave Interactions; Notes, APS Joint Symposium, Chicago, Ill., 1992.
- [2] Luebbers, R.; Hunsberger, F.; Kunz, K.; A Frequency-Dependant Finite-Difference Time-Domain Formulation for Dispersive Materials; IEEE, Trans. on Elec-Mag Comp., Vol. 32, No. 3, Aug. 1990.
- [3] Mur, G.; Absorbing Boundary Conditions for the Finite-Difference Approximation of the Time-Domain Electromagnetic Field Equations; IEEE, Trans. on Elec-Mag Comp., Vol. EMC-23, No. 4, Nov. 1981.
- [4] Miller, S.; A Survey of Parallel Computing; Amherst Systems Inc., Buffalo, N.Y., 1989.
- [5] Yee, K.; Numerical Solution of Initial Boundary Value Problems Involving Maxwell's Equations in Isotropic Media; IEEE Trans. on Ant. and Prop., Vol. AP-14, No. 3, May 1966.
- [6] Holland, R.; THREDE: A Free-Field EMP Coupling and Scattering Code; IEEE, Trans. on Nuc. Sci., Vol. NS-24, No. 6, Dec. 1977.

A STUDY OF COUPLED OSCILLATORY NEURAL NETWORK MODELS

**John A. Greenfield
Graduate Student
Department of Electrical and Computer Engineering**

**University of New Mexico
EECE Building
Albuquerque, NM 87131-1356**

**Final Report for:
Summer Research Program
Phillips Laboratory**

**Sponsored by:
Air Force Office of Scientific Research
Bolling Air Force Base, Washington, D.C.**

September 1992

A STUDY OF COUPLED OSCILLATORY NEURAL NETWORK MODELS

John A. Greenfield
Graduate Student
Department of Electrical and Computer Engineering
University of New Mexico

Abstract

Oscillatory neural network architectures were studied. Three different algorithms for artificial oscillatory neural networks, based on research by Freeman and Baird at the University of California at Berkeley, were examined, and two of the models were implemented as programs under the Khoros system. A study of these models shows that they may prove promising for some applications.

A STUDY OF COUPLED OSCILLATORY NEURAL NETWORK MODELS

John A. Greenfield

INTRODUCTION:

Many aspects of satellite control and simulation require large amounts of processing capacity. One way that this can be obtained is through the massively parallel capabilities of artificial neural networks. One of the new areas of artificial neural network research is the area of coupled neural oscillators.

The use of coupled oscillatory neural networks, more closely approximates the method of processing used by biological neural networks than does the more common technique of steady state artificial neural networks. It is argued that the dynamic nature of biological neural networks is one of the aspects which makes them perform so much better than current artificial neural networks and that the oscillatory neural network models should outperform the older steady state models [1,2,4,6]. It is clear from the literature that the oscillatory model is closer to the biological network than the static model, but will this translate into an improvement in capability for applications of this network? Oscillatory processing may be better for the biological network for reasons which do not exist for artificial network applications. For instance, the biological neurons finite life and inherent noisy behavior may be offset by an improved redundancy and noise immunity of an oscillatory system, where these benefits are of less value for a more reliable silicon neuron implementation. It is also possible that the oscillation is needed primarily to enable long distance transfer of information over the lossy biological connections, a problem which does not exist for most artificial neural net implementations. On the other hand, it may be that the oscillatory network has a performance advantage over the steady-state network in noise immunity or processing power that outweighs any penalties in the new network for real applications. This study was performed in an attempt to evaluate these new models for practical applications. All models were implemented under the Phoros integrated software development environment in order to facilitate their use and visualization of their results.

Procedure:

The oscillatory networks studied, function through a learning of attractors in energy space. These networks are capable of learning steady-state, periodic, or chaotic attractors, but for this project the implementations were limited to periodic attractors only. The models were based primarily on reference [4].

The first model of oscillatory neural network that was investigated was based on the *projection algorithm* [4]. In this model a set S of linearly independent vectors of the form:

$$\overline{r x^s} e^{i \theta^s} e^{i \omega^s t} \quad (1)$$

where the global amplitudes are of the form:

$$\frac{dr_s}{dt} = u_s r_s - r_s \sum_{j=1}^{N/2} a_{sj} r_j^2 \quad (2)$$

and the phases are:

$$\frac{d\Phi_s}{dt} = \omega_s + \sum_{j=1}^{N/2} b_{sj} r_j^2$$

Where there are N network nodes and N/2 cycles. The node states are produced by:

$$\frac{dx_i}{dt} = -\tau x_i + \sum_{j=1}^N T_{ij} x_j - \sum_{jkl=1}^N T_{ijl} x_j x_k x_l + b_i \delta(t)$$

and the connection weights T are formed by the projection operation(learning rule) :

$$T_{ij} = \sum_{mn=1}^N P_{im} J_{mn} P_{nj}^{-1} \quad T_{ijkl} = \sum_{mn=1}^N P_{im} A_{mn} P_{nj}^{-1} P_{kl} P_{nl}^{-1}$$

Where the NxN matrix P contains the real and imaginary components of the complex eigenvectors $x'e^{j\omega}$ as columns. J is an NxN matrix of complex conjugate eigenvalues in diagonal blocks and A is an NxN matrix of 2x2 blocks of repeated coefficients a_{ij} of the normal form equations (1,2) above.

$$J = \begin{matrix} \alpha_1 & -\omega_1 & 0 & 0 & \dots \\ \omega_1 & \alpha_1 & 0 & 0 & \dots \\ 0 & 0 & \alpha_2 & -\omega_2 & 0 \\ 0 & 0 & \omega_2 & \alpha_2 & 0 \\ \vdots & \vdots & \vdots & \vdots & \ddots \end{matrix} \quad A = \begin{matrix} a_{11} & a_{11} & a_{12} & a_{12} & \dots \\ a_{11} & a_{11} & a_{12} & a_{12} & \dots \\ a_{21} & a_{21} & a_{22} & a_{22} & \dots \\ a_{21} & a_{21} & a_{22} & a_{22} & \dots \\ \vdots & \vdots & \vdots & \vdots & \ddots \end{matrix}$$

This algorithm was implemented as separate training and classification programs as shown in the following two program listings.

| | |
|---|---|
| <pre> -AUTHORS John Greenfield and Carla Williams -AUTHORS_END -SHORT_PROG_DESCRIPTION Baird Oscillating neural network training algorithm. -SHORT_PROG_DESCRIPTION_END -SHORT_LIB_DESCRIPTION Baird Oscillating neural network training algorithm. -SHORT_LIB_DESCRIPTION_END -MAN1_LONG_DESCRIPTION .I osc_t is the training portion of a Baird Oscillating Neural Network. It establishes weight matrices to be used with the corresponding classification program (osc_c). -MAN1_LONG_DESCRIPTION_END .SH Theory: .LP The theory of the Baird oscillating neural network is discussed in the reference [1]. This program uses a Hebbian learning rule to produce a weight matrix for both excitatory and inhibitory connections for the network. .SH Reference: .LP B. Baird and F. Eckman, "A Normal Form Projection Algorithm for Associative Memory." .SH Program parameters: .LP PROJECTION MATRIX: a VIFF image that contains the real and imaginary components of the complex eigenvectors of the periodic vector field to be learned. The matrix is stored in row/column order in a single band of size N*N, where N is the number of elements in the desired input vector. .LP INVERSE PROJECTION MATRIX: a VIFF image that contains inverse of the projection matrix. For a symmetric matrix this is the transpose of the projection matrix. The matrix is stored in row/column form in a single band of size N*. .LP COEFFICIENT MATRIX: a VIFF image that contains repeated 2x2 blocks of repeated coefficients of the normal form equations to be learned. The matrix is stored in row/column form in a single band of size N*N. .LP J MATRIX: a VIFF image that contains the complex conjugate eigenvalues in diagonal blocks. The matrix is stored in row/column form in a single band of size N*N. .LP WEIGHTS: a VIFF image which is used to store the derived weights. This file is used as an input to the classification program. -MAN1_LONG_DESCRIPTION_END -MAN1_EXAMPLES osc_t ... -MAN1_EXAMPLES_END -MAN1_RESTRICTIONS All input images MUST be of data storage type FLOAT. </pre> | <pre> The output "weight" image is data storage type FLOAT. -MAN1_RESTRICTIONS_END -MAN1_SEE_ALSO osc_c(1) -MAN1_SEE_ALSO_END -MAN3_LONG_DESCRIPTION .I osc_t is the library training portion of a Baird Oscillating Neural Network. It establishes weight matrices to be used with the corresponding classification program (osc_c). -MAN3_LONG_DESCRIPTION_END -MAN3_RESTRICTIONS All input images MUST be of data storage type FLOAT. The output "weight" image is data storage type FLOAT. -MAN3_RESTRICTIONS_END -MAN3_SEE_ALSO osc_c(3) -MAN3_SEE_ALSO_END -USAGE_ADDITIONS -USAGE_ADDITIONS_END -INCLUDE_INCLUDES -INCLUDE_INCLUDES_END -INCLUDE_ADDITIONS -INCLUDE_ADDITIONS_END -INCLUDE_MACROS -INCLUDE_MACROS_END -MAIN_VARIABLE_LIST struct avimage *pimg, *pinvimg, *alimg, *ajimg, *atimg, *readimage(), *createimage(); int N; /* number of nodes */ char *program = "osc_t"; -MAIN_VARIABLE_LIST_END -MAIN_BEFORE_LIB_CALL if (check_args()) { printf (stderr,"%s: illegal arguments on command line.\n", program); exit(1); } /* Read and error check input projection matrix image */ if ((pimg = readimage (osc_t->il_file)) == NULL) { (void) printf (stderr,"%s: Cannot read projection matrix (%s).\n", program, osc_t->il_file); exit(1); } if (! (proptype (program, pimg, VFF_TYP_FLOAT, TRUE))) { printf (stderr,"%s: Data storage type for projection matrix must be FLOA program); </pre> |
|---|---|

Figure 1. Program Listing for Oscillating Neural Network Training Program

```

        exit(1);
    }
    (void) proper_num_images (program, Pimg, 1, TRUE);
    (void) proper_map_enable (program, Pimg, VFF_MAP_OPTIONAL, TRUE);
}
/* Check that number of rows equal number of columns */
if ( (Pimg->row_size == Pimg->col_size) )
{
    printf (stderr, "%s: Projection matrix is not square.\n", program);
    printf (stderr, "Number of rows is %d, number of columns is %d.\n",
        Pimg->col_size, Pimg->row_size);
    exit(1);
}
N = Pimg->row_size;

/* Read and error check input inverse projection matrix image */
if ( (Pinvmg = readimage (osc_t->i2_file)) == NULL )
{
    (void) printf (stderr, "%s: Cannot read inverse projection matrix (%s).\n",
        program, osc_t->i2_file);
    exit(1);
}
if ( ( ! (propertytype (program, Pinvmg, VFF_TYP_FLOAT, TRUE)) ) )
{
    printf (stderr, "%s: Data storage type for inverse proj. matrix must be F",
        program);
    exit(1);
}
(void) proper_num_images (program, Pinvmg, 1, TRUE);
(void) proper_map_enable (program, Pinvmg, VFF_MAP_OPTIONAL, TRUE);
/* Check that number of rows equal number of columns */
if ( (Pinvmg->row_size == Pinvmg->col_size) )
{
    printf (stderr, "%s: Inverse projection matrix is not square.\n", program);
    printf (stderr, "Number of rows is %d, number of columns is %d.\n",
        Pinvmg->col_size, Pinvmg->row_size);
    exit(1);
}

/* Check that Pinvmg is same size as Pimg */
if ( ( ! (Pinvmg->row_size == N) ) )
{
    printf (stderr, "%s: Inverse projection matrix is not same size as projection matrix",
        program);
    printf (stderr, "Projection matrix is size %d, inverse is size %d.\n",
        N, Pinvmg->row_size);
    exit(1);
}

/* Read and error check input coefficient matrix image */
if ( (aimg = readimage (osc_t->i3_file)) == NULL )
{
    (void) printf (stderr, "%s: Cannot read coefficient matrix (%s).\n",
        program, osc_t->i3_file);
    exit(1);
}
if ( ( ! (propertytype (program, aimg, VFF_TYP_FLOAT, TRUE)) ) )
{
    printf (stderr, "%s: Data storage type for coefficient matrix must be FLO",
        program);
    exit(1);
}
(void) proper_num_images (program, aimg, 1, TRUE);
(void) proper_map_enable (program, aimg, VFF_MAP_OPTIONAL, TRUE);
/* Check that number of rows equal number of columns */
if ( ( ! (aimg->row_size == aimg->col_size) ) )
{
    printf (stderr, "%s: Coefficient matrix is not square.\n", program);
    printf (stderr, "Number of rows is %d, number of columns is %d.\n",
        aimg->col_size, aimg->row_size);
    exit(1);
}

/* Check that a matrix is same size as Pimg */
if ( ( ! (aimg->row_size == N) ) )
{
    printf (stderr, "%s: Coefficient matrix is not same size as projection m",
        program);
    printf (stderr, "Projection matrix is size %d, coefficient matrix is size %d",
        N, aimg->row_size);
    exit(1);
}

/* Read and error check input complex conjugate eigenvalues matrix image */
if ( (Jimg = readimage (osc_t->i4_file)) == NULL )
{
    (void) printf (stderr, "%s: Cannot read complex conjugate eigenvalue matr",
        program, osc_t->i4_file);
    exit(1);
}
if ( ( ! (propertytype (program, Jimg, VFF_TYP_FLOAT, TRUE)) ) )
{
    printf (stderr, "%s: Data storage type for complex conjugate eigenvalue m",
        program);
    exit(1);
}
(void) proper_num_images (program, Jimg, 1, TRUE);
(void) proper_map_enable (program, Jimg, VFF_MAP_OPTIONAL, TRUE);
/* Check that number of rows equal number of columns */
if ( ( ! (Jimg->row_size == Jimg->col_size) ) )
{
    printf (stderr, "%s: Complex conjugate eigenvalue matrix is not square.\n",
        program);
    printf (stderr, "Number of rows is %d, number of columns is %d.\n",
        Jimg->col_size, Jimg->row_size);
    exit(1);
}

/* Check that a matrix is same size as Pimg */
if ( ( ! (Jimg->row_size == N) ) )
{
    printf (stderr, "%s: Complex conjugate eigenvalue matrix is not same siz",
        program);
    printf (stderr, "Projection matrix is size %d, J matrix is size %d.\n",
        N, Jimg->row_size);
    exit(1);
}

/* Create the output weight image */
wtimg = createlimage
    ((unsigned long) N,
    (unsigned long) N,
    (unsigned long) VFF_TYP_FLOAT,
    (unsigned long) 1,
    (unsigned long) N*N+1,
    "Weight image created by osc_t",
    (unsigned long) 0,
    (unsigned long) 0,
    (unsigned long) 0,
    (unsigned long) VFF_MS_NONE,
    (unsigned long) VFF_MAP_TYP_NONE,
    (unsigned long) VFF_LOC_IMPLICIT,
    (unsigned long) 0);
if (wtimg == NULL)
{

```

Figure 1. Program Listing for Oscillating Neural Network Training Program (cont.)

```

(void)printf(stderr,"%s: Unable to allocate weight image!\n",
    program);
exit(1);
}
free (wtimg->imagedata);
-MAIN_BEFORE_LIB_CALL_END

-MAIN_LIBRARY_CALL
if (! losc_t (Pimg, Pinvmg, aimg, Jimg, wtimg))
{
(void)printf (stderr,"%s: losc_t failed.\n",program);
exit(1);
}
-MAIN_LIBRARY_CALL_END

-MAIN_AFTER_LIB_CALL
/* Output weight image */
writeimage (losc_t->wt_file, wtimg);
-MAIN_AFTER_LIB_CALL_END

-LIBRARY_INCLUDES
-LIBRARY_INCLUDES_END

-LIBRARY_INPUT
.IP "Pimg" 15
the projection matrix used for training.
.IP "Pinvmg" 15
the inverse of the projection matrix.
.IP "aimg" 15
the coefficient matrix.
.IP "Jimg" 15
the complex conjugate of the eigenvalues matrix.
-LIBRARY_INPUT_END

-LIBRARY_OUTPUT
.IP "wtimg" 15
the resulting weight matrix after training.
-LIBRARY_OUTPUT_END

-LIBRARY_DEF
int losc_t (Pimg, Pinvmg, aimg, Jimg, wtimg)
-LIBRARY_DEF_END

-LIBRARY_CODE
{
    int N, i, j, k, l, m, n, sizeT, sizeW;
    int temp, index1, index2, index3, index4, index5, index6;
    float *P, *Pinv, *a, *J, *W, *T, *T2;
    char *program = "losc_t";

    /* Extract matrix data from image structures */
    P = (float *) Pimg->imagedata;
    Pinv = (float *) Pinvmg->imagedata;
    a = (float *) aimg->imagedata;
    J = (float *) Jimg->imagedata;
    N = Pimg->row_size; /* number of nodes */

    /* Allocate memory for weight matrix and initialize to zeros */
    sizeT = N * N;
    sizeW = sizeT * sizeT * sizeof(float);
    if ((W = (float *) malloc (unsigned sizeW * sizeof(float))) == NULL)
    {
        (void)printf (stderr,"%s: unable to allocate W matrix.\n",program);
        return(0);
    }
}

```

```

}
for (l=0; l<sizeW; l++)
    W[l] = 0.0;
T = W;
T2 = & W[sizeT];

/* This code implements the training algorithm for the first
/* coupled oscillator in Baird's paper.
/*
/*
for (i=0; i<N; i++) {
    for (j=0; j<N; j++) {
        index1 = i*N + j;
        T[index1] = 0.0;
        for (m=0; m<N; m++) {
            index2 = i*N + m;
            for (n=0; n<N; n++) {
                index3 = m*N + n;
                index4 = n*N + j;
                T[index1] += P[index2] * J[index3] * Pinv[index4];
            }
        }
        for (k=0; k<N; k++) {
            temp = i*N*N + j*N*N + k*N;
            for (l=0; l<N; l++) {
                index1 = temp + l;
                T2[index1] = 0.0;
                for (m=0; m<N; m++)
                    for (n=0; n<N; n++) {
                        index2 = i*N + m;
                        index3 = m*N + n;
                        index4 = m*N + j;
                        index5 = n*N + k;
                        index6 = n*N + l;
                        T2[index1] += P[index2] * a[index3] * Pinv[index4] *
                    }
                }
            }
        }
    }

    /* Insert weights into image structure */
    wtimg->imagedata = (char *) W;
    return(1);
}
-LIBRARY_CODE_END
-LIBRARY_MOOS
-LIBRARY_MOOS_END

```

Figure 1. Program Listing for Oscillating Neural Network Training Program (cont.)

| | |
|---|---|
| <pre> -AUTHORS J. Greenfield and C. Williams -AUTHORS_END -SHORT_PROG_DESCRIPTION Baird Oscillating neural network classification algorithm. -SHORT_PROG_DESCRIPTION_END -SHORT_LIB_DESCRIPTION Baird Oscillating neural network classification algorithm. -SHORT_LIB_DESCRIPTION_END -I osc.c is the classification portion of a pair of programs that simulate an Oscillating neural network, using the Normal form projection algorithm from [1]. The corresponding training program (osc.t) produces both the excitation and inhibition weight matrices required by this classification algorithm. This program retrieves the memorized oscillatory pattern that is the smallest Hamming distance from the initial input pattern. Thus a single static input pattern produces a stable dynamic oscillation. -SH Theory: .LP The theory of the Oscillating neural network is discussed in Reference [1]. -SH Reference: .LP [1] D. Baird and F. Eckman, "A Normal Form Projection Algorithm for Associative Memory." -SH Program Parameters: .LP TESTING DATA (t): a VIFF image that contains the input vectors to be classified. Each vector is defined as an image band where the total number of elements in each vector (band) = number of rows * number of columns. -LP WEIGHTS (wt): a VIFF image that contains the weights computed by the training program (osc.t). This is used to classify the testing data. -LP NUMBER OF STEPS (maxos): the iteration limit used to stop oscillation of the network (default is 1000). -LP STEP SIZE (h): step size for the differential equation solver. -LP DELAY CONSTANT (tau): time delay constant. -LP IMAGE FILE (o): a VIFF image which is used to store the output vectors computed by the oscillating network. Each vector is defined as a band with the vector elements for each oscillation step contained in a single row. The order and number of output vectors corresponds to that of the input vectors. -LP ASCII FILE (f): the filename of an ASCII file to which the classification stats will be printed. During classification, the program will print the output of the network while it is oscillating. If the ASCII FILE is not specified, the classification stats will be printed to standard output. -MAN1_LONG_DESCRIPTION_END -MAN1_EXAMPLES osc.c -l1 invect.xv -maxos 200 -h 0.001 -tau 1 -wt weight.xv -o classout.xv -MAN1_EXAMPLES_END -MAN1_RESTRICTIONS All input images MUST be of data storage type FLOAT. </pre> | <pre> The output "vector" image is data storage type FLOAT. -MAN1_RESTRICTIONS_END -MAN1_SEE_ALSO osc.t(1) -MAN1_SEE_ALSO_END -MAN3_LONG_DESCRIPTION .I osc.c is the library classification portion of a pair of programs that simulate a Oscillating neural network, using the Normal form projection algorithm from [1]. The corresponding training program (osc.t) produces both the excitation and inhibition weight matrices required by this classification algorithm. This program retrieves the memorized oscillatory pattern that is the smallest Hamming distance from the initial input pattern. Thus a single static input pattern produces a stable dynamic oscillation. -SH Reference: .LP [1] D. Baird and F. Eckman, "A Normal Form Projection Algorithm for Associative Memory." -MAN3_LONG_DESCRIPTION_END -MAN3_RESTRICTIONS All input images MUST be of data storage type FLOAT. The output "vector" image is data storage type FLOAT. -MAN3_RESTRICTIONS_END -MAN3_SEE_ALSO osc.t(3) -MAN3_SEE_ALSO_END -USAGE_ADDITIONS -USAGE_ADDITIONS_END -INCLUDE_INCLUDES -INCLUDE_INCLUDES_END -INCLUDE_ADDITIONS -INCLUDE_ADDITIONS_END -INCLUDE_MACROS -INCLUDE_MACROS_END -MAIN_VARIABLE_LIST struct xvimage "data, "wtimg, "outvec, "readimage(), "createimage(); int notv, N; /* input testing data */ /* input weights matrix */ /* computed output vectors */ /* number of nodes */ /* print device for ascii output of stats */ FILE "prntdev; char "program" = "osc.c"; -MAIN_VARIABLE_LIST_END -MAIN_BEFORE_LIB_CALL if (check_args()) { fprintf(stderr,"%s: illegal arguments on command line.\n", program); exit(1); } /* Read and error check training data */ if ((data = readimage (osc_c->t_file)) == NULL) { </pre> |
|---|---|

Figure 2. Program Listing for Oscillating Neural Network Classifier Program


```

(void) fprintf(stderr, "%s: Cannot read testing data (%s).\n",
program, osc_c->tf_file);
exit(1);
}
if (! (propertytype (program, data, VFF_TYP_FLOAT, TRUE)))
{
fprintf(stderr, "%s: Data storage type for training data must be FLOAT.",
program);
exit(1);
}
(void) proper_num_images (program, data, 1, TRUE);
(void) proper_map_enable (program, data, VFF_MAP_OPTIONAL, TRUE);
notv = data->num_data_bands;
N = (data->col_size) * (data->row_size);

/* Read and error check weight matrix */
if ((wtimg = readimage (osc_c->wt_file)) == NULL)
{
(void) fprintf(stderr, "%s: Cannot read weights (%s).\n",
program, osc_c->wt_file);
exit(1);
}
if (! (propertytype (program, wtimg, VFF_TYP_FLOAT, TRUE)))
{
fprintf(stderr, "%s: Data storage type for weights must be FLOAT.",
program);
exit(1);
}
(void) proper_num_images (program, wtimg, 1, TRUE);
(void) proper_map_enable (program, wtimg, VFF_MAP_OPTIONAL, TRUE);

/* Check that size of vectors for data and weights match */
if (! (N == wtimg->row_size))
{
fprintf(stderr, "%s: Weight image does not match size of vectors.\n",
program);
fprintf(stderr, "Should have %d, but contains %d size vectors.\n",
N, wtimg->row_size);
exit(1);
}

/* Create the output vector oscillation image */
outvec = createimage ((unsigned long) osc_c->maxos_int,
(unsigned long) N,
(unsigned long) 1,
(unsigned long) notv,
"Output vector image created by osc_c",
(unsigned long) 0,
(unsigned long) 0,
(unsigned long) VFF_MS_NONE,
(unsigned long) VFF_MAP_NONE,
(unsigned long) VFF_LOC_IMPLICIT,
(unsigned long) 0);
if (outvec == NULL)
{
(void) fprintf(stderr, "%s: Unable to allocate output vector image!\n",
program);
exit(1);
}
free (outvec->imagedata);

/* Open ascii output file for classification stats */
if (osc_c->sf_file)

```

```

if (! write_ascii(osc_c->f_file, fprintfdev))
{
(void) fprintf(stderr, "%s: Can't open ascii output file %s.\n",
program, osc_c->f_file);
exit(1);
}
else
{
fprintfdev = stdout;
MAIN_BEFORE_LIB_CALL_END
MAIN_LIBRARY_CALL
if (! losc_c (data, wtimg, outvec, osc_c->maxos_int, osc_c->h_float,
osc_c->tau_float, fprintfdev))
{
(void) fprintf(stderr, "%s: losc_c failed.\n", program);
exit(1);
}
MAIN_LIBRARY_CALL_END
MAIN_AFTER_LIB_CALL
/* Output the computed output vector image */
if (osc_c->o_flag)
writeimage(osc_c->o_file, outvec);
MAIN_AFTER_LIB_CALL_END
LIBRARY_INCLUDES
LIBRARY_INCLUDES_END
LIBRARY_INPUT
.IP "data" 15
the input data vectors used for testing.
.IP "wtimg" 15
the weight image obtained by training (using osc_t).
.IP "maxos" 15
the maximum number of oscillations to be used.
.IP "h" 15
step size for differential equation solver.
.IP "tau" 15
time delay constant.
.IP "fprintfdev" 15
print device name for classification stats.
LIBRARY_INPUT_END
LIBRARY_OUTPUT
.IP "outvec" 15
the output vector oscillations computed for the input testing data.
LIBRARY_OUTPUT_END
LIBRARY_DEF
int losc_c (data, wtimg, outvec, maxos, h, tau, fprintfdev)
struct ximage *data, *wtimg, *outvec;
int maxos;
float h, tau;
FILE *fprintfdev;
LIBRARY_DEF_END
LIBRARY_CODE
{
int notv, N, sizeT, cv, i, j, k, l, t, index1, index2;
float sum;
float *bvect, *W, *T, *T2, *Ovect;
float *b, *xvec, *x, *nx;
char *program = "losc_c";

```

Figure 2. Program Listing for Oscillating Neural Network Classifier Program (cont.)

```

/* Extract testing data from image structure */
bvec = (float *) data->imagedata;
notv = data->num_data_bands;

/* Extract weight matrix from image structure */
W = (float *) wimg->imagedata;
N = wimg->row_size;
sizeT = N * N;
T = W;
T2 = &sizeT;

/* Allocate memory for computed output vector oscillations */
if ((Ovect = (float *) malloc((N*maxos*notv+sizeof(float))) == NULL)
{
(void) fprintf(stderr, "%s: Unable to allocate Ovect matrix.\n", program);
return(0);
}
for (i=0; i<(N*maxos*notv); i++)
Ovect[i] = 0.0;

/* Allocate memory for output vector */
if ((ix = (float *) malloc((unsigned)N*sizeof(float))) == NULL)
{
(void) fprintf(stderr, "%s: Unable to allocate x vector.\n", program);
return(0);
}

/* Allocate memory for intermediate output vector */
if ((inx = (float *) malloc((unsigned)N*sizeof(float))) == NULL)
{
(void) fprintf(stderr, "%s: Unable to allocate inx vector.\n", program);
return(0);
}

(void) fprintf(stderr, "Classification Stats for OSC:\n");
(void) printf("Printdev, %s\nClassification Stats for OSC:\n", notv);
(void) printf("Printdev, %s\nNumber of steps: %d\n", h);
(void) printf("Printdev, %s\nStep size: %f\n", h);
(void) printf("Printdev, %s\nDelay constant: %f\n", tau);
(void) printf("Printdev, %s\nTotal number of vectors: %d\n", notv);

/* Process input testing vectors, one at a time */
for (tv=0; tv<notv; tv++)
{
/* Extract individual vector */
b = &bvec[N*tv];
xvec = &Ovect[N*maxos*tv];

/* Oscillate on an individual vector */
(void) printf("Printdev, %s\nInput vector %d, resulting network oscillations:\n",
tv);
.....
/* This code implements the classification part of the first
/* coupled oscillator in Baird's paper
.....
for (i=0; i<N; i++)
x[i] = 0.0;
for (t=0; t<maxos; t++){
for (i=0; i<N; i++){
sum = 0.0;
for (j=0; j<N; j++){
nx[i] = x[i];
index1 = i*N + j;
sum += T[index1] * x[j];
for (k=0; k<N; k++){
for (l=0; l<N; l++){

```

```

Index2 = i*N*N + j*N*N + k*N + l;
sum += T[Index2] * x[l] * x[k] * x[l];
}
}
nx[i] += h * (tau * x[i] + sum);
if (t==0)
nx[i] += b[i];
for (i=0; i<N; i++){
x[i] = nx[i];
xvec[N*t+i] = x[i];
}

/* Print iteration stats */
(void) printf("Printdev, %s\nStep %d: Output vector = ", t+1);
for (i=0; i<N; i++){
(void) printf("Printdev, %s", x[i]);
(void) printf("Printdev, %s\n", "");
}

outvec->imagedata = (char *) Ovect;

/* Cleanup */
if (x != NULL) free((char *) x);
if (nx != NULL) free((char *) nx);
return(1);
}
-LIBRARY_CODE_END
-LIBRARY_MODS
-LIBRARY_MODS_END

```

Figure 2. Program Listing for Oscillating Neural Network Classifier Program (cont.)

The algorithm implementation was tested on the following example from Baird and Eeckman [4].

For a four node network ($N=4$), two oscillatory attractors of the same frequency are stored, $\omega_1 = \omega_2 = 250$ rad/sec. .

$$P = \frac{1}{\sqrt{5}} \begin{bmatrix} 1 & 0 & 2 & 0 \\ 2 & 0 & -1 & 0 \\ 0 & 1 & 0 & 2 \\ 0 & 2 & 0 & -1 \end{bmatrix}, \quad J = \begin{bmatrix} 2 & -250 & 0 & 0 \\ 250 & 2 & 0 & 0 \\ 0 & 0 & 2 & -250 \\ 0 & 0 & 250 & 2 \end{bmatrix}, \quad A = \begin{bmatrix} 1 & 1 & 10 & 10 \\ 1 & 1 & 10 & 10 \\ 10 & 10 & 1 & 1 \\ 10 & 10 & 1 & 1 \end{bmatrix}$$

The results for two input vectors are shown in the following figure.

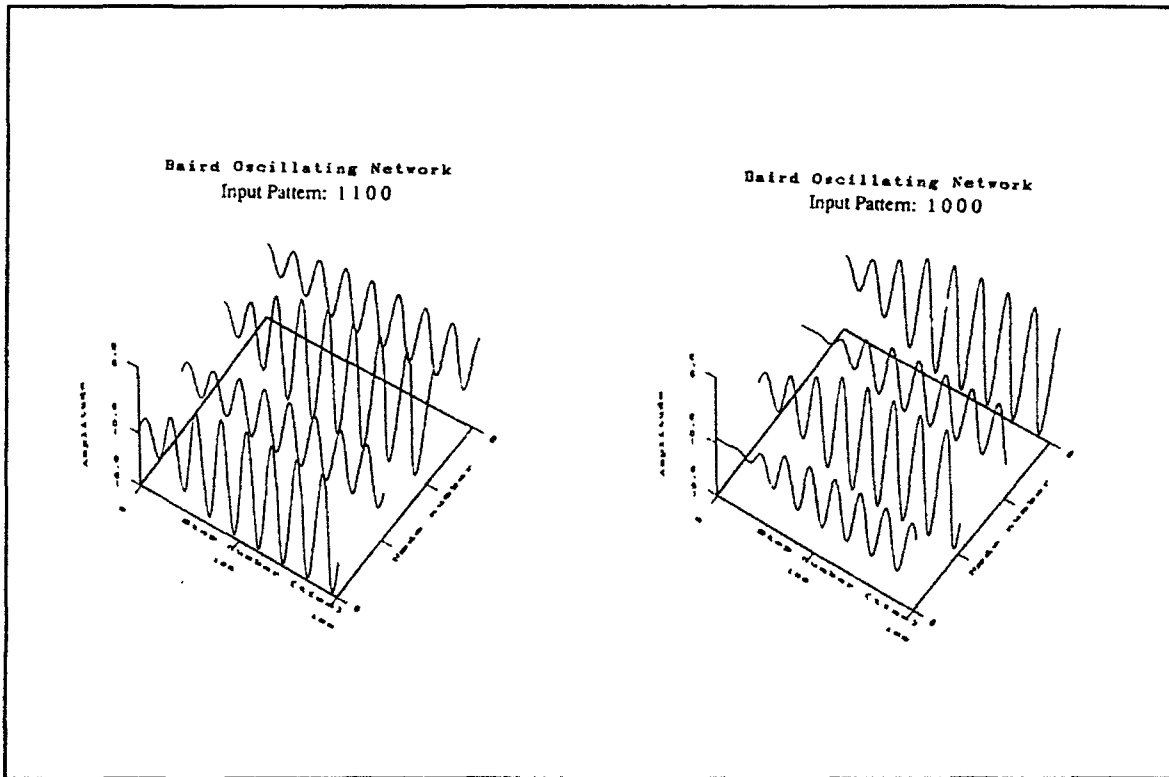


Fig. 3 Results for Oscillating Neural Network Example.

This network is an autoassociative memory that stores periodic signals and recalls the signal which is the

smallest Hamming distance from the static input vector. The network thus identifies a waveform based on an instantaneous sample. This could be a very valuable feature for certain applications. It should be noted that the operations required to simulate this network on a sequential computer are $O(N^4)$, a higher complexity than most steady-state content addressable memories. A hardware implementation of this network would perform these operations in parallel, and be approximately the same complexity as any continuous valued steady state network.

It will be noted that the code that implements this network uses a simple first order Eulerian method to solve the differential equation. A more accurate fourth order Runge-Kutta method was tried, but the results were not stable. This would seem to indicate a stiff set of equations, which might be best solved iteratively with an explicit Eulerian solution, but since the simple solution produced acceptable results this was not attempted. An iterative solution would significantly increase the processing time required.

The second network model is simpler to implement in hardware and is $O(N^2)$ on a sequential computer, but has the same theoretical basis as the first model. In this network a simple classifier network has a winner-take-all network folded into it resulting in the following network:

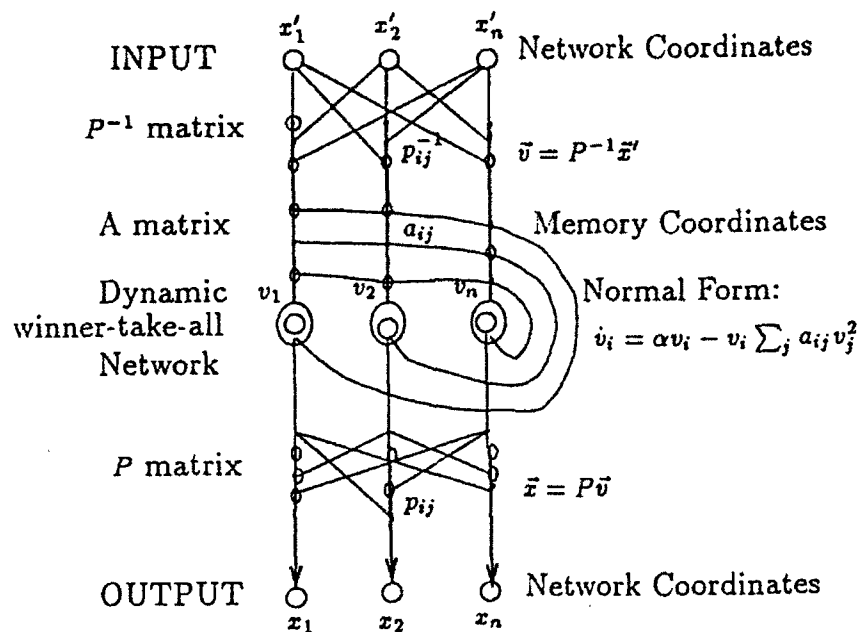


Fig. 4 Projection Network Diagram (from Baird [4], page 15).

This network is implemented by the following code:

```

-ALGORITHM
J. Greenfield and C. Williams
-ALGORITHM_END

-EXCEPT_DESCRIPTION
Basic Projection neural network classification algorithm.
-EXCEPT_DESCRIPTION_END

-EXCEPT_LHS_DESCRIPTION
Basic Projection neural network classification algorithm.
-EXCEPT_LHS_DESCRIPTION_END

-NAME_LONG_DESCRIPTION
1. (pre)
is the classification program that simulates a Basic
Projection neural network.
2. (pre)
Theory:
The theory of the Projection neural network is discussed
in Baird and Eckmann [1].
3. (pre)
References:
1. B. Baird and F. Eckmann, "A Normal Form Projection Algorithm
for Associative Memory."
4. (pre)
Program Parameters:
1. (pre)
TESTING DATA (td): a VIFF image that contains the input vectors to be
classified. Each vector is defined as an image band where the total number
of elements in each vector (band) is number of rows * number of columns.
2. (pre)
PROJECTION MATRIX (pm): a VIFF image that contains the real and
imaginary components of the complex eigenvectors of the periodic
vector field to be learned. The matrix is stored in row/column
form in a single band of size N*M, where N is the number of elements
in each input vector.
3. (pre)
INVERSE PROJECTION MATRIX (ipm): a VIFF image that contains the
inverse of the projection matrix. For a symmetrical matrix
this is the transpose of the projection matrix. The matrix is
stored in row/column form in a single band of size N*M.
4. (pre)
COEFFICIENT MATRIX (cm): a VIFF image that contains repeated
1x1 blocks of repeated coefficients of the normal form equations
to be recalled. The matrix is stored in row/column form in a
single band of size N*M.
5. (pre)
NUMBER OF STEPS (maxsteps): the iteration limit used to stop
oscillation of the network (default is 1000).
6. (pre)
STEP SIZE (hs): step size for the differential equation solver.
7. (pre)
DELAY CONSTANT (ta): time delay constant.
8. (pre)
IMAGE FILE (if): a VIFF image which is used to store the output vectors
computed by the oscillating network. Each vector is defined as a band with the
vector elements for each oscillation step contained in a single row. The
order and number of output vectors corresponds to that of the input vectors.
9. (pre)
ASCII FILE (af): the filename of an ASCII file to which the classification
state will be printed.
During classification, the program will print the output of the network
while it is oscillating.
If the ASCII FILE is not specified, the classification state will be
printed to standard output.
-NAME_LONG_DESCRIPTION_END

-NAME_SHORT_DESCRIPTION
pre -td input.vv -ipm inverse.vv -maxsteps 1000 -hs weight.vv -ta classout.vv
-NAME_SHORT_DESCRIPTION_END

-NAME_RESTRICTIONS
All input images MUST be of data storage type FLOAT.
The output "vector" image is data storage type FLOAT.
-NAME_RESTRICTIONS_END

-NAME_SEE_ALSO
-NAME_SEE_ALSO_END

-NAME_LONG_DESCRIPTION
1. (pre)
is the library classification program that simulates a Basic
Projection neural network.
-NAME_LONG_DESCRIPTION_END

-NAME_RESTRICTIONS
All input images MUST be of data storage type FLOAT.
The output "vector" image is data storage type FLOAT.
-NAME_RESTRICTIONS_END

-NAME_SEE_ALSO
-NAME_SEE_ALSO_END

-NAME_ADDITIONS
-NAME_ADDITIONS_END

-NAME_INCLUDES
-NAME_INCLUDES_END

-NAME_INCLUDES
-NAME_INCLUDES_END

-NAME_VARIABLE_LIST
struct names:
// Input testing data //
// projection matrix //
// inverse projection matrix //
// coefficient matrix //
// computed output vectors //
// readimage //
// writeimage //
// number of testing vectors //

```

```

// number of nodes //
// print device for test output of state //
FILE *prntdev;
char *program = "pre";
-NAME_VARIABLE_LIST_END

if (check_argv())
{
    fprintf(stderr, "Error: illegal arguments on command line\n");
    program = "pre";
    exit(1);
}

/* Read and error check training data */
if (!data = readimage (prntdev, ifile)) == NULL)
{
    (void) fprintf (stderr, "Error: Cannot read training data (%s)\n",
        program, prntdev->file);
    exit(1);
}
if (! (proper_type (program, data, VIFF_TYP_FLOAT, TRUE)))
{
    (void) fprintf (stderr, "Error: Data storage type for training data must be FLOAT.\n");
    exit(1);
}
(void) proper_map_enable (program, data, 1, TRUE);
(void) proper_map_enable (program, data, VIFF_MAP_OPTIONAL, TRUE);
new = data->new_data_bands;
M = (data->new_size) * (data->new_size);

/* Read and error check input projection matrix image */
if (! (pm = readimage (prntdev, ifile)) == NULL)
{
    (void) fprintf (stderr, "Error: Cannot read projection matrix (%s)\n",
        program, prntdev->file);
    exit(1);
}
if (! (proper_type (program, pm, VIFF_TYP_FLOAT, TRUE)))
{
    (void) fprintf (stderr, "Error: Data storage type for projection matrix must be FLOAT.\n");
    exit(1);
}
(void) proper_map_enable (program, pm, 1, TRUE);
(void) proper_map_enable (program, pm, VIFF_MAP_OPTIONAL, TRUE);

/* Check that number of rows equal number of columns */
if (! (pm->row_size == pm->col_size))
{
    (void) fprintf (stderr, "Error: Projection matrix is not square\n");
    (void) fprintf (stderr, "Number of rows is %d, number of columns is %d\n",
        pm->row_size, pm->col_size);
    exit(1);
}

/* Check that pm data is same size as input data */
if (! (pm->row_size == M))
{
    (void) fprintf (stderr, "Error: Projection matrix is not same size as input data\n");
    exit(1);
}

(void) fprintf (stderr, "Input data is size %d, projection matrix is size %d\n",
    M, pm->row_size);
exit(1);

/* Read and error check input inverse projection matrix image */
if (! (ipm = readimage (prntdev, ifile)) == NULL)
{
    (void) fprintf (stderr, "Error: Cannot read inverse projection matrix (%s)\n",
        program, prntdev->file);
    exit(1);
}
if (! (proper_type (program, ipm, VIFF_TYP_FLOAT, TRUE)))
{
    (void) fprintf (stderr, "Error: Data storage type for inverse projection matrix must be FLOAT.\n");
    exit(1);
}
(void) proper_map_enable (program, ipm, 1, TRUE);
(void) proper_map_enable (program, ipm, VIFF_MAP_OPTIONAL, TRUE);

/* Check that number of rows equal number of columns */
if (! (ipm->row_size == ipm->col_size))
{
    (void) fprintf (stderr, "Error: Inverse projection matrix is not square\n");
    (void) fprintf (stderr, "Number of rows is %d, number of columns is %d\n",
        ipm->row_size, ipm->col_size);
    exit(1);
}

/* Check that ipm is same size as pm */
if (! (ipm->row_size == M))
{
    (void) fprintf (stderr, "Error: Inverse projection matrix is not same size as projection matrix\n");
    (void) fprintf (stderr, "Projection matrix is size %d, inverse is size %d\n",
        M, ipm->row_size);
    exit(1);
}

/* Read and error check input coefficient matrix image */
if (! (cm = readimage (prntdev, ifile)) == NULL)
{
    (void) fprintf (stderr, "Error: Cannot read coefficient matrix (%s)\n",
        program, prntdev->file);
    exit(1);
}
if (! (proper_type (program, cm, VIFF_TYP_FLOAT, TRUE)))
{
    (void) fprintf (stderr, "Error: Data storage type for coefficient matrix must be FLOAT.\n");
    exit(1);
}
(void) proper_map_enable (program, cm, 1, TRUE);
(void) proper_map_enable (program, cm, VIFF_MAP_OPTIONAL, TRUE);

/* Check that number of rows equal number of columns */
if (! (cm->row_size == cm->col_size))
{
    (void) fprintf (stderr, "Error: Coefficient matrix is not square\n");
    (void) fprintf (stderr, "Number of rows is %d, number of columns is %d\n",
        cm->row_size, cm->col_size);
    exit(1);
}

```

Figure 5. Program Listing for Oscillating Neural Network Classifier Program

| | |
|---|---|
| <pre> static_alig_row_size, alig_row_size); exit(1); } /* Check that a matrix is same size as Proj */ if ((alig_row_size == N)) { fprintf(stderr, "Error: Coefficient matrix is not same size as projection matrix 'in'."); fprintf(stderr, "Projection matrix is size %d, coefficient matrix is size %d.\n", N, alig_row_size); exit(1); } /* Create the output vector oscillation image */ outvec = createimage ((unsigned long) proj->image_int, (unsigned long) N, (unsigned long) 1, (unsigned long) outvec, "Output vector image created by proj", (unsigned long) 0, (unsigned long) 0, (unsigned long) VTF_NO_MOVE, (unsigned long) VTF_HAPPY_MOVE, (unsigned long) VTF_LOC_HPLICITY, (unsigned long) 0); if (outvec == NULL) { fprintf(stderr, "Error: Unable to allocate output vector image.\n"); program(); exit(1); } free (outvec->image_data); /* Open serial output file for classification state */ if (proj->of_file) { if (!write_serial(proj->of_file, printdev)) { fprintf(stderr, "Error: Can't open serial output file to 'in'."); program(); exit(1); } } else printf("a's done:"); MAIN_BEFORE_LIB_CALL_DND MAIN_LIBRARY_CALL if (! (proj->data, Proj, Fining, alig, outvec, proj->image_int, proj->h_float, proj->selphs_float, printdev)) { fprintf(stderr, "Error: Proj failed.\n"); program(); exit(1); } MAIN_LIBRARY_CALL_DND MAIN_AFTER_LIB_CALL /* Output the computed output vector image */ if (proj->of_file) writeimage(proj->of_file, outvec); MAIN_AFTER_LIB_CALL_DND -LIBRARY_INCLUDES -LIBRARY_INCLUDES_DND -LIBRARY_INPUT -IP "data" is the input data vectors used for testing. -IP "maxos" is the maximum number of oscillations to be used. -IP "h" is step size for differential equation solver. -IP "alpha" is time delay constant. -IP "printdev" is print device name for classification state. -LIBRARY_INPUT_DND -LIBRARY_OUTPUT -IP "outvec" is the output class vector oscillations computed for the input testing data. -LIBRARY_OUTPUT_DND -LIBRARY_IPF int iproj (data, Proj, Fining, alig, outvec, maxos, h, alpha, printdev); int main; float h, alpha; FILE "printdev"; -LIBRARY_IPF_DND -LIBRARY_CODE { int ntw, W, to, i, j, t, index, maxl; float max, sum; float "bvec", "P", "Fvec", "a", "Ovec"; float "b", "mvec", "a", "v", "nv"; char "program" = "iproj"; /* Extract matrix data from image structure */ bvec = (float *) data->image_data; ntw = data->num_data_bands; /* number testing vectors */ P = (float *) Proj->image_data; Fvec = (float *) Fining->image_data; a = (float *) alig->image_data; N = Proj->row_size; /* number of nodes */ /* Allocate memory for computed output vector oscillations */ if (Ovec = (float *) malloc("maxos" * ntw * sizeof(float)) == NULL) { fprintf(stderr, "Error: Unable to allocate Ovec matrix.\n"); program(); return(0); } for (i=0; i<N*maxos; i++) </pre> | <pre> Ovec[i] = 0.0; /* Allocate memory for output vector */ if (u = (float *) malloc(sizeof(float) * N) == NULL) { fprintf(stderr, "Error: Unable to allocate u vector.\n"); program(); return(0); } /* Allocate memory for intermediate output vectors */ if (v = (float *) malloc(sizeof(float) * N) == NULL) { fprintf(stderr, "Error: Unable to allocate v vector.\n"); program(); return(0); } if (w = (float *) malloc(sizeof(float) * N) == NULL) { fprintf(stderr, "Error: Unable to allocate w vector.\n"); program(); return(0); } (void) printf (printdev, "Classification State for PROJ:\n"); (void) printf (printdev, "Number of steps: %d\n", maxos); (void) printf (printdev, "Step size: %f\n", h); (void) printf (printdev, "Delay constant: %f\n", alpha); (void) printf (printdev, "Total number of vectors: %d\n", ntw); /* Process input testing vectors, one at a time */ for (tw=0; tw<ntw; tw++) { /* Extract individual vector */ b = & bvec[N*tw]; vvec = & Ovec[N*maxos*tw]; /* Oscillate on an individual vector */ fprintf (printdev, "Input vector %d, resulting network oscillations:\n", tw+1); fprintf (printdev, "Step 0: Input vector = "); for (i=0; i<N; i++) { fprintf (printdev, "%g", b[i]); } fprintf (printdev, "\n"); /* This code implements the classification part of the second /* coupled oscillator is said's paper */ for (i=0; i<N; i++) { w[i] = b[i]; } for (tw=0; tw<maxos; tw++) { for (i=0; i<N; i++) { w[i] = 0; for (j=0; j<N; j++) { index = i*N + j; w[index] = P[j] * v[j]; } } sum = 0.0; maxl = -1; for (i=0; i<N; i++) { sum = 0.0; w[i] = w[i]; for (j=0; j<N; j++) { index = i*N + j; sum = a[index] * v[j] + w[index]; } w[i] = h * v[i] + (alpha - sum); if (w[i] > maxl) maxl = w[i]; if (maxl > 15) w[i] = 15.0; maxl = i; } vvec[N*tw] = maxl; } /* Print iteration state */ fprintf (printdev, "Step %d: Output vector = ", tw+1); for (i=0; i<N; i++) { fprintf (printdev, "%g", v[i]); } fprintf (printdev, "\n"); outvec->image_data = (char *) Ovec; /* Cleanup */ if (u != NULL) free(u); if (v != NULL) free(v); if (w != NULL) free(w); return(1); } -LIBRARY_CODE_DND -LIBRARY_MAIN -LIBRARY_MAIN_DND </pre> |
|---|---|

Figure 5. Program Listing for Oscillating Neural Network Classifier Program (cont.)

The network was tested for a similar example to the first network, with the following results:

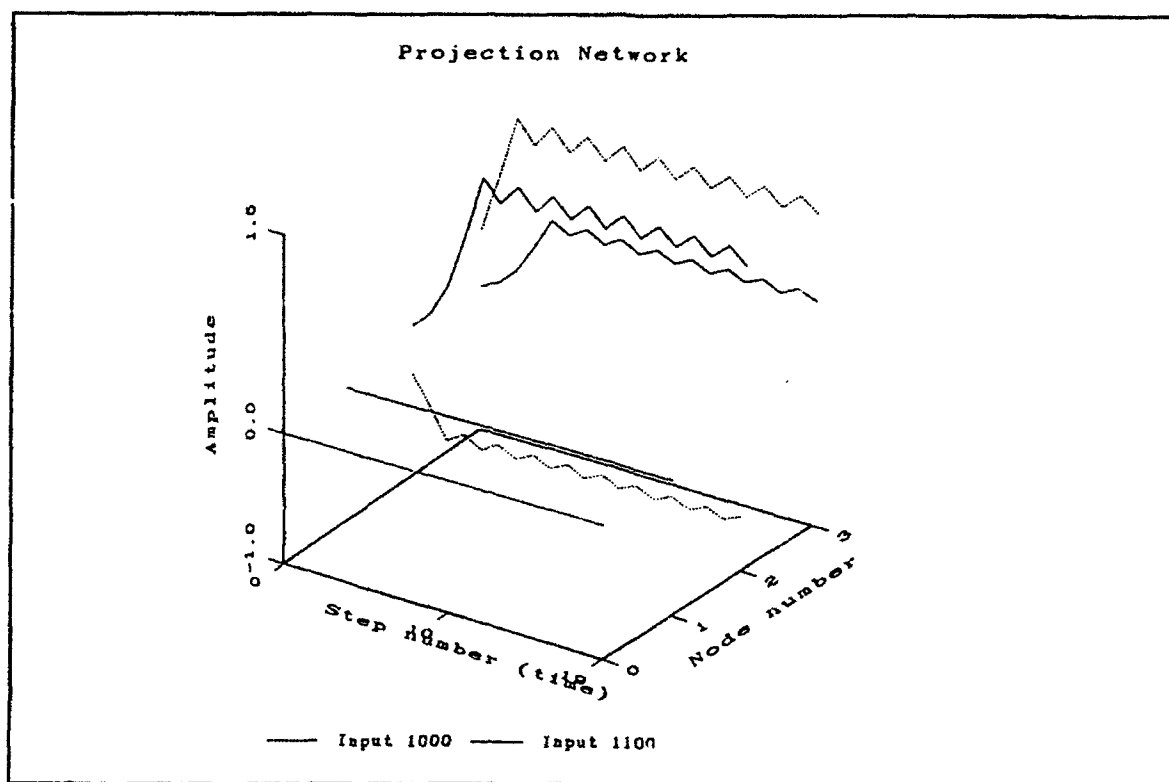


Fig. 6 Results for Projection Network Example.

It should be noted that while this model should have been trained to produce the same results as the first model, the results shown here significantly different. It was not possible to determine the reason for this discrepancy in the time available for this project. This network should be very simple to produce in hardware, since it is similar to existing neural networks.

The third network studied was based on the same theory, but designed to more closely simulate biological network architecture. The network has the following appearance:

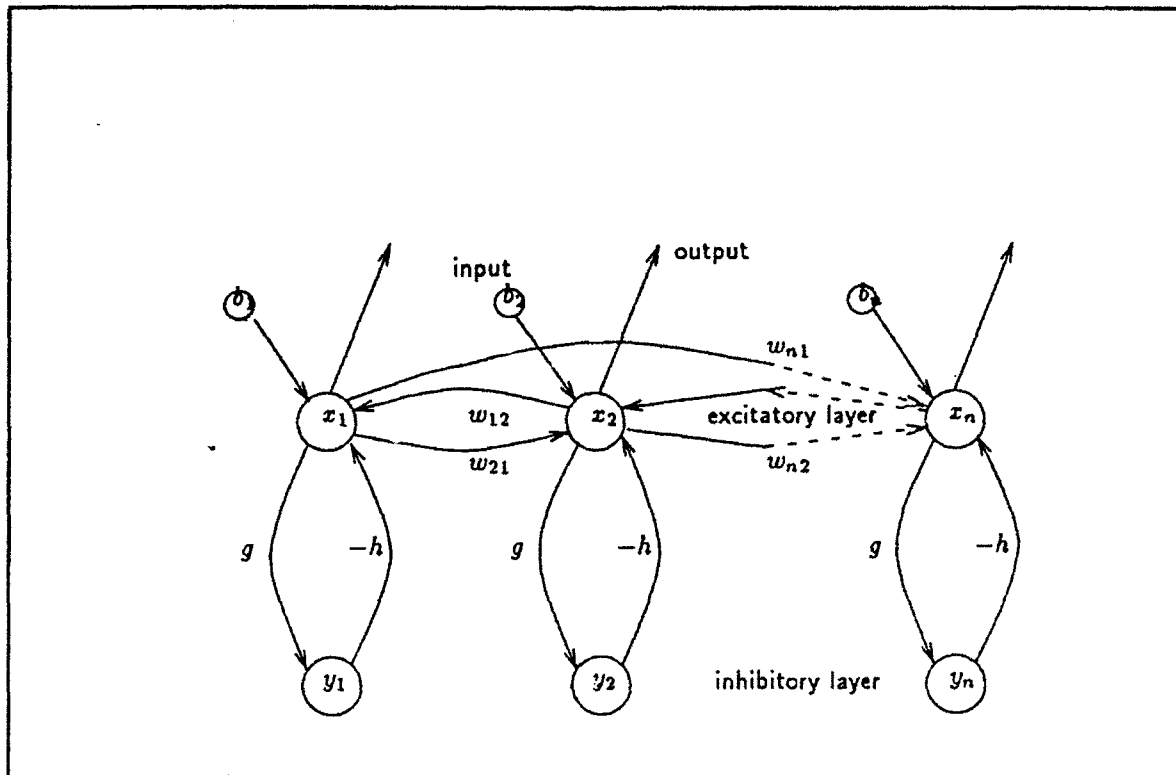


Fig. 7 Biological Subnetwork Diagram (from Baird [4], page 28).

An attempt was made to write a program to simulate this network, but the set of equations required seems to be stiff and was even more sensitive to error than the first network. It was never possible to obtain stable oscillations from this simulation. If more time had been available, an iterative solution of the explicit Eulerian form might have been successful.

CONCLUSION:

The capability of these networks to learn periodic or chaotic attractors offers several potential advantages. First, they lend themselves to the recognition of different periodic input signals. Second, the response time of the hardware version may in fact be faster than current steady-state network implementations. Third, chaotic attractors offer significant noise tolerance potential. Finally, if a chaotic attractor can be found to match a desired input, then recognition can be performed very efficiently.

Unfortunately, there are some potential disadvantages with these networks. They are difficult to implement simulations for, and are not currently as efficient as steady-state networks in identifying constant inputs with constant outputs. Much of the theoretical artificial neural network design research to date has focused on stopping networks from oscillating, rather than designing them to oscillate. Since much of the current implementation of neural network applications involves experiential data rather than theoretical foundations, it will be more difficult to use this hard won knowledge with these radically different networks. The first network model may be somewhat difficult to implement in hardware, the second offers no clear guidance on proper training algorithms, and the third was not simulateable in the short time available.

It would be very valuable to attempt to use these networks to perform some time varying signal recognition task, and compare this with a buffered input steady-state network implementation for the same task. This would allow a comparative evaluation of the difficulty of implementing this radically different type of network and how much performance benefit could be obtained. It would also be very useful to perform studies with chaotic attractors, since this area offers the potential benefits of a combination of neural networks and fuzzy logic / chaos theory. Another useful study would be to use networks of this type to implement individual oscillatory associative networks which would encode their results as a phase label and then to use these as elements in an array of coupled oscillators as described by Baldi and Meir [5].

REFERENCES:

- [1] B. Baird. "A Bifurcation Theory Approach to Vector Field Programming for Periodic Attractors." Proc. Int. Joint Conf. on Neural Networks, Wash. D.C., pages 1:381-388, June 1989.
- [2] B. Baird. "Bifurcation and Learning in Network Models of Oscillating Cortex." Emergent Computation, S. Forest, ed, pages 365-384. North Holland, 1990. also in *Physica D*, 42.
- [3] B. Baird and F. Eeckman. "A Hierarchical sensory-motor Architecture of Oscillating Cortical Area Subnetworks." Analysis and Modeling of Neural Systems II, F. Eeckman, ed., Norwell, MA, 1992. Kluwer.
- [4] B. Baird and F. Eeckman. "A Normal Form Projection Algorithm for Associative Memory." UC Berkeley Math Department, Unpublished paper.
- [5] P. Baldi and R. Meir. "Computing with Arrays of Coupled Oscillators: An Application to Preattentive Texture Discrimination." Neural Computation, Vol. 2, pages 458-471. 1990.
- [6] Y. Yao and W. Freeman. "Model of Biological Pattern Recognition with Spatially Chaotic Dynamics." Neural Networks, Vol 3, pages 153-170, 1990.

**HIGH TEMPERATURE HEAT PIPE MODELING
UNDER LOW POWER HEAT LOADS**

AND

**CRYOGENIC PHASE CHANGE MATERIAL DEVICES
IN SPACE APPLICATIONS**

**Steven E. Griffin
Graduate Student
Department of Mechanical Engineering**

**University of Texas at San Antonio
6900 North Loop 1604 West
San Antonio, TX 78249**

**Final Report for
Summer Research Program
Phillips Laboratory**

**Sponsored by:
Air Force Office of Scientific Research
Bolling Air Force Base, Washington, D.C.**

September 1992

HIGH TEMPERATURE HEAT PIPE MODELING
AND
CRYOGENIC PHASE CHANGE MATERIAL DEVICES

Steven E. Griffin
Department of Mechanical Engineering
University of Texas at San Antonio

Abstract

An experimental and analytical investigation into the effects and duration of low power throughput in liquid metal heat pipes is under study by Phillips National Laboratory and Los Alamos National Laboratory. The current study indicates that low-temperature and low-power throughput heat pipe modeling will provide a substantial basis for evaluating failure due to local evaporator dry-out. Failure occurs when the working fluid migrates to a cold region in the pipe where it freezes and fails to return to the evaporator section. Eventually, a sufficient inventory is lost to the cold region causing a local evaporator dry-out condition.

Devices incorporating a cryogenic phase change material are being considered for their high thermal effectiveness in satellite thermal control of infrared sensors at temperatures near 120 K. The approach is to evaluate the overall performance of several designs based on both canister type and conduction enhancement methods. The goal is to improve the low thermal conduction and retain the high latent thermal storage characteristics of the working phase change material: 2-methylpentane.

HIGH TEMPERATURE HEAT PIPE MODELING

Introduction

Heat pipes have been under investigation since their introduction by Grover in 1964. Today heat pipe modeling has taken many turns at evaluating performance limits based on operation, design, and application. During normal operation, a heat pipe may function indefinitely at design temperatures but rely heavily on the power throughput required by both its design and application.

Space applications require various throughput stages to accommodate thermal control. Quite often the heat pipe systems undergo cycles of normal and low design power throughput. At low levels, the fluid inventory may enter a below fusion operation region and be depleted as the result of migrational freeze fronts forming along the condenser length. For long-term low-power operation systems, failure may occur within the evaporator due to a fluid inventory loss caused by the fluid freezing along the condenser length and failing to return to the evaporator.

Currently, both Phillips National Laboratory and Los Alamos National Laboratory are researching the effect of this type of local dry-out to establish an empirical model for predicting rates of freeze migration in liquid metal heat pipes operating well below their design limits.

The following describes the experimental approach of the key investigators Joseph Secary of Phillips Laboratory and Michael Merrigan and Michael Keddy of Los Alamos to determine failure characteristics of potassium heat pipes during progressive migration of the working fluid to the frozen region of the heat pipe.

Experimental

Low temperature experiments (LTE) are desired for two reasons. The first simplifies instrumentation, insulation, and experimental procedures over the requirements of the higher temperature heat pipes. The second enables direct observation of heat pipe transport phenomenon.

Instrumentation and insulation are considerably less complicated and costly for low temperature heat pipe testing than for high. Consequently, operating temperatures below 470 K are desired to simplify equipment handling and data collection.

Heat pipe fluids evaluated for low temperature applications should in general exhibit low vapor pressure and density near their triple point to permit sufficient free molecular flow behavior. Fluid features should include low-toxicity, hazard potential and nuisance factor, while remaining compatible and nonreactive with any of the construction material. The fluid should have a relatively low saturation vapor pressure to minimize the hazard of an unlikely container failure by rupture or leaking. Using the above criteria, the working fluid (octadecane) was chosen over other fluids as the most favorable because it not only satisfies the requirements but also provides the most available table properties.

Initially, experimental evaluation of the octadecane's performance as a heat pipe fluid determined if it exhibited satisfactory heat carrying and wicking capabilities. This experiment used a quartz envelope and a homogeneous 250 mesh stainless steel wick placed only within the evaporator section. Testing occurred at successively greater heights until a capillary limit was discovered at a specific static lift where the evaporator temperature rose sharply.

The LTE approach uses transparent pyrex tubing to evaluate deposit characteristics of a fluid's mass migration from the evaporator's molten region along the condenser's frozen region. The heat pipe consist of an inner pyrex tubing which has been cut into several subsections, numbered with a scribe, weighed to 0.0001 grams, and placed in an outer pyrex envelope as shown in Figure 1.

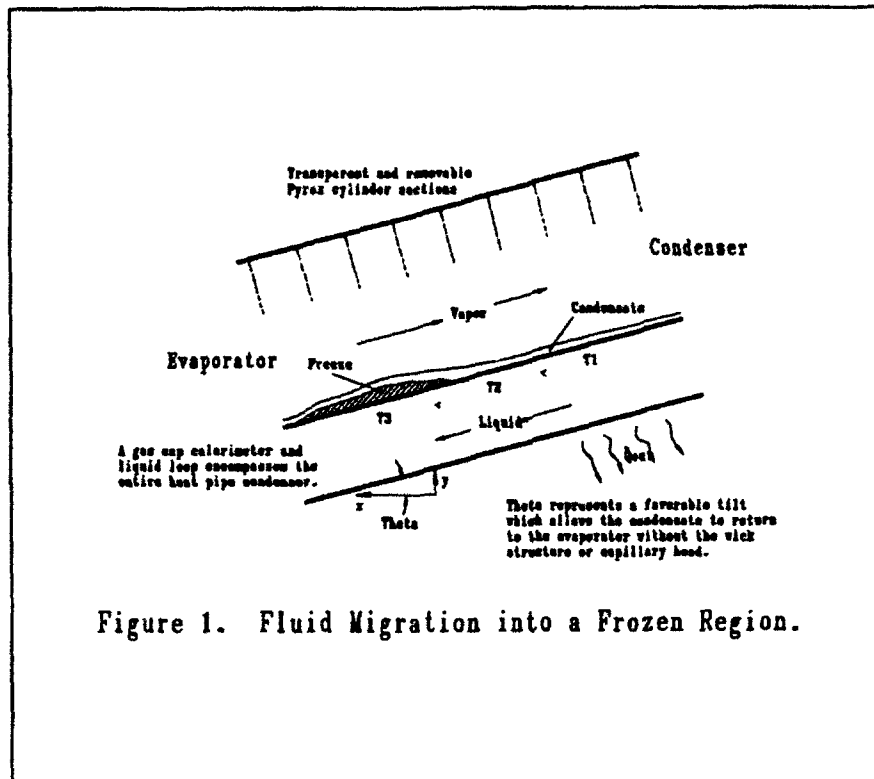


Figure 1. Fluid Migration into a Frozen Region.

The water and gas mixture temperature in the heat sink are adjusted until the freeze front is located at some conveniently observable location on one of the numbered pyrex cylinder sections. Temperatures and times are recorded during the duration of the test which generally last from two to three weeks. After completing the test, the pyrex tube sections of the inner core are disassembled to provide direct mass distribution measurements along the heat pipe. The mass migration rate is determined from the mass distribution measurements and the operating time. Later, a functional dependence of mass migration rates on temperature and power throughput for the various test will be analyzed [2].

Conclusion

The heat pipe experimentation has only begun with the verification of the octadecane fluid as a satisfactory heat carrying and capable wicking fluid for low temperature experiments. Further experiments will be based on test durations ranging from 500 to 1000 hours. The heat loads and temperatures will range from 15 to 35 watts and 340 to 420 K. Eventually, liquid metal heat pipes will be evaluated based on the results and empirical models developed from prior experiments. The overall results will provide a formulation showing that failure by internal migration of the working fluid can be prevented in space power and other applications.

CRYOGENIC PHASE CHANGE MATERIAL DEVICES

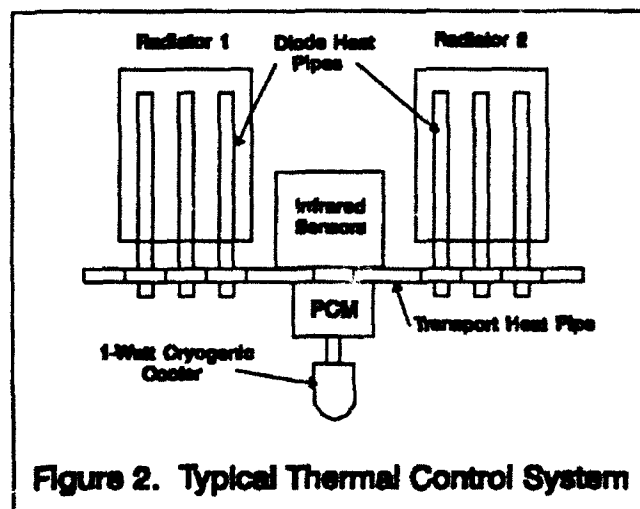
Introduction

Current satellite technology focuses on several methods for providing thermal control throughout the orbital life. Typical thermal control systems (TCS) include cryogenic phase change devices and diode heat pipes because of their passive performance and energy directing characteristics. In satellite applications, pulsed heat loads are applied to the phase change material (PCM) and effect the required amount of thermal storage media.

In Figure 2, satellite radiators are mounted on opposite sides and are normal to the orbital plane and flight direction. Consequently, the radiators alternate in shadow and sun throughout the orbit. The colder shadowed radiator radiates dissipated electrical sensor energy and parasitic heat leakage from the TCS. During the alternating crossover period, the shadow radiator becomes insulated and the sun radiator becomes shadowed so that neither the shadowed nor the sun radiator is cool enough to reject heat. During this period, sensor heat and parasitic heat leakage is absorbed by a PCM canister where heat melts the subcooled material. When the shadowed radiator cools to its operating temperature, it radiates again and the PCM refreezes.

The heat pipes transport heat from sensors and the PCM to the emitting radiator. The diode heat pipes block any reversing heat flows which occur when the insulated radiator is at a higher temperature than the sensors and PCM. Consequently, a set of sensors are thermally controlled via the PCM's fusion temperature which make consistent melt/freeze cycles and behavior paramount in this type of system.

The following describes the material selection, canister type, and conduction enhancement methods for evaluating different phase change canisters at cryogenic temperatures near 120 K and 5 kilo-Joules thermal storage.



Methodology

Phase change satellite applications involve various design constraints such as weight, size, thermal storage capacity, and operating temperature. The latter two requirements are prerequisites for selecting a phase change material that demonstrates:

- 1) Consistent melt/freeze cycles and behavior,
- 2) High heat of fusion and high density,
- 3) Chemical stability and container compatibility,
- 4) Low room temperature vapor pressure.

Using the above criterion, 2-methylpentane was selected due to its high heat of transition (72.9 J/g), reasonably high density (0.8 g/cc), chemically non-toxic and stable nature, and compatibility with many materials including aluminum.

Grumman Corporation's chief investigator Fred Edelstein published an SAE technical paper [3] on the behavior of PCM materials used in space thermal control of infrared sensors. The paper reveals that although 2-methylpentane appears to be the best PCM within the 115 K to 120 K range, it and other hydrocarbons, exhibit severe supercooling as high as 30 K below the transition temperature.

After several studies, the transition temperature range was sharply reduced by the addition of 3 percent acetone. After testing, the supercooling exhibited only 4 K when starting from a 100 percent liquid concentration. When some solid is present, virtually no supercooling effects remain and the material refreezes near its desired 119.3 K. As a result, an extra amount of PCM solid should remain when the PCM begins refreezing to avoid supercooling.

After the difficulty of seeding the PCM for consistent melt/freeze cycles, efforts continued to design a phase change canister. One type, a square canister was fabricated and tested successfully by Grumman. Other designs, shown in Figure 3, are under study for their size and weight difference, along with their ability to successfully transfer heat from the heater to the cold finger or heat flow meter.

To complicate matters further, the container should provide the minimum temperature drop between the PCM and sensor interface due to the PCM's low thermal conductivity. Furthermore, the canister must accommodate internal pressure changes due to the PCM volume variations during cyclic thermal loads.

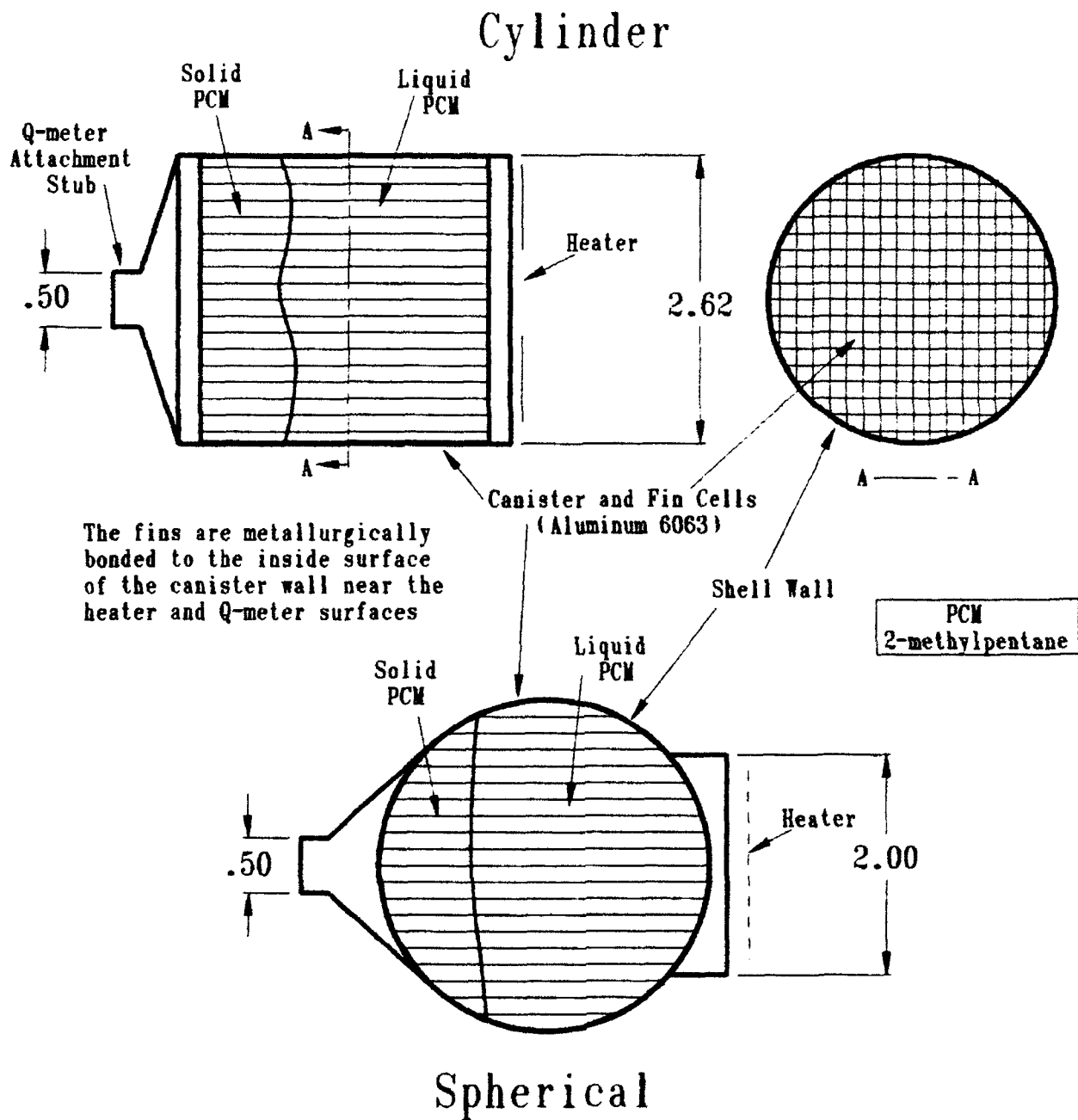


Figure 3. Phase Change Canisters

Conduction enhancement methods for improving the heat transfer capabilities of the phase change materials are providing viable alternatives to using larger PCM canisters. Figure 4 illustrates several fin variations. The rectangular fin provides the simplest construction and is the type used in Grumman's research. The other fin types, (concentric cylinders, cylindrical fins, and Archimedes spiral) have yet to be evaluated. Their effectiveness at improving PCM heat flow and flux absorption will be determined later.

Database: Thermal_Storage_Unit_Cores
View : RECTANGULAR-FIN3 (modified)
Task: Obj-20

Units : CM
Display : No stored Option

Object: 4-BORE4, (ARCINDEXES-CONG-1, Biall) (Mod)

Bin: 1-MAIN
Update Level: Full

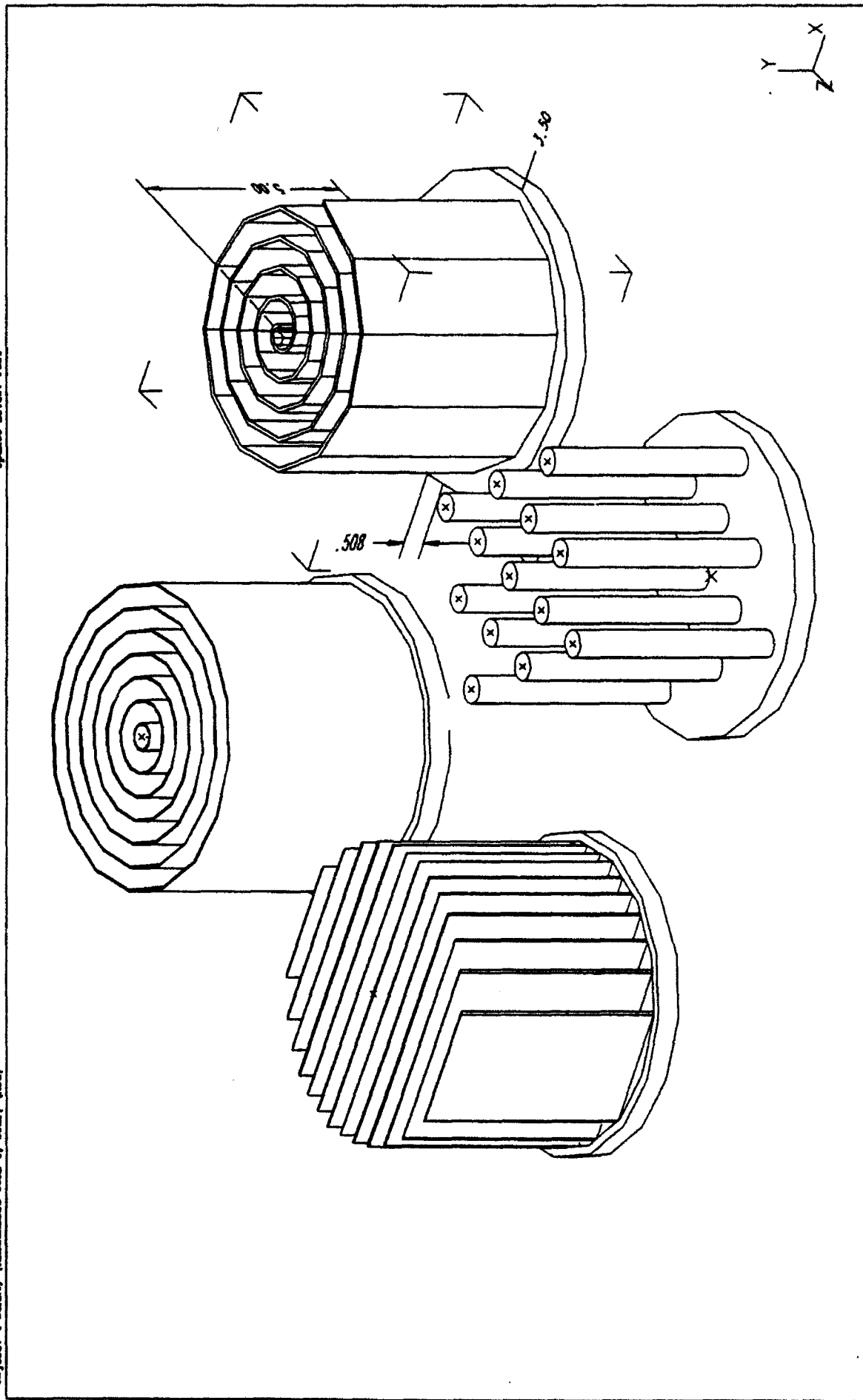


FIGURE 4. Pin Variations

Conclusion

The use of phase change materials to improve thermal control in space power applications is becoming of great importance. The selection of the phase change material, canister design, and the fin's thermal effectiveness are all important design choices.

Phillips Laboratory is currently evaluating a phase change canister using 2-methylpentane for infrared sensor thermal control. The system is expected to provide over 11,000 melt/freeze cycles within a range of 115 to 120 K while the heat load cycling time should provide a storage capacity range of 1000 to 5000 Joules. The cryogenic phase change device is expected to hold 25 to 40 percent more material to accommodate recrystallization and avoid subcooling.

The effect of this research on evaluating various phase change devices will have broader ramifications. The research will have direct applicability to higher operating temperatures which allow design optimization for applications such as high density electronics and lasers.

References

- [1] Faghri, A and M. Buchko. (1991). *Experimental and Numerical Analysis of Low-Temperature Heat Pipes with Multiple Heat Sources*. American Society of Mechanical Engineers, 113 (Aug): 728-33.
- [2] Keddy, Michael, Michael Merrigan, and Joseph Secary. (1992). *Establishing Low-Power Operating Limits for Liquid Metal Heat Pipes*. 8th International Heat Pipe Conference. Beijing, China.
- [3] Edelstein, Fred. (1991). *The Behavior of Cryogenic Phase Change Materials Used for IR Sensor Thermal Control in Space*. SAE Technical Papers, 911555.

**DESIGN AND CHARACTERIZATION OF A MAGNETOPLASMA-DYNAMIC
THRUSTER AND OPTICAL DIAGNOSTIC SYSTEM**

**Mohanjit S. Jolly
Graduate Student
Department of Aeronautics and Astronautics**

**Massachusetts Institute of Technology
77 Massachusetts Avenue
Cambridge, MA 02139**

**Final Report for:
Summer Research Program
Phillips Laboratory**

**Sponsored by:
Air Force Office of Scientific Research
Edwards Air Force Base, CA**

September 1992

DESIGN AND CHARACTERIZATION OF A MAGNETOPLASMA-DYNAMIC THRUSTER AND OPTICAL DIAGNOSTIC SYSTEM

**Mohanjit S. Jolly
Graduate Student
Department of Aeronautics and Astronautics
Massachusetts Institute of Technology**

Abstract

For the past two decades, there has been considerable theoretical and experimental research in the field of Magnetoplasma-dynamic (MPD) thrusters to prove their viability as a practical and cost effective space propulsion concept for satellite station keeping and orbital transfer. The physics of these electric propulsion systems stay are still not fully understood. The MPD performance is significantly hindered by the Onset phenomenon which occurs at a certain current level (onset current) at which point the thruster efficiency and thrust decrease substantially accompanied by an increase in electrode ablation. To further understand Onset and the underlying physics, a self field MPD thruster was designed and manufactured for the study of plasma parameters such electron temperature, electron density and ionization fraction at Onset. The Onset level for the 3 inch long, 2 inch diameter cylindrical thruster was determined to be at the Pulse Forming inductor-capacitor Network (PFN) voltage level of 280 volts and at approximately 5.8 kiloAmps current level.

DESIGN AND CHARACTERIZATION OF A MAGNETOPLASMADYNAMIC THRUSTER AND OPTICAL DIAGNOSTIC SYSTEM

I. Introduction

During the past two decades, there has been considerable research in the field of Magnetoplasmadynamic (MPD) thrusters. MPD's are electric engines that can be used as plasma accelerators for space propulsion applications such as station keeping and orbital transfer. Early work in the field has been summarized by Jahn [1]. The technology of MPD thrusters has recently been reviewed by Myers [2]. MPDs are typically coaxial devices analogous to Marshall guns, operated primarily in a high interaction regime where most of the acceleration is due to the $j \times B$ (Lorentz) effect. The magnetic field used to accelerate the propellant may be induced by the current itself or may be externally applied with solenoids. The former is known as a "self-field" MPD while the latter is referred to as an "applied-field". With high specific impulse (Isp), MPD systems are much more fuel efficient than their conventional chemical counterparts resulting in a higher payload ratio. MPD thrusters have Isp greater than 1000 seconds with a thrust level of tens of newtons. The efficiency of conversion of electric to kinetic energy increases with increasing current I and decreasing mass flow rate according to the work done in the field for the past two decades. The current increase also leads to a higher Isp. The phenomenon known as "onset", characterized by the development of large (10%) fluctuations in the electrode voltage and increased cathode erosion, occurs at some characteristic current squared to mass flow ratio and limits the thruster efficiency beyond that characteristic current level. Much theoretical effort has been devoted towards explaining this phenomenon. The present experimental study is designed to study plasma parameters at or near the Onset level. Experimentally, this occurs not far from the conditions at which the exhaust speed equals the Alfvén critical ionization velocity, but the actual physics of these instabilities is not yet clear, and several partial models exist which attempt to explain the effect on the basis of a variety of processes, including micro-instabilities, depletion of the anode by radial pinching forces, or the dynamics of cathode arc 'roots' [3].

Sanchez et al has proposed that a quasi-static electrothermal instability may develop in these thrusters at or near full ionization and that this process may result in onset effects [4]. In MPD devices, Coulombic collisions between ions and electrons dominate and the conductivity increases with electron temperature,

$$\sigma \sim T_e^{1.5} \quad (1)$$

Below full ionization, local excursions of Ohmic power dissipation simply produce more ionized species which is main power loss mechanism in a MPD thruster. The electron

temperature is limited to 2-3 eV. Near full ionization, however, these fluctuations heat the electrons, increasing the conductivity and causing a positive increase in the local current density. The result is more Ohmic heating and a positive feedback which may lead to the formation of constricted arcs. The theory predicts a linear instability at 90% ionization in a typical thruster. Small waves are heavily damped by electron diffusion while large waves are not produced due to the finite residence time in the thruster; the maximum growth-rate wavelength is a few centimeters, on the same scale as the thruster.

Due to the performance limits created by the onset phenomenon, there is a strong interest in elucidating the underlying physics. In an effort aimed primarily at an evaluation of the electrothermal instability theory, a collaborative effort between MIT and Phillips Laboratory (EAFB) was initiated. The experimental work over summer '92 consisted primarily of design and fabrication of a Megawatt level MPD thruster along with calibration and set-up of a diagnostic system for future emission spectroscopy experiments to determine plasma parameters such as electron density, electron temperature and ionization fraction to validate the electrothermal instability model currently under development at MIT.

II. Relevant Physics

Experimental thrusters typically use Argon or Hydrogen as the working gas. For this particular study, Argon was used. The gas enters the thruster through a Boron Nitride backplate. It is then ionized in the chamber via electronic collisions and accelerated by the means of the Lorentz force. MPD plasmas are relatively cool (several eV) but not dense enough ($n < 10^{15} \text{ cm}^{-3}$) for local thermodynamic equilibrium (LTE) to occur between the electrons and the atomic levels, and for three-body recombination in the plasma bulk to be effective [5,6]. Thus the excited state number densities do not follow a Boltzmann distribution and the ionization fraction is not given by ionizational or Saha equilibrium where equilibrium exists entirely due to collisions amongst the levels and between the levels and the electrons. Instead the ionization process is largely energy and forward-rate controlled.

The net ionization rate, for example, is given by the difference between two-body (e-a) and three body (e-e-i) recombining collisions, written in a form similar to:

$$n_e = n_e n_a S_{ac} - n_e^3 S_{ca} \quad (2)$$

where S_{ac} and S_{ca} are ionization and recombination rate coefficients, respectively, and are due to collisions only. In non-equilibrium plasmas, which is usually the case with MPD thrusters, radiation and ambipolar diffusion processes play an important role [7]. The finite rate processes that control the state of the plasma are:

1. Electron-atom excitation/deexcitation collisions.
2. Electron-atom ionization and electron-electron-ion recombination collisions.
3. Net deexcitation due to radiative decay and its inverse.
4. Net recombination due to radiative recombination and its inverse.
5. Recombination due to ambipolar diffusion to the wall.

These plasmas are quasi-coronal in that, with the exception of resonant (ground state) transitions, inelastic collisions with electrons is the dominant excitation and ionization mechanism. However the plasmas are sufficiently dense that collisional de-excitation competes with spontaneous emission and decay. The de-excitation is not sufficiently fast, however, to ensure LTE. It is expected that LTE is approached for the highest bound states near the continuum (ionized) limit as the transition line strengths go as v^3 and these are quite small at those levels.

Since the electron temperature is much less than the ionization energy (15.5 eV for Argon), ionization is dominated by multi-step processes. It is therefore important to understand the rates of these intermediate steps. Inelastic collision cross-sections are typically calculated assuming thermal distributions for the electrons. It is possible that this assumption does not hold in MPD plasmas, especially near the electrodes where the electric fields are as high as 100 kV/m.

In addition to non-equilibrium, there is the issue of unsteadiness or time dependence of the populations. The fundamental time scale of the plasma is the residence time within the device, which is about 10ms. The excited states of each species reach steady-state with respect to their ground states in about 10 nsec. Due to the slow recombination rates, however the ground states require about 10 msec to reach steady-state among themselves.

Although recombination in the bulk of the plasma is very slow, ambipolar diffusion to the walls of the device and subsequent recombination there can be significant and must be taken into account in the models. It is not clear whether the collisions are predominantly elastic or inelastic and, if the latter is true, whether excitation or de-excitation occurs.

III Approach

The research had two objectives:

- A. Designing and manufacturing a workable MPD thruster
- B. Determining the onset level for the thruster

Although the chief objectives for the summer are mentioned above, it is important to briefly discuss the plasma parameters to be measured in the near future.

III.1 Ionization Fraction Measurements

One of the most important plasma parameter is the ionization fraction. The electrothermal instability model developed by Martinez and Preble at MIT claims to work at

ionization fraction greater than .90. The present experimental effort is designed to verify that particular model. The two main problems with these measurements are that most atoms are in the ground states of the neutral and ionized species where the energy gaps preclude single optical photon-process diagnostics; and that near full ionization, the measurement of neutral population can be obviously quite difficult. The approach in this effort is outlined below.

Emission spectroscopy can be used to measure a number of plasma parameters. Absolute line intensity measurements can be used to determine relative upper-level number densities for both neutrals and ions [8,9]. The emitted intensity of an atomic, ionic, or molecular spectral line is proportional to the population of the upper level to the transition probability, and to the energy of the quantum as explained by Griem [10].

$$\epsilon_{ul} = A_{ul} n_i h \nu_{ul} / 4\pi \quad (3)$$

where h is Planck's constant, n is the number density of the species i , in the excited state u , ν_{ul} is the frequency of the photons emitted due to transition from the upper excited level u to the lower level l . ϵ is the volumetric emission coefficient of the line. Since the technique for directly measuring the neutral population is unavailable, excited state populations will be determined spectroscopically using the above equation and a Collisional-Radiative-Diffusive (CRD) MPD model developed by Eric Sheppard of the Massachusetts Institute of Technology will be used to extrapolate to the neutral population and subsequently the ionization fraction using finite rate equations along with species equations of density, momentum and energy.

The absolute intensity method described above relies heavily on absolute intensity calibrations. An absolute measurement of the total intensity of a spectral line emitted from an optically thin plasma yields the density of atoms or ions in the upper state of the line integrated along the line of sight. The most direct method for the measurement of total line intensities consists of observing a suitable spectral range through a spectrometer equipped with a broad exit slit that admits most of the line to the photo diode array. Care has to be taken, however, to determine the continuum contribution to the light coming through the entrance slit of the spectrometer.

III.11 Electron Temperature Measurement

Electron temperature measurements will be conducted both spectroscopically using the relative line intensity technique and via a triple probe. During the pulsed firings, there are obviously transients. The object of the study will be to get time integrated data over the quasi steady-state region of the firing. (~700 msec).

Relative line intensities of the working gas can be used to determine the electron

temperature using a Boltzmann approximation assuming that the higher energy levels are in local thermodynamic equilibrium (LTE). Taking the ratio R of the emission coefficients ϵ_1 and ϵ_2 of two emitted lines, T_e can be obtained via the following equation:

$$\epsilon_1/\epsilon_2 = [A_1 v_1 g_1 / (A_2 v_2 g_2)] \exp[-(E_1 - E_2)/kT] \quad (4)$$

where A_1 , A_2 are the transition probabilities, v_1 and v_2 are the line frequencies, g_1 and g_2 are the respective degeneracies and E_1 and E_2 are the energies of the upper levels of transition. As mentioned earlier, one should select energy levels closer to the ionization limit, which can be assumed to be in equilibrium among themselves. For improved accuracy, a number of lines should be measured and a Boltzmann plot fit should be used for temperature measurement.

III.III Electron Density Measurement

These measurements like the electron temperature can be performed spectroscopically or with a triple probe[11,12]. In a plasma, as each atom interacts with its neighbors, there occurs a shift in the energy level from which an optical transition may occur. Long range interactions with charged particles cause a change in the energy level of the emitter resulting in what is known as Stark Broadening. The perturbed potential due to the electric field caused by a neighboring particle causes the shift in higher energy states. This Stark effect is dependent mainly on electron density as shown by the following expression[13]:

$$n_e = 10^{20} (\Delta\lambda / 4 \text{ \AA})^{2/3} \quad (5)$$

where $\Delta\lambda$ is the Full Width at Half Maximum (FWHM) of the hydrogen β line.

In MPD thruster investigations, the working gas is usually seeded with Hydrogen to take advantage of the Stark broadening diagnostic technique. The broadening effect is much more profound in Hydrogen than in Argon. Care must be taken, however, to make sure that the seeded hydrogen is only a few percent (by volume) of the gas entering the thruster to not change the voltage-current characteristics of the plasma.

A triple probe, which is much easier to use can be used to measure both temperature and density as described by Tilley [14] but with greater uncertainty in the measured values. The electron temperature can be evaluated by an analysis of the Brehmstrahlung or continuum radiation as well. The CRD model requires only the electron temperature, electron density, measured line intensities and the thruster geometry as inputs to extrapolate to population distribution and ionization fraction for Argon. Next few sections

describe the physical set-up of the experiment.

IV Optical Diagnostics

The common requirement of all the chosen analysis methods are spectral line profiles from the plasma that are resolved in both space and wavelength. The desired data is a two-dimensional array with the vertical dimension corresponding to a line intensity in the plasma and the horizontal dimension representing wavelength. Quantitatively, the spatial resolution needs to be great enough to distinguish structure with the length scales of the plasma device. The required wavelength resolution in the spectrometer is specified by the widths of the observed spectral lines. Again, the analytic techniques require knowledge of the line profile on a wavelength scale substantially smaller than the total width. At least ten or so data points are required across the profile for the Abel inversion process to work correctly. The thruster has to be mounted on a translation stage with a small step size (1 mm).

V Apparatus

The apparatus necessary to make the necessary measurements can be divided into three subsystems: the plasma generation system, the optical system, and the data acquisition system.

V.1 Plasma Generation System

As mentioned earlier, an MPD thruster was designed and manufactured for this study. A thruster assembly drawing of the designed MPD is shown below in figure 1.

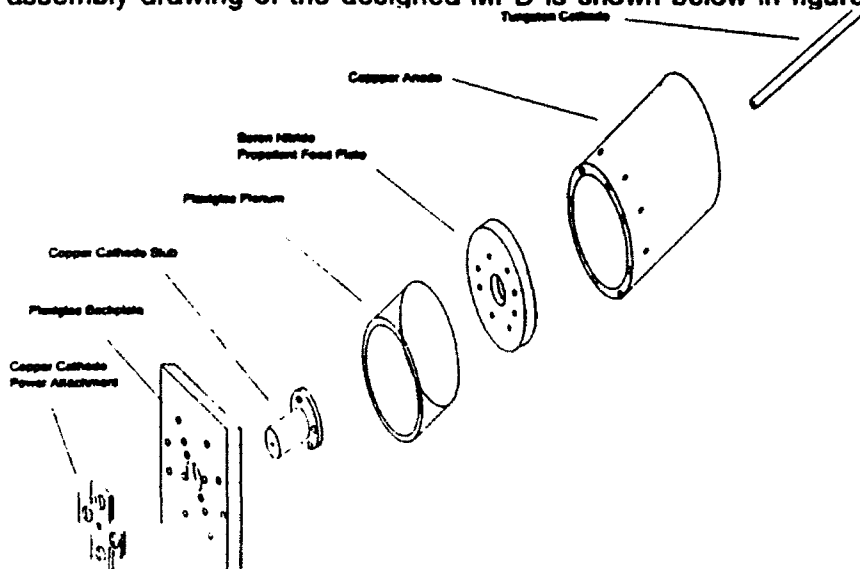


Figure 1: A Magnetoplasma-dynamic (MPD) Thruster Assembly Drawing

The cylindrical MPD consisted of a copper anode and a thoriated Tungsten cathode. A special stand was constructed from plexiglass for the thruster. The translation stage was mounted on the stand and the thruster was attached to it with a plexiglass "U" bracket as shown in figure 2.

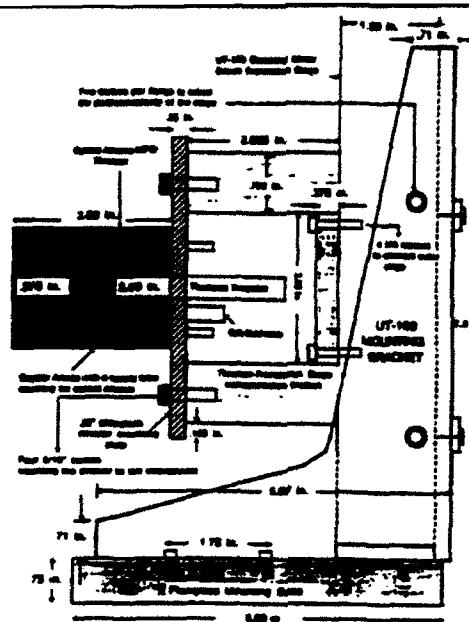


Figure 2: Thruster-Translation Stage Connection Bracket

The thruster was aligned with a quartz window to allow optical access from the thruster to the spectrometer.

MPDs are designed for and are effective only in very low pressure environment. A vacuum chamber was therefore needed for the experiments. The vacuum system used for the study is shown in figure 3.

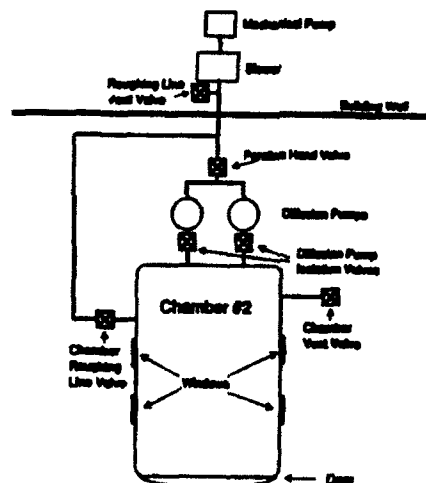


Figure 3: The MPD Vacuum System

The vacuum facility consisted of an 8 foot diameter by 12 foot long stainless steel cylinder. The chamber had 3 plexiglass and 1 quartz portal for optical access. A Stokes mechanical pump, a Roots blower and two Varian 10 inch diffusion pumps were used to bring the chamber pressure to .2 millitorr range before firing the thruster. Chamber vacuum pressure is measured with a Varian 843 vacuum ionization gauge.

The propellant system is a choked flow pulsed gas system. A .25 inch propellant line feeds from a T-bottle and regulator into a 24 liter spherical plenum (nominal 15 inch diameter) located outside the vacuum chamber. An Omega pressure gage measures absolute plenum pressure, and a thermocouple attached to the plenum tank measures the propellant temperature.

A schematic of the propellant system is shown in Figure 4.

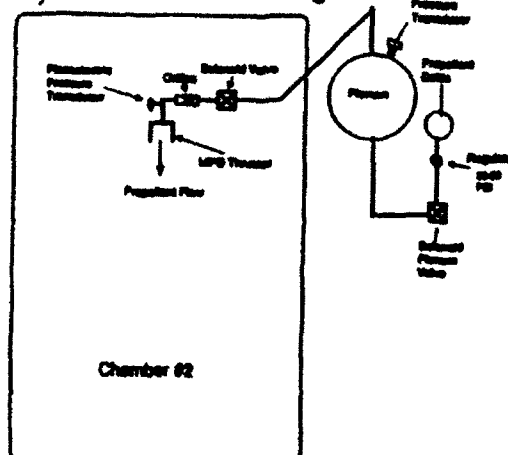


Figure 4: MPD Propellant System

From the plenum, a propellant line feeds through the vacuum chamber to a Valcor solenoid valve. The valve is located as close as possible to the MPD thruster to help reduce delay times in the gas pulse to the thruster. Immediately following the valve is a 2 millimeter diameter Fox precision orifice, which serves as a choke point for the propellant flow. A Kistler piezoelectric pressure transducer is attached downstream of the orifice. The transducer output reflects the gas pulse profile required to determine the time delay before starting the thruster. The propellant line feeds into .25 inch Tygon tubing to the MPD thruster.

During thruster operation, a fast acting solenoid valve opens to release a 60 millisecond gas pulse, which typically achieves steady state flow in about 15 milliseconds. A typical gas pulse profile is shown in figure 5.

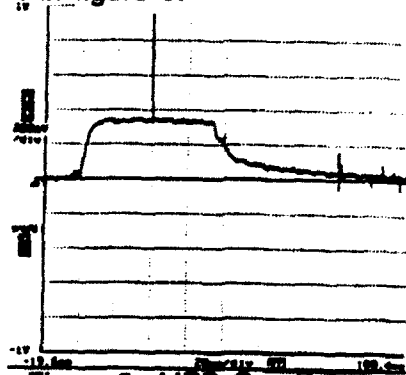


Figure 5: MPD Gas Pulse

It is during this steady flow that the thruster is fired. Two Rapid Systems R4000 controllers, programmed with an IBM PC based computer, regulate the timing between gas pulse initiation and thruster start.

MPD thruster firing requires accurate mass flow measurement and calibration. For calibration, propellant fills the plenum to maximum system pressure, and then is discharged through the thruster into the vacuum tank. The calibration theory is based on the ideal gas

law, $PV=nRT$, which is accurate for the low pressure, low density argon used in the tests. Mass flow which is proportional to the plenum pressure for choked flow, is related to the rate of change of pressure by the following expression:

$$\dot{m} = - \frac{MV}{RT} \frac{dP}{dT} = cP \quad (6)$$

where M is the molecular weight, V is plenum volume, R is the universal gas constant, T is plenum gas temperature, P is the plenum gas pressure and c is the proportionality constant. Figure 6 shows the pressure drop in the plenum.

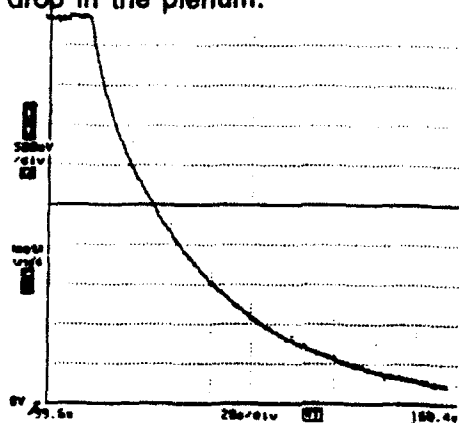


Figure 6: Plenum Pressure Drop

Equation 6 is based on the assumption that the process is isothermal. The solution to the equation is an exponential function of pressure versus time. A Tektronix DSA601 digital signal analyzer was used to record plenum pressure versus time. The pressure history is then fit to an exponential function to yield the constant of proportionality between mass flow and plenum pressure.

A schematic of the electrical system is shown in figure 7.

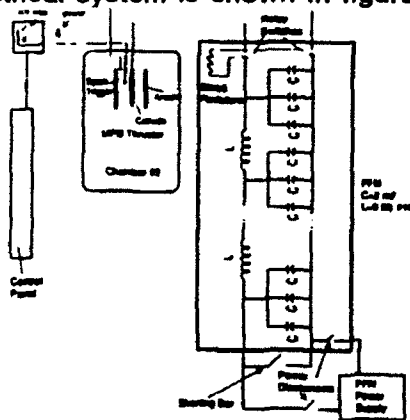


Figure 7: MPD Electrical System

The power source for the quasi-steady MPD thruster is a pulse forming network (PFN). The PFN is a ten section LC network with a nominal .01 ohm output impedance. Each section consists of three 2000 microfarad, 800 volt Maxwell capacitors connected in parallel and a 5 turn, .53 microhenry inductor. Together they release a one to two millisecond current

pulse at upto 30 kAmps and 400 volts, depending on the thruster used. The PFN stores approximately 20 kilojoules electric energy, which corresponds to a maximum thruster power on the order of 10 Megawatts. A Del Electronics Corp power supply supplies upto to 8 kWe of power to the PFN

Thruster firing sequence is shown in figure 8.

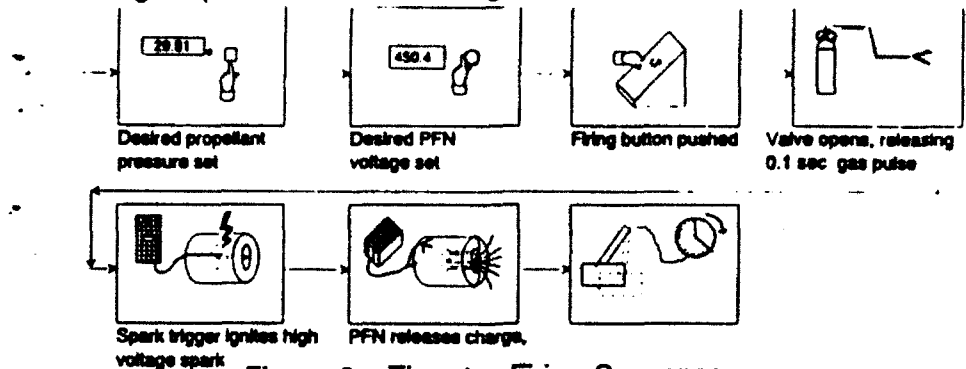


Figure 8: Thruster Firing Sequence

Thruster operation is initiated in the MPD thruster via a spark trigger system. The spark trigger is a .01 inch tungsten wire fed through a thruster propellant injection hole. This spark trigger wire is used to provide an initial high voltage spark that ionizes the propellant and initiates thruster operation. The spark trigger circuit is essentially a 70 microfarad, 2.5 kilovolt Maxwell capacitor charged by a Del Electronics Corp 5 kilovolt, 200 milliamp power supply. A high voltage relay is used to transfer the capacitor high voltage to the spark trigger. Thruster current is measured by a Pearson Electronics current pulse transformer which saturates at 20 kAmps for a one millisecond pulse. Voltage across the thruster is measured using two Tektronix 1000x voltage probes attached to the power feedthroughs. A Tektronix DAS 601 digital signal analyzer record thruster current and voltage. A typical thruster voltage and current traces are shown in figures 9 and 10, respectively.

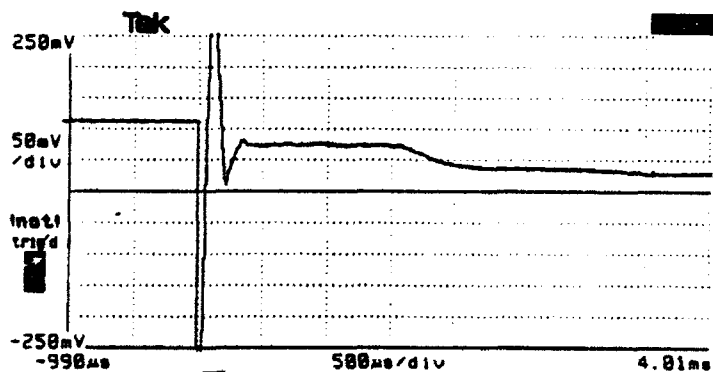


Figure 9: A Typical MPD Voltage Profile

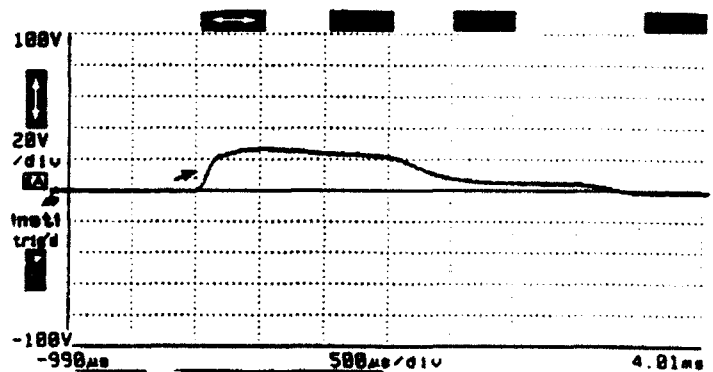


Figure 10: A Typical MPD Current Pulse

V.11 Optical System

The proper design of the optical system is crucial to the success and accuracy of the spectral diagnostic methods. The effect of each component of the optical train must be clearly understood if one is to reliably interpret the data. This point is especially directed to the issue of spatial resolution which governed much of the optical design. The simplest way to achieve spatial resolution is to pick out only that light which leaves the source parallel to some reference point. In this case the observed light represents an integration along the line of sight. In the case of an axisymmetric plasma discharge such as the one used in this study, the integration can be analytically folded to yield a radial profile through the Abel inversion, as mentioned earlier [15].

As shown in figure 11, there are nine elements in the optical path for directing and manipulating the plasma emission.

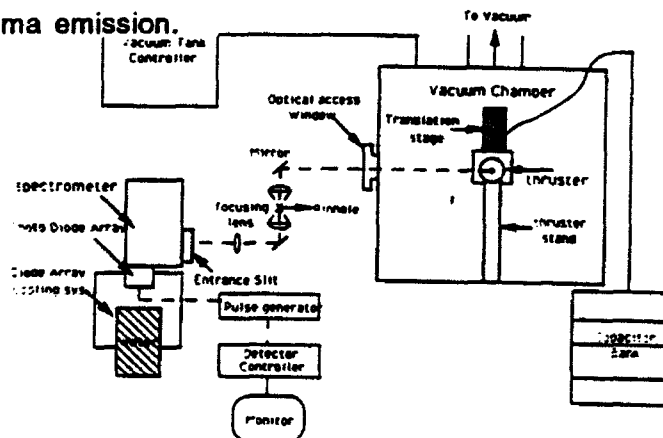


Figure 11: Optical Set-Up For Emission Spectroscopy

A quartz portal lies first in the train. The following two elements are four inch diameter first-surface mirrors, to guide the desired light into the optical axis of the spectrometer. A fourth element is a two inch 250mm focal length UV grade lens. At the focal point of this lens lies a .25mm pinhole. This pinhole provides the needed spatial resolution. The theoretical spatial resolution can be calculated as shown in the following equation:

$$\delta d/f = D/L \quad (7)$$

The ratio of the pinhole diameter, δd , to the focal length, f , is equal to the ratio of the spatial resolution size, D , to the distance from the lens to the discharge, L . The theoretical value was 1.9 mm for the optical setup used in this study. A second lens recollimates the light. The collimated light is focused towards the entrance slit of the spectrometer using a 250mm focal length plano convex lens. A third mirror finally reflects the light onto the entrance slit.

A 1.26 m focal length Spex Industries 1269 spectrometer was used with a 1200 grooves/mm blazed at approximately 10,000 Angstroms. This results in a theoretical resolving power of 123,000 in first order. This implies, for instance, a theoretical

resolution of .03 Angstroms at 4000 Angstroms in first order.

V.III Data Acquisition System

The heart of the diagnostics setup is a device capable of digitizing and recording the two-dimensional array of information presented by the spectrometer. A Princeton Instruments IRY-512 Photo Diode Array (PDA) along with a ST-120 Detector Controller serves this purpose. A Princeton Instruments PG-10 signal generator was used for gating purposes. An IBM PC with a Princeton Instruments NSMA data acquisition software were used to record digitized images.

VI Procedure

The experimental procedure for obtaining the data is straightforward. For each diagnostic technique (Absolute or relative intensity), a suitable wavelength regime should be chosen and the spectrometer tuned to it using the CD2 spectrometer motion controller. The data acquisition system was triggered at the appropriate time by the master timing circuitry. For time resolved measurements, a Princeton Instruments PG-10 Pulse Generator was used. Four preliminary procedures were required, however, in order to calibrate the spectrometer and the data acquisition system for future firings and spectroscopic measurements.

VI.1 Optical Focus

Accurate interpretation of a line profile relies on accurate knowledge of the system resolution in wavelength. The highest obtainable resolution is, in theory, fixed by the spectrometer. As noted before, this value is about .01 Angstroms. In the arrangement used in this experiment, the PDA face was coincident with the spectrometer exit plane. The PDA target has a physical resolution of 512 pixels. Physically each pixel is .028 millimeters wide. In first order, the spectral dispersion at 5000 Angstroms is 6.47 A/mm. Combining these numbers, the PDA resolution is about .16 A/pixel. It is important to note that the resolution is directly proportional to dispersion. To experimentally confirm how the actual focus approaches the theoretical value, a mercury spectrum lamp was used. The linewidth of the cool discharge should be vanishingly small. Thus, any observed broadening should be due to the optical focus. Repeated adjustments of the PDA resulted in a 3.5 pixel resolution, or .55 Angstroms in first order. The resolution was defined as the full width at half maximum of the mercury 4358 Angstroms line. The difference between actual and theoretical focus is attributed to side channel cross talk in the detector where adjacent pixels are affected by the charge of their neighbors. The resolution could be improved by going to higher orders of light but the light intensity decreases proportionally. Figure 12 shows a typical mercury profile.

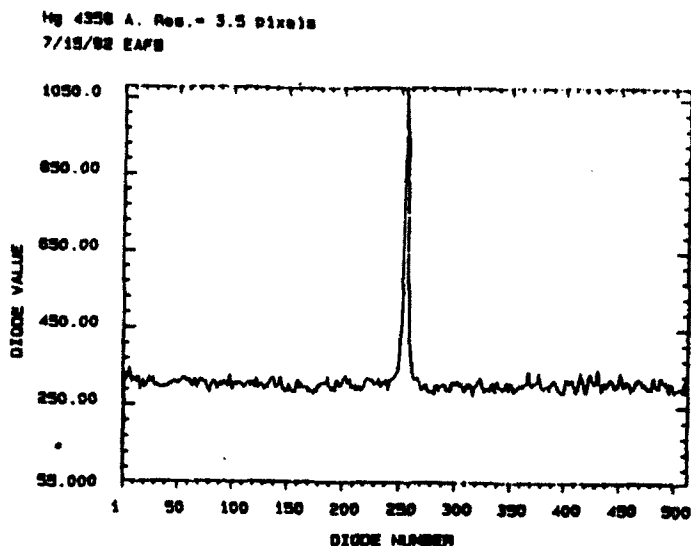


Figure 12: A Typical Mercury Profile Used For Resolution Measurement

The plots for the He-Ne 6328 and Argon 4880 angstrom lines are attached in Appendix A.

VI.11 PDA Response Calibration

If a completely uniform light source (in both wavelength and space) was placed at the start of the optical train, the image recorded by the PDA would not be uniform. A variety of factors cause this variation ranging from misalignment of lenses to PDA cross talk. All of these factors can be accounted for by an experimentally determined response function. This correction can be found by imaging a known uniform source on the PDA face and designating the recorded image as the response function. An Oriel tungsten filament lamp was used for this absolute intensity calibration. A factory provided calibration was used to determine the transfer function for the PDA as described a little later.

In addition, a linear PDA response to incident intensity is also required. Although the PDA specifications claim a dynamic range of 1 to 16383, the linear range may be substantially less. To confirm this, a helium neon laser and series of neutral density filters were used to bring various levels of intensity to the PDA. The relative response would then indicate the linear regime. The test showed a linear regime upto 1000 counts. The incoming light intensity during the testing, therefore, should be kept under 1000 counts with the help of neutral density filters. The results are shown in figure 13.

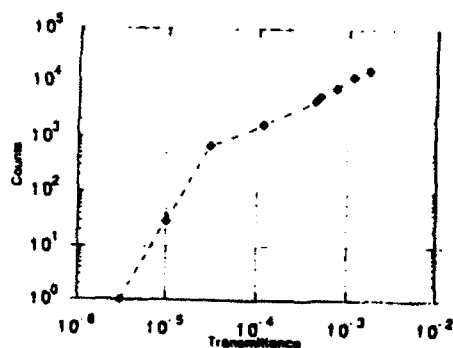


Figure 13: Detector Intensity Response

VI.III Wavelength Calibration

The relative intensity calculation for electron temperature require comparison of lines markedly different in wavelength. A calibration of the system with respect to wavelength is therefore necessary. Argon and Mercury low pressure spectrum lamps were used for this purpose. The grating was adjusted inside the spectrometer until the wavelengths being studied appeared at pixel 256. The lines looked at were Mercury 4358, Argon 4880 and Hene 6328. These lines were also used to compare the theoretical and actual PDA resolution. This was done by first getting a known line at a certain pixel value and moving the grating to subsequently move the peak on the PD monitor. The CD2 provides the movement in wavelength units while the number of pixels or diodes could be gotten from the monitor. The values were found to be very comparable to the theoretical value ($\sim .16\text{\AA}/\text{pixel}$).

VI.IV Intensity Calibration

Since the crux of the emission measurements will deal with absolute intensity measurements, an absolute intensity calibration was necessary to convert from the spectrometer units (diode values) to actual irradiance values (Watts per square meter per steradian). To do so, an Oriel Tungsten filament lamp was used. By placing the lamp in the plane of the MPD discharge axis and accounting for the transmittance of the neutral density and bandpass filters placed in the optical train, a transfer function was arrived at to relate the data system intensity units to the spectral radiance of the source in watts per square meter per steradian. The factory provided calibration was used to arrive at the transfer function. Figure 14 gives the optical transfer function over wavelength.

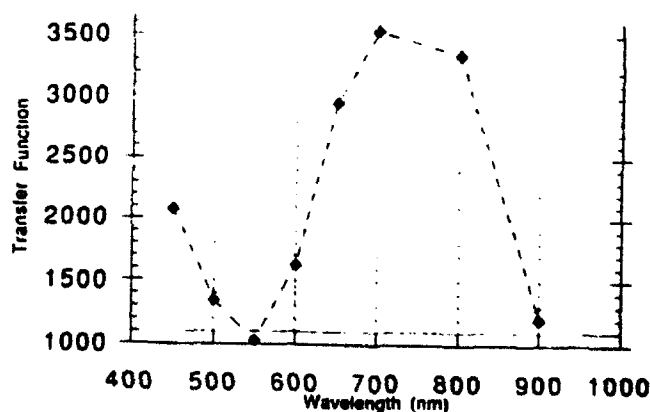


Figure 14: Absolute Intensity Calibration of the Spectrometer

V MPD DESIGN:

As mentioned earlier, the MPD had was coaxial in geometry. The thoriated Tungsten cathode was .375 in. in diameter and 5 in. long. The anode was high purity Copper cylinder

having a 1.75 in. inner diameter. The insulating back plate was made of Boron Nitride with propellant inlet holes at two different radii for uniform distribution. The schematics of the different thruster parts are attached in appendix B. The thruster was mounted on a plexiglass back plate which was in turn attached to a Klinger Instruments UT100 translation stage. The thruster was also designed with a plexiglass plenum in the back where the gas would have a chance to diffuse before entering the chamber. The propellant was transported to the thruster from the plenum via two Tygon tubes connected in turn to two .25 in. stainless steel tubes that were press fitted into the plexiglass back plate. A tungsten wire was used as a spark trigger. Precaution had to be exercised when compiling the thruster to guarantee that no gas was leaking behind the thruster and that the spark trigger hole and the propellant feed holes were properly insulated with epoxy or silicon rubber material (RTV).

VI RESULTS AND CONCLUSIONS:

The thruster was designed and fabricated successfully. Approximately 100 firings were successfully accomplished in order to get the voltage-current characteristics at different mass flow rates. The spectrometer was successfully calibrated in wavelength and intensity. The optics were set up and aligned using a 1mW level Helium-Neon laser. The thruster was fired successfully at several different mass flow rates. The goal was to find the onset level and best results were gotten at .4 g/sec. The V-I characteristic for .4g/sec is shown in figure 15.

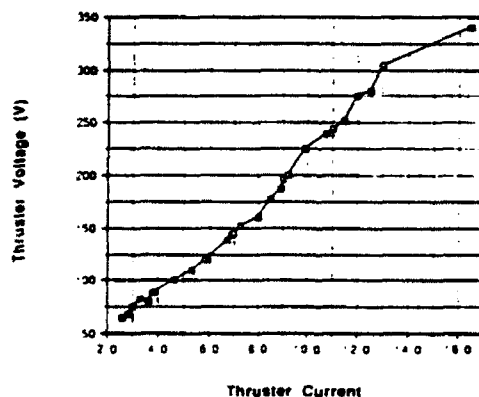


Figure 15: V-I Characteristic for .4 g/sec MPD Firing

The current and voltage profiles at onset are given in figures 16 and 17 respectively.

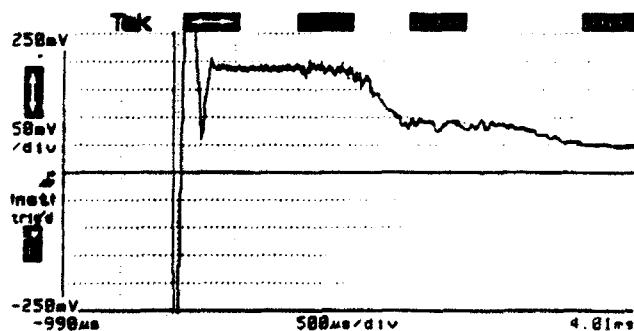


Figure 16: MPD Voltage Profile at Onset

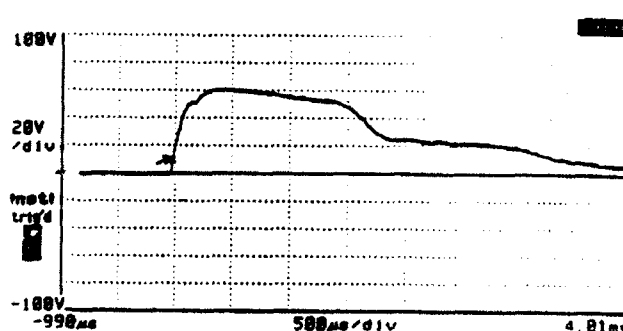


Figure 17: MPD Current Profile at Onset

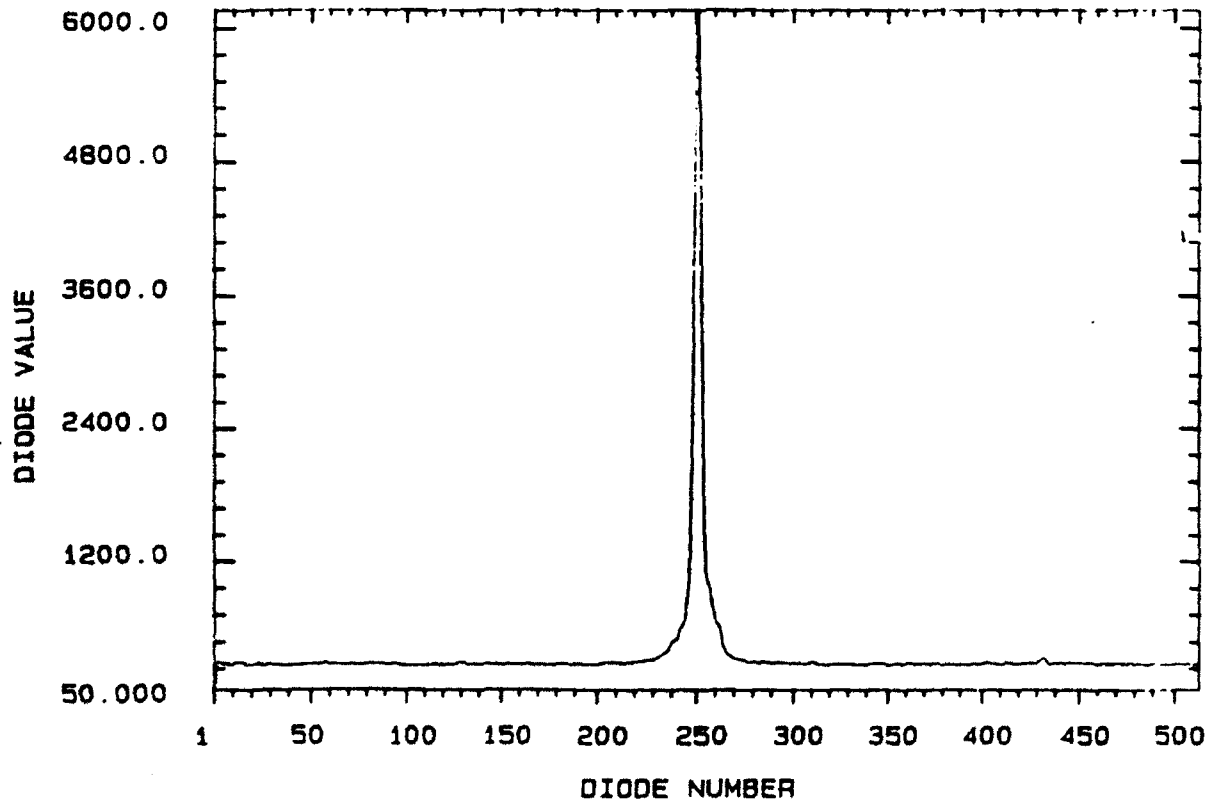
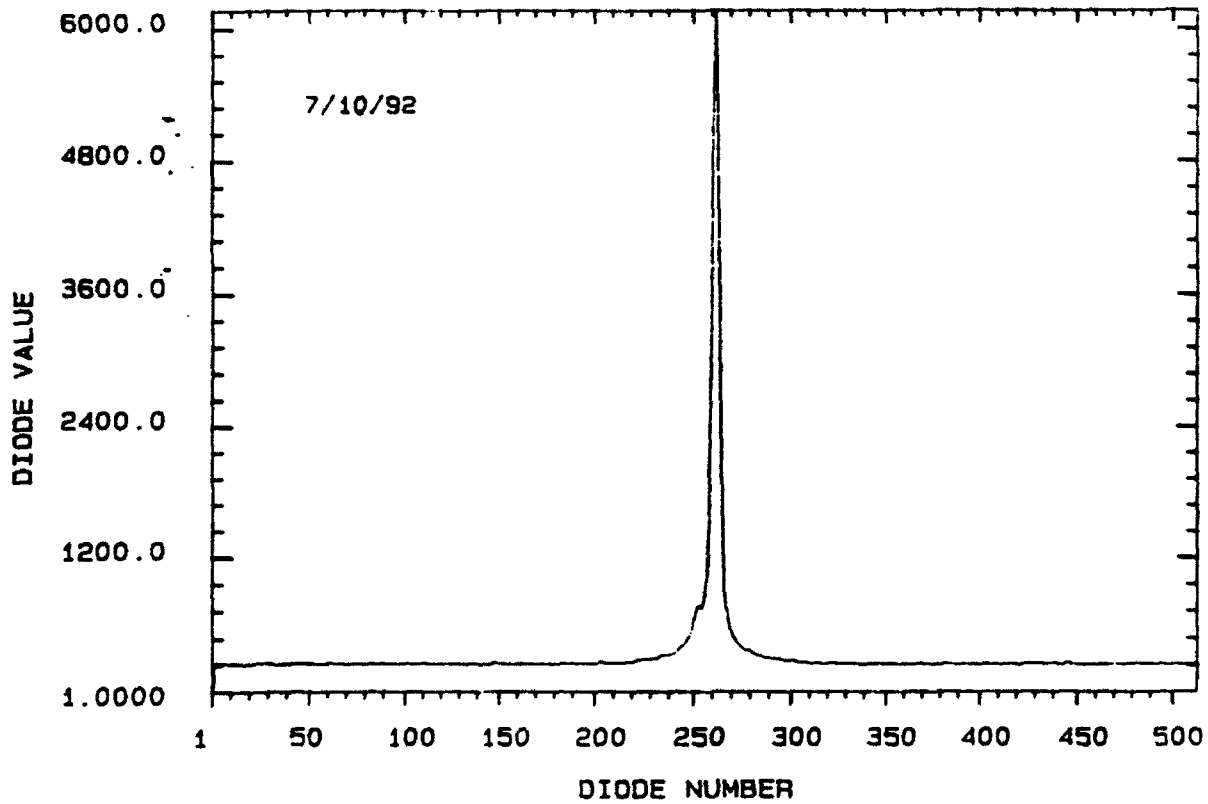
Onset level was reached at the PFN voltage of 279 volts at approximately 5.8 kiloamps. The gas pulse was about 60 milliseconds long with the spark occurring roughly 30 milliseconds after the start of the gas pulse, as shown previously in figure 5. The current pulse itself was about a millisecond long, with the quasi-steady state region being 700 microsecond wide. The Princeton Instruments gating device PG10 had to be used since the spectral analysis was to be performed on the steady state region and not the transients. If the detector were left ungated, the measured values of the electron temperature and density would have considerable errors.

VII FUTURE EXPERIMENTS

This report summarizes the preliminary steps of the MPD experimentation to be performed at the Phillips Laboratory, Edwards Air Force Base in the near future. The collaborative effort between the laboratory and MIT is designed to measure plasma parameters such as electron temperature, electron density and ionization fraction close to or at the Onset level to verify the electrothermal instability model. With the optical set-up complete and the thruster successfully designed, manufactured and characterized, the author will conduct emission spectroscopy experiments during Fall 1992 and Spring 1993. The thruster and optical set-up will be available for any further studies to be conducted on MPDs to further understand and eventually resolve the problem of Onset.

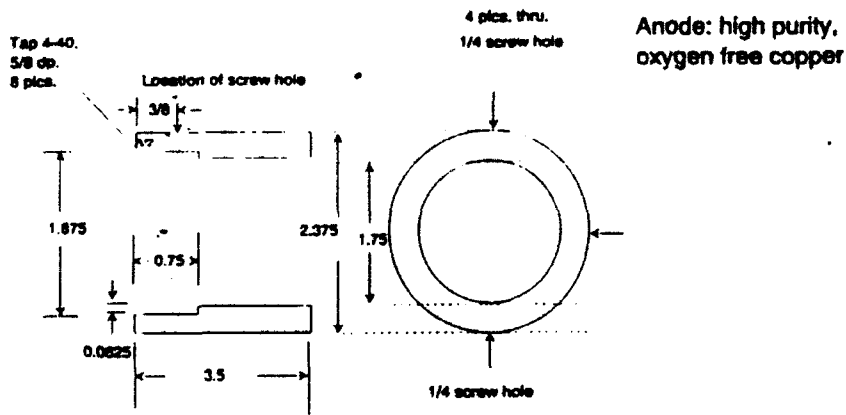
Appendix A

Line Profiles of Helium-Neon Laser and Argon Used For Resolution Measurement

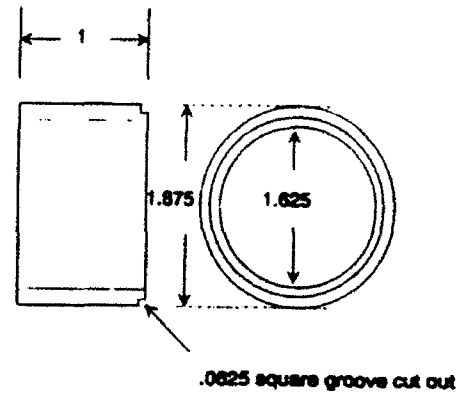


Appendix B

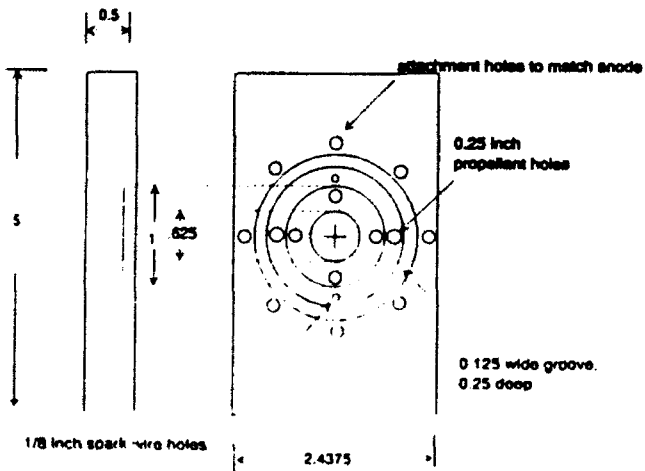
Schematics of Different MPD Thruster Components



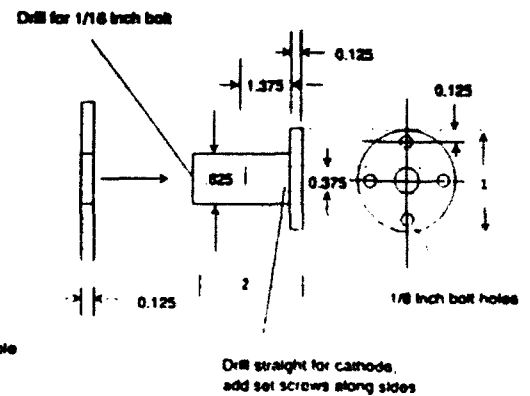
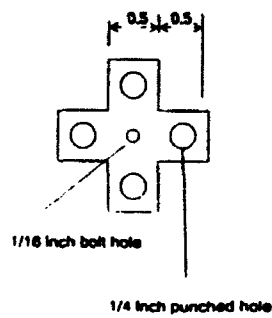
Copper Anode



Plexiglas Plenum



Backplate



Cathode Stub

References Cited

- [1]. Jahn, R. G., *Physics of Electric Propulsion*, McGraw-Hill Book Co., New York, 1968.
- [2]. Myers, R. M., Mantenieks, M. A., and LaPointe, M.R., "MPD Thruster Technology," AIAA Paper 91-3568, Sept. 1991.
- [3]. Rudolph, L.K., R.G. Jahn, K.E. Clark, and W.F. von Vaskowsky, "Onset Phenomena in Self-Field MPD Arcjets," AIAA Paper 78-653.
- [4]. Niewood E., J. Preble, D. Hastings, and M. Martinez-Sanchez, "Electrothermal and Modified Two Stream Instability in MPD Thrusters", AIAA-2607, 21st IEPC, 1990.
- [5]. Scholz, P.D. and T.P. Anderson, "Local Thermodynamic Equilibrium in an RF Argon Plasma", J. of Quant. Spect. Radiative Transfer, Vol. 8, pp. 1411-1418.
- [6]. Burgess, D. D., and J. Cooper, " A New Method of Measuring Electron Temperatures in Plasmas in the Absence of Local Thermodynamic Equilibrium," Proc. Phys. Soc., Vol. 86, 1965, pp. 1333-1341.
- [7]. Kilfoyle, D. B., M. Martinez-Sanchez, D.J. Heimerdinger, and E.J. Sheppard, "Spectroscopic Investigation of the Exit Plane of an MPD Thruster", IEPC-88-027.
- [8]. *Plasma Diagnostics*, ed. by W. Lochte-Holtgreven, North Holland Publishing Co., Amsterdam, 1968, p.184.
- [9]. Robinson, D., and P.D. Lenn, "Plasma Diagnostics by Spectroscopic Methods," Applied Optics, Vol. 6, No. 6, June 1967, pp. 983-1000.
- [10]. Griem, H.R., *Plasma Spectroscopy*, McGraw-Hill Book Co., New York, 1964.
- [11]. Michels, C.J., J.R. Rose, and D.R. Sigman, "Electron Number Density and Temperature in MPD-Arc Thruster Exhausts," AIAA Journal, Vol. 10, No. 11, Nov. 1972, pp. 1395-1396.
- [12]. Robinson, D. and R.W. Nicholls, J. of Quant. Spect. Radiative Transfer, Vol. 1, No. 76, 1961.
- [13]. *Plasma Diagnostic Techniques*, ed. by R.H. Huddleston and S.L. Leonard, Academic Press, New York, 1965, p. 269.
- [14]. Tilley, D.L., A.J. Kelly and R.G. Jahn, "The Application of The Triple Probe Method to MPD Thruster Plumes", AIAA-90-2667, 21st IEPC.
- [15]. Cremers, C.J. and R.C. Birkebak, "Application of the Abel Integral Equation to Spectrographic Data," Applied Optics, Vol. 5, June 1966, p. 1057-1064.

**DESIGN OF A DIGITAL LOOP COMPENSATION FILTER OF AN ADAPTIVE
OPTICS SYSTEM FOR ATMOSPHERIC TURBULENCE COMPENSATION**

**Kurt W. Kunzler
Graduate Student
Department of Electrical Engineering**

**University of Utah
3280 Merrill Engineering Building
Salt Lake City, UT 84112**

**Final Report for:
Summer Research Program
Starfire Optical Range, Phillips Laboratory/LITE
Kirtland Air Force Base, Albuquerque, NM 87117**

**Sponsored by:
Air Force Office of Scientific Research
Bolling Air Force Base, Washington, D.C.**

September 1992

DESIGN OF A DIGITAL LOOP COMPENSATION FILTER OF AN ADAPTIVE OPTICS SYSTEM FOR ATMOSPHERIC TURBULENCE COMPENSATION

Kurt W. Kunzler
Graduate Student
Department of Electrical Engineering
University of Utah

Starfire Optical Range, Phillips Laboratory/LITE
Kirtland Air Force Base, Albuquerque, NM 87117

ABSTRACT

This report describes the design of a digital loop compensation filter of an adaptive optics system. The adaptive optics system allows one to correct aberrations the light wave encounters on its travel through the atmosphere to an astronomical telescope. A wavefront sensor measures the optical distortions whereby the deformable mirror can be formed to nullify these distortion effects. An overall system model was derived in order to model the system and design a digital or discrete-time control system. The motivation for controlling the deformable mirror via a digital controller as opposed to an analog controller is due to the advantages of easily performing complex control calculations, easily changing controller characteristics, and having far superior characteristics from the viewpoint of internal noise and drift effects. The digital controller is essentially a digital loop compensation filter. It was thought that one might want to change the characteristics of the digital loop compensation filter during one evening in order to enhance performance due to changing environmental conditions. Consequently, a generalized single pole / single zero filter was designed using a bilinear transformation with frequency prewarping in order to have the ability to change the characteristics of the filter. In order to employ higher order infinite impulse response filters, an adaptive scheme was used to automatically adjust a variable number of feedforward and feedback coefficients so that the filter transfer function is a best fit to a set of design specifications. Due to the inherent time lag in the adaptive optics system a steady-state error occurs. A theoretical optimal control scheme was found that exhibited minimum settling time with zero steady-state error. Using this optimal control scheme, several adaptive control algorithms were attempted. The adaptive control scheme consisted of an adaptive filter directly modeling the deformable mirror and the overall electronic time delay in terms of phase. Then the characteristics of the adaptive filter would be used to adjust the digital loop compensation filter in real-time. Resulting in an adaptive controller which optimally reduces the steady-state error and possess a minimum settling time response given a specific input to the system. However, in order to implement this adaptive controller scheme, further research is necessary to accurately model the deformable mirror using an adaptive filter in real-time operation.

DESIGN OF A DIGITAL LOOP COMPENSATION FILTER OF AN ADAPTIVE OPTICS SYSTEM FOR ATMOSPHERIC TURBULENCE COMPENSATION

Kurt W. Kunzler

Introduction

The adaptive optics (AO) system allows one to correct aberrations the light wave encounters on its travel through the atmosphere to an astronomical telescope. Atmospheric turbulence tends to disorder the refractive index of the air. Consequently, wavefronts of light get distorted as a result of atmospheric turbulence. These wavefronts travel through the atmosphere and have different optical paths, thus the wavefronts get out of phase. The basic concept of adaptive optics is to measure the incoming wavefront of light from a bright point source and to in turn place the phase conjugate on the deformable mirror. Real-time electronic processing of the wavefront information is required because the deformable mirror must adjust accordingly before the incoming wavefront changes once again.

An artificial point like source of light, an artificial guide star, is used in the adaptive optics process. The light from the artificial guide star is analyzed using a Hartman sensor. The Hartman sensor splits up the wavefronts in various subapertures in which the light comes to a focus. The displacement of each spot from the ideal position determines the actual wavefront tilt in that particular subaperture. Each subaperture has a corresponding location on the deformable mirror. Then these localized wavefront slope measurements are used in the wavefront reconstruction algorithm. The output from the reconstruction algorithm is then temporally filtered by the controller. Finally, the controller places the phase conjugate on the deformable mirror ideally resulting in a wavefront possessing common phase.

Currently, the adaptive optics controller is analog. This paper presents the design of a corresponding digital controller for the adaptive optics system. Section I describes in detail the actual modeling of the current adaptive optics system. The development of a digital single pole / single zero filter having variable characteristics is presented in Section II. In order to employ higher order infinite impulse response (IIR) filters, an adaptive scheme was used to automatically adjust a variable number of feedforward and feedback coefficients so that the filter transfer function is a best fit to a set of design specifications. This multiple order IIR filter is described in Section III. A stability analysis of the digital control system is described in section IV. Finally, the theory of an optimal and adaptive controller is discussed in the final section, Section V.

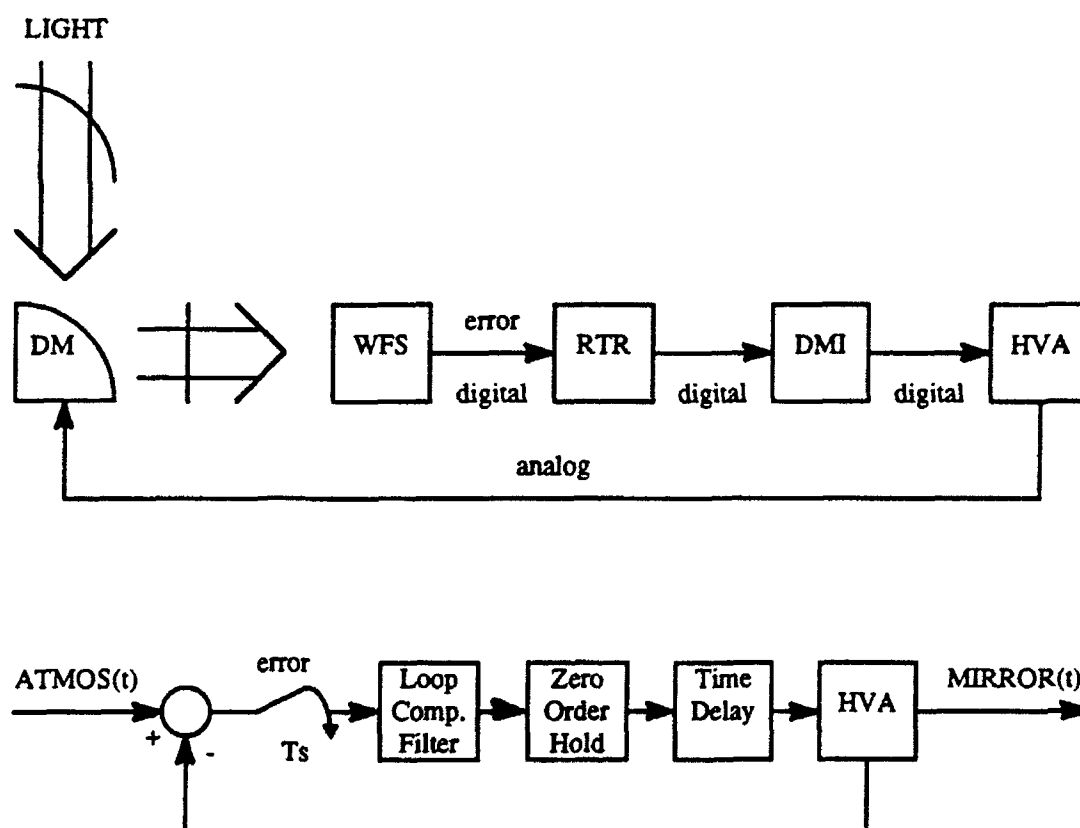
I. MODEL OF THE ADAPTIVE OPTICS SYSTEM

In the analysis and design of digital control systems, it is necessary to mathematically model the deformable mirror's actuators accurately. This model should describe the dynamics of the system as completely as possible. The actual description of the adaptive optics system model is presented below.

The input ATMOSPHERE(t) of the adaptive optics system model is the wave-front slope measurement. The closed loop signal MIRROR(t) is the adjustment due to the current position of the deformable mirror actuators. Consequently, the difference of these two signals is the current slope (or phase) error associated with the deformable mirror. This error is then sampled in order to model the actual wave-front sensor (WFS) which measures the phase error of the deformable mirror and outputs a discrete-time signal. The real-time reconstructor (RTR) is modeled as a gain ($K=1$) with no dynamics because it simply converts the slope measurement data into phase measurement data. The deformable mirror interface (DMI) contains the loop compensation (digital loop compensation filter) which is modeled exactly with a discrete-time transfer function. A zero order hold (ZOH) is used to model the digital to analog (D/A) interface. The high voltage actuator (HVA) interface converts the

phase measurement data into actual displacement information for the actuators. Consequently, the HVA interface is essentially a gain. This gain is modeled with the RTR gain. The high voltage actuators were modeled given an actual frequency response. The electronic time delay is modeled as a function that is translated by some time T_d in seconds. This time delay is modeled using a 2nd order Pade approximation. The two diagrams and the chart below summarize how the actual components in the adaptive optics system were modeled.

Adaptive Optics System and Model



WFS - Wave-Front Sensor
 RTR - Real-Time Reconstructor
 DMI - Deformable Mirror Interface
 HVA - High Voltage Actuator
 DM - Deformable Mirror

Model Components

WFS: $ERROR(t) = ATMOS(t) - MIRROR(t)$

Sampling Theorem: $error(n) = ERROR(t)|_{t = nTs}$

where T_s is the sampling period.

$$T_s = (3 \text{ pulses cvl}) * (200 \text{ usec/pulse}) = 600 \text{ usec}$$

usec = microseconds

RTR: $K = 1$ (unity gain)

DMI: $H(z) = (C1*z)/(z - C2)$

Digital Transfer Function

where $C1$ and $C2$ are constants that vary the loop compensation (gain and corner frequency).

DMI/HVA: $H(s) = (1 - e^{(-s*T_s)})/s$

Continuous Transfer Function

Zero order hold (i.e. D/A)

HVA/DM: $H(s) = 4/\{(s/104.618k + 1)*(s/197.392k + 1)\}$

Continuous Transfer Function

where $k = 1000$.

Time
Delay:

Translation of a function in the continuous-time domain.

$f(t - T_d)$ where T_d is the time delay in sec.

$$L[f(t - T_d)] = e^{(-s*T_d)} * F(s)$$

where L denotes the Laplace transform.

Due to the nonlinearity involved with the exponential function, a

2nd order Pade approximation (Maclaurin Series) is used.

$$e^{(-s \cdot T_d)} = 1 - T_d \cdot s + (1/2!) \cdot (s T_d)^2 - \dots$$

II. SINGLE POLE/SINGLE ZERO DIGITAL FILTER

The advantage of a discrete-time filter is that the gain and cutoff (or corner) frequency can be changed by simply changing coefficients in the difference (or filter) equation. If this change is desired with an analog filter, then the physical components must be changed. This procedure can be much more time consuming as compared to changing coefficient values in software.

There are several methods commonly available for obtaining a discrete-time equivalent of a continuous time filter. It is desirable to have a discrete-time filter having approximately the same dynamic characteristics, transient and frequency response, as the original continuous-time filter. However, this is not possible. Certain techniques used to find a discrete-time equivalent filter of a continuous-time filter can closely match transient or frequency response characteristics but not both. Since it is easy to visualize a low pass filter with some arbitrary gain and cutoff frequency with a Bode plot (frequency response), the bilinear transformation method with frequency prewarping will be used to discretize the continuous time filter. When discretizing continuous-time filters it is important to note that not only the particular method used, but also the sampling frequency used, will affect the dynamic characteristics of the resulting filter.

When discretizing a continuous-time filter using the frequency prewarping technique, the cutoff frequency (-3 dB point) is adjusted. Consequently, it will bring the -3 dB point in the digital domain to the desired frequency point corresponding to the continuous domain.

Given the filter equation, one can obtain a transfer function in the z-domain quite easily. However, if we find the frequency response in the z-plane, the simplicity of the logarithmic plots will be lost since $z = e^{j\omega T}$ in the z-plane. This problem can be

overcome by transforming the transfer function in the z-plane into that in the w-domain. The transformation is commonly known as the w transformation or the bilinear transformation. Although the w-plane resembles the s-plane geometrically, the frequency prewarping technique must be performed prior to calculating the frequency response. These calculation are performed below.

Digital filter equation: [1st order]

$$y(n) = C1 * x(n) + C2 * y(n-1)$$

$x(n)$ - sampled input
 $y(n)$ - output
 $y(n-1)$ - output delayed by one sample

The corresponding transfer function in the z-domain:

$$H(z) = (C1 * z) / (z - C2)$$

Bode plot analysis of $H(z)$ using the bilinear transform:

$$z = (1 + Tw/2) / (1 - Tw/2)$$

and $w = jv$

$$H(jv) = \{C1(1+jv/(2/T))\} / \{(1-C2)(1+jv/(2(1-C2)))/(T(1+C2)))\}$$

$H(jv)$ can be used to make a Bode plot of the transfer function. However, the frequency axis in the w-domain is distorted. The relationship between the fictitious frequency v and the actual frequency w is as follows:

$$v = (2/T) * \tan(w * T/2)$$

If a bandwidth is specified, say w_c , the system needs to be designed for a bandwidth v_c , where

$$v_c = (2/T) * \tan(w_c * T/2).$$

Consequently,

$$\text{gain} = C1/(1-C2)$$

and

$$w_c = (2/T) * (1-C2)/(1+C2)$$

Thus, C1 and C2 can be solved given these two equations (2 equations and 2 unknowns).

$$C2 = ((2/T) - wc) / ((2/T) + wc)$$

$$C1 = \text{gain} * (1 - C2).$$

III. POLE AND ZERO ADAPTATION FOR DIGITAL DESIGN SYNTHESIS

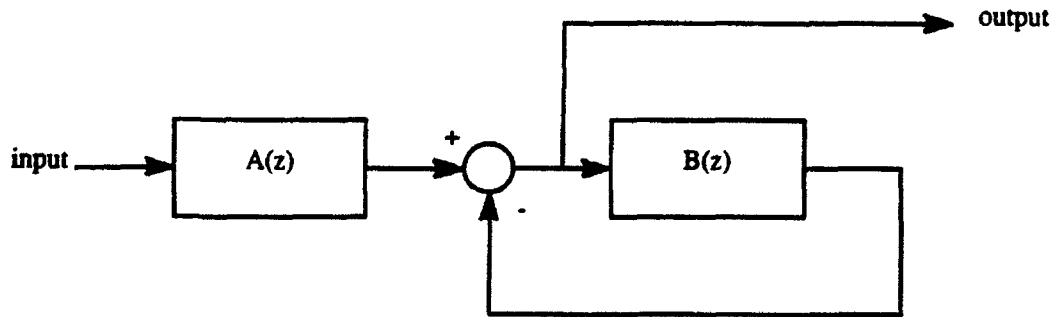
It can be very useful to have the option of choosing the number of output and input coefficients for an infinite impulse response (IIR) digital filter and automatically adapting these coefficients given certain filter specifications. The coefficient values, used to synthesize IIR digital filters, are found using adaptive modeling techniques. Direct modeling was used to synthesize the forward or nonrecursive portion of the IIR filter. On the other hand, inverse modeling was used to synthesize the feedback or recursive portion of the IIR filter.

The form of the IIR filter to be synthesized is shown below. The transfer function is as follows:

$$H(z) = A(z) / (1 - B(z))$$

$$\text{where } A(z) = a_0 + a_1 * z^{-1} + \dots + a_n * z^{-n}$$

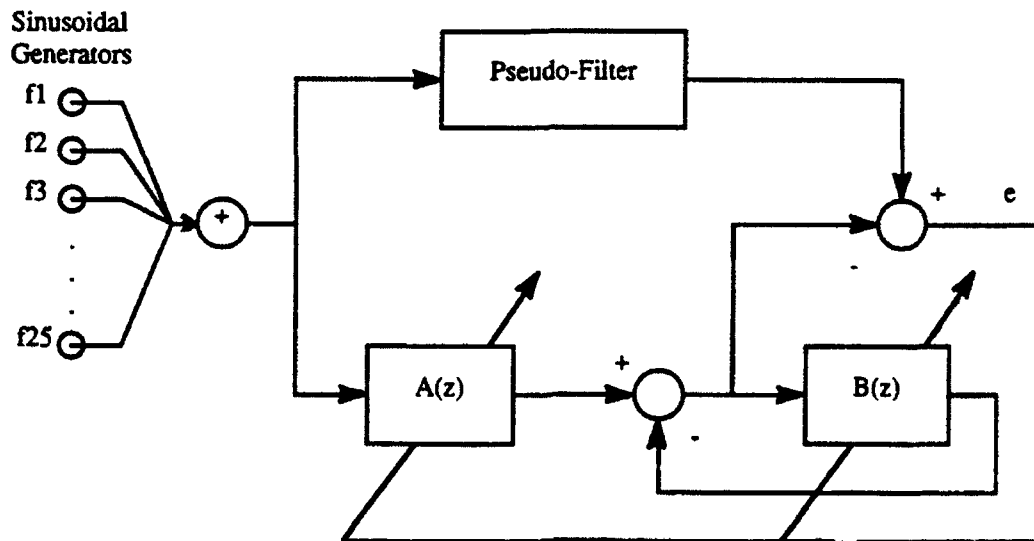
$$\text{and } B(z) = b_1 * z^{-1} + b_2 * z^{-2} + \dots + b_m * z^{-m}.$$



The filter has $n+1$ feedforward coefficients and m feedback coefficients. The goal is to develop an adaptation process that will adjust these weights so that the filter transfer

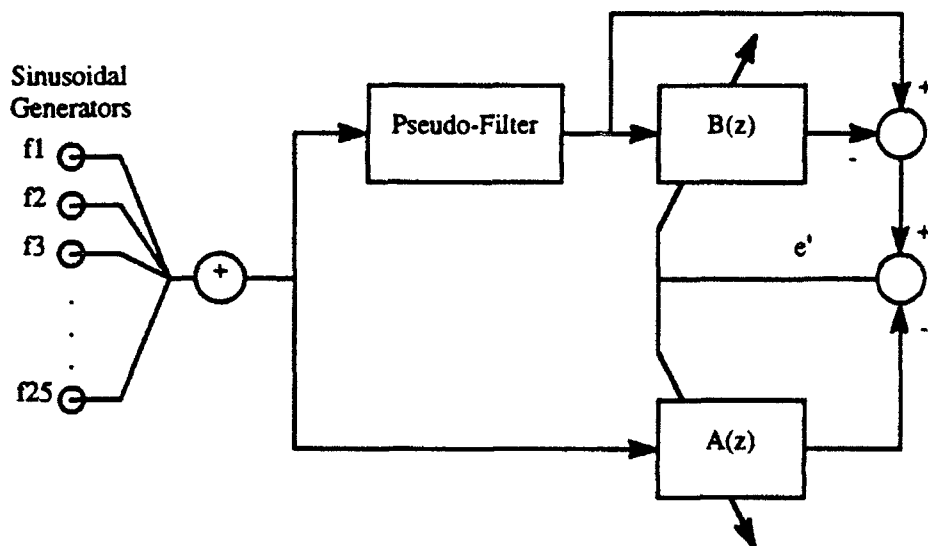
function is a best fit to certain filter design specifications. These filter design specifications are represented by a "pseudo-filter".

The figure below shows a digital filter scheme that adjusts the coefficients using an IIR algorithm.



The 25 sinusoidal inputs have 25 corresponding specification frequencies which are equally spaced up to the Nyquist frequency. Consequently, $A(z)$ and $B(z)$ adapt to the given design specifications. However, the IIR algorithm has some associated difficulties. The error surfaces are not always unimodal and the adaptive filter can become unstable due to the poles of the transfer function $(1 - B(z))$ being located outside of the unit circle in the z -plane. Consequently, in order to avoid this problem, another adaptation scheme was used which does not involve an IIR adaptation algorithm and is solely used just for filter synthesis applications. This new scheme consists of adapting $A(z)$ and $B(z)$ separately as adaptive transversal filters.

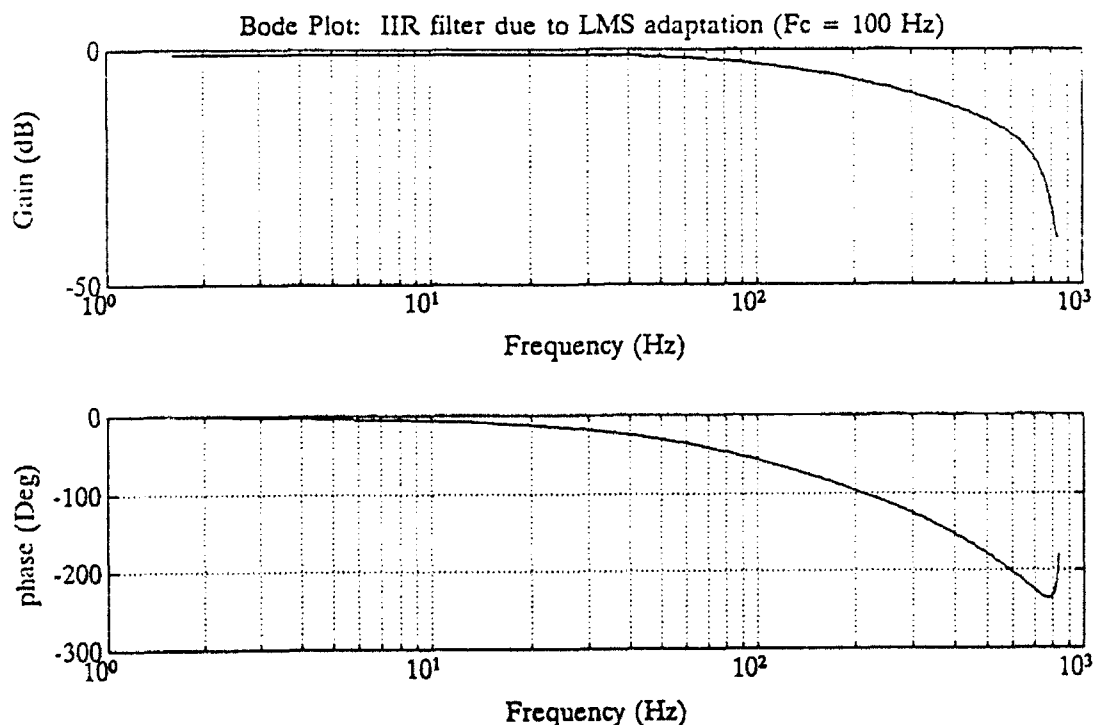
The figure below depicts the simultaneous direct and inverse modeling method.

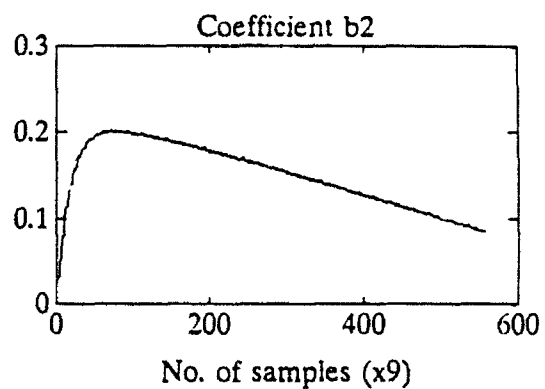
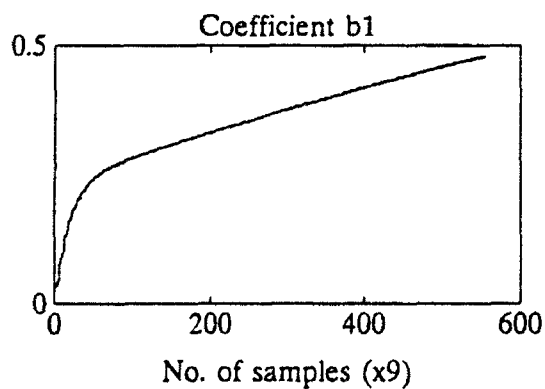
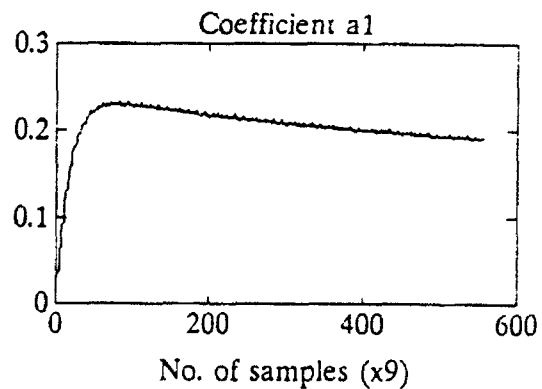
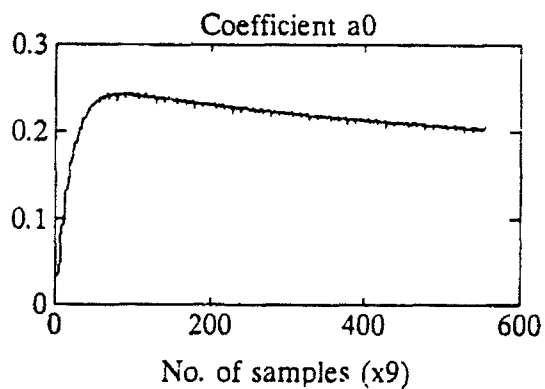
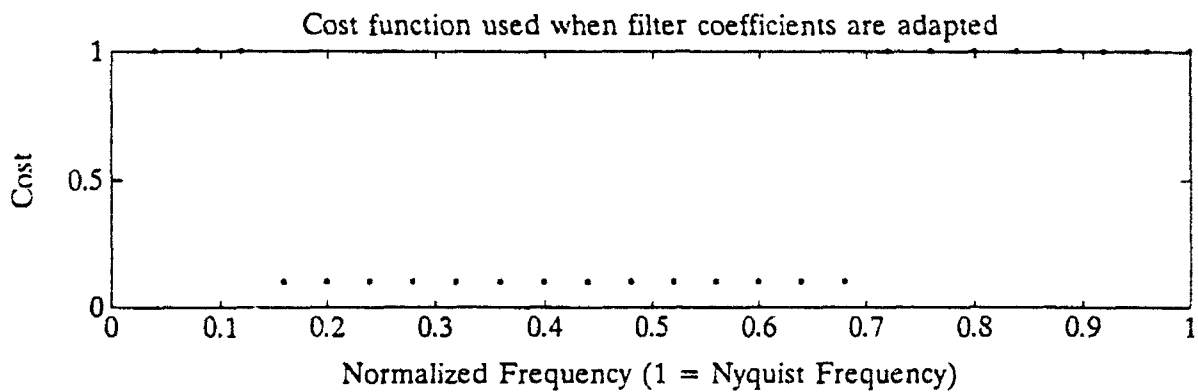
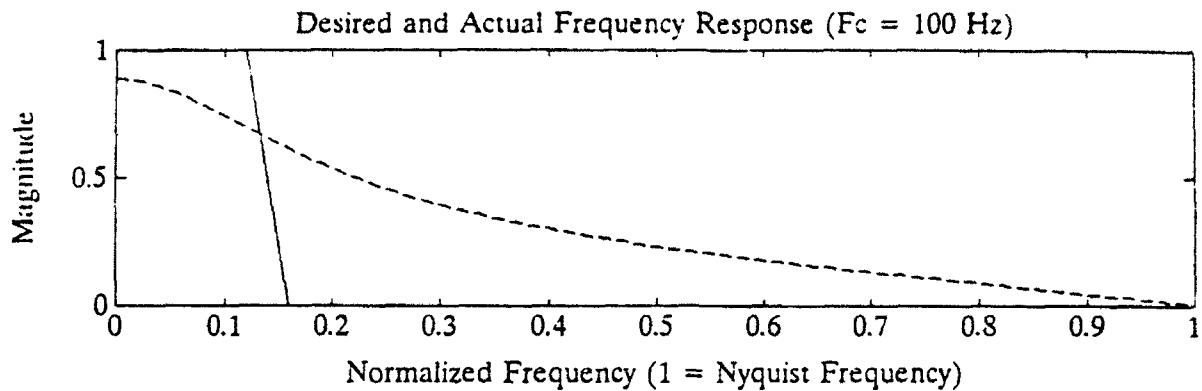


This algorithm adapts $A(z)$ and $B(z)$ separately using a least mean squared (LMS) technique. This approach does not quite minimize the expected value of the mean squared error of the actual filter and the pseudo-filter (e^2 above). However, this method adjusts $A(z)$ and $B(z)$ such that the expected value of e'^2 is minimized. It was observed that the adjusted values of $A(z)$ and $B(z)$ using the simultaneous direct and inverse modeling method came very close to minimizing e^2 . Once $A(z)$ and $B(z)$ are found using the simultaneous direct and inverse modeling method, the IIR filter is constructed by using $A(z)$ and $B(z)$ in the first figure in this section.

This obscure approach is used because the mean square of e'^2 is a quadratic function of the coefficients of $A(z)$ and $B(z)$. Thus, the error surface is unimodal. Consequently, no stability problems arise and a LMS algorithm can be implemented efficiently. Note that $A(z)$ is adjusted so that, ideally, $A(z)$ cancels the zeroes of the pseudo-filter, while $B(z)$ is adjusted such that $1 - B(z)$ cancels the poles of the pseudo-filter. $A(z)$ is adjusted in the direct modeling mode and $B(z)$ is adjusted in the inverse modeling mode.

This method of IIR filter design has been tested using computer implementation. This can be used to design a loop compensation filter for the deformable mirror interface. However, when using a single pole single zero filter, the bilinear transform method would have much better results as compared to this adaptation method. Using 25 specification frequencies limits the resolution of the adaptive filter specifications to $1/25$ of the Nyquist frequency. Consequently, a cost function was implemented in order to make the adapting filter adhere more closely to critical filter specifications. The loop compensation filter of the adaptive optics system is simply a lowpass filter with an arbitrary cutoff frequency and gain depending on the current application of the system. Thus, the cost function was designed solely to make the frequency response of the adapting filter better. One example of this adaptation process can be seen below. A Bode plot of the filter is also displayed. The desired and actual frequency response can be compared. The actual adaptation of the coefficients as a function of the number of samples can also be seen. It should be noted that this process is not exact, however, the computer simulation shows that the actual frequency response is quite good given the number of coefficients and the number of samples used.





IV. STABILITY ANALYSIS OF THE ADAPTIVE OPTICS SYSTEM

A stability analysis determines the actual criteria needed for the loop compensation filter such that the overall system is stable. The actual model used to find the overall stability of the system has been described in Section I. The actual method used to find the overall stability of the system is described below.

To test the performance of the adaptive optics system, the system response must be analyzed. To analyze the behavior of the system, the digital transfer function equivalent of the plant (HVA) and the electronic time delay when it is preceded by a zero order hold must be determined. Then the overall system must be modeled as a single input single output (SISO) closed loop discrete-time control system. Thus, phase error from a single aperture on the WFS determines the actual displacement of the actuators on the corresponding part of the DM. This analysis was performed on the adaptive optics model using a timing diagram of an Adaptive Optics Associates (AOA) WFS with an AOA/Lincoln Labs (LL) camera and using an input of three pulses from a copper vapor laser. Consequently, the Adaptive Optics system has a corresponding sampling rate of 600 microseconds. The system has two different modes of operation. One mode uses star data and the other mode uses artificial beacon data (A-data). The only difference between the two modes of operation from a control systems point of view is the actual electronic time delay involved with the closed-loop system.

System Time Delays

| | |
|---------------------------|-----------------------|
| AOA WFS reading A-data | 528 microsecond delay |
| AOA WFS reading STAR-data | 795 microsecond delay |

The stability and response of the system was determined using both the Bode plot method and the root locus method. Both methods entailed using a system model which did not include noise. The Bode plot method uses two main specifications, gain margin and phase margin, to measure relative stability of the system. On the other hand, the stability analysis using the root locus method can be determined from the

locations of the closed-loop poles in the z-plane. Closed-loop zeroes do not affect the absolute stability of the system and therefore may be located anywhere in the z-plane.

A table displaying the cutoff frequency of the loop compensation for a critically stable system and an overdamped step response for the various WFS modes can be seen below. The system was modeled with the RTR having a unity gain. It should be noted that all cutoff frequencies listed are not absolute values.

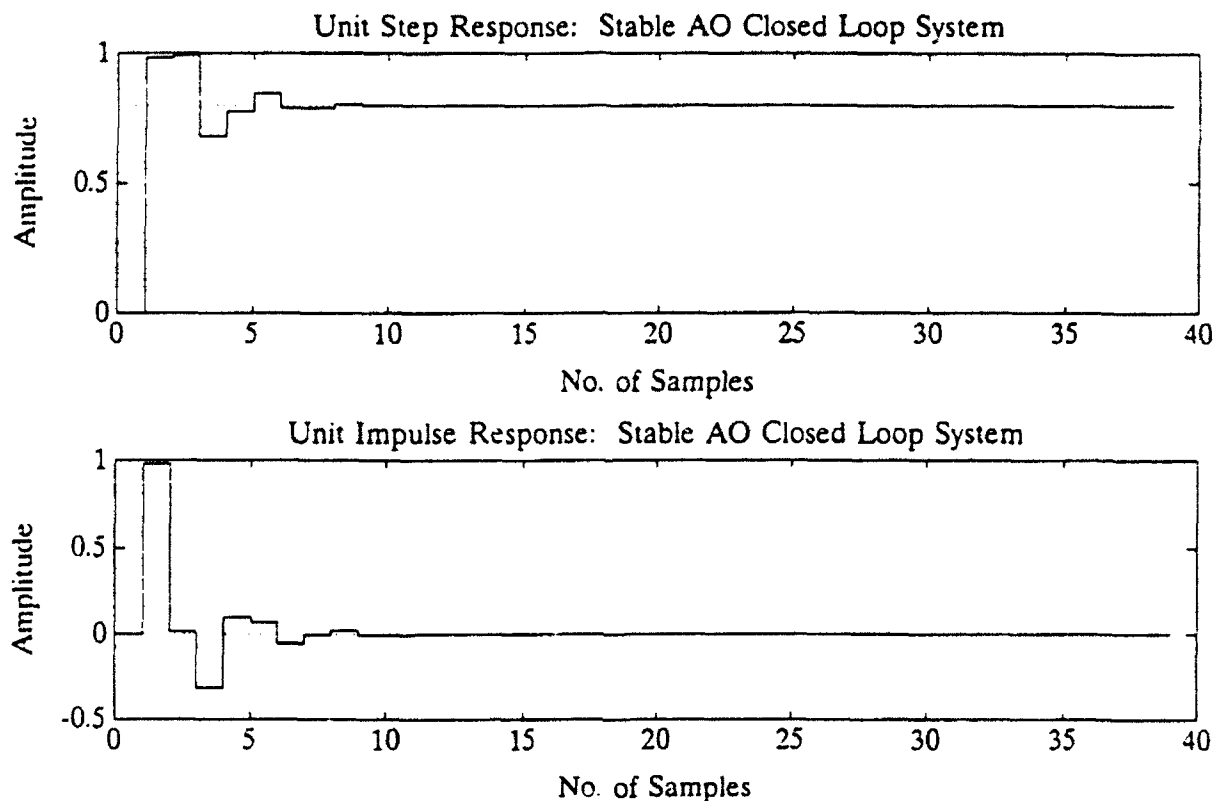
| <u>Sampling Rate</u> | <u>Time Delay</u> | <u>Critical Fc</u> | <u>Overdamped Fc</u> |
|----------------------|-------------------|--------------------|----------------------|
| 600 usec | 528 usec | 235 Hz | 30 Hz |
| | 795 usec | 110 Hz | 20 Hz |

usec = microseconds

The example shows a stable system with a fairly good unit step and unit impulse response. Notice the steady-state (SS) error involved with the step response of the stable system. This undesirable result can be minimized by adjusting the gain of the loop compensation filter. When the gain is adjusted to minimize the SS error, a trade-off between SS error and settling time arises. Considering the high sampling rate used, it becomes evident that the cost of the increased settling time does not become a significant factor as compared to the obvious effects of the SS error on the system. Consequently, it would be advantageous to minimize the SS error by adjusting the gain of the loop compensation filter.

It is important to point out that an increase or decrease in the sampling period T_s (i.e. the number of pulses used from the copper vapor laser) modifies the system dynamics and may destabilize the closed-loop system. Consequently, the loop compensation filter must be adjusted to overcome this destabilization problem. Another problem to be noted is that any time lag, including an electronic time delay, produces phase lag and reduces the stability margin in a closed-loop system. Time delay in the system also creates steady-state error. Steady-state (i.e. phase) error implies that the resulting image from the deformable mirror will not be optimized to the system's full potential. Again the loop compensation filter must be adjusted to

ensure stability of the system and to reduce steady-state error. It should be noted that this stability analysis did not include any noise. Thus, the actual loop compensation must be adjusted further to maximize the trade-off between noise rejection (signal-to-noise ratio) and system response according to various environmental conditions. One possible solution to the steady-state error problem is designing a controller that is optimal in the sense of minimizing the steady-state error and settling time.



V. THEORY OF AN OPTIMALLY ADAPTIVE CONTROLLER

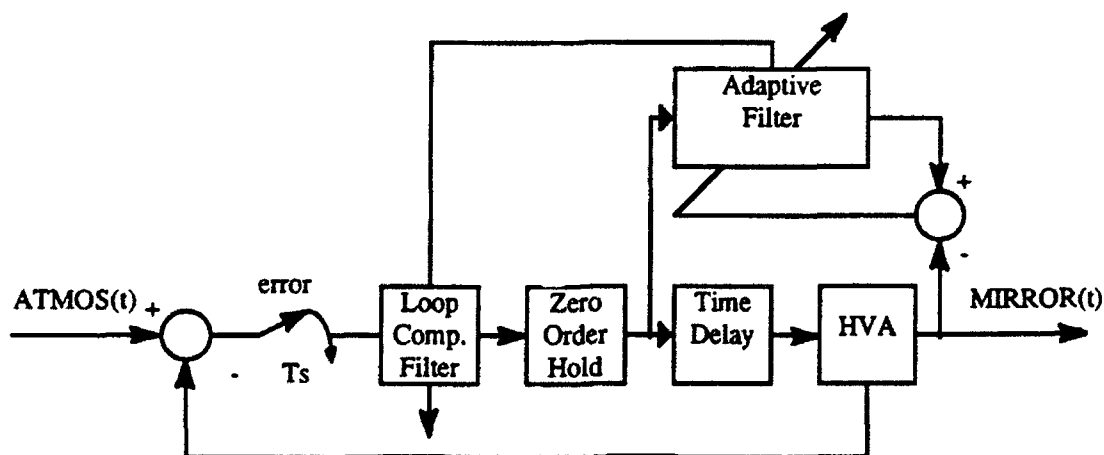
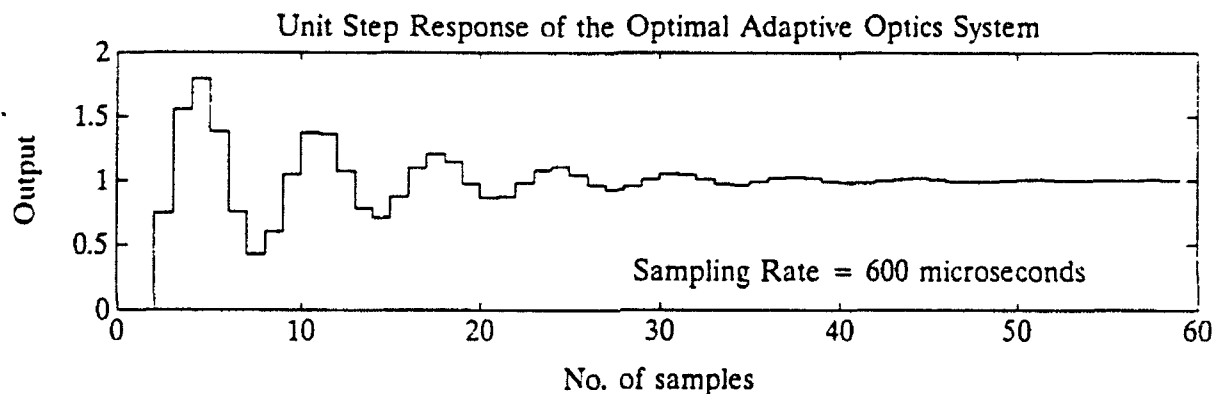
An optimal controller can only be optimized to a single type of input. The optimal controller will exhibit the best response characteristics for the type of input it is designed for, but will not exhibit optimal response characteristics for other types of inputs. In fact, the response of the system to another type of input may cause the

system to behave unsatisfactorily or may even become unstable. Besides this response problem, there are two major limitations of this optimal controller. The physical limitation consists of the fact that the controller's input to the plant (actuator) may saturate the plant and the mathematical limitation consists of the problem brought about by certain improper cancellation of poles and zeroes by the controller. Another solution to the steady-state error problem might be to develop an adaptive controller that adapts the loop compensation filter's coefficients to minimize the steady-state error given changing environmental conditions.

The description of the optimal controller will use the adaptive optics model introduced in Section I. Due to the time lag in the system, $e^{-s \cdot T_d}$, the designed closed loop system must involve at least the same magnitude of the time lag. Otherwise, the system would have to respond before an input was given. Consequently, this type of a system could not be physically realizable. It is commonly known that the transfer function of the actuators can be represented as $MIRROR(z)/ATMOS(z) = A(z) / B(z)$ where $A(z) = a_1 z^{-1} + a_2 z^{-2} + \dots + a_n z^{-n}$ and $B(z) = b_1 z^{-1} + b_2 z^{-2} + \dots + b_m z^{-m}$. Assuming the input to the system is varying slowly, the controller will optimize the adaptive optics system using a step input. Thus, the controller's transfer function is $loop\ comp(z)/error(z) = B(z)/C(z)$ where $C(z) = (a_1 + a_2 + \dots + a_n) - a_1 z^{-1} - a_2 z^{-2} - \dots - a_n z^{-n}$. Thus, the closed loop transfer function is equal to $A(z) / (a_1 + a_2 + \dots + a_n)$. As expected, the response to a unit step input displayed minimum settling time and zero steady-state error which can be seen below.

The adaptive control scheme, seen below, consisted of an adaptive filter directly modeling the deformable mirror and the overall electronic time delay. An ultra fast figure sensor would be used to measure the result of the deformable mirror in terms of phase. Then the characteristics of the adaptive filter would be used to optimally adjust the digital loop compensation filter as described above.

Several different IIR LMS recursive adaptive filters, similar to the IIR filter described in Section III, were tested by computer simulation to determine the modeling accuracy. The accuracy was determined by comparing the frequency response of the electronic time delay and the deformable mirror with the frequency response of the adaptive filter. The LMS adaptive filters used were a direct model IIR LMS filter, a direct and simultaneous model IIR LMS filter (described in Section III), and a hyperstable adaptive recursive filter, proposed by Larimore, which uses a finite impulse response filter to smooth out the error.



This hyperstable adaptive recursive filter's convergence has been proved in certain situations. Several different FIR filters with the hyperstable adaptive recursive filter were tested. However, none of these adaptive filters have been adequately modeling the plant. The best results have come from the hyperstable adaptive recursive filter. The adaptation error had a magnitude of 10^{-8} during computer simulations. However, when attempting to adjust the controller's coefficients, the system would go unstable. Consequently, further research is required to sufficiently adapt the controller's coefficients to create minimum settling time and zero steady-state error.

Conclusion

A discrete-time control system was designed using an overall adaptive optics system model. The motivation for controlling the deformable mirror via a digital controller as opposed to an analog controller is due to the advantages of easily performing complex control calculations, easily changing controller characteristics, and having far superior characteristics from the viewpoint of internal noise and drift effects. In fact, optimal control schemes that are not possible with analog controllers are made possible by digital controllers. The digital controller is essentially a digital loop compensation filter. The digital loop compensation filter's characteristics can be changed in real-time in order to enhance performance due to changing environmental conditions. Consequently, a generalized single pole / single zero filter was designed using a bilinear transformation with frequency prewarping. In order to employ higher order infinite impulse response filters, an adaptive scheme was used to automatically adjust a variable number of feedforward and feedback coefficients so that the filter transfer function is a best fit to a set of design specifications. Due to the inherent time lag in the adaptive optics system a steady-state error occurs. A theoretical optimal control scheme was found that exhibited minimum settling time with zero steady-state error. Using this optimal control scheme, several adaptive control algorithms were attempted. The adaptive control scheme consisted of an adaptive filter directly

modeling the deformable mirror and the overall electronic time delay in terms of phase. Then the characteristics of the adaptive filter would be used to adjust the digital loop compensation filter in real-time. Resulting in an adaptive controller which optimally reduces the steady-state error and possess a minimum settling time response given a specific input to the system. However, in order to implement this adaptive controller scheme, further research is necessary to accurately model the deformable mirror using an adaptive filter in real-time operation.

References

R. Q. Fugate et. al., "Measurement of atmospheric wavefront distortion using scattered light from a laser guide-star," *Nature* **353**, 144-146 (1991).

Madan M. Gupta, *Adaptive Methods for Control System Design*, IEEE Press, New York, 1986.

Simon Haykin, *Adaptive Filter Theory*, 2nd edition, Prentice Hall, Englewood Cliffs, NJ, 1991.

C. R. Johnson, Jr., M. G. Larimore, J. R. Treichler, and B. D. O. Anderson, "SHARF convergence properties," *IEEE Trans. Acoust. Speech Signal Process.*, vol. ASSP-29, p.659, June 1981.

M. G. Larimore, J. R. Treichler, and C. R. Johnson, Jr., "SHARF: an algorithm for adapting IIR digital filters," *IEEE Trans. Acoust. Speech Signal Process.*, vol. ASSP-28, p.428, Aug. 1980.

James W. Nilsson, *Electric Circuits*, 2nd Edition, Addison Wesley, Menlo Park, CA, 1986

Alan V. Oppenheim & Ronald W. Schaffer, *Discrete-Time Signal Processing*, Prentice Hall, Englewood Cliffs, NJ, 1989.

J. R. Treichler, M. G. Larimore, and C. R. Johnson, Jr., "Simple adaptive IIR filtering," *Proc. 1978 ICASSP*, p.118, Apr. 1978.

Robert K. Tyson, *Principles of Adaptive Optics*, Academic Press, Inc., New York, 1991.

**COMPACT TOROID MASS ENTRAINMENT SENSITIVITY
TO INITIAL DENSITY DISTRIBUTIONS USING
NUMERICAL SIMULATION**

**Robert John Leiweke
Graduate Research Associate
Department of Aeronautical & Astronautical Engineering**

**The Ohio State University
2036 Neil Avenue Mall, Room 326
Columbus, Ohio 43210**

**Final Report for:
AFOSR Summer Research Program
Phillips Laboratory**

**Sponsored by:
Air Force Office of Scientific Research
Kirtland Air Force Base, Albuquerque, NM**

September, 1992

**COMPACT TOROID MASS ENTRAINMENT SENSITIVITY
TO INITIAL DENSITY DISTRIBUTIONS USING
NUMERICAL SIMULATION**

**Robert John Leiweke
Graduate Research Associate
Department of Aeronautical and Astronautical Engineering
The Ohio State University**

Abstract

Numerical simulation of Compact Toroid (CT) mass entrainment for the MARAUDER (Magnetically Accelerated Rings to Achieve Ultrahigh Directed Energy and Radiation) program was studied with a number of argon density distributions initially in the neutral state. The simulations were accomplished using MACH2, a two-dimensional arbitrary Lagrangian Eulerian magnetohydrodynamics (MHD) code. The baseline model, termed the Realistic Working Model, is a strong function of r and z . It was conjectured that the radial dependence was dominant, so the initial density model for argon with gradients in the poloidal plane (r - z) was collapsed into the form of a short annulus with a radial gradient. The mass entrainment for this annulus compared well with the realistic model from which it was formed, suggesting, but not proving *radial* dependence of initial density distribution. This result induced further investigations into mass entrainment which focused on radial gradient distributions. Simulations of annuli distributed as a Gaussian in z were also studied. The results suggest that for geometries with $\Delta r/r \ll 1$, mass entrainment is maximized by keeping the greatest densities away from the walls (electrodes). The present experimental injection distribution is *not* the most ideal for maximizing MARAUDER CT mass entrainment.

COMPACT TOROID MASS ENTRAINMENT SENSITIVITY TO INITIAL DENSITY DISTRIBUTIONS USING NUMERICAL SIMULATION

Robert John Leiweke

INTRODUCTION

The MARAUDER (Magnetically Accelerated Rings to Achieve Ultrahigh Directed Energy and Radiation) program at Phillips Laboratory studies the formation, compression, and acceleration of Compact Toroid (CT) plasmas for use as possible sources of intense x-rays, high-power microwaves, very fast opening switches, and an alternative path to inertial confinement fusion.¹ The experiment utilizes Shiva Star, a 9.4 MJ capacitor bank (1300 μ f, 120 kV) at lower capacitance and voltage to create the CT formation and compression discharge currents of 2 MA and 3 MA, respectively. Formation of a CT begins with the radial injection of a neutral gas (such as argon, hydrogen, deuterium, nitrogen) into the gap of an evacuated coaxial gun permeated with a 0.1 to 0.2 T poloidal magnetic field. The poloidal magnetic field is "frozen" in place at the conducting coaxial electrodes. During the 0.25MJ formation discharge, toroidal magnetic flux fills the volume behind the injected gas, which is subsequently ionized by the induced current across the radial gap.² The toroidal magnetic pressure which varies as $1/r^2$, acts as a massless piston that stretches the embedded poloidal field and accelerates the plasma downstream.² Magnetic and hydrodynamic boundary layers leave some mass remaining at the walls. The mass left behind in the muzzle bridges the radial gap and becomes an efficient current return path (for example, see Figures 8a, 8b, or 8c).

MODELING PARAMETERS

The fraction of the total injected mass that becomes entrained within the expansion volume during the formation stage is of general interest to the MARAUDER program. It had been previously shown that the mass fraction depends on the initial mass density distribution.⁴ Previously, an approximation to the actual MARAUDER initial density distribution was calculated³ in order to provide a Realistic Working Model (RWM) on which this study is based. All dynamic simulations were

performed with MACH2, a two-dimensional arbitrary Lagrangian Eulerian magnetohydrodynamics (MHD) code.⁵ MACH2 ignores hydrodynamic viscosity since thermal conductivity plays a more dominant role. The MACH2 code has time-dependant models for both the formation and compression discharge of the MARAUDER experiment.²

Figure 1 shows the initial poloidal magnetic field is threading the right half cross-section of the gun, and is consistent with experimental probe measurements.⁶ The formation bank has a capacitance of $110\text{ }\mu\text{F}$, is charged to 70 kV (0.25 MJ), and has a total inductance of 23.1 nH.⁴ The compression bank has a capacitance of $440\text{ }\mu\text{F}$, is charged to 70 kV (1 MJ), and has a total inductance of 100 nH.⁴ At $6\text{ }\mu\text{s}$ the formation current is crowbarred to prevent flow reversal and the compression discharge begins at $7\text{ }\mu\text{s}$.⁴ Initial mass was chosen to be 1.46 mg of argon. Wall (electrode) boundary conditions are defined to be closed and conducting with a velocity condition imposed due to the magnetic boundary layer.

The computational grid consists of the right half cross-section (r-z plane) of the coaxial gun muzzle and expansion volume, as shown in Figure 2. The radius of the inner and outer electrodes are

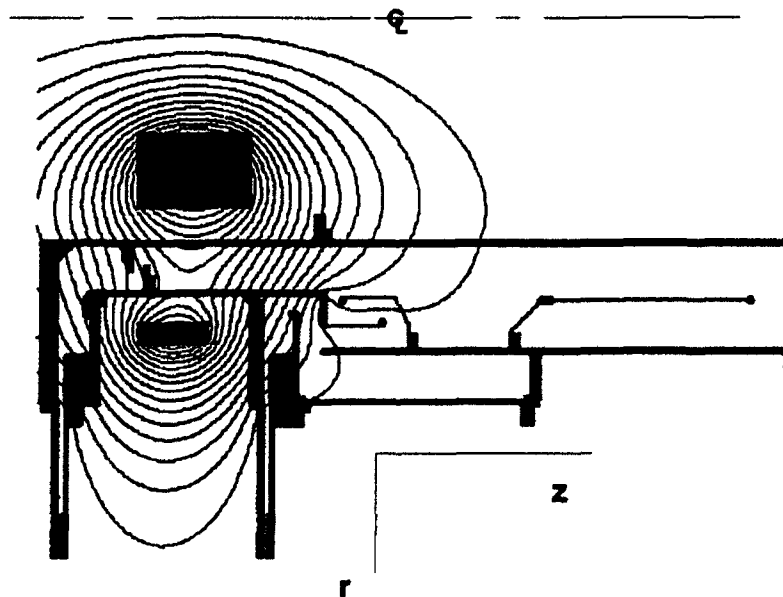


FIGURE 1

43.77 cm and 52.39 cm, respectively. The annularized density distributions are placed within the 7.62 cm wide gap at the mass injection point. All density models used in the study assume azimuthal symmetry. The computation begins at time zero with the formation current and runs until $15\mu\text{s}$ has elapsed. Mass entrainment is defined to be the fraction of the total mass that is pushed into the expansion volume $14\mu\text{s}$ after the formation current begins. The closed boundary at the top of the expansion domain in Figures 2,3 does not significantly effect the mass entrainment results since backpressure information does not have an opportunity to propagate upstream within the computational time window.

METHODOLOGY

In an attempt to reduce the number of variables within parameter space, the RWM mass distribution shown in Figure 3a, was collapsed axially into a short annulus, which has been termed the Annularized Realistic Working Model (ARWM) in Figure 3b.

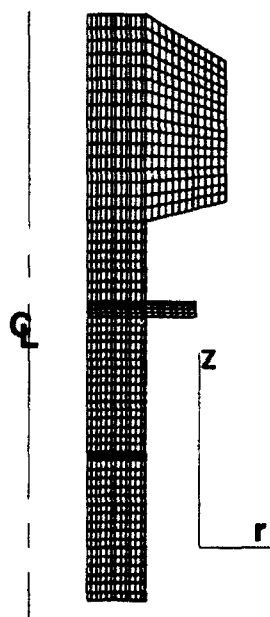


FIGURE 2

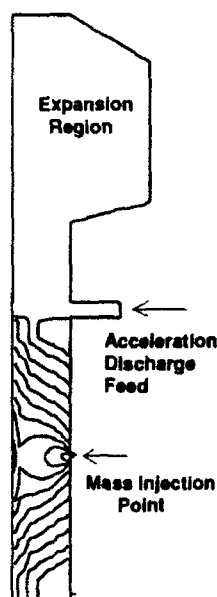


FIGURE 3A

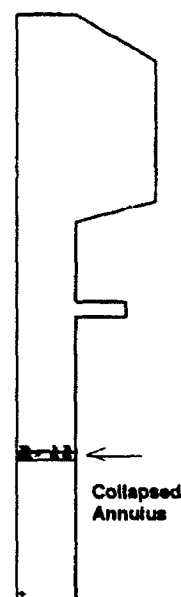


FIGURE 3B

The entrainment results for this new annular distribution closely matches those of the RWM (see Table 1). The basic mathematical form for the ARWM models chosen is

$$\rho_i(r,z)=\phi_i(r) \exp\{-A(z-z_0)^2\} , \quad i=1,2 \quad 0.4477\text{m} < r < 0.5239\text{m} \quad (1)$$

$$\text{where } \phi_1(r)=a_n r^n + a_{n-1} r^{n-1} + \dots + a_1 r + a_0 , \quad n=-2,0,2,4,6,9,17 \quad (2)$$

$$\text{or } \phi_2(r)=\alpha(r+k)^{-2} + \beta(r+k)^2 + \gamma , \quad (3)$$

where z_0 is the axial mass injection point and A, k, a_j 's, α, β, γ are constants. The functional form of equation 3 was chosen to closely resemble the ARWM's radial distribution characteristics and is termed the Fitted-ARWM (FARWM), as displayed in Figure 4. One additional dynamic simulation with a third function⁴

$$\phi_3(r,z)=r^{\zeta(z)} , \quad \zeta(z)=17-34\{|z/z_0-1|\} \quad (4)$$

in an attempt to analytically fit a distribution calculated prior to the RWM.³ Listed in Table 1, case 3 is the same analytical function as FARWM (case 2), but the radial grid resolution was doubled.

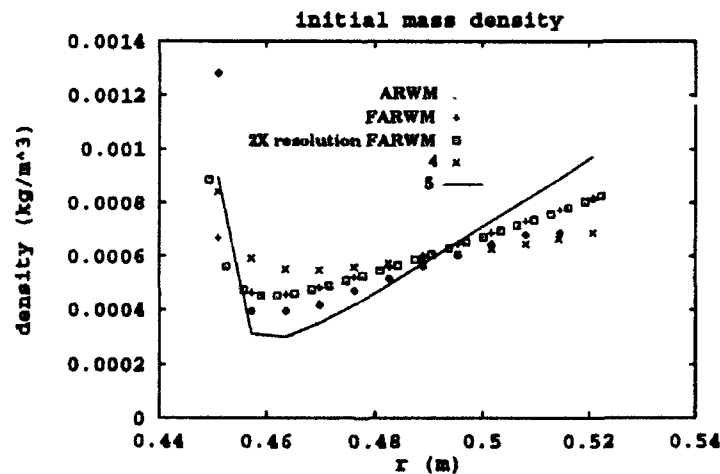


FIGURE 4

Cases 4 and 5 are variations on FARWM in which the minimum density is greater than or less than that of FARWM at the same radial location, respectively. The effective result is a redistribution of mass either toward or away from the electrodes (see Figure 4). In addition to the RWM, ARWM, and five FARWM variants, there are twenty case studies based on equation 2. Five of these cases are shown in Figure 5. Each case was considered both as an "axially collapsed" annulus by taking $A=0 \text{ m}^2$ in equation (1), and as "axially expanded" Gaussian distribution by taking $A=300 \text{ m}^2$.

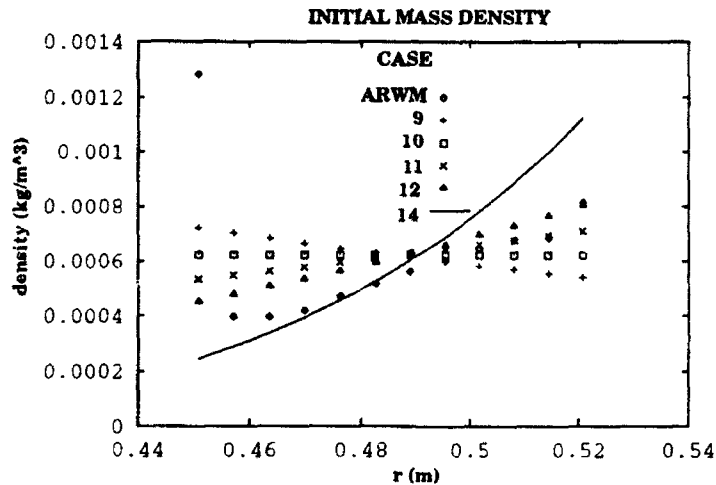


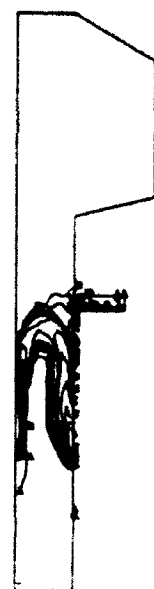
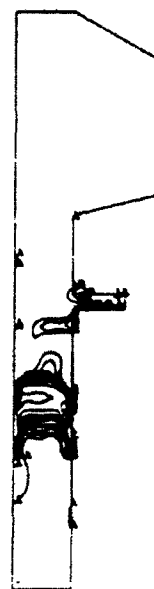
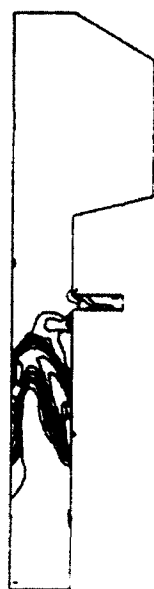
FIGURE 5

In case 6, the mass is lumped into the middle of the radial gap. Since $\Delta r/r$ is small, it is important to note from Figure 5 that the radial density variation for cases 9 and 11 becomes small.

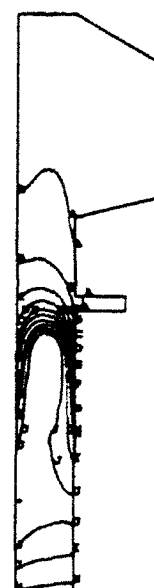
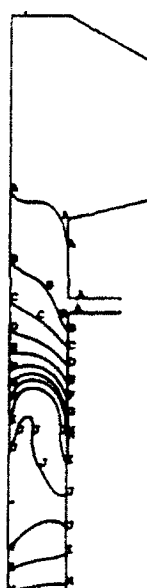
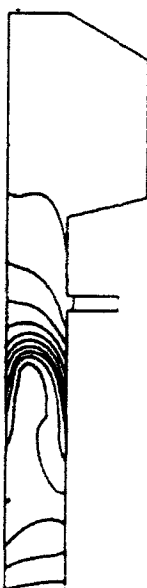
RESULTS

Figures 6, 7, and 8 compare mass density and poloidal magnetic flux for cases 1, 9, and 5 at the times $3\mu\text{s}$, $6\mu\text{s}$, and $12\mu\text{s}$, respectively. The density in case 9 and the toroidal magnetic field pressure both vary as $1/r^2$. Thus, irrespective of axial distribution, case 9 is expected to result in the highest mass entrainment since, as shown in Figure 6b, a radially uniform acceleration produced by the $\mathbf{J} \times \mathbf{B}$ force density encourages a significant portion of mass to move parallel to the electrodes.

mass
density



magnetic
flux



initial
density
vs. r

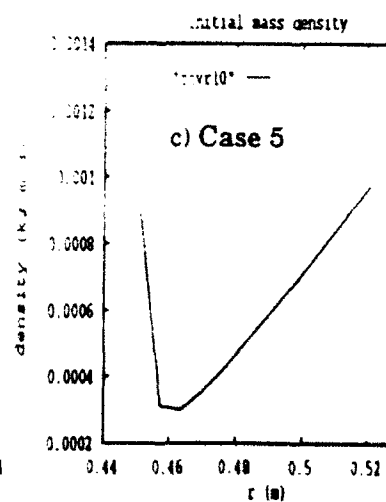
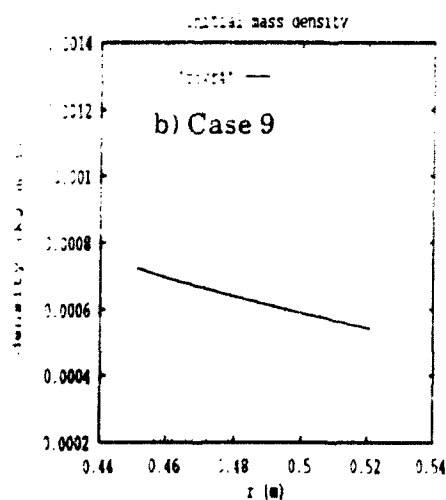
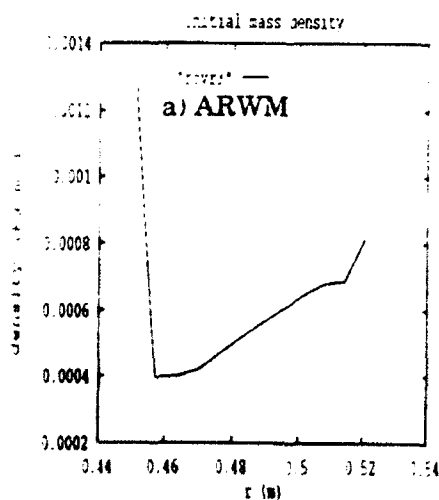


Fig. 6. The mass density and magnetic flux distributions at $t = 3 \mu s$ for the three initial density distributions shown below, which are, from left to right: a) the ARWM model, b) case 9, and c) case 5 respectively.

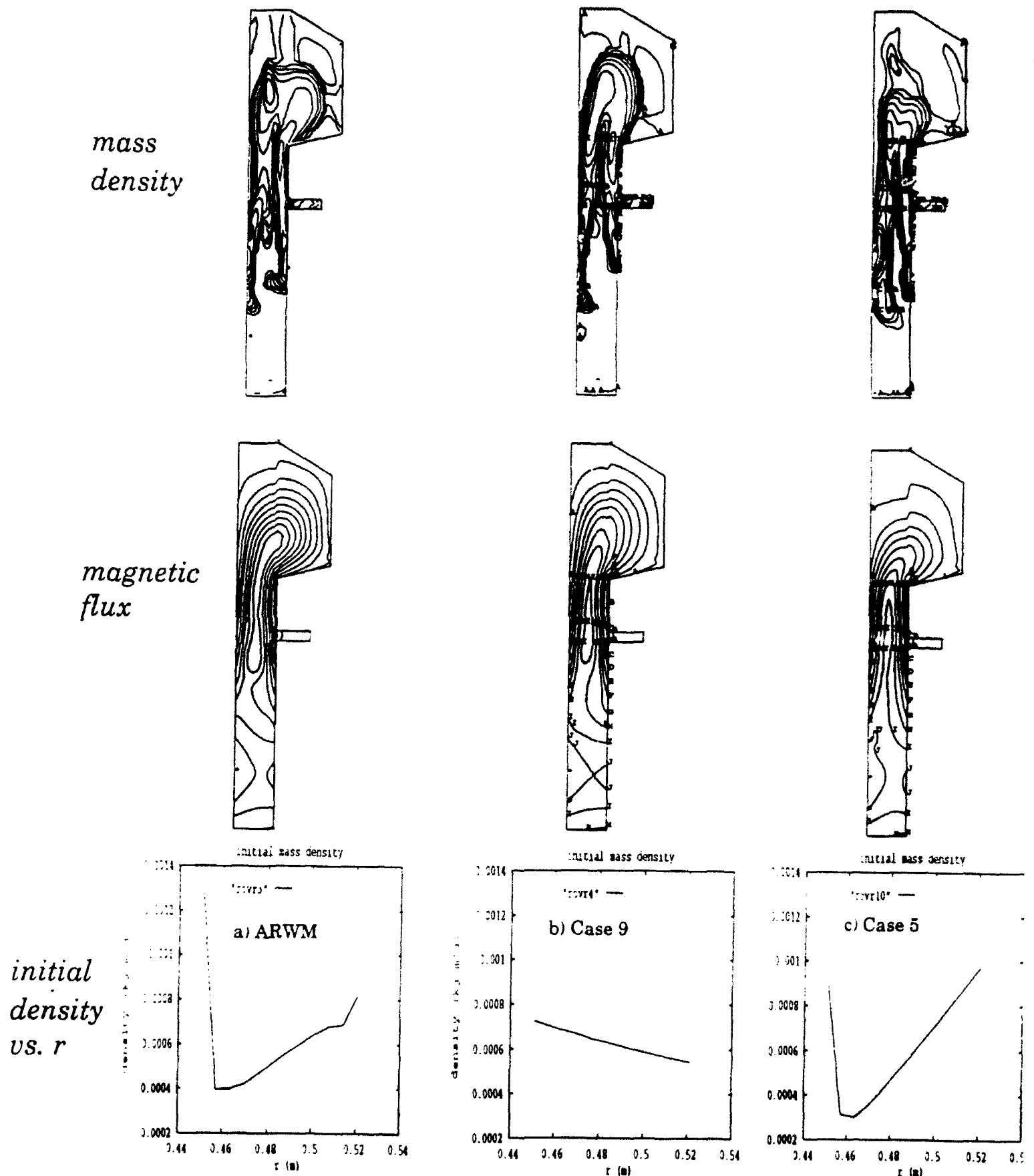


Fig. 7. The mass density and magnetic flux distributions at $t = 6 \mu\text{s}$ for the three initial density distributions shown below, which are, from left to right: a) the ARWM model, b) case 9, and c) case 5 respectively.

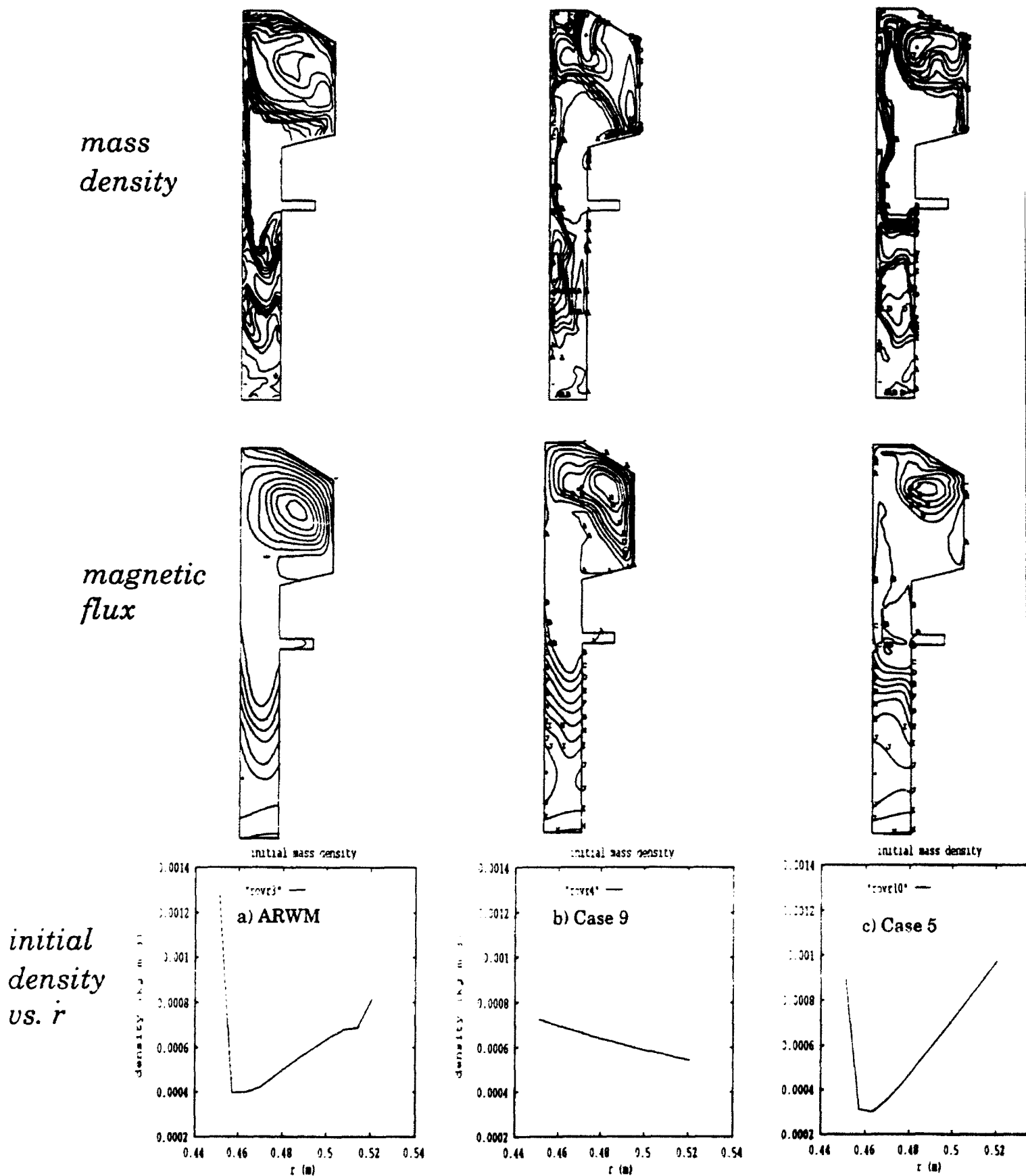


Fig. 8. The mass density (above) and the magnetic flux (below) distributions at $t = 12 \mu s$ for the three initial density distributions shown below, which are, from left to right: a) the ARWM model, b) case 9, and c) case 5 respectively.

| CASE | $\phi(r)$ | <u>% MASS ENTRAINED</u> | |
|------|---|-------------------------|----------|
| | | ANNULUS | EXPANDED |
| 1 | ARWM | 63 | --- |
| 2 | FARWM | 68 | 72 |
| 3 | FARWM, 2X resolution | 70 | --- |
| 4 | FARWM, Min = 1.5 Min[Case 2] | 87 | --- |
| 5 | FARWM, Min = 0.5 Min[Case 2] | 51 | --- |
| 6 | $-a_2 r^2 + a_1 r + a_0, \quad a_j > 0$ | 87 | 87 |
| 7 | $1/r^{17}$ | 44 | 53 |
| 8 | $1/r^6$ | 88 | 88 |
| 9 | $1/r^2$ | 93 | 78 |
| 10 | a_0 | 93 | 78 |
| 11 | r^2 | 91 | 76 |
| 12 | r^4 | 78 | 72 |
| 13 | r^6 | 67 | 78 |
| 14 | $(r-k)^4 \sim r^9$ | 57 | 65 |
| 15 | r^{17} | 39 | 55 |
| 16 | $r^{\zeta(z)}$ | --- | 60 |

Realistic Working Model Yield (RWM) = 58%

TABLE 1

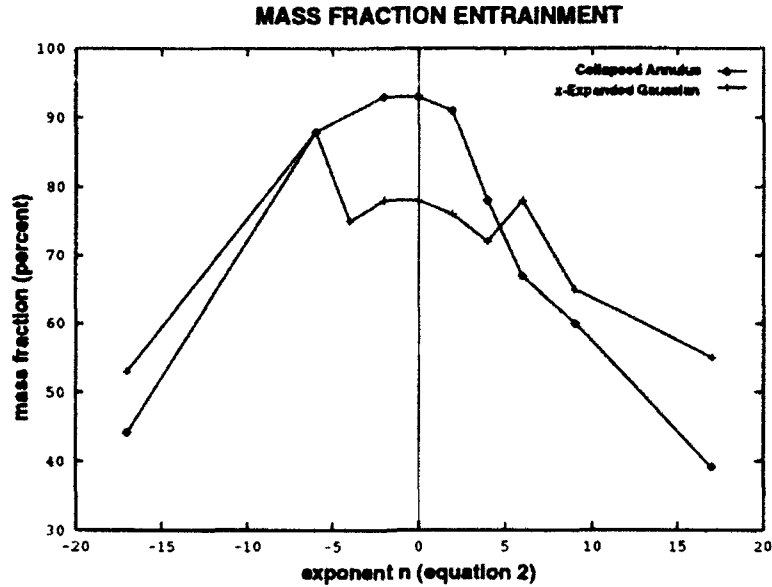


FIGURE 9

For annuli and their expansions having no minimum or maximum within the open radial domain, Figure 9 shows that the yield monotonically decreases with increasing exponent magnitude in equation 2. The slight asymmetry about $n=0$ is most likely attributed to the non-uniform magnetic field pressure across the gap. Because $\Delta r/r \ll 1$, case 10 (constant) and 11 (r^2) are similar to $1/r^2$, and the results are nearly the same for both classes (see Table 1). As expected, case 9 ($1/r^2$) yields the largest mass entrainment for the annuli class (93%). Surprisingly, this is not true when expanded; case 8 ($1/r^6$) yields a global maximum of 88% as compared to 78% for case 9.

In Figure 9, annularization and expansion results diverge for distribution exponents $|n| > 5$ and $0 < |n| < 5$. Considering the region $0 < |n| < 5$ in Figure 9, one might be led to expect that case 6 ($\rho(r) = -a_2 r^2 + a_1 r + a_0$), when axially expanded, would yield less entrained mass than its annularized counterpart, since mass lumped symmetrically into the gap's middle may be considered as an "extrapolation" away from the constant distribution case. On the contrary, case 6 annulus entrainment is invariant to axial expansion, remaining at 87%. Most importantly however, the overall effect for both annularized and expanded classes is decreasing entrainment with increasing exponent magnitude.

Figure 10 illustrates increasing entrainment with increasing FARWM minimum density,

including the ARWM. As the minimum density is increased, mass is distributed more towards the gap's middle where the magnetic pressure is moderate and the boundary layer effects are small. Coincidentally, annular cases 4 {FARWM, $\text{Min}=1.5\text{Min}(\text{case } 2)$ } and 6 $\{\rho(r)=-a_2r^2+a_1r+a_0\}$ have drastically different distribution functions but yield 87% entrainment (see Table 1).

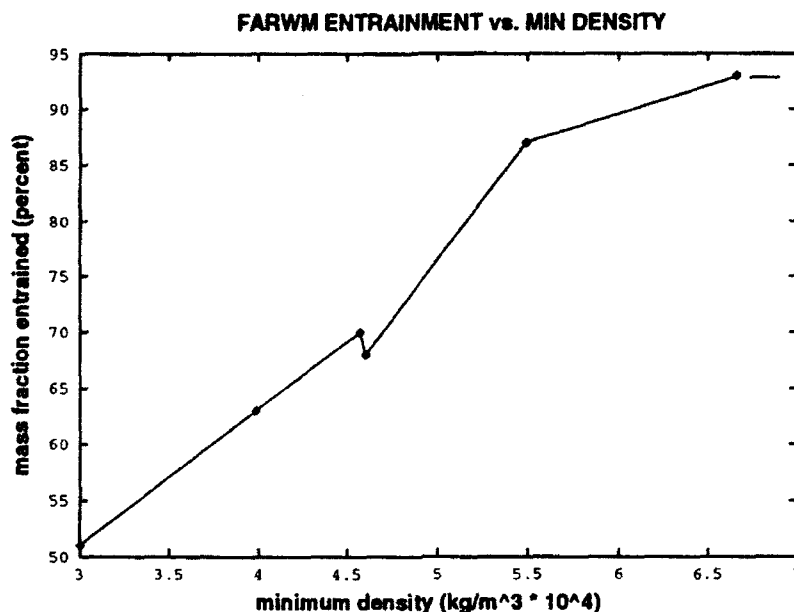


FIGURE 10

Case 14 (see equation 4) is an analytical "surface" fit of an early attempt to calculate a realistic working model. Results for this model (60%) are comparable to the RWM (58%). However, a large discrepancy was encountered between this case (14) and the density field that it is intended to fit (7%). This discrepancy has not yet been resolved.

CONCLUSIONS

The radial effect on mass entrainment is more dominant when density minima are within an order of magnitude of that at the electrodes. For distributions which have no minimum in this domain, annularization of a poloidal density field yields entrainment deviations up to 15% of the non-annularized value. Trends indicate that Compact Toroid (CT) mass entrainment will be increased by keeping the maximum density away from the electrodes. Based on the Realistic Working Model dynamic simulation and the indicated trends, the present experimental injection density distribution is *not* the most ideal for maximizing MARAUDER CT mass entrainment.

ACKNOWLEDGEMENTS

This work is a direct response to questions posed by Jim Degnan. Enlightening discussions with R.E. Peterkin, Jr., Jim Degnan, Norm Roderick, George Marklin, David Bell and Melissa Douglas. Thanks go to Edward L. Ruden for his review comments. Sincere gratitude is expressed towards R. E. Peterkin, Jr. for unconditional provision of patience, support, and constructive criticisms that lie somewhat beyond the call of duty.

REFERENCES

- [1] R. E. Peterkin, Jr., *et al.*, "A Compact Torus Plasma Flow Switch", *Digest of Technical Paper: Eighth IEEE International Pulsed Power Conference*, 17-19 June 1991, San Diego, CA, R. White and K. Prestwich eds., p. 277 (IEEE, New York, NY, 1991.).
- [2] R. E. Peterkin, Jr., *et al.*, "A Long Conduction Time Compact Torus Plasma Opening Switch", *Proceedings of the XVth International Symposium on Discharges and Electrical Insulation in Vacuum*, 6-10 September 1992, Darmstadt, Germany, in press, (1992).
- [3] G. Marklin, from the set of MACH2 calculations of initial density distributions intended to produce a realistic working model for MARAUDER, 1992.
- [4] R. E. Peterkin, Jr., private communications, 1992.
- [5] M. H. Frese, "MACH2: A Two-Dimensional Magnetohydrodynamic Simulation Code For Complex Experimental Configurations," AMRC-R-874, updated March 1990.
- [6] G. Marklin, MARAUDER poloidal field calculations, 1992.

**FIDELITY OF POLARIZATION RECOVERY USING A DOUBLE FIBER-COUPLED
PHASE-CONJUGATE MIRROR**

Darron D. Lockett, M.S. *
Department of Physics
Clark Atlanta University
Atlanta, GA 30314

In Collaboration with:
Mark T. Gruneisen, Ph.D.
Nonlinear Optics Branch
PL/LITN
KAFB, NM 87117

Final Report for:
Summer Research Program
Phillips Laboratory

Sponsored by:
Air Force Office of Scientific Research
Kirtland Air Force Base, New Mexico 87117

August 1992

*Focal Point: Mark Kramer, Ph.D.

**FIDELITY OF POLARIZATION RECOVERY USING A DOUBLE FIBER-COUPLED
PHASE-CONJUGATE MIRROR**

**Darron D. Lockett, M.S.
Department of Physics
Clark Atlanta University**

Abstract

Modal phase dispersion, diffusion, and polarization scrambling degrade wavefront transmission in multimode optical fibers. We report the investigation of polarization recovery using a double fiber-coupled phase conjugate mirror. A marked dependence of the polarization on the degree of fiber mode excitation is experimentally observed. Greater than 95% polarization recovery is reported.

INTRODUCTION:

There has been much work done in the area of laser beam propagation in optical fibers over recent decades. Optical fibers serve as a useful medium through which to propagate light because of their isolation from environmental interactions. Also, optical fibers eliminate the necessity for cumbersome beam stirring optics. However, for the case of multimode fibers, an input wavefront will experience degradation and distortion upon propagation.

A detailed theoretical model of this phenomenon is given by Yariv¹. He shows that the beam is invariably "smeared" as it propagates in the fiber. He also explains this smearing in terms of phase velocity dispersion and diffusion of the optical fiber modes which are excited by the laser beam. Later work by Yariv and his colleagues indicates that the polarization of the beam is also distorted as the light propagates the fiber. Modal phase compensation can be eliminated by using a single-mode optical fiber to propagate a Gaussian wavefront. However, mode matching the laser to the fiber adds difficulty to the alignment. Moreover, a laser beam with a non-Gaussian profile will not couple efficiently into the single-mode fiber. Multi-mode fibers are well suited for propagating non-Gaussian wavefronts.

Previous works^{2,3} indicate that phase conjugation can be employed to compensate for modal dispersion and diffusion in multimode optical fibers. In the work of these references, a resolution chart is imaged into a step-index multimode fiber. The fiber output is directed into a crystal of barium titanate (BaTiO_3) in which degenerate four wave mixing is used to generate the phase-conjugate of the input wavefront. The phase-conjugate wavefront retraverses the same optical fiber, resulting in the reconstruction of the original input resolution chart.

DISCUSSION OF PROBLEM

In this paper we discuss a geometry initially suggested by Gruneisen et. al⁴ for wavefront reconstruction and phase locking of the outputs of two HeNe lasers. This scheme employs the properties of both phase conjugation and optical fibers. The two beams are coupled into two multimode step-index fibers. They then propagate in a photo-refractive BaTiO₃ (barium titanate) crystal which is oriented to form a double phase-conjugate mirror. This combination automatically compensates for modal dispersion and diffusion.

In the work of Gruneisen, the outputs of two multi-longitudinal mode HeNe lasers are encoded with image information from two transparencies. The transparencies consist of horizontal and vertical bars of various spatial frequencies. These wavefronts containing the image information of one horizontal bar pattern and that of one vertical bar pattern are then injected into two multimode step-index fibers. After propagating in the fibers, the image information is completely scrambled, and the two fiber outputs are directed into a barium titanate crystal oriented to form a double phase-conjugate mirror. Light originating from laser 2 is then the wavefront conjugate of the light originating from laser 1 and vice versa. Each conjugate wavefront propagates the other fiber, and the original wavefronts are reconstructed. Also, automatic phase locking is obtained.

It is already shown that the fidelity of the true phase conjugation degrades as the input-beam numerical aperture increases.⁵ Thus, in order to take advantage of the true phase-conjugation feature of the fiber-coupled phase conjugate mirror, the angular spread of the input beam must be restricted so as to excite only a small fraction of the fiber modes.

It is of our interest to investigate the effect of increasing the

angular spread of the fiber output-beam, and its effect on the fidelity of the true phase conjugation. An increase in the angular spread of the fiber output-beam, and thus, an increase in the degree of modal excitation can be accomplished by either of two means. It can be increased by either increasing the fiber length, or higher-order modes can be excited mechanically. The latter case makes use of a mode scrambling device which "crimps" down on the fiber forcing excitation.

The work of this report aids in answering the question as to how well the image beam information can be restored under the extreme condition of higher-order modal excitation. In order to obtain a quantitative measure of recovery, we undertook a study to determine the fidelity and dependence of the polarization on the increasing degree of modal excitation. The results are reported.

METHODOLOGY

Two mutually incoherent HeNe laser beams with equal path lengths and output powers of 12mW and 13mW, respectively, are focussed into two similar step-index multimode optical fibers with core diameter of 200 microns. The fiber input numerical aperture is 0.039. The input beam diameter of the two lasers is measured to be 1.35mm. The focussing angle of the beams into the fibers is $.44^\circ$. This was accomplished with the use of 17.5cm focal length lenses.

The input beams are initially linearly polarized before entering the fibers. Mode scrambling and depolarization take place as the beams propagate in the fibers. Each spot size of the output beams is measured at a distance of 12 inches away from the fibers. Using this information and simple trigonometric manipulations, the angular spread of the fiber output is obtained, and thus, the numerical aperture of the fiber outputs ($NA = \sin /2$) is obtained. The polarization states of the output of only one of the fibers is measured in this report. A description of the polarization analyses will

be discussed later in this report. Each beam is now collimated by a lens before entering a polarizing beam splitter oriented to pass horizontally polarized light only. The beams are now directed into a BaTiO_3 crystal oriented to form a double phase conjugate mirror.

BaTiO_3 is a photorefractive material. Light-induced changes of the refractive index take place in this material. These changes of the index give rise to scattering of laser beams. Photo-electrons are generated. They migrate in the lattice, and subsequently, are trapped at new sites. The resulting space-charges give rise to an electric field in the material, which causes changes in the index of refraction via the electro-optic effect. In the case of the double phase conjugate mirror, each beam interferes with its own scattered light to generate a set of refractive index gratings within the crystal. Competition between these two sets of gratings leads to selective reinforcement of similar gratings and washout of dissimilar gratings.⁶ Each field then diffracts from the surviving gratings in the form of the phase conjugate of the other field.

The conjugate beam originating from laser 1 retro-propagates the path of the input beam of laser 2, and vice versa. As mentioned earlier, the polarization states of the light propagating fiber 2 only are analyzed. In order to analyze the phase conjugate beam without disturbing the incoming laser beam, a one-half inch uncoated beam splitter with reflectivity of 4% is used. The polarization states of the conjugate beam are measured at 3° with respect to the normal of the linear polarizer positioned just after the laser. This angle is chosen because at 3° the power reflectivity of the "s" polarization component of light is the same as that of the "p" polarization component of light. Below are illustrations of the geometry and the BaTiO_3 crystal.

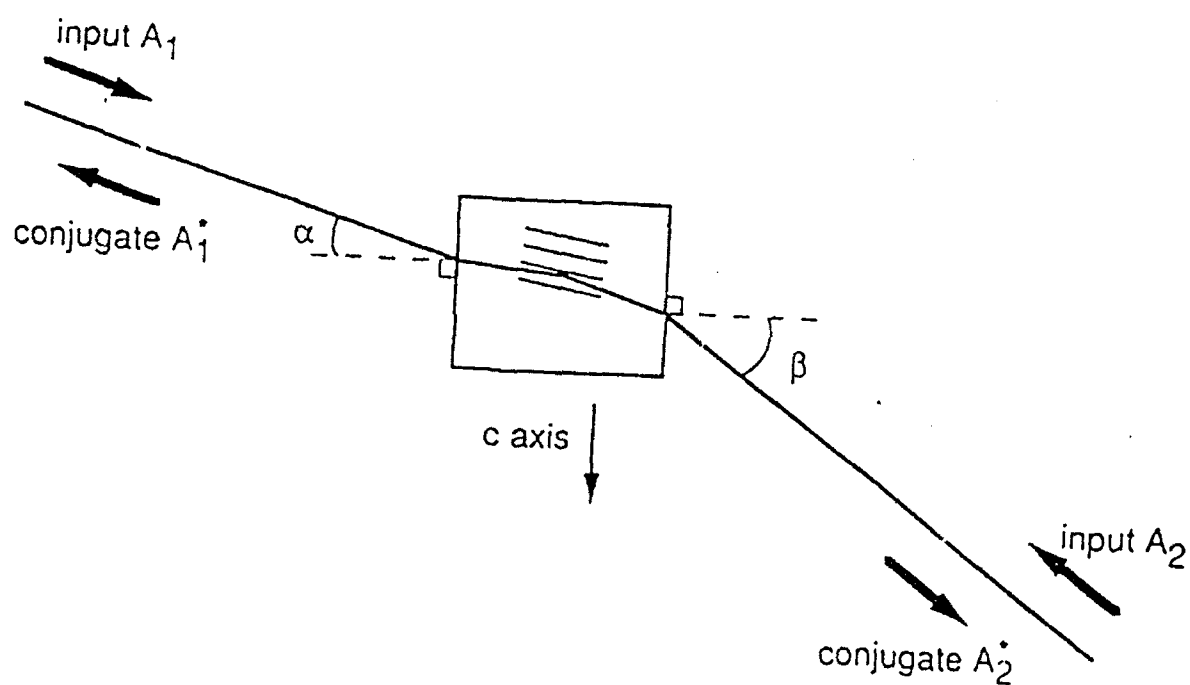
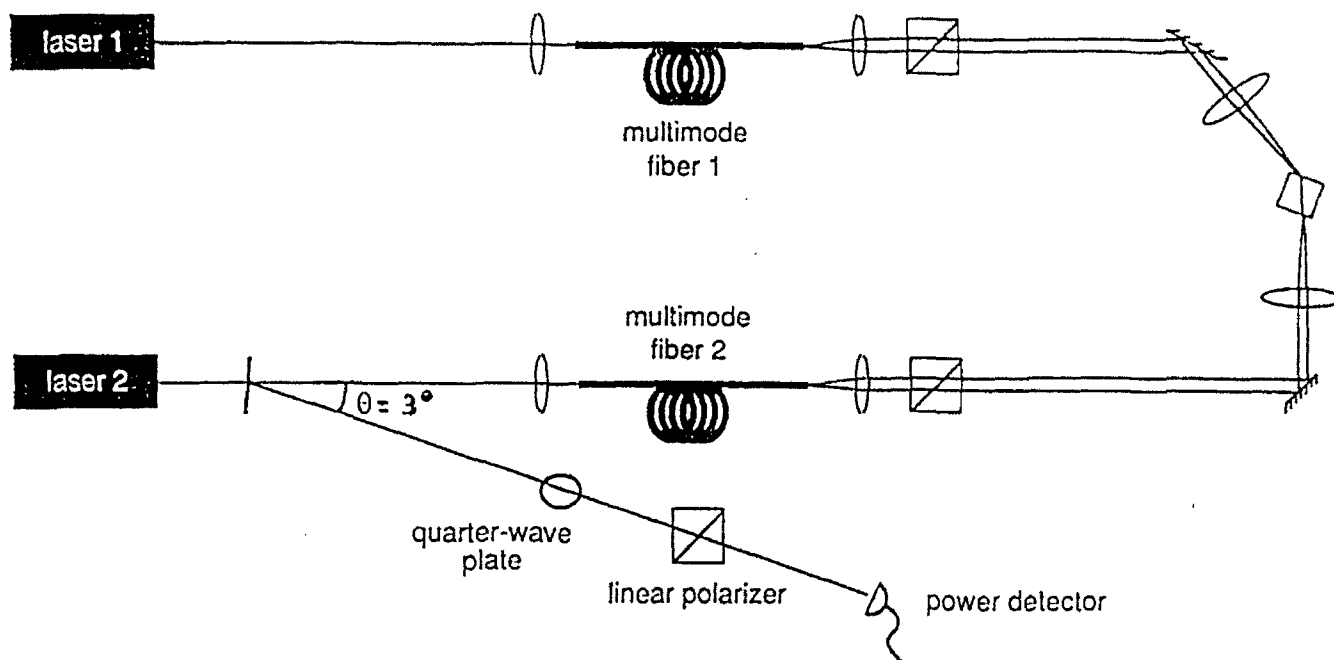


Fig. 1. Double phase-conjugate mirror geometry.

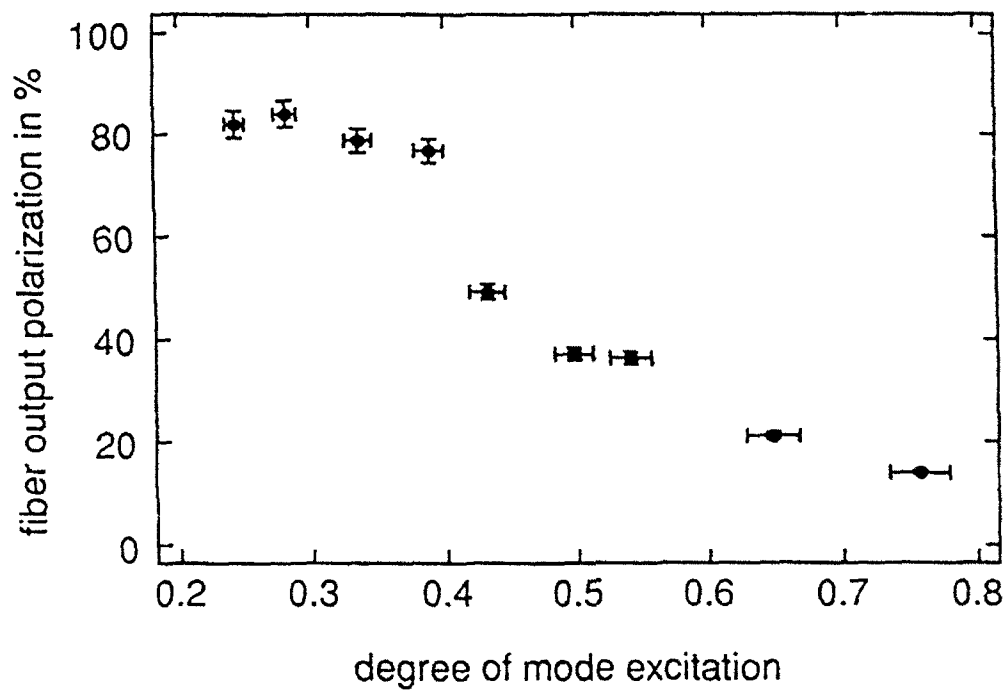
The numerical apertures of the two fiber outputs are kept equal and varied nine times by a mechanical mode scrambler that "crimps" down on the fiber, causing the excitation of higher order modes. The polarization states of the fiber output light and its conjugate beam are determined each time the numerical aperture is changed. Polarization measurements are obtained by determining the Stoke's Parameters^{7,8,9}. This was done with the use of a linear polarizer mounted to rotate at various angles, a quarter-wave plate, and a power detector.

The Stoke's Parameters are obtained by making seven measurements of power detected through a filter that passes (1) horizontally polarized light only - I₁; (2) vertically polarized light only - I₂; (3) linearly polarized light at +45° only - I₃; (4) linearly polarized light at -45° only - I₄; (5) right hand circularly polarized light only - I₅; (6) left hand circularly polarized light only - I₆; and (7) all polarization states equally and reduced by the Fresnel losses - I₇.

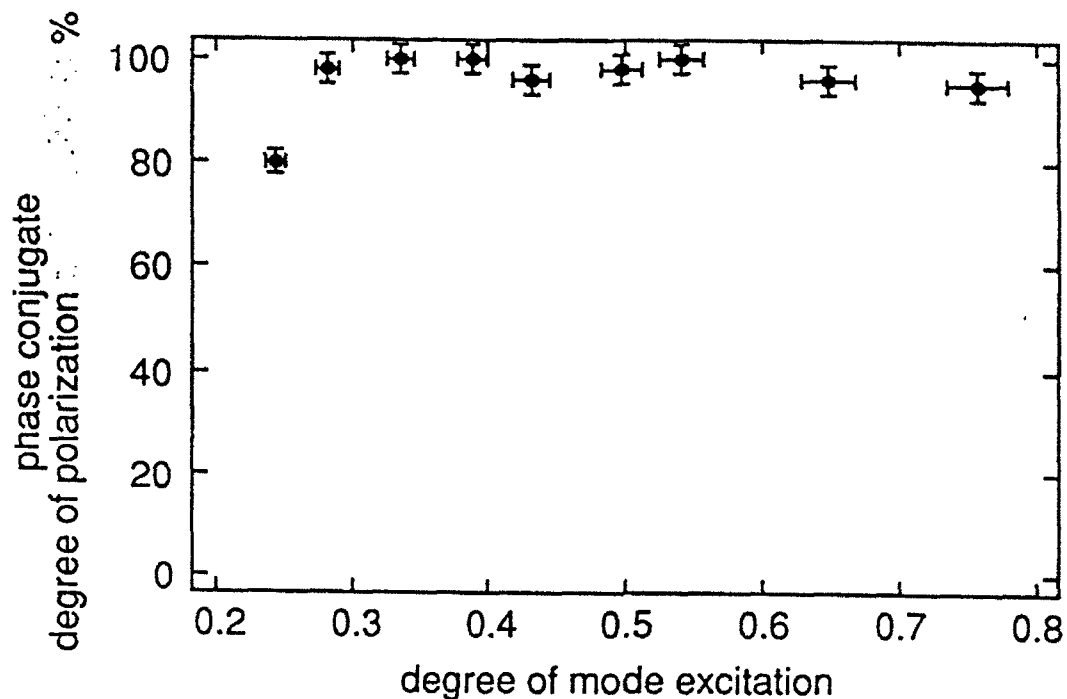
Stoke's Parameters consist of four numbers: S_t = the incident power corrected for Fresnel losses = I₇; S₁ = the degree of polarization with respect to the horizontal and vertical axes = I₁ - I₂; S₂ = the degree of plane polarization with respect to the ±45° axes = I₃ - I₄; and S₃ = the degree of circular polarization = I₅ - I₆. These four numbers can be used to obtain the polarized fraction of light, $S_p = \text{SQRT}(S_1^2 + S_2^2 + S_3^2) / S_t$.

RESULTS OF MEASUREMENTS:

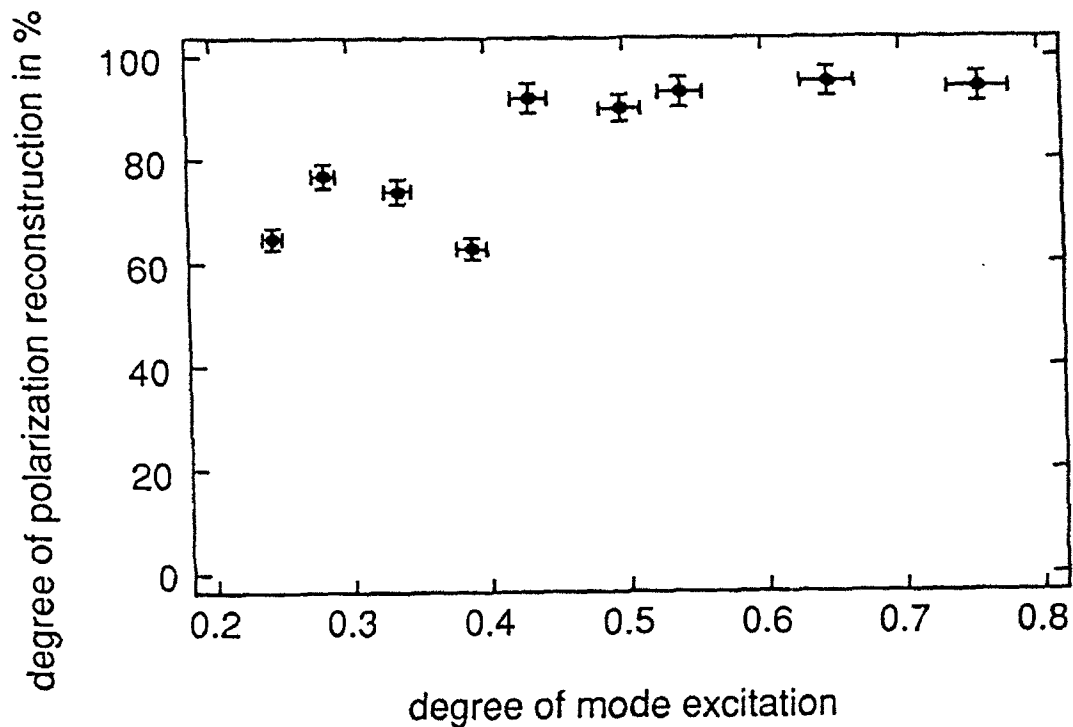
The following plots are obtained from the measurements in this report. The dependence of the polarization on the degree of mode excitation is shown for both the fiber output light and the phase conjugate light. Also, the coupling efficiency as a function of mode excitation is given.



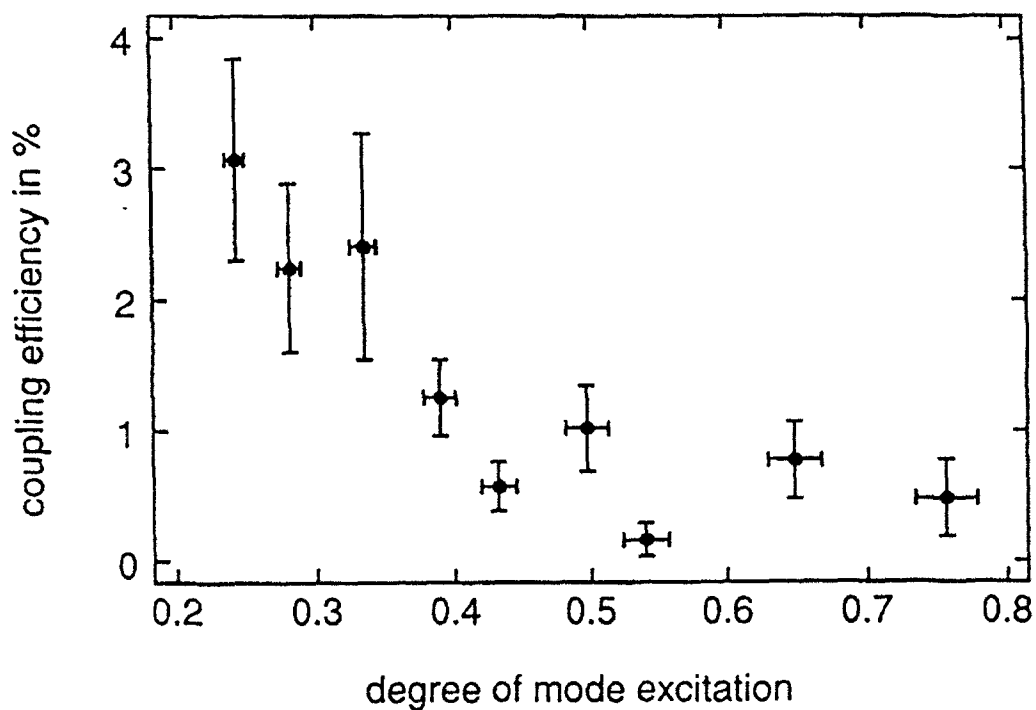
Above is a plot of the degree of the fiber output polarization as a function of the normalized degree of mode excitation. The data points include error bars to indicate ± 3 percent error in recording these data. The output-beam polarization degrades as the higher-order modes are excited. When the . 25% of the modes are excited the output-beam is 80% polarized and falls off to about 15% polarized as the modes are excited to 75%.



Above is a plot of the degree of polarization of the phase conjugate as a function of normalized mode excitation. The degree of polarization of the phase conjugate beam remains stable in the neighborhood of 80 to 100% as the degree of mode excitation is increased. Again, ± 3 percent error is indicated by the error bars.



Above is a plot of the degree of polarization reconstruction as a function of the normalized degree of mode excitation. The degree of polarization reconstruction is the power ratio of the horizontally polarized light of the conjugate beam to the horizontally polarized laser output-light injected into the fiber. For fiber modes excited by more than .43%, the degree of polarization reconstruction is essentially constant around 90%. The error bars indicate $\pm 3\%$ error.



Above is a plot of the degree of coupling efficiency as a function of the normalized degree of mode excitation. The coupling efficiency is the ratio of the power of the conjugate beam to the output power of the laser. In this plot, the error bars represent maximum and minimum values that were recorded because of time fluctuations of the data. The coupling efficiency is degraded as the degree of mode excitation is increased. As the higher-order modes are excited, the intensity of the phase conjugate beam degrades.

CONCLUSION

In conclusion, we have experimentally shown that the fidelity of the fiber output-beam's polarization degrades as the higher-order modes are excited. Polarization can be recovered using the double fiber-coupled phase conjugate mirror. This permits numerous applications involving sensors, multichannel switching, and polarization sensitive experiments.

Perhaps the next step in this topic would be to perform the same measurements in the other fiber-output and conjugate beams. Intuitively, we expect to obtain similar measurements and dependencies. Also, it would be interesting to perform the same analysis by increasing the fiber lengths rather than mechanically exciting the higher-order modes. A comparison of the two results would give some idea as to the appropriateness of the use mode scrambling devices in this experiment. This is of interest because of the possibility of the mode scrambling device producing invalid data due to stress-induced birefringence of the optical fibers.

REFERENCES

1. A. Yariv, Applied Physics Letters 51, 88 (1976).
2. B. Fischer and Shmuel Sternklar, Applied Physics Letters 46, 113 (1985).
3. K. Kyuma and A. Yariv, Applied Physics Letters 49, 11 (1986).
4. M. Gruneisen, S. Chakmakjian, and E. Seeberger, Presented at the Nonlinear Optics Conference in Maui, Hawaii (Aug. 1992).
5. Y. Tomita, R. Yahalom, and A. Yariv, Optical Society of America, 12, 1017 (1987).
6. P. Gunter and J. Huignard, *Topics in Applied Physics: Photorefractive Materials and Their Applications I.*, 61 (Springer-Verlag, 1988), Chaps. 1-3.
7. W. McMaster, American Journal of Physics 22, 351 (1954).
8. L. Cohen, Bell Syst. Technical Journal 50, 23 (1971).
9. Cpt. K. Yakiel, Presented in Ph.D. Thesis Dissertation, Air Force Institute of Technology (1992).

THIS PAGE INTENTIONALLY LEFT BLANK

SIMULATION OF FLUID FLOW IN TWO DIMENSIONS USING A HEXAGONAL LATTICE GAS

**Francis H. Maurais
Graduate Student
Mathematical Sciences Department**

**Worcester Polytechnic Institute
100 Institute Road
Worcester, MA 01609**

**Final Report for:
AFOSR Summer Research Program
Phillips Laboratory**

**Sponsored by:
Air Force Office of Scientific Research
Bolling Air Force Base, Washington, D.C.**

August 1992

SIMULATION OF FLUID FLOW IN TWO DIMENSIONS USING A HEXAGONAL LATTICE GAS

**Francis H. Maurais
Graduate Student
Mathematical Sciences Department
Worcester Polytechnic Institute**

Abstract

A "lattice gas" or cellular automata model for simulating hydrodynamics in two dimensions is implemented. The lattice gas models consist of automata which propagate along a regular, two-dimensional lattice of sites and obey global rules for collisions, which are applied using only information "local" to a particular site. A hexagonal lattice, invariant under $\frac{\pi}{3}$ rotations, is required to insure isotropy. Thus, the hexagonal lattice gas macroscopically exhibits continuum properties of two-dimensional hydrodynamics. Test simulations are reported for a seven-bit model in which shear flow develops into vortices illustrating a Kelvin-Helmholtz instability.

SIMULATION OF FLUID FLOW IN TWO DIMENSIONS USING A HEXAGONAL LATTICE GAS

Francis H. Maurais

Introduction

In the last decade, cellular automata have been "rediscovered" in their application to hydrodynamics. In 1984, Wolfram extended his study of one-dimensional "elementary" cellular automata into two dimensions, observing in each case that cellular automata can be grouped into four classes, some of which produce complicated growth patterns [2, 3]. Immediate applications of such models were found in turbulent flows and other classical hydrodynamics, utilizing a specific type of cellular automata called "lattice gas models".

These models are simple in construction: automata¹ populate a regular lattice of sites and have a small, finite set of possible states—i.e. six velocities. As these automata propagate about the lattice, they obey a global set of collision rules. However, these rules are *applied* locally—that is, to update a particular lattice site at time t , one need only know the state of the site and its nearest neighboring sites (i.e. those which are one lattice bond away) at the previous time step $t - 1$. Thus, we have dynamical systems in which space and time are discrete where "lattice gas models" can be shown to simulate complex continuum behavior [3]—in this case, hydrodynamical phenomena.

Compared to finite difference methods, which implement floating point arithmetic and favor the most significant bits, and, as a result, become unstable over time, lattice gas models prove to be extremely stable by executing calculations with only small integers. Moreover, because updating the lattice requires knowledge of only a local neighborhood of sites, lattice gas models maintain an "exactly computable" structure naturally suited for massively parallel machines [1, 4], thereby greatly reducing computation time and facilitating large-scale simulations.

Methodology

The model presented here was initially based on the original hexagonal lattice gas model presented by Frisch et al. in 1986, referred to as the FHP-I model [5]. In its final form, however, the 7-bit model discussed here most closely resembles the FHP-III model.

The Lattice

Frisch, Hasslacher, and Pomeau have shown that lattice gas models utilizing a triangular lattice², invariant under $\frac{\pi}{3}$ rotations, insures a diagonal momentum flux tensor, while a square lattice cannot, being invariant only under $\frac{\pi}{2}$ rotations [1]. We have implemented our simulation model on a two-dimensional hexagonal lattice, represented in Figure 1.

¹ Each individual automaton is not equivalent to a single fluid particle or molecule.

² Alternatively speaking, a lattice of close-packed hexagons—hence the term, "Hexagonal Lattice Gas".

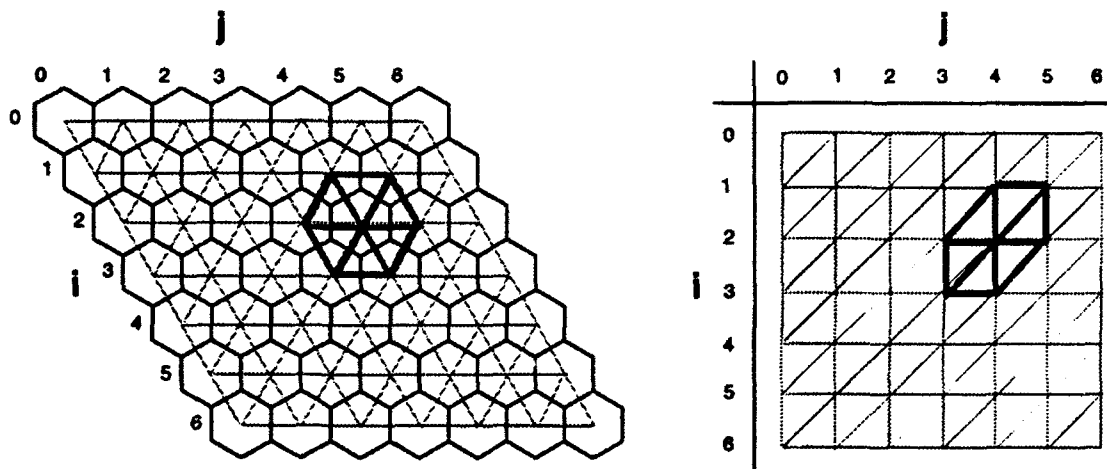


Figure 1: Site (2,4) with nearest neighbors

Here, we see a “skewed” hexagonal lattice superimposed on a square lattice, with a site bonded to its six nearest neighbors³. This provides for an isotropic flux tensor *and* allows for easy referencing to lattice sites, using an cartesian coordinate system. Only one automaton may occupy a lattice bond at a time: that is, at a particular site and time, only one automaton may arrive from each of the six directions.

Initially then, the configuration at a site S was encoded by a 6-bit word, with each bit representing a bond connected to S . A bit value of 1 would imply a bond was occupied—a automaton arriving at site S from the direction represented by the bit position—while a value of 0 would indicate no automaton arriving from that direction. In Figure 4 the direction assigned to each bit is given. After preliminary testing, it was suggested that a seventh bit, representing a possible “rest” automaton having velocity zero, would improve the model. Given an n -bit model, then, it is possible to find n automata present at each site—consequently, the number of possible site configurations is 2^n .

Boundary Conditions

Special rules are necessarily applied to all boundary points on the lattice as well as any obstacles present in the flow field. There are no obstacles in our present simulation, and periodic boundary conditions are applied. As automata propagate off one edge, they are wrapped around to the opposite edge, maintaining the same velocity (see Figure 3). Thus, the periodic boundary conditions map the two-dimensional hexagonal lattice onto a toral surface.

Lattice Updating

Once initial conditions are prescribed, the automata are set into motion. At each site of the lattice, collision rules are applied if possible, and automata are propagated (i.e. automata with non-zero velocities are moved one lattice link in their velocity direction). The result of each site update is written to temporary storage to negate possible “rippling effects” from occurring: in essence, automata are prevented

³All lattice bonds are assumed to be equal in length.


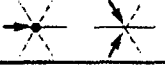


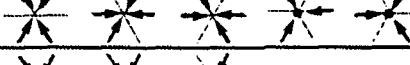
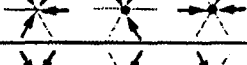

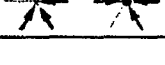
| N | Configurations | folds |
|---|---|-------|
| 2 |  | 1 |
| 2 |  | 6 |
| 3 |  | 1 |
| 3 |  | 6 |
| 4 |  | 1 |
| 4 |  | 6 |
| 5 |  | 1 |
| 5 |  | 6 |

Figure 2: Collision Rules for the model: Automata arriving at a site are represented by arrows while rest automata are centered black dots. N represents the number of automata involved in the collision, and "folds" is the number of equivalent collisions obtained by $\frac{\pi}{3}$ rotations for each configuration in the row. If a configuration in the table is encountered, it is replaced by one of the "legal exchanges" located on the same row.

from influencing more than one site per iteration. Collision Rules are applied from a look-up table of legal collision-producing configurations, illustrated in Figure 2 (also see [6], p. 304). For the intended 6-bit model, only row 1 and a portion of row 3 contained legal collision-producing configurations, as rest automata were not allowed. The entire table represents all collision rules for the 7-bit model.

This updating process continues over the number of iterations required. Collision rules are constructed to conserve both automata number and momentum. However, in order to simulate large scale hydrodynamics, the models must avoid any "spurious" conservation laws [5]. Triple collisions (in Figure 2, the first two configurations of row 3) do remove such spurious conservations, although not as effectively as do rest automata. Collisions for the the 7-bit model are the maximum set of rules to preserve mass and momentum while removing spurious conservations. Collision rules are both deterministic and non-deterministic: deterministic rules assign a particular input configuration in a row only one choice of output (Figure 2, rows 2 and 8), while non-deterministic rules randomly choose an outcome from the other configurations listed in the same row with all choices equiprobable.

Continuum Behavior

As mentioned earlier, individual lattice gas automaton should not be thought of as single fluid particles. Physical fluids, too, are composed of discrete particles, but on a large scale, exhibit the continuous flow described by hydrodynamical differential equations [7]. In a sense, one must step back from the lattice to observe the model's general flow patterns rather than the movements of individual automata.

To achieve this distancing, large lattices must first be implemented (on the order of 10^6 sites and sub-

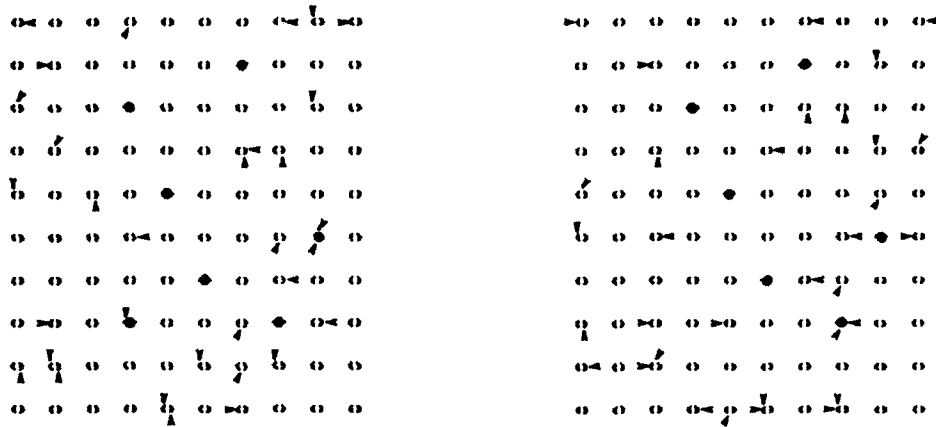


Figure 3: Lattice configurations at respective times t and $t + 1$: Both moving (arrows) and rest (dots) automata from time t are subjected to collision rules and propagation, which results in the lattice configuration at time $t + 1$. Notice the effects of the "periodic boundary conditions" on automata located on the lattice's outer edges.

sequently larger numbers of automata). Next, the lattice is subdivided into regions, from which averages of momentum⁴ are extracted from the automata present. In this model, the lattice is divided into smaller squares with sides having length (termed the "scale factor") determined by the user at run-time.⁵ As an example, for a lattice containing 1200×1200 sites, a scale factor of 8 would imply a resulting output image size of 150×150 . In other words, the lattice is divided into regions of size 8×8 sites, with all automata in each region contributing its momentum to a single, average momentum vector. After this single momentum vector is computed, each region is assigned a value and a corresponding color from the colorwheel, depicted in Figure 4. This value encodes the average flow direction over each region. In this manner, we are able to take miniaturized "snapshots" of the lattice at regular intervals to view the continuum behavior over the entire simulation time.

Results

Coding and small-scale testing were performed concurrently in developing a working model for the Hexagonal Lattice Gas. Recently, tests have been done here to locate the model's accuracy in simulating large-scale hydrodynamics. As an initial example, conditions were imposed to develop vortices formed from a Kelvin-Helmholtz Instability [8]. A sinusoidal flow is injected into an opposing flow field at time $t = 0$, and vortices develop as the flow becomes turbulent. Figure 5 depicts a time sequence of frames for this instability.

⁴Because we assume automata have unit mass, momentum and velocity are interchangeable here.

⁵In multiple tests, lattice sizes of at least 1200×1200 and scale factors of 8 or 10 were found to produce the best results.

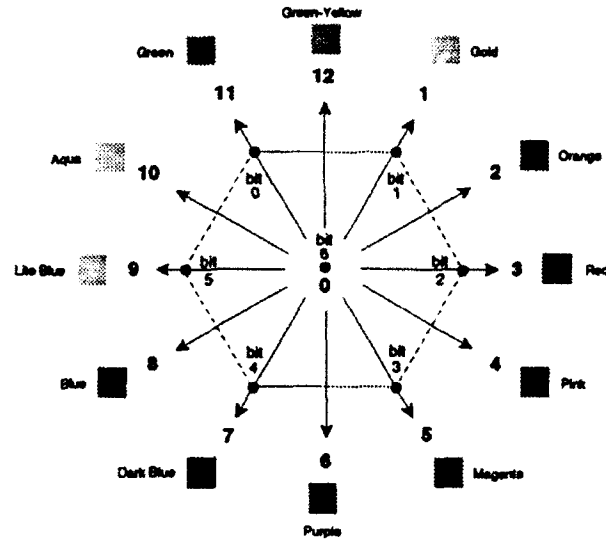


Figure 4: Colorwheel of flow directions: a region's average momentum vector is assigned one of twelve directions and colors for final output. "Bit" numbers indicate positions for possible automata arrivals on the hexagon, which are listed in Appendix B.

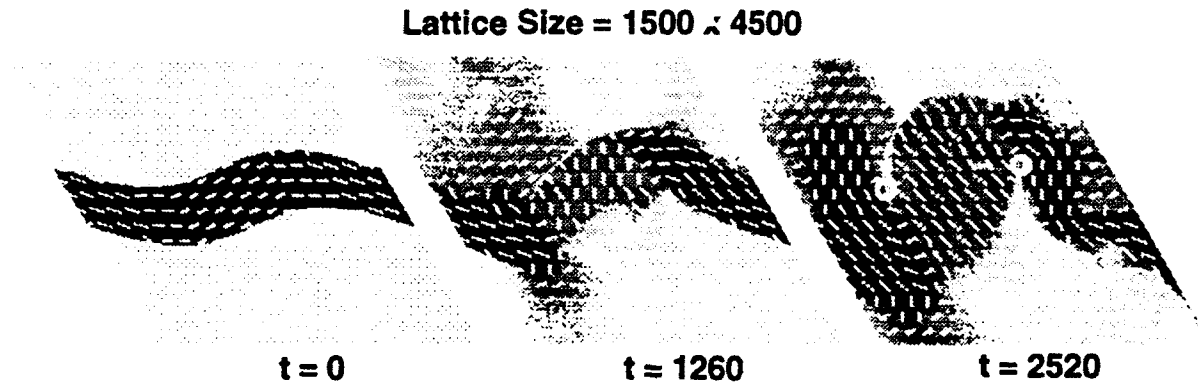


Figure 5: Time Lapse for the Kelvin-Helmholtz instability: t gives the iteration number for this simulation done on a skewed 1500×4500 lattice (6.75 million sites) with 13.5 million automata. Output was averaged into a 150×450 cell image, whose central-third portion was extracted for each iteration depicted. Here, a sinusoidal flow towards the right is injected into an opposing flow field at time $t = 0$, with vortices (indicated by white circles) forming after approximately 2500 iterations. White contour lines are superimposed as a visual aid for flow directions.

Conclusions

Some evidence is provided that discrete automata-based models may be implemented to simulate continuous systems such as hydrodynamics. To substantiate this further, test simulations done here must be analyzed and compared to data extracted from classical hydrodynamic phenomena (i.e. a Kelvin-Helmholtz instability). Furthermore, as typical speeds for present simulations were only on the order of 68,000 updates per second (33 seconds per iteration on a 1500×1500 lattice), subsequent computer simulations should be executed on parallel machines.

Code was written and tested on a NeXTstation Turbo located in the Simulation Laboratory of Phillips Laboratory's Atmospheric Structures Branch at Hanscom AFB (PL/GP). Special thanks are offered to Jeff Yepez and Don Grantham for their guidance throughout the summer.

Appendix A. Source Code—Hexagonal Lattice Gas

```
// FILE:      hlgs.h (header file for source file "hlgs.c")
#define PI      3.14159
#define BIT_SIZE  7
#define CONFIG_NUM  128
#define LOOP( N )  for ( i = 0 ; i < N ; i++ ) for ( j = 0 ; j < N ; j++ )
#define GETRAND    ( ( float ) rand ( ) / RAND_MAX )
#define NEWLINE    printf ( "\n" )
#define $_f        [ ( ( LATTICE_SIZE ) / Radius ) * i ) + j ]
#define $          [ i ] [ j ]
#define $_( x , y ) [ x ] [ y ]
#define UPPERLEFT  [ IM[ i ] ] [ j ]
#define UPPERRIGHT [ IM[ i ] ] [ IP[ j ] ]
#define RIGHT      [ i ] [ IP[ j ] ]
#define LOWERRIGHT [ IP[ i ] ] [ j ]
#define LOWERLEFT  [ IP[ i ] ] [ IM[ j ] ]
#define LEFT       [ i ] [ IM[ j ] ]
#define deg15      0.262
#define deg45      0.785
#define deg75      1.309      // in radians
#define deg105     1.833
#define deg145     2.356
#define deg175     2.880

// FILE:      hlgs.c
// FUNCTION:   implementation of hexagonal lattice gas cellular automaton to
//             approach to the Kelvin-Helmholtz instability
// DATE:      11 June 92 - 10 August 92
#include <stdio.h>
#include <stdlib.h>
#include <math.h>
#include <time.h>
#include "hlgs.h"
#define LATTICE_SIZE 1500

int      i , j , c , Radius , IP [ LATTICE_SIZE ] , IM [ LATTICE_SIZE ] ;
int      n_non_collisions=0, b2=0 , b3=0 , b4=0 , b5=0 , ca = 0;
unsigned char  S [ LATTICE_SIZE ][ LATTICE_SIZE ] , SNEXT [ LATTICE_SIZE ][ LATTICE_SIZE ] ,
               *F , site [ BIT_SIZE ] , *neighbor [ BIT_SIZE ] ;

void set_periodic_boundary_conditions ( )
{
    for ( i=0 ; i < LATTICE_SIZE ; i++ )
    {
        IP[ i ] = i +1 ;
        IM[ i ] = i -1 ;      // for applying periodic boundary conditions
    }
    IP [ LATTICE_SIZE -1 ] = 0 ;
    IM [ 0 ] = LATTICE_SIZE -1 ;
}

void set_initial_conditions ( )
{
    float      amp = (LATTICE_SIZE /15) , off1 , off2 , lamda = LATTICE_SIZE ;
    float      bound1 , bound2 , val ;

    off1 = (LATTICE_SIZE / 2 ) - (LATTICE_SIZE/15) ;
    off2 = (LATTICE_SIZE / 2 ) + (LATTICE_SIZE/15) ;
    LOOP ( LATTICE_SIZE )
    {
        bound1 = amp * sin ( 2 * PI * j / lamda ) + off1 ;
```

```

bound2 = amp * sin ( 2 * PI * j / lamda ) + off2 ;
val = fabs ( cos ( ( 2 * PI * ( j ) ) / lamda ) ) ;
if ( ( i >= bound1 ) && ( i <= bound2 ) )
    switch( 4 * j / LATTICE_SIZE )
    {
        case 0:
            if ( GETRAND < val )
                S $ = 33 ;      // pink
            else
                S $ = 96 ;      // red
            break ;
        case 1:
            if ( GETRAND > val )
                S $ = 96 ;      // red
            else
                S $ = 48 ;      // orange
            break ;
        case 2:
            if ( GETRAND < val )
                S $ = 48 ;      // orange
            else
                S $ = 96 ;      // red
            break ;
        case 3:
            if ( GETRAND > val )
                S $ = 96 ;      // red
            else
                S $ = 33 ;      // pink
            break ;
    }
    else
        S $ = 68 ;    // light blue
}
}

void reset_lattice ( )
{
    LOOP ( LATTICE_SIZE )
    {
        S $= SNEXT $;      // temporary storage in updating
        SNEXT $= 0 ;
    }
}

void set_neighbors ( )
{
    neighbor[ 0 ] = &SNEXT UPPERLEFT ;
    neighbor[ 1 ] = &SNEXT UPPERRIGHT ;
    neighbor[ 2 ] = &SNEXT RIGHT ;
    neighbor[ 3 ] = &SNEXT LOWERRIGHT ;
    neighbor[ 4 ] = &SNEXT LOWERLEFT ;
    neighbor[ 5 ] = &SNEXT LEFT ;
    neighbor[ 6 ] = &SNEXT $ ;
}

void set_site ( int i , int j )
{
    site[ 0 ] = S $ & 8 ;
    site[ 1 ] = S $ & 16 ;
    site[ 2 ] = S $ & 32 ;
    site[ 3 ] = S $ & 1 ;
    site[ 4 ] = S $ & 2 ;
    site[ 5 ] = S $ & 4 ;
    site[ 6 ] = S $ & 64 ;
}

```

// neighbor[] gets the addresses of the
// neighboring sites

// extracts "bit" information from sites


```

}

void propagate ( )
{
    set_neighbors ( ) ;
    set_site ( i , j ) ;
    for ( c = 0 ; c < BIT_SIZE ; c++ )
        *neighbor[ c ] += site [ c ] ;
}

void choose2 ( unsigned char *config , unsigned char a , unsigned char b , unsigned char c )
{
    if ( *config == a )
        switch ( (int) (GETRAND * 2) )
        {
            case 0 :      *config = c ;      break ;
            case 1 :      *config = b ;      break ;
        }
    else if ( *config == b )
        switch ( (int) (GETRAND * 2) )
        {
            case 0 :      *config = a ;      break ;      // chooses a random outcome from 2 alternatives
            case 1 :      *config = c ;      break ;
        }
    else
        switch ( (int) (GETRAND * 2) )
        {
            case 0 :      *config = b ;      break ;
            case 1 :      *config = a ;      break ;
        }
}

void choose4 ( unsigned char *config , unsigned char a , unsigned char b , unsigned char c ,
              unsigned char d , unsigned char e )
{
    if ( *config == a )
        switch ( (int) (GETRAND * 4) )
        {
            case 0 :      *config = b ;      break ;
            case 1 :      *config = c ;      break ;
            case 2 :      *config = d ;      break ;
            case 3 :      *config = e ;      break ;
        }
    else if ( *config == b )
        switch ( (int) (GETRAND * 4) )
        {
            case 0 :      *config = c ;      break ;
            case 1 :      *config = d ;      break ;
            case 2 :      *config = e ;      break ;
            case 3 :      *config = a ;      break ;
        }
    else if ( *config == c )
        switch ( (int) (GETRAND * 4) )
        {
            case 0 :      *config = d ;      break ;
            case 1 :      *config = e ;      break ;      // chooses a random outcome from 4 alternatives
            case 2 :      *config = a ;      break ;
            case 3 :      *config = b ;      break ;
        }
    else if ( *config == d )
        switch ( (int) (GETRAND * 4) )
        {
            case 0 :      *config = e ;      break ;
            case 1 :      *config = a ;      break ;
        }
}

```

```

        case 2 :      *config = b ;      break ;
        case 3 :      *config = c ;      break ;
    }
else
    switch ( (int) (GETRAND * 4) )
    {
        case 0 :      *config = a ;      break ;
        case 1 :      *config = b ;      break ;
        case 2 :      *config = c ;      break ;
        case 3 :      *config = d ;      break ;
    }
}

void update_lattice ( )
{
    switch ( S % )
    {
        case 9 :
        case 18 :
        case 36 : choose3 ( &S % , 9 , 18 , 36 ) ; b2++ ; break ;          // 2-body collisions

        case 5 :      S % = 66 ;      b2++ ;      break ;
        case 10 :     S % = 68 ;      b2++ ;      break ;
        case 17 :     S % = 96 ;      b2++ ;      break ;
        case 20 :     S % = 72 ;      b2++ ;      break ;
        case 34 :     S % = 65 ;      b2++ ;      break ;
        case 40 :     S % = 80 ;      b2++ ;      break ;
        case 65 :     S % = 34 ;      b2++ ;      break ;          // 2-body collisions with rest particle
        case 66 :     S % = 5 ;      b2++ ;      break ;
        case 68 :     S % = 10 ;     b2++ ;      break ;
        case 72 :     S % = 20 ;     b2++ ;      break ;
        case 80 :     S % = 40 ;     b2++ ;      break ;
        case 96 :     S % = 17 ;     b2++ ;      break ;

        case 21 :
        case 42 :          // 3-body collisions possibly with a rest particle
        case 73 :
        case 82 :
        case 100 : choose5 ( &S % , 21 , 42 , 73 , 82 , 100 ) ;      b3++ ;      break ;

        case 85 :
        case 106 :         // 4-body collisions possibly with a rest particle
        case 27 :
        case 45 :
        case 54 : choose5 ( &S % , 85 , 106 , 27 , 45 , 54 ) ;      b4++ ;      break ;

        case 11 :
        case 38 :
        case 69 : choose3 ( &S % , 11 , 38 , 69 ) ;      b3++ ;      break ;
        case 13 :
        case 22 :
        case 74 : choose3 ( &S % , 13 , 22 , 74 ) ;      b3++ ;      break ;
        case 19 :
        case 37 :
        case 98 : choose3 ( &S % , 19 , 37 , 98 ) ;      b3++ ;      break ;
        case 25 :          // 3-body collisions with a "spectator" or rest particle
        case 52 :
        case 104 : choose3 ( &S % , 25 , 52 , 104 ) ;      b3++ ;      break ;
        case 26 :
        case 44 :
        case 84 : choose3 ( &S % , 26 , 44 , 84 ) ;      b3++ ;      break ;
        case 41 :
        case 50 :
        case 81 : choose3 ( &S % , 41 , 50 , 81 ) ;      b3++ ;      break ;
    }
}

```

```

case 23 :
case 75 :
case 102 : choose3 (&S $ , 23 , 75 , 102 ) ; b4++ ; break ;
case 29 :
case 90 :
case 108 : choose3 (&S $ , 29 , 90 , 108 ) ; b4++ ; break ;
case 43 :
case 83 :
case 101 : choose3 (&S $ , 43 , 83 , 101 ) ; b4++ ; break ;
case 46 : // 4-body collisions with a "spectator" or rest particle
case 77 :
case 86 : choose3 (&S $ , 46 , 77 , 86 ) ; b4++ ; break ;
case 53 :
case 105 :
case 114 : choose3 (&S $ , 53 , 105 , 114 ) ; b4++ ; break ;
case 58 :
case 89 :
case 116 : choose3 (&S $ , 58 , 89 , 116 ) ; b4++ ; break ;

case 91 :
case 109 :
case 118 : choose3 ( &S $ , 91 , 109 , 118 ) ; b5++ ; break ; // 5-body collisions

case 31 : S $ = 110 ; b5++ ; break ;
case 47 : S $ = 87 ; b5++ ; break ;
case 55 : S $ = 107 ; b5++ ; break ;
case 59 : S $ = 117 ; b5++ ; break ;
case 61 : S $ = 122 ; b5++ ; break ;
case 62 : S $ = 93 ; b5++ ; break ; // 5-body collisions with a
case 87 : S $ = 47 ; b5++ ; break ; // "spectator" or rest particle
case 93 : S $ = 62 ; b5++ ; break ;
case 107 : S $ = 55 ; b5++ ; break ;
case 110 : S $ = 31 ; b5++ ; break ;
case 117 : S $ = 59 ; b5++ ; break ;
case 122 : S $ = 61 ; b5++ ; break ;

default : n_non_collisions++ ; break ;
}
propagate ( ) ;
}

unsigned char choose_bin ( float angle )
{
if ( angle >= 0.0 )
if ( angle >= deg105 )
if ( angle >= deg145 )
if ( angle >= deg175 )
return 9 ;
else return 10 ;
else return 11 ;
else if ( angle >= deg15 )
if ( angle >= deg45 )
if ( angle >= deg75 )
return 12 ;
else return 1 ;
else return 2 ;
else return 3 ;
else // chooses which direction (color) a region is assigned
if ( angle <= -deg105 )
if ( angle <= -deg145 )
if ( angle <= -deg175 )
return 9 ;
else return 8 ;

```

```

        else return 7 ;
    else if ( angle <= -deg15 )
        if ( angle <= -deg45 )
            if ( angle <= -deg75 )
                return 6 ;
            else return 5 ;
        else return 4 ;
    else return 3 ;
}

void get_component ( unsigned char ch , float *xcomp , float *ycomp )
{
    float          x = 0 , y = 0 ;

    switch ( ch )
    {
        case 0 :   x = 0.0 ;   y = 0.0 ;   break ;
        case 1 :   x = 0.5 ;   y = -0.86602 ; break ;
        case 2 :   x = -0.5 ;   y = -0.86602 ; break ;      // breaks down particle velocities
        case 4 :   x = -1.0 ;   y = 0.0 ;   break ;          // into "x" and "y" components
        case 8 :   x = -0.5 ;   y = 0.86602 ; break ;
        case 16 :  x = 0.5 ;    y = 0.86602 ; break ;
        case 32 :  x = 1.0 ;    y = 0.0 ;   break ;

        default :  x = 0.0 ;    y = 0.0 ;

    }
    *xcomp += x ;
    *ycomp += y ;
}

unsigned char get_momvector ( )
{
    int          iloop , jloop , ifront , jfront , ii , jj ;
    float        xcomp = 0 , ycomp = 0 ;

    ii = i * Radius ;          // divides lattice into subregions
    jj = j * Radius ;          // and computes average momenta
    ifront = ii + Radius ;
    jfront = jj + Radius ;
    for ( iloop = ii ; iloop <= ifront ; iloop++ )
        for ( jloop = jj ; jloop <= jfront ; jloop++ )
        {
            set_site ( iloop , jloop ) ;
            for ( c = 0 ; c < BIT_SIZE - 1 ; c++ )
                get_component ( site[ c ] , &xcomp , &ycomp ) ;
        }
    if ( xcomp == 0 )
    {
        if ( ycomp == 0 )
            return 0 ;
        else if ( ycomp > 0 )
            return 12 ;
        else
            return 6 ;
    }
    else
        return (choose_bin ( atan2 ( ycomp , xcomp ) ) ) ;
}

void main ( int argc , char** argv )
{
    FILE          *out_stream ;
    char          outfile [ 30 ] ;
    int           images , t , total_iterations , frequency, N = LATTICE_SIZE * LATTICE_SIZE;

```

```

if ( argc < 4 )
{
    printf ( "usage: hlgs (iterations) (output frequency) (Radius)\n" );
    exit ( 0 );
}
total_iterations = atoi ( argv [ 1 ] );
frequency = atoi ( argv [ 2 ] );          // processes command line info
Radius = atoi ( argv [ 3 ] );
images = ( total_iterations / frequency ) + 1 ;
sprintf ( outfile, "my%d-%s.%d", LATTICE_SIZE, argv[1], images );
if ( ( out_stream = fopen ( outfile, "wb" ) ) == NULL )
{
    fprintf ( stderr, "ERROR: Can't open output file: %s\n", outfile );
    exit ( 1 );
}
F = (unsigned char *)calloc(((LATTICE_SIZE) / Radius)*((LATTICE_SIZE) / Radius),
sizeof ( char ) );
if ( F == NULL )
{
    printf ( "ERROR: Memory Allocation \n" );
    exit ( 1 );
}
srand ( ( unsigned int ) time (NULL) ) ;      // seeds random number generator
set_periodic_boundary_conditions ( ) ;
set_configuration_table ( ) ;
set_initial_conditions ( ) ;
LOOP ( ( LATTICE_SIZE ) / Radius )             // writes S to out_stream F
    F $_f = get_momvector ( ) ;
fwrite ( F, ((LATTICE_SIZE) / Radius ) * ((LATTICE_SIZE) / Radius ) , 1 , out_stream ) ;
for ( t = 1 ; t <= total_iterations ; t++ )
{
    n_non_collisions = b2 = b3 = b4 = b5 = 0 ;
    LOOP ( LATTICE_SIZE )
        update_lattice ( ) ;
    reset_lattice ( ) ;                        // writes SNEXT to S + clears SNEXT
    if ( ( t % frequency ) == 0 )
    {
        LOOP ( ( LATTICE_SIZE ) / Radius )      // writes S to out_stream F
            F $_f = get_momvector ( ) ;
        fwrite ( F, ((LATTICE_SIZE) / Radius ) * ((LATTICE_SIZE) / Radius ) , 1 , out_stream ) ;
    }
}
fclose ( out_stream ) ;
}

```

Appendix B. HLG Site Configurations

The following tables list possible site configurations for the 7-bit Hexagonal Lattice Gas model. Positions on the hexagon are labeled with bits 0 through 6, beginning in the upper-left node of the hexagon and continuing clockwise, with the central "rest" position assigned bit 6 (see Figure 4). Automata arriving from a position set its bit value to 1. N gives the code number for each configuration—simply the decimal value of the bits (i.e. The code $N = 17$ represents bit-configuration 0010001, the binary representation of the decimal number 17.) Listed on the right is the configuration as it would appear on the lattice. A centered black dot indicates a rest automaton present.

| N | bit# 6543210 | site | N | bit# 6543210 | site | N | bit# 6543210 | site | N | bit# 6543210 | site |
|-----|-----------------|-----------|-----|-----------------|------------|-----|-----------------|------------|-----|-----------------|-------------|
| 0 | 0000000 | () | 16 | 0010000 | () / | 32 | 0100000 | -() | 48 | 0110000 | -() |
| 1 | 0000001 | () | 17 | 0010001 | () / | 33 | 0100001 | - () | 49 | 0110001 | - () |
| 2 | 0000010 | /() | 18 | 0010010 | /() / | 34 | 0100010 | -/() | 50 | 0110010 | -/() |
| 3 | 0000011 | / () | 19 | 0010011 | / () / | 35 | 0100011 | -/ () | 51 | 0110011 | -/ () |
| 4 | 0000100 | ()- | 20 | 0010100 | ()- / | 36 | 0100100 | -()- | 52 | 0110100 | -()- |
| 5 | 0000101 | ()- | 21 | 0010101 | ()- / | 37 | 0100101 | - ()- | 53 | 0110101 | - ()- |
| 6 | 0000110 | /()- | 22 | 0010110 | /()- / | 38 | 0100110 | -/()- | 54 | 0110110 | -/()- |
| 7 | 0000111 | / ()- | 23 | 0010111 | / ()- / | 39 | 0100111 | -/ ()- | 55 | 0110111 | -/ ()- |
| 8 | 0001000 | () | 24 | 0011000 | () / | 40 | 0101000 | -() | 56 | 0111000 | -() / |
| 9 | 0001001 | () | 25 | 0011001 | () / | 41 | 0101001 | - () | 57 | 0111001 | - () / |
| 10 | 0001010 | /() | 26 | 0011010 | /() / | 42 | 0101010 | -/() | 58 | 0111010 | -/() / |
| 11 | 0001011 | / () | 27 | 0011011 | / () / | 43 | 0101011 | -/ () | 59 | 0111011 | -/ () / |
| 12 | 0001100 | ()- | 28 | 0011100 | ()- / | 44 | 0101100 | -()- | 60 | 0111100 | -()- / |
| 13 | 0001101 | ()- | 29 | 0011101 | ()- / | 45 | 0101101 | - ()- | 61 | 0111101 | - ()- / |
| 14 | 0001110 | /()- | 30 | 0011110 | /()- / | 46 | 0101110 | -/()- | 62 | 0111110 | -/()- / |
| 15 | 0001111 | / ()- | 31 | 0011111 | / ()- / | 47 | 0101111 | -/ ()- | 63 | 0111111 | -/ ()- / |

| N | bit# 6543210 | site | N | bit# 6543210 | site | N | bit# 6543210 | site | N | bit# 6543210 | site |
|-------|-----------------|------|----|-----------------|------|-----|-----------------|------|-----|-----------------|------|
| <hr/> | | | | | | | | | | | |
| 64 | 1000000 | ● | 80 | 1010000 | ● | 96 | 1100000 | -● | 112 | 1110000 | -● |
| 65 | 1000001 | ● | 81 | 1010001 | ● | 97 | 1100001 | -● | 113 | 1110001 | -● |
| 66 | 1000010 | ● | 82 | 1010010 | ● | 98 | 1100010 | -● | 114 | 1110010 | -● |
| 67 | 1000011 | ● | 83 | 1010011 | ● | 99 | 1100011 | -● | 115 | 1110011 | -● |
| 68 | 1000100 | ●- | 84 | 1010100 | ●- | 100 | 1100100 | -●- | 116 | 1110100 | -●- |
| 69 | 1000101 | ●- | 85 | 1010101 | ●- | 101 | 1100101 | -●- | 117 | 1110101 | -●- |
| 70 | 1000110 | ●- | 86 | 1010110 | ●- | 102 | 1100110 | -●- | 118 | 1110110 | -●- |
| 71 | 1000111 | ●- | 87 | 1010111 | ●- | 103 | 1100111 | -●- | 119 | 1110111 | -●- |
| 72 | 1001000 | ● | 88 | 1011000 | ● | 104 | 1101000 | -● | 120 | 1111000 | -● |
| 73 | 1001001 | ● | 89 | 1011001 | ● | 105 | 1101001 | -● | 121 | 1111001 | -● |
| 74 | 1001010 | ● | 90 | 1011010 | ● | 106 | 1101010 | -● | 122 | 1111010 | -● |
| 75 | 1001011 | ● | 91 | 1011011 | ● | 107 | 1101011 | -● | 123 | 1111011 | -● |
| 76 | 1001100 | ●- | 92 | 1011100 | ●- | 108 | 1101100 | -●- | 124 | 1111100 | -●- |
| 77 | 1001101 | ●- | 93 | 1011101 | ●- | 109 | 1101101 | -●- | 125 | 1111101 | -●- |
| 78 | 1001110 | ●- | 94 | 1011110 | ●- | 110 | 1101110 | -●- | 126 | 1111110 | -●- |
| 79 | 1001111 | ●- | 95 | 1011111 | ●- | 111 | 1101111 | -●- | 127 | 1111111 | -●- |

References

- [1] U. Frisch, B. Hasslacher, and Y. Pomeau, "Lattice-gas automata for the Navier-Stokes equation", *Phys. Rev. Letts.* **56**, No. 14, (1986) 1505-1508.
- [2] S. Wolfram, "Statistical mechanics of cellular automata", *Rev. Mod. Phys.*, **55**, (1983) 601-644.
- [3] N. H. Packhard and S. Wolfram, "Two Dimensional Cellular Automata", *J. Stat. Phys.* **38**, Nos. 5/6, (1985) 901-946.
- [4] G. Vichniac, "Simulating Physics with Cellular Automata", *Physica* **10D**, (1984) 96-116.
- [5] U. Frisch, D. d'Humières, B. Hasslacher, P. Lallemand, Y. Pomeau, and J.P. Rivet, "Lattice Gas Hydrodynamics in Two and Three Dimensions", *Lattice Gas Methods for Partial Differential Equations*, G. Doolen, Ed. , (Redwood City, CA: Adison-Wesley, 1990) 75-135.
- [6] D. d'Humières and P. Lallemand, "Numerical Simulations of Hydrodynamics with Lattice Gas Automata in Two Dimensions", *Lattice Gas Methods for Partial Differential Equations*, G. Doolen, Ed. , (Redwood City, CA: Adison-Wesley, 1990) 299-332.
- [7] S. Wolfram, "Cellular Automata Fluids 1: Basic Theory", *Lattice Gas Methods for Partial Differential Equations*, G. Doolen, Ed. , (Redwood City, CA: Adison-Wesley, 1990) 19-73.
- [8] COLOR PLATES, *Lattice Gas Methods for Partial Differential Equations*, G. Doolen, Ed. , (Redwood City, CA: Adison-Wesley, 1990)

**PROGRESS ON THE WORKING FLUID EXPERIMENT:
FORMATION OF A PLASMA WORKING FLUID
FOR COMPRESSION BY LINER IMPLOSION**

**Jane Messerschmitt
Research Fellow
Weber Research Institute
Department of Electrical Engineering**

**Polytechnic University
333 Jay Street
Brooklyn, New York 11201**

**Final Report for :
AFOSR Summer Research Program
Phillips Laboratory**

**Sponsored by:
Air Force Office of Scientific Research
Kirtland Air Force Base, Albuquerque, New Mexico**

September, 1992

**PROGRESS ON THE WORKING FLUID EXPERIMENT:
FORMATION OF A PLASMA WORKING FLUID FOR
COMPRESSION BY LINER IMPLOSION**

Jane Messerschmitt
Research Fellow
Weber Research Institute
Department of Electrical Engineering
Polytechnic University

ABSTRACT

The working fluid experiment investigates various methods of forming a medium with the plasma parameters required for its use as a working fluid for concentric solid liner implosion. Such a working fluid would make quasi-spherical implosions possible with a cylindrical driver. A hydrogen filled coaxial plasma gun is discharged into a volume simulating a solid liner. Upgrades to the experiment including pressure diagnostics and the construction of a high energy capacitor bank are described.

INTRODUCTION

An experiment to develop a suitable intermediate compression media for use in concentric solid liner implosions is currently underway at the Phillips Laboratory High Energy Plasma Division. The solid liner is imploded radially by a discharge driven by the SHIVA STAR 10 MJ Capacitor Bank. A fluid inserted between the target and the solid liner as a compression media will permit a quasi-spherical implosion of the target. The compression media requirements are that it be dense, cool, uniform and long lived. The material sound speed is inversely proportional to the mass density. A dense, low molecular weight plasma prevents the formation of shock waves during implosion. This translates into experimental goals of electron density on the order of 10^{18} cm^{-3} and temperature of 1-2 eV. Low temperatures also minimize ablation of the walls and, therefore, energy-sapping impurities. The Working Fluid eXperiment (WFX) was designed to establish the most efficient methods of producing this plasma. Preliminary project goals were achieved with an upgraded design featuring a converging outer conductor and a vane structure. Additional diagnostics and a higher energy source were developed to advance the scheme.

EXPERIMENTAL SETUP

A prefill in the range 10-100 torr of hydrogen fills the evacuated plasma gun and payload volume simulating the liner volume. A surface discharge is initiated across a coaxial insulator with the gun using a 35 kJ capacitor bank discharge. The deposit of post-initiation energy to the arc causes it to lift onto the outer conductor and propagate down the gun. This current sheath pushes the hydrogen ahead of it along the cylindrical region. The tapered outer conductor compresses the plasma making it hotter and denser. The plasma is pushed through the vanes into the payload region. The vanes strip the embedded magnetic field from the plasma and provide a return path for the current. Present diagnostics are B-dot probes in various locations and optical techniques. An Optical Multichannel Analyzer (OMA) gives time resolved spectra for the visible emission from the plasma. The viewing fiber optics are placed

chordally in the payload. The electron density and electron temperature are measured from the H_β and H_γ spectral lines. An optical search for impurities indicate the system is clean. A Multichannel Plate (MCP) camera records the longitudinally integrated plasma luminosity at a given time. A Cordin high speed framing camera was used to photograph the payload volume in time increments to measure the evolution of the plasma. Uniformity information was obtained from the photographic data.

Various percentages of helium, argon and nitrogen were mixed with hydrogen to obtain further information using the OMA. The ion temperature could be determined from the spectral lines of the seed gas. The spectral lines of the seed gas were not measurable until its percentage was so high that it drained energy from the hydrogen. The method changed the experiment too dramatically to be useful.

PRESSURE DIAGNOSTICS

The neutral density of the plasma in the payload volume is calculated from the electron temperature and electron density using the Saha relation. An independent measurement of pressure is desired because that is an important parameter and would provide a check on the equilibrium conditions assumed by the Saha equation and provide information on pressure uniformity. Initial pressures of 100 bar are required. The first attempt to measure pressure was a probe made from a wafer of piezo-electric material mounted in a metallic tube. Integrated voltage signals were observed on an oscilloscope. Low impulse tests indicated a potential nonlinearity in the pressure-voltage characteristics. When tested with WFX, oscillations were observed and attributed to either harmonics generated in the mounting tube or plasma swirling motion upon entering the payload region.

An Endevco 2000 psi pressure transducer was tested for compatibility with WFX. The transducer uses solid state resistors that change value with applied stress. The resistors are in a Wheatstone bridge configuration and

produce a signal proportional to the applied pressure. Piezo-resistive transducers have a high output signal and low output impedance and intrinsic noise. It is, however, quite sensitive to external noise. Pulsed power circuits are prone to electrical noise due to the high fields during operation. Semiconductor devices are rarely used with pulsed power equipment because they are very sensitive to fields. To overcome this obstacle the transducer and its required hardware were encased in a metal enclosure. A feed-through is used for the output signal. Switches are a significant source of noise on pulsed power generators. The transducer was inserted on the payload of WFX and the bank triggers were activated. The noise test indicated that the transducer shielding was acceptable. WFX experiments indicate that exposure to the plasma produces noise impinged on the signal. A metallic film will coat the transducer surface to shield it from IR radiation. The semiconductor resistors in transducers react strongly to wavelengths in the infrared regime.

CURRENT DIAGNOSTICS

A material is said to be birefringent when the internal electric displacement vector, D , and the electric field vector, E , are not parallel. A consequence of this effect is that the direction of energy propagation and of phase advance are not necessarily parallel. This is usually quantified as a dielectric tensor with nonzero off-diagonal elements. The susceptibility tensor is determined by the spatial arrangement and the type of atoms in the unit cell and their effects on the dispersion electrons. External stresses can induce optical anisotropy in non-crystalline materials. Birefringence induced by a magnetic field is called the magneto optic or Faraday effect. The magnetic field, rather than the molecular structure, imparts the perturbation to the electron motion. The magnetic field causes a rotation per unit dielectric length of the plane of polarization of the incident light propagating along the field direction. The rotation is proportional to the field intensity.

If the incident light is plane polarized in a single direction, the angle of rotation can be measured relative to the incident polarization. Linear polarization can be considered as the sum of a right and a left hand circular polarization. The perturbation manifests in purely imaginary, complex conjugate off diagonal dielectric tensor elements in the directions orthogonal to propagation. One polarization is an eigenvector of the resulting dispersion matrix, and is unaffected by the anisotropy. The other polarization couples to the electron motion. The sum of the two circularly polarized waves is a linearly polarized wave which has been rotated through an angle proportional to the applied magnetic field and the sample length.

The most useful relation for angle of rotation measurements in solid dielectrics is:

$$d\frac{\theta}{dz} = VH$$

θ is the angle through which the polarization plane has rotated after passage through the media in the direction of H , the magnetic field intensity through a length, z . V is a constant of the medium called Verdet's constant.

The Faraday effect can be used as a current diagnostic. To produce the appreciable magnetic field necessary to induce the Faraday effect, the current density must be large. High current measurements can be difficult to obtain. Magneto optic current measurements have the advantage of being electrically non-intrusive to the plasma sheath and invariant to noise. The fiber optic cable is wound around a cylindrical support structure. The radius of curvature of the winds are large to reduce birefringence due to mechanical stress. A single mode fiber, Lightwave Technologies type F1506C, was used because of its low internal birefringence. A HeNe laser and a polarizer produce a single polarization light beam, which is directed into the fiber. The rotated output light is passed through another polarizer, oriented perpendicular to the first polarizer. The Faraday effect is sign invariant. The two polarizers provide a method of determining the direction of B . Since the two polarizers are crossed, a zero in the signal indicates either a 2π rotation or zero B .

A photodiode converts the light output to a voltage which is viewed on an oscilloscope.

THE 12 CAN BANK

It was experimentally determined, and confirmed by calculations, that the present capacitor bank did not supply sufficient driving force for WFX.

High current capacitor banks need to be carefully constructed to ensure safe, efficient energy delivery. Each of the twelve capacitors are $6\mu\text{f}$, 60kV and therefore capable of storing approximately $1/3$ coulomb. These high energy density capacitors are designed to withstand high reversal. Large reversals stress the capacitors severely because the dipoles comprising the dielectric must rotate completely to align with the field. Connection to the positive terminal is made through a bolt and a 'donut'. The bolt is torqued to 150 ft-lbs. The donut compresses a copper crush ring to the inner electrode. This assures a good current joint and compresses the donut to the dielectric that the probability of surface tracking is greatly reduced. The bank is supported by a Unistrut frame. Each capacitor weighs 275 pounds and the connection hardware another 500 pounds. Unistrut is strong, easy to assemble, and versatile. Feet were put on the bottom to aid in leveling the structure. A parallel plate transmission lines connect the capacitors to the switching elements and to WFX. Parallel plate transmission line adds a low inductance to the system while also making good current joints to the capacitors. The buss plates are $1/2$ " thick aluminum. Precautions against field enhancing sharp edges were taken:

- The plate and hole edges have a large radius.
- The screws are imbedded in the plate and their heads covered with conducting epoxy, then sanded level to plate.
- The plates were smoothed with fine grain sandpaper to eliminate scratches.

Mylar sheets are used for the dielectric between the transmission line plates. Sheets provide protection from punch-through. Solid dielectrics contain minuscule pockets of air, called voids. In a void, the electric field is higher and the breakdown strength is lower than in the bulk dielectric. In highly stressed dielectrics, this situation will promote breakdown in the void, referred to as punch-through. Layers of dielectric reduce the risk of finding a void longer than one sheet thickness. The mylar sheets are cut for the transmission line dimensions plus one foot around. The additional dielectric guards against surface tracking between the plates. The mylar is carefully cut to avoid crinkles or marks which would make the dielectric thickness even slightly nonuniform.

The capacitors are discharged in parallel simultaneously with a four railgap switch element. Railgap switches provide good multichannelling, which is critical for high current switching because it distributes the coulomb transfer and current among the channels, preventing destructive shock waves and excessive electrode erosion. The railgap elements have a plastic tongue that extends under the hot buss plate to retard surface tracking. The railgap electrodes are charged to $\pm 40\text{kV}$. Switching is activated by applying a high voltage pulse to the rail. Typical pulse voltages are 50kV . The rail crosssection is triangular and spaced asymmetrically in the interelectrode gap. During charging, the electric field is uniform. The trigger pulse distorts the uniformity of the fields and produces fast switching.

CONCLUSIONS

WFX has progressed nicely this summer. A new and very successful compression configuration was tested. The limits to the present diagnostics were reached. Several prefill gas mixtures were unsuccessfully attempted for diagnostic purposes. High pressure and current diagnostics are ready to be implemented and the 12 Can Bank is built.

REFERENCES

- [1] L.C. Carswell, F.M. Lehr, A. Alaniz, J.D. Beason, J.F Crawford, J.H. Degnan, J.M. Gahl, J.D. Graham, J.H. Holmes, T.W. Hussey, G.F.Kiuttu, R.E. Peterkin, N.F. Roderick, P.J. Turchi, "Formation of Plasma Working Fluid for Compression by Liner Implosions", submitted to J. of Applied Physics (1992)

- [2] Lynn Vesser, R. Caird, B.L. Freeman, D.R. Kania, P.J. Kruse, R.T. Trainor, E.L. Zimmerman, "Single Mode Fiber Optic Sensor for High Currents", Proc. Sixth IEEE International Pulsed Power Conference.

- [3] R.A. Nuttelman, J.H. Degnan, G.F. Kiuttu, R.E. Reinovsky, W.L. Baker, in Megagauss Physics and Technology, Plenum Press, New York, 1980

- [4] G.C. Baldwin, An Introduction to Nonlinear Optics, Plenum Press, New York, 1969

**CORRELATING INJECTOR PERFORMANCE FOR
USE AS ENGINEERING DESIGN CRITERIA**

Michael P. Moses

Graduate Student

**Department of Aeronautical and
Astronautical Engineering**

**Purdue University
West Lafayette, IN 47907**

Final Report for:

**AFOSR Summer Research Program
Phillips Laboratory
Edwards Air Force Base, CA**

Sponsored by:

Air Force Office of Scientific Research

August 1992

**Correlating Injector Performance for
use as Engineering Design Criteria**

**Michael P. Moses
Graduate Student**

**Department of Aeronautical and
Astronautical Engineering
Purdue University**

Abstract

Liquid jet atomization is dependent on flow conditions such as Reynolds Number, Weber Number and both liquid and gas phase properties. The L/D ratio, a variable describing injector geometry, also strongly influences the atomization process. In order to develop liquid rocket engine injector design criteria, a correlation of spray characteristics (cone angle and breakup length) to the net circulation of the liquid jet is proposed. The development of this correlation will be conducted as part of an in-house research effort of the United States Air Force Phillips Laboratory Propulsion Directorate.

Correlating Injector Performance for use as Engineering Design Criteria

Michael P. Moses

Introduction

The jet atomization process is crucial to understanding combustion and stability processes in liquid rocket engines. A knowledge of spray characteristics is required input into droplet evaporation and combustion models. Injector performance is also closely tied to liquid rocket combustion stability and efficiency. For these reasons, the Phillips Laboratory is conducting extensive research and testing in the area of injector performance. In support of the Injector Design Impacts on Spray Characteristics program being conducted at the Propulsion Directorate of Phillips Lab, Edwards Air Force Base, a new correlation procedure is being developed to provide design criteria suitable for engineers to perform injector tradeoff studies. This new correlation will include the effects of orifice geometry, as well as liquid and gas phase fluid properties, on the atomization behavior of liquid jets.

Nomenclature

| | |
|----------------|--|
| L | orifice length (in) |
| D | orifice diameter (in) |
| P _m | manifold pressure (liquid) |
| P _c | chamber pressure (gas) |
| ΔP | differential pressure across injector |
| π _l | density of liquid (lb/ft ³) |
| μ _l | viscosity of liquid (cP) |
| σ _l | surface tension of liquid (lb/sec ²) |
| π _g | density of gas (lb/ft ³) |
| μ _g | viscosity of gas (cP) |

| | |
|------------|---------------------------------------|
| L_b | breakup length (in) |
| 2θ | cone angle (degrees) |
| Re | Reynolds Number |
| We | Weber Number |
| Γ | circulation |
| I | jet impulse |
| r | orifice radius |
| U_0 | average injection velocity (ft/sec) |
| δ^* | boundary layer displacement thickness |

Background

The injectors examined in this study are plain-orifice types, consisting of a single, sharp-edged orifice, as shown in Figure 1.

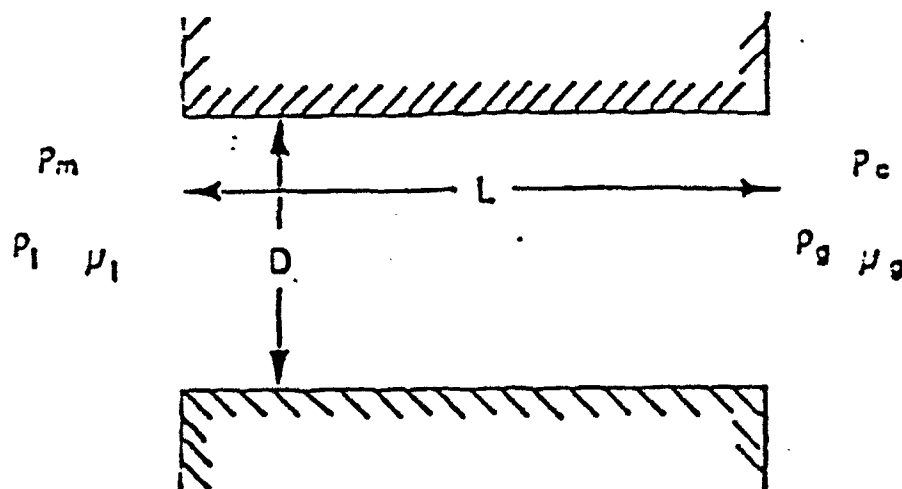


Figure 1. Plain Orifice Injector

The geometric parameter governing the performance of this type of atomizer is L/D , the dimensionless ratio of the orifice length, L , to the orifice diameter, D .

The operating parameter that has the greatest effect on injector performance is ΔP , the pressure differential between the manifold, P_m , and the chamber, P_c . The gas and liquid phase fluid properties of density, ρ , and viscosity, μ , also play an important part in atomization. The non-dimensional variables that are commonly used to describe atomization are Reynolds Number (Re) and Weber Number (We), as defined below.

$$Re = \frac{\rho_l U_o D}{\mu_l}$$

$$We = \frac{\rho_l U_o^2 D}{\sigma}$$

The fundamental features of an atomizing jet are breakup length and spray cone angle, as shown in Figure 2. Breakup length, L_b , is the length of the intact liquid core downstream of the orifice exit. Spray cone angle, 2θ , is defined as the average angle of the droplet spray measured at a distance of 60 orifice diameters downstream.

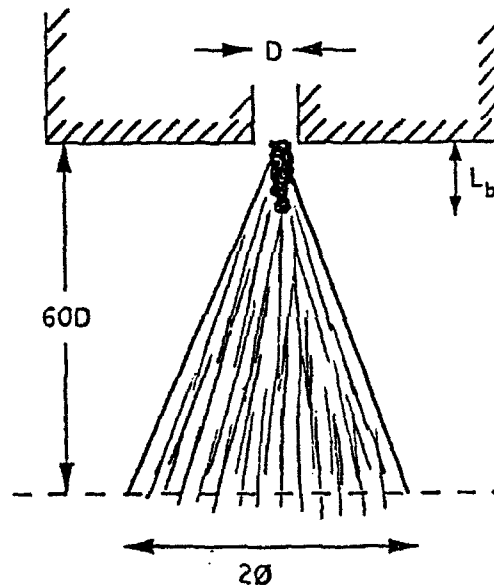


Figure 2. Spray Characteristics

Effects of Injection Pressure (Velocity)

A liquid jet injected into a quiescent atmosphere will breakup a short distance downstream of the orifice exit plane. This breakup length is dependent on the liquid flow within the orifice passage. As injection velocity increases, the behavior and stability of the jet changes. Figure 3 is a representation of the jet stability curve, broken down into separate flow regimes.

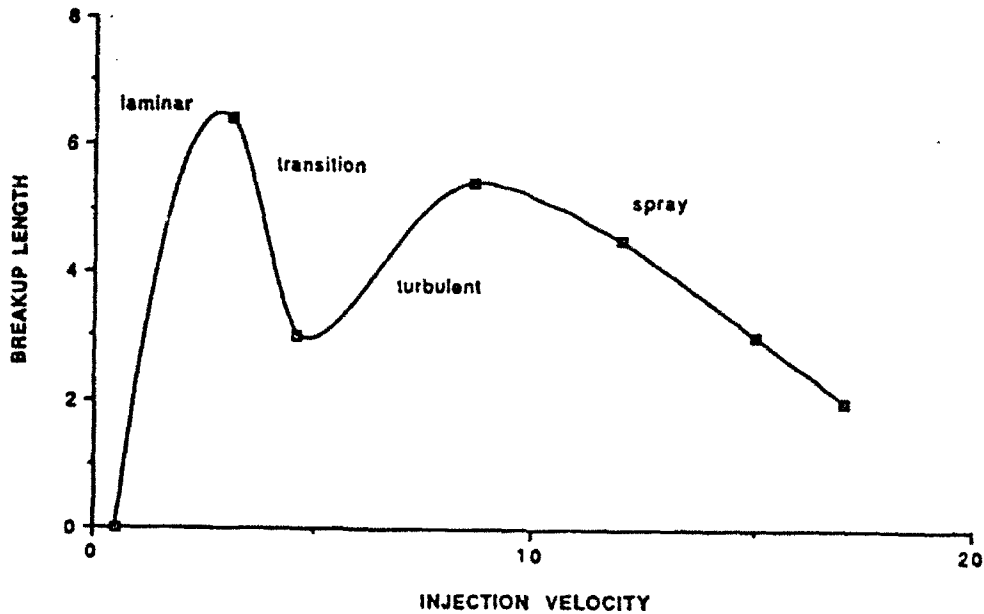


Figure 3. Jet Stability and Breakup Curve (Hiroyasu, et. al. 1982)

In the laminar flow regime, breakup length increases as the injection velocity (manifold pressure) increases. But then the trend reverses in the transition region, and the jet breaks up closer to the exit plane. When the flow becomes turbulent, breakup length again starts to increase as injection velocity increases. As velocity is further increased, the breakup length decreases to small values, such that the jet disintegrates almost immediately upon exiting the injector. Liquid rocket engine injectors operate in this spray regime, with very large Reynolds numbers.

Effects of Orifice L/D

Work by many authors (Arai, et.al. 1985, Reitz and Bracco 1979, Ruiz and Chigier 1991, Varde, et.al. 1984, Wu, et.al. 1991) has shown a general trend in the effect that L/D ratio has on both breakup length and cone angle. Figures 4 and 5 are presented by Arai, et.al (1984) and reflect the effects of L/D on breakup length and cone angle respectively.

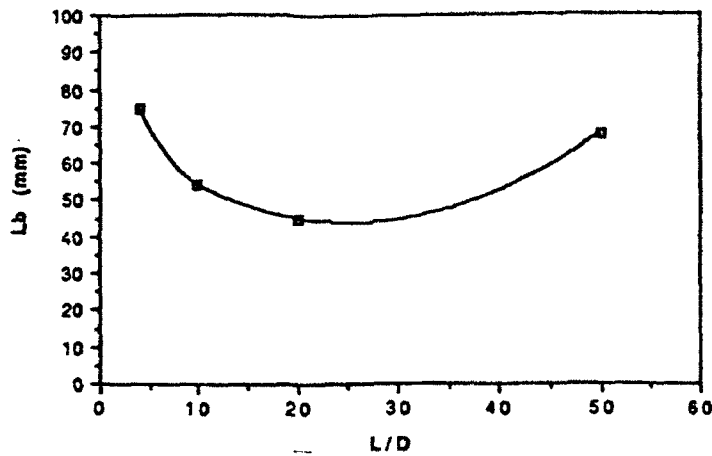


Figure 4. L/D Effect on Breakup Length (Arai, et. al. 1984)

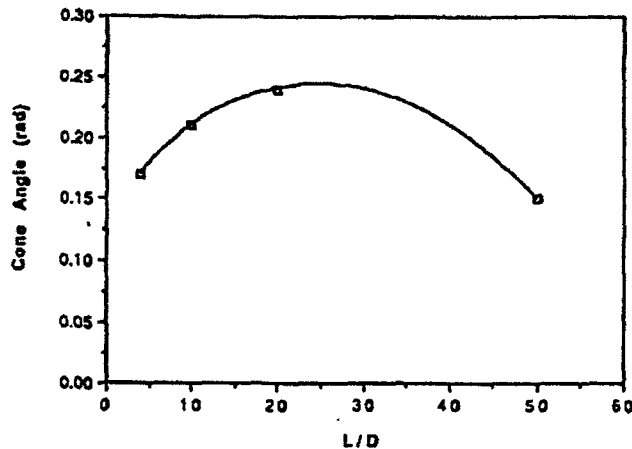


Figure 5. L/D Effect on Cone Angle (Arai, et. al. 1984)

As L/D increases, the breakup length gradually decreases, reaching a minimum. At the same time, cone angle is increasing to a maximum value. The L/D that produces the maximum cone angle also produces the minimum breakup length. Hiroyasu, et. al. (1991) reports this value of L/D to be equal to 20. Wu, et. al. (1983) reports a value of 10, while Varde (1985) claims a much lower number of 5. Further increasing L/D beyond this point will increase the breakup length and decrease the cone angle. Wu, et. al. (1983) proposes that this is related to the flow within the injector passage. At small values of L/D , vena contracta effects increase the radial velocity component of the jet, increasing the spray angle. As L/D increases, the flow reattaches and boundary layers begin to develop, thus changing the velocity profile of the jet and decreasing cone angle. This effect is visually depicted in Figure 6.

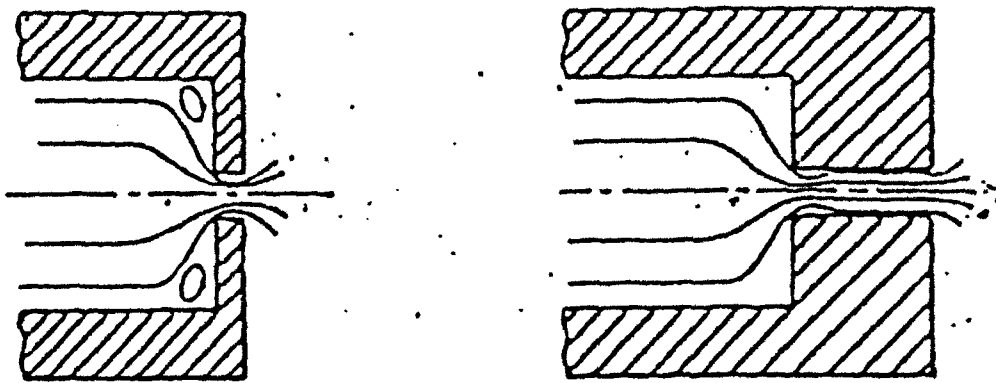


Figure 6. Orifice Flow Streamlines (Lefebvre 1989)

Correlations

Many authors have developed correlations to predict model spray cone angle. A few are presented here in order to emphasis the parameters that influence cone angle.

Abramovich (Ohrn 1991)

$$\tan \theta = 0.013 (1 + \rho_g / \rho_l)$$

Reitz and Bracco (1979)

$$\tan \theta = \frac{4 \pi}{A} \left(\frac{\rho_g}{\rho_l} \right)^{0.5} F \left(\frac{\rho_l Re^2}{\rho_g We} \right)$$

$$A = F (L / D)$$

Arai, et.al (1984)

$$\theta \text{ [rad]} = 0.05 \left(\frac{\rho_g \Delta P D^2}{\mu_g^2} \right)^{0.25}$$

Relatively few studies have investigated the effects of L/D as well as flow conditions on the spray characteristics. It is for this reason that we propose a new correlation parameter.

Technical Approach

As shown in the previous section, jet atomization is governed not only by the flow variables (Re , We) but also to a large extent by the injector geometry and its effect on the jet velocity profile at the exit. Therefore we are motivated to pursue a correlation that will hold for variable geometries and test conditions, for use as a design parameter in the development of liquid rocket engine injector.

If we consider the flow through a sharp-edged orifice, as shown in Figure 7,

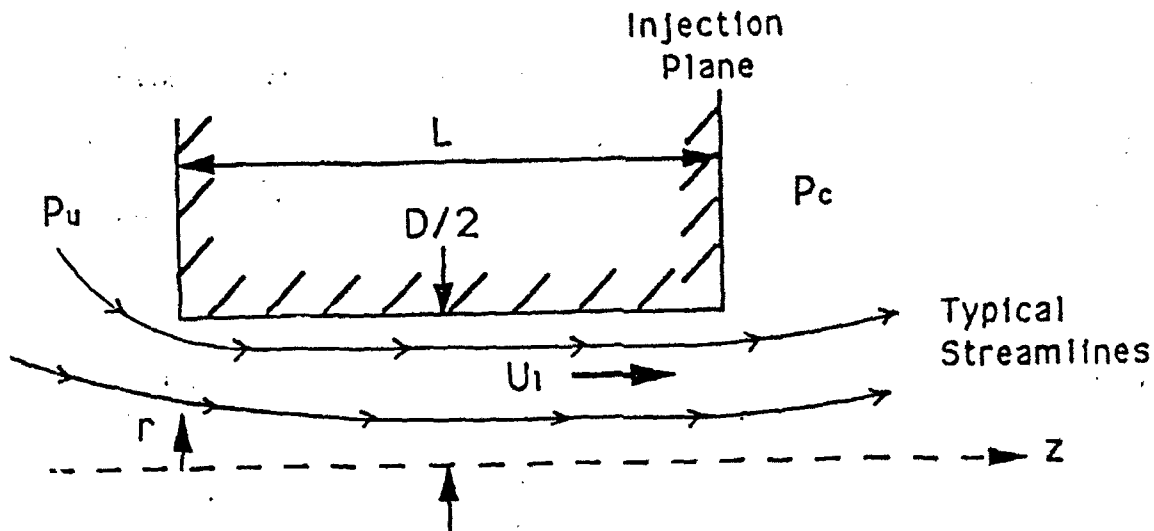


Figure 7. Flow in Orifice Passage

we know that viscous forces will generate a vorticity in the boundary layer that will give rise to a net circulation, Γ . In addition, the impulse of the jet into the quiescent ambient gas will give rise to an additional component of the circulation due to the ring vortex formed at the periphery of the jet. Therefore a net circulation of the form

$$\Gamma = \Gamma_I + \Gamma_V \quad (1)$$

where Γ_I = jet impulse circulation
 Γ_V = viscous flow circulation.

will include effects of velocity profile development within the injector passage as well as aerodynamic effects due to interactions of the liquid jet with the ambient gas. Γ therefore

represents destabilizing influences on the jet, and we believe will be an ideal parameter to use in the correlation of spray characteristics like cone angle and breakup length.

Impulse Circulation

Heister and Karagozian (1990) present the circulation due to the impulse of a liquid jet into a quiescent atmosphere as

$$\Gamma I = \frac{I}{2 \pi r \rho g} \quad (2)$$

where r is the radius of the injector passage and I represents the impulse per unit length (or thrust per unit velocity) of the jet,

$$I = \frac{\rho_l U_0^2 \pi r^2}{U_0} \quad (3)$$

The term U_0 represents the average velocity of the flow in the injector passage,

$$U_0 = \frac{\int_0^r \frac{U(r) r dr}{\pi r^2}}{\quad} \quad (4)$$

By combining equations (2) and (3), we can write the jet impulse circulation as

$$\Gamma I = \left(\frac{\rho_l}{\rho g} \right) \frac{U_0 D}{4} \quad (5)$$

It is important to note the strong effect of density ratio in this term. Several researchers (McCarthy and Molloy 1974, Ruiz and Chigier 1987, Varde 1985) have noted the importance of this ratio on atomization cone angles as shown in the correlations presented in the previous section. Therefore the ΓI term should properly model the effects of aerodynamic interaction of the liquid jet with the surrounding gas.

Viscous Circulation

The evaluation of the Γ_v term due to viscous forces is somewhat more difficult to evaluate. Using the definition of circulation, we may write

$$\Gamma_v = \oint_0 U(r) dr \quad (6)$$

where the closed curve of integration includes the passage centerline and wall as well as the vertical surfaces at the inlet and exit of the injector (see Figure 7).

By virtue of the no-slip boundary condition, we know that $U(r)=0$ at the injector wall. If we assume a well-behaved inlet and exit flow (that is, flow streamlines are exactly parallel with the z direction), then the velocity at these planes is normal to the direction of integration and no net circulation will be generated at these surfaces. In this case, Equation (6) becomes

$$\Gamma_v = \int_0^L U_{cl} dz \quad (7)$$

which implies that the only contributions come from the centerline velocity of the channel where $U(r)=U_{cl}$.

It is however not obvious that this assumption is accurate when modeling the conditions experienced in liquid rocket engine injectors. Significant curvature of the inlet velocity streamlines can occur as shown earlier in Figure 7. The assumption of parallel streamlines is quite accurate at the orifice exit if the boundary layers are thin. In order to check this assumption, a first order estimate of the boundary layer thickness at the orifice exit can be derived by assuming a flat plate boundary layer development within the injector channel (Schlichting 1955). Table 1 summarizes the results of these calculations for several injectors.

Table 1. Boundary Layer Thickness Calculations

| | Fluid | L/D | ReD | d*/r |
|----------------|-------|-----|---------|--------|
| LOX/HC doublet | LOX | 2.4 | 355,000 | 0.0145 |
| LOX/HC doublet | RP-1 | 3.8 | 191,000 | 0.0236 |
| SSME | LOX | 20 | 322,000 | 0.08 |
| Injector 2a | Perc | 1 | 184,000 | 0.008 |
| Injector 2b | Perc | 10 | 180,000 | 0.052 |

It can be seen that the boundary layer displacement thickness δ^* is on the order of 1-2% of the orifice radius except in the case of the very long SSME LOX injector post. Injectors 2a and 2b are two of the four orifices tested in this study. Therefore we will proceed with the correlation, using the assumption of thin boundary layers. The viscous circulation term becomes

$$\Gamma_v = \int_0^L U_{cl} dz = U_o L \quad (8)$$

where U_o will be approximated by Bernoulli's equation.

$$U_o = \left(\frac{2 \Delta P}{\rho_l} \right)^{0.5} \quad (9)$$

$$\Delta P = P_m - P_c$$

We can now combine Equations (5) and (8), yielding an overall circulation term as

$$\Gamma = U_o \left(L + \left(\frac{\rho_l}{\rho_g} \right) \frac{D}{4} \right) \quad (10)$$

and plugging in for U_o as given by Equation (9)

$$\Gamma = \left(\frac{2 \Delta P}{\rho_l} \right)^{0.5} \left(L + \left(\frac{\rho_l}{\rho_g} \right) \frac{D}{4} \right) \quad (11)$$

Equation (11) represents the total disruptive force tending to cause jet atomization. By comparing Γ to Re and We , which represent the forces of liquid viscosity and surface tension tending to resist atomization, a correlation to predict spray cone angle and breakup length

should result. This correlation should be quite successful because Γ includes not only the details of the particular flow environment (ΔP , ρ_l), but also the effects of liquid/gas density ratio and geometric effects on the velocity profile (L , D).

Experimental Facility

This study is being conducted by Phillips Laboratory, located at Edwards Air Force Base, CA. The Air Force has constructed a cold flow facility that can perform injector performance analysis and research under simulated rocket engine operating conditions.

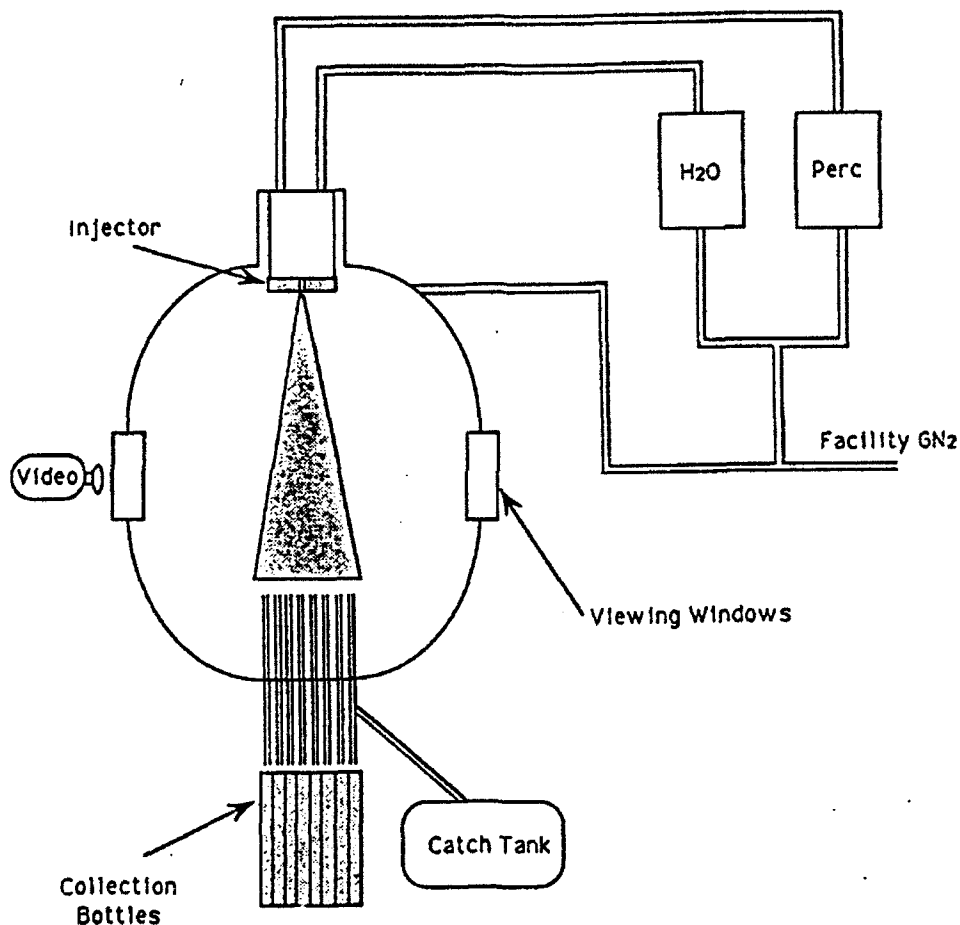


Figure 8. Experimental Facility

The facility depicted in Figure 8 consists of two 250 gallon supply tanks rated to 2000 psia, a 2500 psia GN2 pressurizing system, an optically accessible pressure vessel rated to 2000 psia in which the injectors are flowed, a catch tank and 28 collection bottles. The facility is capable of water flowrates up to 4.75 lb/sec and upstream water supply pressures of 3500 psia (using recirculation pumps not shown in the figure).

The pressure vessel is optimized for liquid rocket engine injector research. It has a 25.25 inch I.D. and is approximately 4 feet long. It has four window ports for use by three different optical particle sizers to study atomization. It also contains a mechanical patternator to obtain mixture ratios at different radii throughout the spray. The injector housing at the tank's top can travel 6 inches vertically as well as rotate 360 degrees.

The injectors used in these tests are designed to minimize a distorted velocity profile up to the discharge orifice. A 1/4 inch square channel with a 32 finish supplies the fluid to the discharge orifice. All the discharge orifices are positioned perpendicularly to the incoming flow and have sharp edged entrances.

Experimental Results

The first stage of testing in this facility was conducted at atmospheric ambient pressures and at injection pressures ranging from 100 to 750 psia. Four injector geometries were tested using perchloroethylene (tetrachloroethylene) as the fuel simulant. A CCD video camera was used to image the spray and allow a measurement of spray cone angle.

Table 2 shows the operating conditions and results for two of the tested injectors. Figures 9 and 10 show plots of cone angle versus Reynolds Number and circulation respectively.

Table 2. Experimental Results

| L/D | ReD | 2θ (deg.) | Γ |
|-----|---------|-----------|------|
| 1 | 72,603 | 10.2 | 1899 |
| 1 | 94,062 | 15.23 | 2453 |
| 1 | 109,565 | 15.33 | 2858 |
| 1 | 125,204 | 17.06 | 3255 |
| 1 | 142,456 | 16.59 | 3698 |
| 1 | 158,990 | 23.93 | 4102 |
| 1 | 172,310 | 22.15 | 4449 |
| 1 | 183,847 | 18.45 | 4742 |
| 10 | 74,818 | 3.1 | 2016 |
| 10 | 92,454 | 3.41 | 2487 |
| 10 | 103,175 | 3.79 | 2772 |
| 10 | 122,939 | 3.51 | 3303 |
| 10 | 138,833 | 3.71 | 3726 |
| 10 | 154,732 | 4.09 | 4155 |
| 10 | 168,128 | 5.97 | 4524 |
| 10 | 180,365 | 5.74 | 4850 |

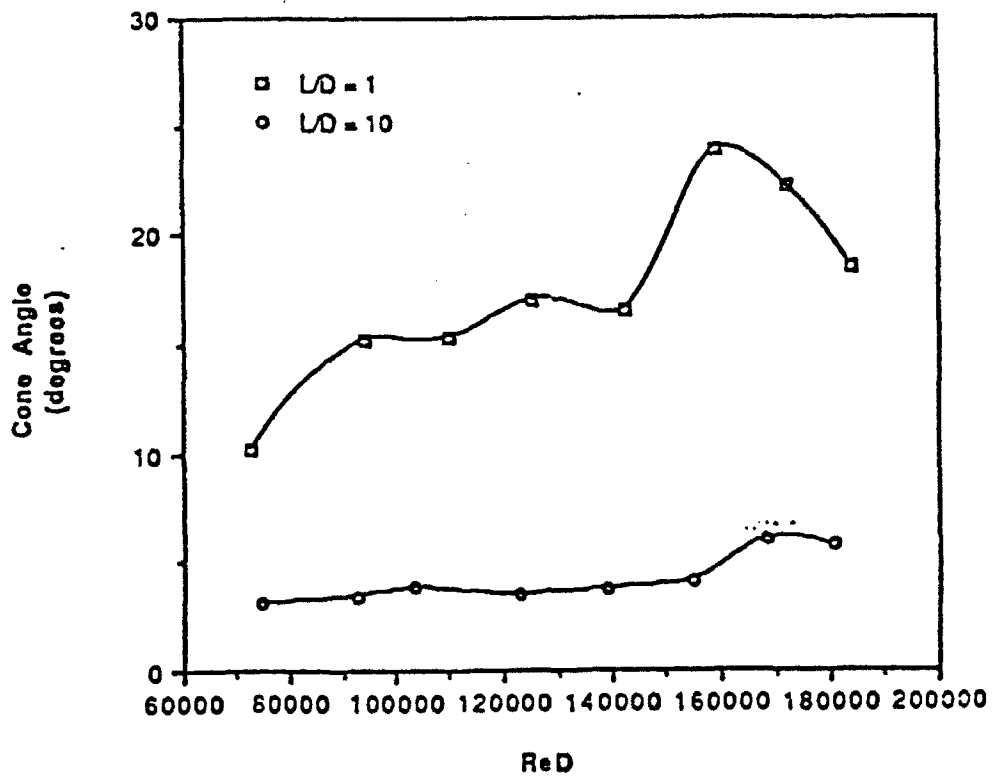


Figure 9. Cone Angle vs. Reynolds Number

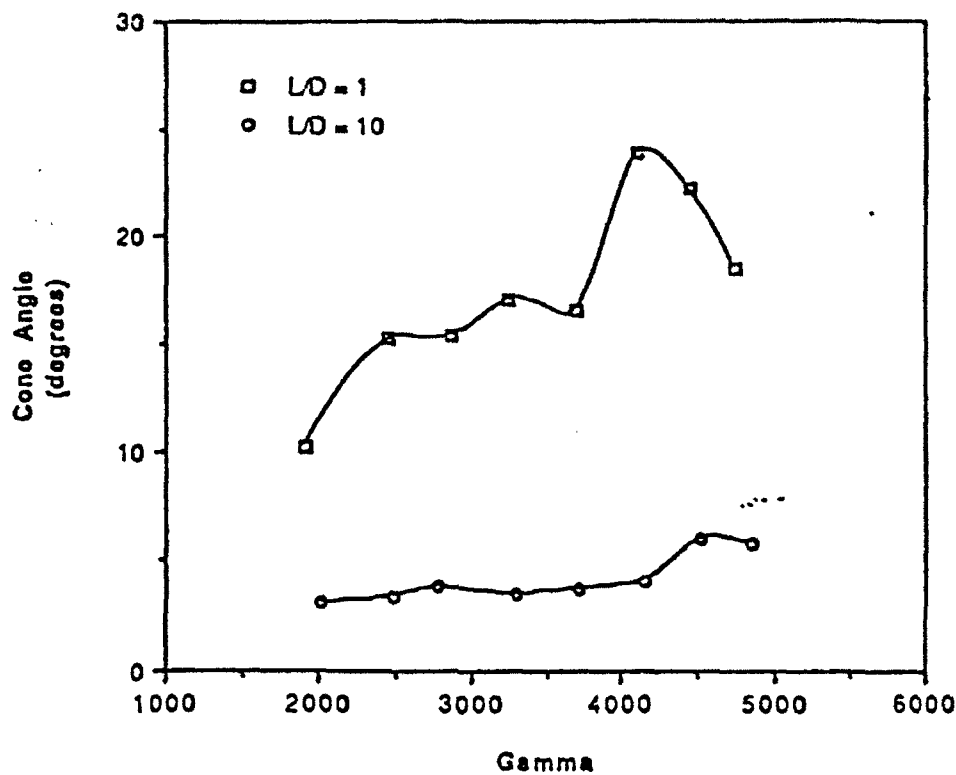


Figure 10. Cone Angle vs. Circulation

It is interesting to note the shape of the curve for L/D of 1 in Figure 9.

The decline of spray cone angle at high Reynolds Numbers ($Re > 160,000$) seems to indicate that there exists a point of maximum cone angle for such a small L/D. Increasing injection pressure beyond this point decreases cone angle. This could quite possibly be due to the increasing importance of aerodynamic effects at high injection velocities.

It can be seen in Figure 10 that the correlation versus circulation doesn't completely model the effects of L/D ratio. Recall, however, that the model assumes a uniform parallel velocity flow at both the injector inlet and exit. In the case of $L/D = 1$ this assumption is violated, thus causing the data to scatter on the graph. The $L/D = 10$ case appears much more well behaved. Further testing at moderate L/D ratios will be required in order to validate the correlation.

Testing in this facility is by no means complete. As of the end of this internship, not enough information or testing was completed in order to offer any hints towards the results of the proposed correlation of spray characteristics versus circulation. It is believed that the uniqueness of this Air Force facility to test at rocket engine conditions will allow for the development of correlations that can be used by design engineers to predict liquid rocket engine injector performance characteristics.

References

- Arai, M., Shimizu, M., and H. Hiroyasu, "Break-Up Length and Spray Angle of a High Speed Jet," ICLASS-85, 1985, pp. IB/4/1-10.
- Arai, M., et.al., "Disintegrating Process and Spray Characterization of Fuel Jet Injected by a Diesel Nozzle," SAE paper 840275, 1984.
- Arai, M., Shimizu, M., and H. Hiroyasu, "Similarity Between the Break-Up Lengths of a High Speed Jet in Atmospheric and Pressurized Conditions," ICLASS-91, 1991.
- Heister, S., and A. Karagozian, "Vortex Modeling of Gaseous Jets in a Compressible Crossflow," *AIAA Journal of Propulsion and Power*, Vol.6, No.1, 1990, pp. 85-92.
- Hiroyasu, H., Shimizu, M., and M. Arai, "The Breakup of a High Speed Jet in a High Pressure Gaseous Atmosphere," ICLASS-82, 1982, pp. 69-74.
- Lefebvre, A., Atomization and Sprays, Hemisphere Publishing Corporation, New York, 1989.
- McCarthy, M., and N. Molloy, "Review of Stability of Liquid Jets and the Influence of Nozzle Design," *The Chemical Engineering Journal*, Vol.7, 1974, pp. 1-20.
- Ohrn, T., Senser, D., and A. Lefebvre, "Geometric Effects on Spray Cone Angle for Plain-Orifice Atomizers," *Atomization and Sprays*, Vol.1, 1991, pp. 253-68.
- Reitz, R., and F. Bracco, "On the Dependence of Spray Angle and Other Spray Parameters on Nozzle Design and Operating Conditions," SAE paper 790494, 1979.
- Ruiz, F., and N. Chigier, "The Effects of Design and Operating Conditions of Fuel Injectors on Flow and Atomization," SAE paper 870100, 1987.
- Ruiz, F., and N. Chigier, "Parametric Experiments on Liquid Jet Atomization Spray angle," *Atomization and Sprays*, Vol.1, 1991, pp. 23-45.
- Schlichting, H., Boundary Layer Theory, McGraw-Hill Publishing Company, 1955.
- Varde, K., "Spray Cone Angle and its Correlation in a High Pressure Fuel Spray," *The Canadian Journal of Chemical Engineering*, Vol.63, April 1985, pp. 183-7.
- Varde, K., and D. Popa, "Diesel Fuel Spray Penetration at High Injection Pressures," SAE paper 830448, 1983.
- Varde, K., Popa D., and L. Varde, "Spray Angle and Atomization in Diesel Sprays," SAE paper 841055, 1984.
- Wu, K., et.al., "Measurements of the Spray Angle of Atomizing Jets," *Journal of Fluids Engineering: Transactions of the ASME*, Vol.105, December 1983, pp. 406-13.

ANALYSIS OF ONYNEX AND MSRP SEISMIC REFRACTION DATA IN NEW ENGLAND

**John Ebel
Associate Professor
Department of Geology and Geophysics**

**Andrew Paulson
Graduate Student
Department of Geology and Geophysics**

**Boston College
Chestnut Hill, MA 02167**

**Final Report for:
Summer Research Program
Phillips Laboratory**

**Sponsored by:
Air Force Office of Scientific Research
Bolling Air Force Base, Washington, D.C.**

September 1992

ANALYSIS OF ONYNEX AND MSRP SEISMIC REFRACTION DATA IN NEW ENGLAND

John Ebel
Associate Professor
Department of Geology and Geophysics

Andrew Paulson
Graduate Student
Department of Geology and Geophysics

Abstract

Using interactive two-dimensional seismic raytracing techniques, seismic velocity models of the crust and upper mantle in New England were constructed from data collected jointly by Phillips Laboratory and Boston College from two seismic refraction experiments. One was from the 1984 Maine Seismic Refraction Experiment (MSRP), with the shotpoints in southcentral Maine and the receivers stretching from Rumford, Maine into the White Mountains in New Hampshire. The second was from the 1988 Ontario-New York-New England Seismic Refraction Experiment (ONYNEX) along a 200 km profile from western New York through Vermont and into southern New Hampshire. From the MSRP data the lower crust and Moho discontinuity in Maine were found to vary noticeably across the Norumbega Fault, with a significantly deeper Moho to the west of the fault. From the ONYNEX data the previously reported ramp feature, separating the Grenville basement in the Adirondack Mountains and the Paleozoic basement in the Northern Appalachians, was found. The ramp is inferred to dip from the surface near the Vermont-New York border to 17 km depth beneath the Vermont-New Hampshire border. The configuration of the ramp indicates that it controlled the emplacement of the geology above it during Paleozoic and Mesozoic time. The results of this study suggest models for ancient continental zones which may be applicable to those in other parts of the world.

INTRODUCTION

In 1984 and again in 1988 the Air Force Geophysics Laboratory (now Phillips Laboratory) and Boston College (called here PL-BC) jointly participated in carrying out piggyback experiments as part of large-scale seismic refraction studies in New England. The two experiments, the Maine Seismic Refraction Experiment (MSRP) in 1984 and the Ontario-New York-New England Seismic Refraction Experiment (ONYNEX) in 1988, were carried out by the U.S. Geological Survey (USGS) to determine the seismic velocity structure of the crust across an ancient continental collision zone. Other participants in parts of MSRP and ONYNEX were the Massachusetts Institute of Technology (MIT) and the Geological Survey of Canada. The PL-BC participation in these experiments was designed to expand the areal coverages of these experiments, to test field methods for recording seismic refraction data, and to provide a detailed data set for waveform studies of explosions in areas of complicated geologic histories. The ultimate goal of the PL-BC research was to improve the methodologies for monitoring nuclear testing treaties in remote parts of the world by learning to model regional seismic waveform data from a well-studied area.

The area of the surveys and the locations of stations of the PL-BC piggyback experiments are shown in Figure 1. For MSRP the PL-BC stations for the first night of the experiment were located in the White Mountains of Maine and New Hampshire to the west of the shots which were fired that night. It is these data which we analyzed during the summer, 1992 research effort. For ONYNEX data primarily from the second night of the experiment, a line of receivers from just northwest of Westport, New York to Manchester, New Hampshire, were modeled. Seismic raytracing through models of the seismic velocity structure of the crust along each of the profiles was used to match the arrival times of the major body wave phases in the observed seismograms.

A number of crustal models for New England, based on the USGS data, have already been published for the MSRP and ONYNEX experiments. For MSRP early work based on first analyses of the data are found in Luetgert et al. (1987) and

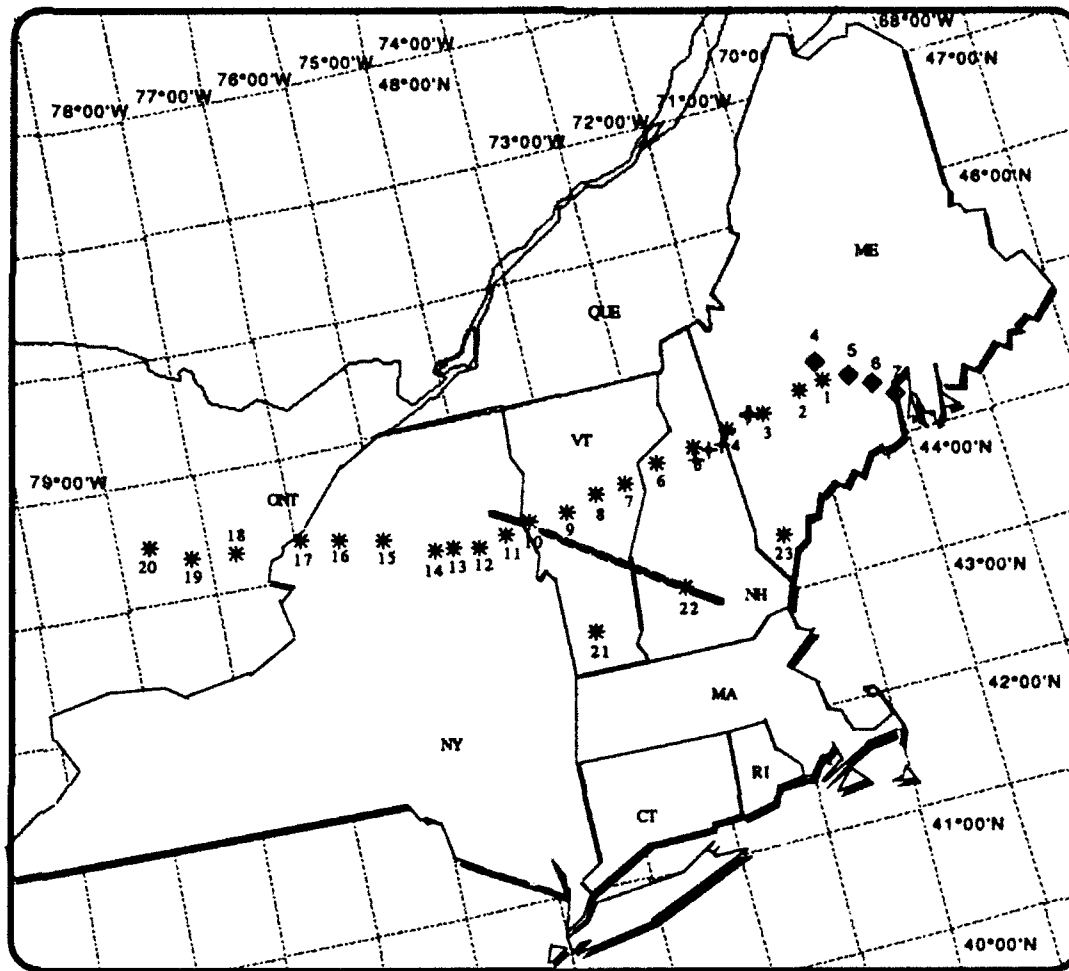


Figure 1. Map of the study area showing the locations of the sources and receivers for this analysis. The shotpoints and receivers from the 1984 Maine Seismic Refraction Experiment used in this study are indicated by the diamonds and crosses respectively. All of the shotpoints for the 1988 Ontario-New York-New England Seismic Refraction Experiment are shown (the stars) as is the trend of the seismic line analyzed in this study.

Klemperer and Luetgert (1987). More recently, a detailed model of the crust for the along-strike profile in central Maine was published by Henket et al. (1991). The data from the long, cross-strike profile from Canada to coastal Maine are still being analyzed by the USGS during the summer of 1992 (J. Luetgert, personal communication, summer, 1992). For ONYNEX a detailed model for the eastern half of the experiment, stretching from Maine into central New York state, was published by Hughes and Luetgert (1991). The results reported in these studies are important because they provide constraints and starting models for the analysis of our data sets. These studies are also important because we chose to use with our observations the same analysis technique (ray tracing using the computer programs developed by Luetgert, 1988) as was used in those previous studies. About halfway through the summer, J. Luetgert provided an improved version of his code, in this case ported to Macintosh computers (Luetgert, 1992). The use of this code greatly facilitated the modeling of the very complex structure sampled by the PL-BC data from the ONYNEX experiment.

GEOLOGIC SETTING AND TECTONIC HISTORY

Because the present seismic structure of New England is a reflection of its past tectonic history, we present a brief summary of the geologic development of New England relevant to the areas studied here. This summary is abstracted from a number of sources, most notably Taylor and Toksoz (1979) and Press and Siever (1982). A summary map of the geology together with the locations of the two study areas are indicated in Figure 2.

During the late precambrian the eastern edge of North America rifted from a landmass to the east and evolved into a passive margin. The edge of the continent in New England at that time ran from what is today western Massachusetts north through central Vermont and then northwest across the northern tip of New Hampshire and along the northern third of the state of Maine. After a long period of drifting a series of collisional events started in New England with the Taconic orogeny about 480 m.y. ago. During this orogenic episode, oceanic sediments from the continental shelf and continental slope were thrust westward and northward upon the eastern edge of North America, forming

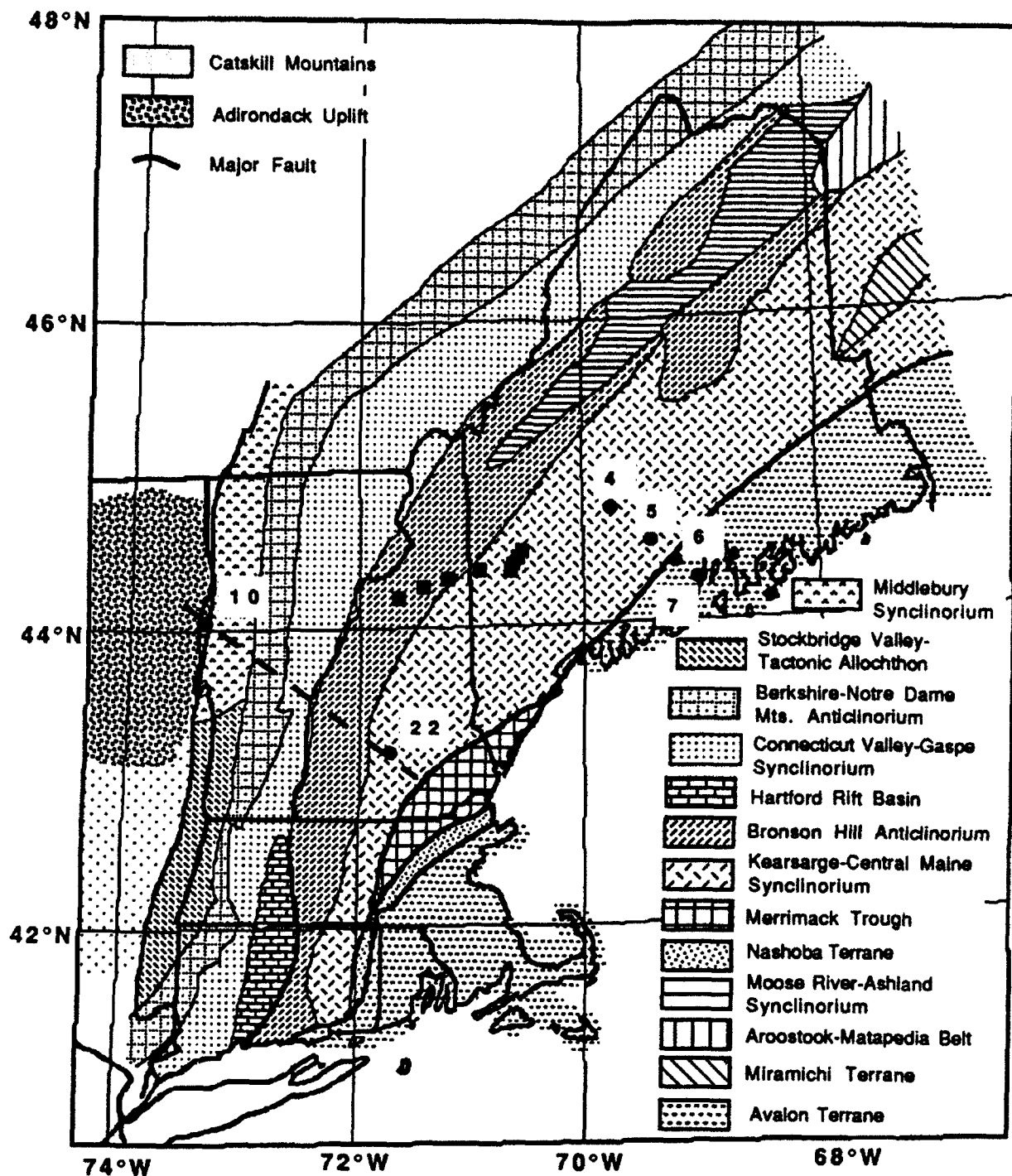


Figure 2. Map of the major geologic terranes and faults in New England. Shotpoints 4, 5, 6 and 7 from the MSRP and the receivers which recorded those shots (squares) are indicated as are shotpoints 10 and 22 from the ONYNEX along with the trend of the PL-BC profile (dashed line).

the Taconic Mountains among other structures. A part of the continental edge also broke off and was thrust up and west, exposed today in various bodies such as the Green Mountains in Vermont. Following the Taconic orogeny there occurred a series of collisions between North America and several island arcs and continental fragments from the east, along with the emplacement of a number of plutons of various ages. In New England, the Norumbega Fault in Maine and the Clinton-Newbury Fault in Massachusetts with its extensions in Connecticut are mapped as the surficial sutures between Avalonia, one of the largest of these continental fragments, and North America. The Acadian orogeny, which took place about 380 m.y. ago, was a brief but intense collisional orogeny, probably of an island arc with North America. The Alleghenian orogeny, which occurred about 300 m.y. ago, was probably associated with the final suture of the African land mass to the eastern North American margin. Subsequent to the Alleghenian orogeny Africa was attached to North America during the period of the existence of the supercontinent of Pangea. The breakup of Pangea in New England began during the Triassic period (about 210 m.y. ago) with the opening (which later failed) of a number of continental rift basins. During the Jurassic (about 180 m.y. ago) new set of basins formed to the east, and these successfully opened to form the Atlantic Ocean. The late Mesozoic (about 120-100 m.y. ago) in New England saw the emplacement of the major plutons which make up the White Mountains. These are thought to have been due to the passage of North America over a mantle hot spot. Finally, during the Cenozoic (since about 80 m.y. years ago) the eastern margin of North America has once again evolved into a passive margin, a state which still exists today.

DATA SETS FOR THIS STUDY

For both the MSRP and ONYNEX experiments the source shots were located and detonated by the USGS. The shotpoints were separated by about 30 km along the refraction lines set up by the USGS, with a subset of all shot points being detonated during each night of shooting. In both the MSRP and ONYNEX experiments the shots ranged in size from 1600 lbs. to 4000 lbs. of ammonium nitrate with one additional 6000 lb. shot in Maine during ONYNEX. The shots were detonated in 8-inch diameter holes, drilled 49-55 meters in the bedrock to ensure

good coupling. One shot point each during MSRP and ONYNEX was in a water-filled quarry. Data from these quarry shots were not used in this study.

The instrumentation and recording configurations for the PL-BC experiments were different during the MSRP and ONYNEX experiments. For the first night of shooting during the MSRP (the data set analyzed here), five PL Terra Technology DCS-302 recorders with 3 Hall-Sears HS-10-1B 1-Hz geophones were spaced about 15 km apart from Rumford, Maine westward to Crawford, New Hampshire. Just west of Rumford Boston College installed at about 1 km station spacing 5 Sprengnether MEQ-800 analog recorders with vertical HS-10 1-Hz sensors and 2 digital Sprengnether DR-200 recorders with 3 Teledyne S-13 1-Hz sensors. For the ONYNEX data set analyzed here PL-BC along with MIT installed a line of seismographs at about 5 km station spacing from Manchester, New Hampshire to just northwest of Port Henry, New York. The primary purpose of this line was to record two shotpoints from near either end of the line. PL put out 25 Terra Technology recorders with Sprengnether S-6000 triaxial geophones, while the Boston College-MIT data were recorded on 9 seismographs, 5 of which were MEQ-800 analog seismographs which were connected to HS-10 seismometers. The other seismographs were DR-200 digital seismographs connected to S-6000 seismometers. All of the instruments during both experiments were calibrated either to WWV radio or GOES satellite time.

As the first step in the analysis of the data, the digital waveforms for both experiments were assembled on the PL VAX computer. The waveforms were then read into the computer program ICON, developed by Dr. John Cipar at PL, where the first arrival times and the arrival times of other important P wave phases were read. Using ICON we constructed record sections of the data, facilitating identification of phases from one waveform to the next. An example of a record section from the ONYNEX data set is shown in Figure 3. We then added to the set of arrival times from the digital data the times of arrival of first and later P-wave arrivals from the analog records. These were read with a visual ocular graded to a 0.1 mm scale. The reading accuracy of the digital waveforms was 0.01 sec, while for the analog waveforms it was 0.02 to 0.04 sec.

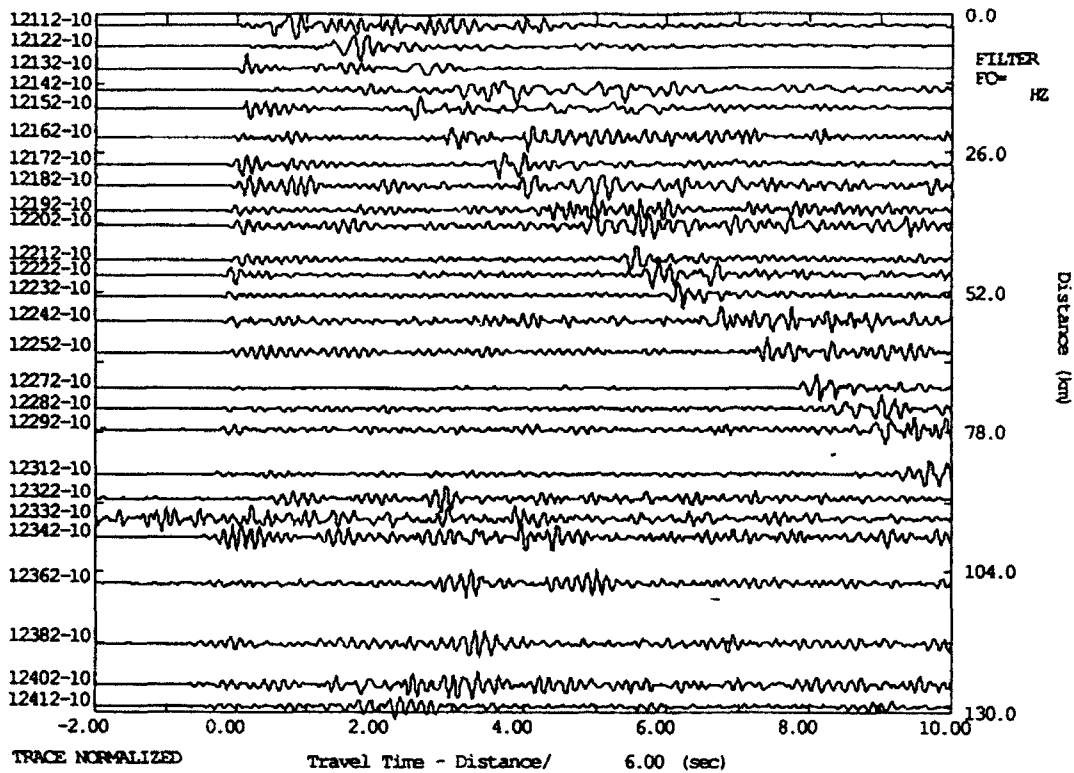


Figure 3. Example of one of the PL-BC seismic sections from the ONYNEX experiment. The traces are from shotpoint 10 to the southwest, with the 0 distance being at shotpoint 10. The time axis represents travel time at a reduced velocity of 6.0 km/s. The amplitudes of the traces are individually normalized.

MODELING RESULTS

MSRP Data Set

The set of seismograms from the MSRP experiment contained a number of P-wave arrivals which were used in the ray-tracing analysis. In many cases the first arrivals were rather emergent, indicating that these arrivals were head waves or waves guided along the top of faster velocity layers in the upper crust. Several later arrivals in the P waveforms were also analyzed. These generally fit the expected travel times for mid-crustal or Moho reflections. Thus, the arrival time data set could be used not only to measure seismic velocities in the upper crust but also to estimate the thickness of the crust in the study area.

The approach in fitting the observed travel times was first to construct a starting crustal model based on the results of Hughes and Luetgert (1991) and Hennett et al. (1991). Rays were then traced through this model from the appropriate source positions to each receiver location, and the predicted travel times were compared to the observed travel times. The crustal model was then changed and the ray tracing redone. This process was repeated a number of times by trial and error until a velocity model which closely matches the travel time data was found. The data were analyzed starting with that from the closest shotpoint and working progressively toward the farthest shotpoint. For the observations from each shotpoint, the first arrivals were matched first followed by the later arrivals in the data set. The deepest reflections, those from the Moho, were fit last for each shotpoint.

Plots of the crustal model which best fit the arrival time observations are shown in Figure 4. Several interesting features can be observed in this model. First, while a low velocity zone from the starting model is preserved in the upper crust, the data set analyzed here is too sparse to either confirm or deny the occurrence of such a feature. Second, the top of the lowermost crustal layer is quite deep between shotpoints 4 and 5 and the receiving stations. It is as deep as 29 km here, whereas it is between 21 km and 27 km deep throughout other parts of New England. The Moho depth of 37-40 km under the central part of this profile is

Western Maine Crustal Models **PL-BC Data 9/25/84**

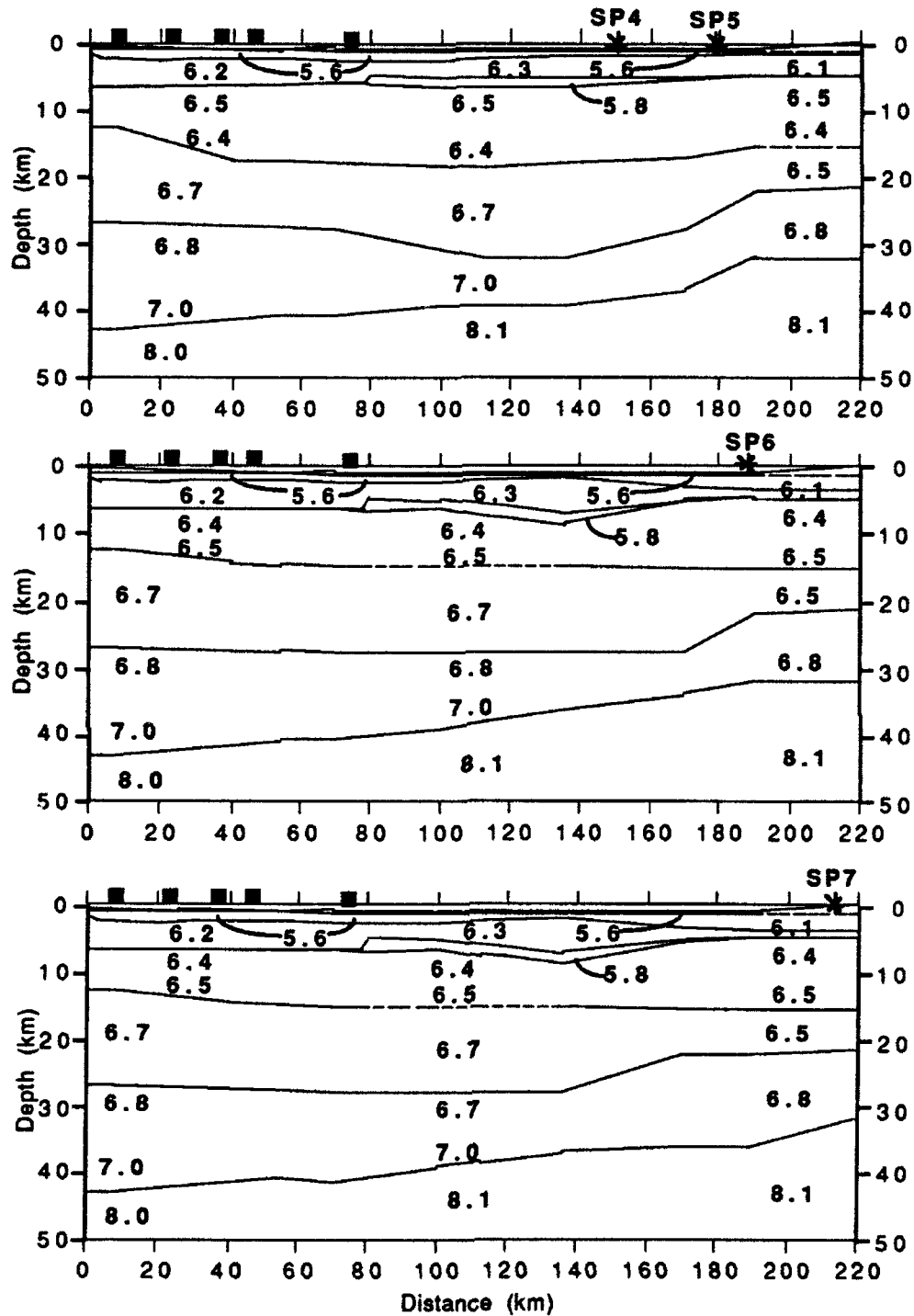


Figure 4. Crustal models for western Maine from the analysis of the MSRP data. Shown are the P-wave velocities in km/s at different points in the models. The shotpoint locations (stars) and receiver locations (solid squares) relative to the model are indicated at the top of each cross section.

quite consistent with the results of Luetgert et al. (1987) and Kafka and Ebel (1988) who reported a local depression in the Moho in this vicinity.

For shotpoints 6 and 7 there are some notable changes in the crustal model needed to fit the data. Specifically, the Moho is shallowed to a depth of 33-35 km near the shotpoints, and the top of the lowermost crust is raised to about 22 km. These changes occur to the east of the Norumbega Fault, and they suggest that the Norumbega Fault represents a major discontinuity in the structure of the lower crust. Curiously, such a discontinuity was not reported either by Klemperer and Luetgert (1987) or Stewart et al. (1987). However, the observations in this study sample a somewhat different part of the crust of Maine than those studies. Thus, it appears that strong lateral changes in the seismic velocity structure of the lower crust of Maine can occur over distances of a few tens of kilometers.

ONYNEX Data Set

Applying to the PL-BC ONYNEX data set the same analysis methods as were described above for the MSRP observations, we first found constraints on the layer thicknesses and velocities under southern New Hampshire and central Vermont and under the easternmost part of the Adirondack Mountains. These constraints were used in the creation of two seismic velocity models for the seismic line which we studied. One model was for the arrivals northwest from shotpoint 22 in Southern New Hampshire (an Appalachian crustal model), while the second was for the arrivals around shotpoint 10 in the Adirondacks of New York (an Adirondack crustal model). Major differences in the seismic velocity structure between these two regions had already been reported by Hughes and Luetgert (1991). A single crustal model was constructed from these two distinct models by ramping the Adirondacks underneath the Appalachians, as previously recognized from the 1980 COCORP profile (Brown et al., 1983) and from the Hughes and Luetgert (1991) study. The seismic velocities and positions of the layer boundaries in the constructed model were varied until rays traced through the model best fit the observed arrival times. The interactive two-dimensional seismic raytracing program MACRAY (Luetgert, 1992) greatly facilitated the ray tracing processing. This analysis lead to the development of a seismic velocity model that

is similar to that found by Hughes and Luetgert (1991) for the region just north of our study area.

The best fitting seismic velocity structure (Figure 5) is well constrained in the upper 20 km as the first arrivals were strong and relatively clear of noise and the source-receiver distances provided observations which primarily sampled the upper half of the crust. An insufficient number of strong/clear second arrivals representing reflections from the deeper parts of the crust and from the top of the mantle lead to more ambiguous readings of their arrival times, and therefore, the velocity structure below 20 km is not as constrained as that of the upper crust.

The northern end of the profile extends into the Adirondack mountains. The Adirondacks velocity crustal model consists of a low velocity layer of seismic velocity 5.45-5.50 km/s. This 0.5 km thick layer represents the weathered rock and ground cover. From 0.5 km to 18 km depth the Adirondacks are characterized by a high P-wave velocity of 6.30-6.55 km/s. This high P-wave velocity reflects the anorthositic composition of the Adirondacks, which consist of 1.0+ b.y. old Grenville basement rocks. The high crustal velocity rocks of the Adirondacks extend from the near surface, at the northwestern part of the profile, to a depth of 17 km under the Vermont-New Hampshire border. The Appalachian crust is also topped by a 0.5 km weathering layer, and below that the P-wave velocities increase from 6.03 km/s to about 6.3 km/s at 15 km depth. An upwarp in the top of the 6.65 km/s layer near the base of the ramp was needed to fit the first arrival time data from shotpoint 22 to the stations at the northwestern part of the profile. A local upward bulge in the Moho surface was also inferred from the arrival times of what were interpreted to be PmP reflected phases in the sections.

The major result of the analysis of the PL-BC ONYNEX data is the position of the ramp under the profile. The ramp is found to dip steadily from the Vermont-New York border downward to the Vermont-New Hampshire border where it flattens out considerably. The bottom of the ramp under this profile occurs approximately due south of the bottom of the ramp under northcentral Vermont found by Hughes and Luetgert (1991). Thus, the edge of the ramp beneath Vermont and New Hampshire strikes approximately due north-south, which is the

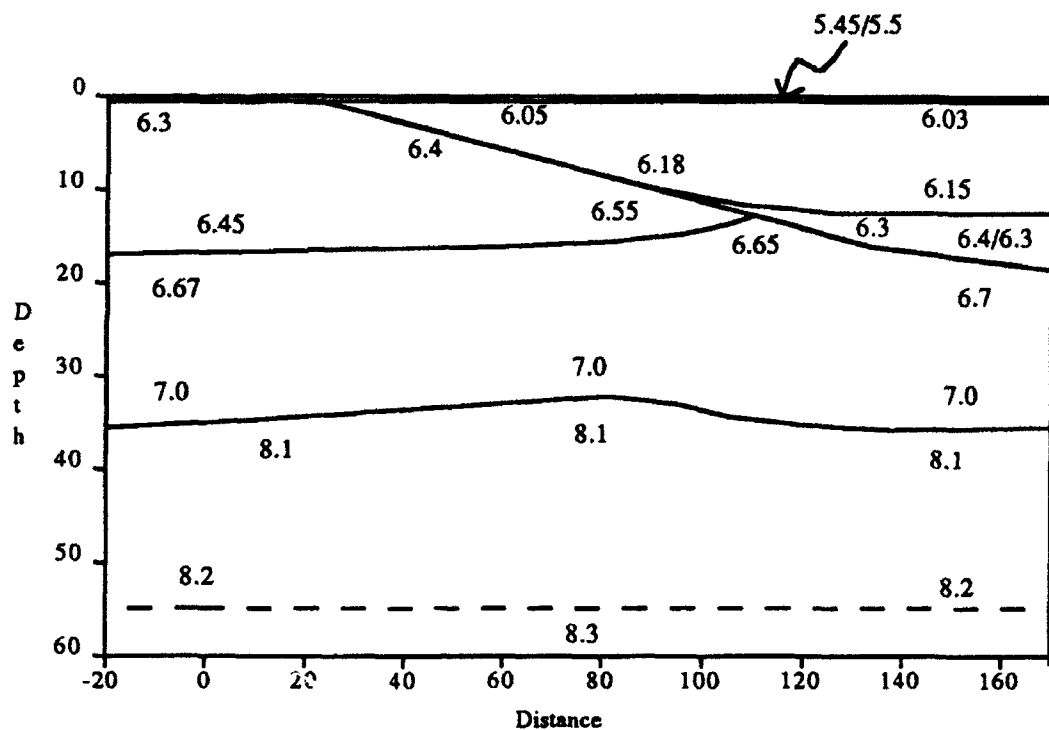


Figure 5. Crustal model for the PL-BC line from the eastern edge of the Adirondack Mountains to southcentral New Hampshire from the ONYNEX data. Shown are the P-wave velocities in km/s at different points in the model.

prevailing trend of most of the surface geology in this area. Given the ancient age of the rocks in the Adirondack Mountains compared to that of the Appalachian rocks, it appears likely that the shape of the Adirondack/Grenville massif has controlled the orientation of the emplacement of the geology and tectonic terranes in Vermont since late precambrian time.

IMPLICATIONS FOR NUCLEAR TEST BAN TREATY MONITORING

One of the most important aspects of using seismology to monitor nuclear test ban treaties, particularly using seismic stations located at regional distances (less than 100 km to 2000 km or so from the sources), is to understand the seismic wave propagation between the sources and the receivers (Pomeroy et al., 1982). Seismological studies in recent years have revealed strong complexity in the structure of the earth's crust in many places (Braile, 1991), and the variation of this complexity from place to place makes it difficult to find general rules to guess the seismic wave propagation characteristics for any particular source-receiver path. The results of this study demonstrate that, for an ancient continental collision belt, major crustal variations can occur over distances of tens of kilometers. In particular, the topography of the Moho can vary by several kilometers, and the interface between older continental shield rocks and younger, overthrust collisional terranes is a smoothly dipping structure with a geometry which is reflected in the overlying surface geology. These results give important clues about what crustal seismic structures may be found in other parts of the world, such as under the Ural Mountains and the Caucasus Mountains in Eurasia. They can be used to postulate possible crustal models for use in nuclear test ban treaty monitoring studies in these and other areas of the world.

REFERENCES

Braile, L.W. (1991). Seismic studies of the earth's crust, *Reviews of Geophysics, Supplement, U.S. National Report to International Union of Geodesy and Geophysics, 1987-1990*, 680-687.

Brown, L., C. Ando, S. Klemperer, J. Oliver, S. Kaufman, B. Czuchra, T. Walsh, Y. Isachsen (1983). Adirondack-Appalachian crustal structure: The COCORP northeast traverse, *Geol. Soc. Am. Bull.*, **94**, 1173-1184.

Hennet, C.G., J.H. Luetgert and R.A. Phinney (1991). The crustal structure in central Maine from coherency processed refraction data, *J. Geophys. Res.*, **96**, 12,023-12,037.

Hughes, S., and J.H. Luetgert (1991). Crustal structure of the western New England Appalachians and the Adirondack Mountains, *J. Geophys. Res.*, **96**, 16,471-16,494.

Hughes, S., and J. Luetgert (1992). Crustal structure of the southeastern Grenville province, northern New York state and eastern Ontario, *J. Geophys. Res.*, **97**, in press.

Kafka, A.L., and J.E. Ebel (1988). Seismic structure of the earth's crust underlying the state of Maine, in *Studies in Maine Geology*, Volume 1, Maine Geological Survey, 137-156.

Klemperer, S.L., and J.H. Luetgert (1987). A comparison of reflection and refraction processing and interpretation methods applied to conventional refraction data from coastal Maine, *Bull. Seism. Soc. Am.*, **77**, 614-630.

Luetgert, J.H. (1988). User's manual for RAY84/R83PLT interactive two-dimensional raytracing/synthetic seismogram package, *U.S. Geological Survey Open-File Report 88-238*, 52 pp.

Luetgert, J.H. (1992). MACRAY interactive two-dimensional seismic raytracing for the Macintosh, *U.S. Geological Survey Open-File Report 92-356*, 43 pp.

Luetgert, J. and C.E. Mann (1990). Avalon terrane in eastern coastal Maine: Seismic refraction-wide-angle reflection data, *Geology*, **18**, 878-881.

Luetgert, J., C.E. Mann, and S.L. Klemperer (1987). Wide-angle deep crustal reflections in the northern Appalachians, *Geophys. J.R. astr. Soc.*, **89**, 183-188.

Pomeroy, P.W., W.J. Best and T.V. McEvilly (1982). Test Ban Treaty Verification with Regional Data--A Review, *Bull. Seism. Soc. Am.*, **72**, S89-S130.

Press, F. and R. Siever (1982). *EARTH*, W.H. Freeman and Co., New York, 613 pp.

Stewart, D.E., J.D. Unger, J.D. Phillips, R. Goldsmith, W.H. Poole, C.P. Spencer, A.G. Green, M.C. Loiselle, and P. St. Julien (1986). The Quebec-western Maine seismic reflection profile: Setting and first year results, in *Reflection Seismology: The Continental Crust*, Geodynamics Series Volume 14, 189-199.

Taylor, S., and M.N. Toksoz (1979). Three-dimensional crust and upper mantle structure of the northeastern United States, *J. Geophys. Res.*, **84**, 7627-7644.

ESTABLISHMENT OF AN ARCJET OPTICAL
DIAGNOSTICS FACILITY AT PHILLIPS LAB

Daniel A. Erwin
Associate Professor
Department of Aerospace Engineering

and

John H. Schilling and Jeff A. Pobst
Research Assistants
Department of Aerospace Engineering

University of Southern California
University Park
Los Angeles, CA 90089

Final Report For:
Summer Research Program
Phillips Laboratory

Sponsored by:
Air Force Office of Scientific Research
Bolling Air Force Base, Washington, D.C.

August, 1992

ESTABLISHMENT OF AN ARCJET OPTICAL
DIAGNOSTICS FACILITY AT PHILLIPS LAB

Daniel A. Erwin, John H. Schilling, and Jeff A. Pobst
Department of Aerospace Engineering
University of Southern California

Abstract

An arcjet optical diagnostic facility was established at the Phillips Laboratory. This facility is expected to provide accurate measures of flow properties in the plume and nozzle region of arcjet thrusters to assist in the development of more efficient arcjet thrusters for spacecraft stationkeeping and orbit-raising applications. A 30-kW arcjet was mounted and successfully operated in a vacuum test chamber capable of accurately duplicating the space environment. Optical elements were installed to allow active or passive measurement of flow properties using the techniques of emission spectroscopy and laser-induced fluorescence. A tunable ring dye laser pumped by a 20-watt CW argon-ion laser were installed and aligned for LIF experiments. Finally, an automated control and data-acquisition system was installed and software developed to conduct a variety of experiments.

A Computational Model of the Magnetospheric Boundary Layer

**David W. Rose
Graduate Student
Department of Mathematics**

**Courant Institute of Mathematical Sciences
New York University
251 Mercer Street
New York, NY 10012**

**Final Report for:
Summer Research Program
Phillips Laboratory**

**Sponsored by:
Air Force Office of Scientific Research
Bolling Air Force Base, Washington, D. C.**

September 1992

A Computational Model of the Magnetospheric Boundary Layer

David W. Rose

Graduate Student

Department of Mathematics

New York University

Abstract

A two-dimensional magnetohydrodynamic model of the magnetospheric boundary layer was studied. The partial differential equations of the model written in magnetic potential-kinetic streamfunction form were discretized by means of a Fourier-Chebyshev series in the two dimensions. This discretization permits both modelling of plasma velocity boundary conditions as well as efficient computation of the quasi-linear differential operators. Physical reasons are given for including both viscosity and resistivity dissipation effects in a model even though the magnetospheric plasma is collisionless. These dissipation effects permit the establishment of uniform boundary conditions on connected components of the boundary for mathematical and numerical well-posedness.

A Computational Model of the Magnetospheric Boundary Layer

David W. Rose

Introduction

The connection between the solar wind and the Earth's magnetosphere is essential in understanding the magnetospheric environment surrounding high-altitude satellites and human inhabited spacecraft. "Space weather" consisting of particle flux, electromagnetic fields and electric currents is a factor to be considered in design and maintenance of satellites, sensitive equipment and even human safety during space-walks. The ability to forecast near space conditions will be necessary for the success of technological applications. However, such capability is limited at the present time, due to the expense of making observations of the geomagnetosphere and the limited understanding of the magnetospheric processes involved.

Model Problem

It is proposed that a portion of geomagnetospheric boundary layer may be studied numerically by use of a Fourier-Chebyshev tau spectral method. Spectral methods are attractive due to their ability to efficiently compute smooth fluid flows and have been used successfully in many hydrodynamic and magnetohydrodynamic (MHD) problems. This is due to the exponential convergence obtainable with spectral discretizations and the efficient calculation of quasi-linear components through use of the Fast Fourier Transform. While it is true that traditionally spectral methods have been only applied to smooth flows, recent positive results have been achieved in applying spectral methods to non-smooth flows. Spectral methods have been applied in the past to laminar and turbulent incompressible flows and have been applied to meteorological simulations [1,5].

The model is that of a magnetohydrodynamic shear layer, which may be compared to the hydrodynamic shear layer for which previous modeling work by others already exists [9]. This shear layer model has been used to explain theoretically how solar wind bearing northward directed magnetic flux would couple to the Earth's magnetosphere [3,11]. The simplest form of this model would be a 2D MHD model of periodic channel flow with resistivity; a more realistic 3D model could be obtained using the Strauss equation [12] form of ideal (resistiveless) MHD with ionospheric resistive coupling at the ends. Only the 2D model will be discussed in this report.

The domain of the problem is described as follows. Take the Earth's magnetic field to be aligned in a uniform direction arbitrarily denoted the x -coordinate and oriented perpendicularly to the solar wind shear. This approximation may be taken either by limitation to the magnetic equatorial plane or else by considering only magnetic-line integrated quantities. We assume that the main component of the Earth's

magnetic field is unaltered in this model and only consider perturbations of the magnetic field transverse to the mean field. We also assume incompressibility of the flow and a uniform density. The computation takes place entirely in the plane perpendicular to the field-aligned direction. The x - and y -coordinates are aligned parallel and perpendicular to the magnetopausal layer, which is assumed fixed in space. In reality, the magnetopause is known not to have a fixed position in space, but determination of the location of the magnetopause requires solution of a free boundary value problem and will not be considered here. (While it is known that the magnetopause moves through space, current satellite observations are too few to determine observationally the motion of the magnetopause.) To further simplify the problem and numerical method, the x -direction is periodic, limiting the method to solutions which are locally periodic along the magnetopausal surface. The essential boundary conditions of the problem are taken on surfaces parallel to the y -axis, at the values $y = -1$ and $y = 1$, corresponding to the Chebyshev approximation used in the numerical method. The specific boundary conditions to be applied will follow the statement of the equations to be solved.

Theoretical studies of the geomagnetic boundary layer indicate that there is an effective diffusion of solar wind plasma into the magnetosphere in spite of it being a collisionless plasma. Theory indicates that high frequency fluctuations of the plasma are responsible for this effective diffusion, which has been estimated [4]. This momentum diffusion is what researchers presume responsible for the generation of field-aligned currents in the auroral zones of the ionosphere [7].

The equations of MHD have been rewritten into potential-streamfunction form,

$$a_t + [a, u] = -\eta j,$$

$$\omega_t + [\omega, u] = [j, a] + \mu \Delta \omega.$$

The dependent variables a , u are the perturbation magnetic (field-aligned) potential and the velocity (field-aligned) streamfunction. The auxiliary variables,

$$j = -\Delta a,$$

$$\omega = -\Delta u$$

are the field-aligned electric current and the field-aligned vorticity of the perturbation. The dissipation coefficients of this model, the resistivity η and the viscous coefficient μ are likewise assumed uniform for simplicity and in the absence of more accurate information. The square brackets are defined mathematically as

$$[a, u] = a_x u_y - a_y u_x$$

and all subscripts denote partial differentiation. The advantages of this form is the automatic satisfaction of incompressible conditions and the reduction of MHD into two scalar equations.

The medium velocity and magnetic field perturbation can be obtained from

$$b = \nabla \times (\hat{s}a),$$

$$v = \nabla \times (\hat{s}u).$$

Note that both the two-dimensionality of the model and the assumption of incompressible density are needed to reduce the vector dynamics of MHD to two scalar differential equations. Also, the vorticity equation replaces the momentum equation, which permits the elimination of pressure, gravity and other gradient forces.

The boundary conditions are those of the time-independent problem, and as the spatial operators are of elliptic type, we expect on general grounds for three boundary conditions to apply, two boundary conditions on the streamfunction (which satisfies in the limit of vanishing velocity gradients a biharmonic equation) and one boundary condition on the magnetic potential. It remains to determine what boundary conditions represent the physical situation best. For the magnetic potential, the simplest choices correspond to a Dirichlet condition or a Neumann condition. For the velocity streamfunction, there are two conditions from four possibilities, for a total of 12 possible boundary conditions. Note that the typical choice in spectral method implementations of Navier-Stokes channel flows, i.e. that the streamfunction and its normal first derivative be specified on the boundary corresponds to the case of a solid boundary and may not necessarily be the appropriate boundary conditions in this case.

The state variables a , u of the magnetospheric medium are then expanded in terms of complex exponentials in x and Chebyshev polynomials in y :

$$a = \sum_{k,l} \hat{a}_{k,l} e^{ikx} T_l(y),$$

$$u = \sum_{k,l} \hat{u}_{k,l} e^{ikx} T_l(y).$$

In the computer simulation, these expansions are truncated to a finite number of terms and the corresponding finite difference equations (in terms of the coefficients) are then solved. The Fourier-Chebyshev decomposition is advantageous both because of the ability of Chebyshev expansions to approximate solutions of boundary value problems and the efficiency with which both Fourier and Chebyshev expansion methods may be solved for on a computer. In particular, differentiation of a Fourier expansion transforms into a diagonal operator on the coefficients, while differentiation of a Chebyshev expansion transforms into a tridiagonal operator. Multiplication of functions can be handled in a pseudospectral manner on a domain of $9/4$ the size in order to eliminate pseudospectral aliasing. The transformations from coefficient space into collocation space (evaluation for a fixed finite set of points) and its inverse are performed with a Fast Fourier transform.

Results

During the summer, programs defining and manipulating functions defined in Fourier-Chebyshev coefficients were written and tested, including the tridimensional solver required to solve the Helmholtz equation with appropriate boundary functions. At this time, all spatial operators required to model the two-dimensional equations given above are prepared for future work.

Conclusions

A mathematically well-posed and computationally efficient model problem has been proposed as a tool for study of the equilibrium and transportational dynamics of the magnetospheric boundary layer. This method is applicable for both time-dependent and steady problems of the magnetosphere, and the spectral implementation permits simulation of non-trivial dynamics including MHD turbulence [10].

It remains to determine the most effective use of the above model in answering questions regarding the magnetospheric boundary layer. While a more thorough bibliographic survey remains to be done, it is clear that modeling of the magnetospheric boundary layer has been of research and observational interest for some time [2,3,4,6,7,8]. Field-aligned currents, which are of interest because of their connection to auroral arcs, arise naturally from the model equations as the curl in the transverse fluctuations of the underlying magnetic field. The use of Chebyshev polynomial expansions across the boundary layer permits the imposition of boundary conditions concerning momentum and magnetic flux transport from the magnetopause while retaining spectral accuracy in calculation of differentiated quantities. With the current trends in vector processing and larger amounts of memory, numerical codes that can realistically model the fluid dynamics of even complex initial-boundary value problems will continue to become more cost effective in verifying and generalizing theoretical models and should become better incorporated into efforts of understanding and predicting the near-Earth space environment.

Bibliography

- [1] C. Canuto, M. Y. Hussaini, A. Quarteroni, T. A. Zang, *Spectral Methods in Fluid Dynamics*, Springer-Verlag, 1988.
- [2] T. E. Eastman, E. W. Hones, Jr., "The Magnetopause Layer and Plasma Boundary Layer of the Magnetosphere" in *Quantitative Modelling of Magnetospheric Processes*, W. P. Olson (ed.), American Geophysical Union (Washington, D. C.), 1979.
- [3] T. E. Eastman, E. W. Hones, Jr., S. J. Bame, J. R. Asbridge, "The Magnetospheric Boundary Layer: Site of Plasma, Momentum and Energy Transfer from the Magnetosheath into the Magnetosphere", *Geoph. Res. Lett.* 3, 685, 1976.
- [4] A. Eviatar, R. A. Wolf, "Transfer Processes in the Magnetopause", *JGR* 73, 5561, 1968.
- [5] D. Gottlieb, "Spectral Methods for Compressible Flow Problems", in Soubbaramayer and J. P. Boujot (eds.) *Ninth International Conference on Numerical Methods in Fluid Dynamics*, Lect. Notes in Physics No. 218, Springer-Verlag, 1984.
- [6] J. Lemaire, "The Magnetospheric Boundary Layer: A Stopper Region for a Gusty Solar Wind", in *Quantitative Modeling of Magnetospheric Processes*, W. P. Olson (ed.), American Geophysical Union (Washington, D. C.), 1979.
- [7] W. Lotko, B. U. Ö. Sonnerup, R. L. Lysak, "Nonsteady Boundary Layer Flow Including Ionospheric Drag and Potential Electric Fields", *JGR*, 92 (A8), 8635, 1987.
- [8] R. L. Lysak, C. T. Dum, "Dynamics of Magnetosphere-Ionosphere Coupling Including Turbulent Transport", *JGR*, 88 (A1), 365, 1983.
- [9] J. W. Murdock, "A Numerical Study of Nonlinear Effects on Boundary-Layer Stability", *AIAA J.*, 15, 1167, 1977.
- [10] A. Pouquet, "Numerical Simulations of MHD Turbulence", *Comp. Physics Comm.*, 49, 97, 1988.
- [11] B. U. Ö. Sonnerup, *JGR*, 85, 2017, 1980.
- [12] H. R. Strauss, "Dynamics of High Beta Tokamaks", *Phys. Fluids*, 20, 1354, 1977.

ESTABLISHMENT OF AN ARCJET OPTICAL
DIAGNOSTICS FACILITY AT PHILLIPS LAB

Daniel A. Erwin
Associate Professor
Department of Aerospace Engineering

and

John H. Schilling and Jeff A. Pobst
Research Assistants
Department of Aerospace Engineering

University of Southern California
University Park
Los Angeles, CA 90089

Final Report For:
Summer Research Program
Phillips Laboratory

Sponsored by:
Air Force Office of Scientific Research
Bolling Air Force Base, Washington, D.C.

August, 1992

**ESTABLISHMENT OF AN ARCJET OPTICAL
DIAGNOSTICS FACILITY AT PHILLIPS LAB**

**Daniel A. Erwin, John H. Schilling, and Jeff A. Pobst
Department of Aerospace Engineering
University of Southern California**

Abstract

An arcjet optical diagnostic facility was established at the Phillips Laboratory. This facility is expected to provide accurate measures of flow properties in the plume and nozzle region of arcjet thrusters to assist in the development of more efficient arcjet thrusters for spacecraft stationkeeping and orbit-raising applications. A 30-kW arcjet was mounted and successfully operated in a vacuum test chamber capable of accurately duplicating the space environment. Optical elements were installed to allow active or passive measurement of flow properties using the techniques of emission spectroscopy and laser-induced fluorescence. A tunable ring dye laser pumped by a 20-watt CW argon-ion laser were installed and aligned for LIF experiments. Finally, an automated control and data-acquisition system was installed and software developed to conduct a variety of experiments.

A STUDY OF AERO-OPTICS

**Brian Staveley
Graduate Student
Department of Mechanical Engineering**

**University of New Mexico
Albuquerque, NM 87131**

**Final Report for:
Summer Research Program
Phillips Laboratory**

**Sponsored by:
Air Force Office of Scientific Research
Kirtland Air Force Base, Albuquerque, NM**

September 1992

A STUDY OF AERO-OPTICS

Brian Staveley
Graduate Student
Department of Mechanical Engineering
University of New Mexico

Abstract

A study of previous work in aero-optics was conducted. An attempt was made to modify a computer program developed by Jumper and Hugo [1] which modeled the passing of a single optical beam through a simulated turbulent boundary layer and measuring the deflection of the beam as it passed through the flow field. The modification was to pass two beams through the scale field at a given distance apart and then compare the two beam deflections. As part of a future study in aero-optics initial design considerations and drawings were produced for a turbulent channel flow facility to be built and operated at Phillips Laboratory.

A STUDY OF AERO-OPTICS

Brian Staveley

INTRODUCTION

The last several years has seen a substantial growth in the field of aero-optics and there promises to be continued growth in the future as additional applications are recognized. Aero-optic effects were first recognized in the mid sixties [2] during star imaging experiments in which substantial image degradation was noticed in images taken from an airborne platform. Fluctuations in the index of refraction cause severe degradation of coherent optical beams as they pass through the turbulent flow field. The focus of research in the field of aero-optics is being redefined to look more closely at the exact structure of turbulent flow fields. Turbulence research has led to the discovery that the assumptions of homogeneous isotropic turbulence can no longer be made if we are to be able to accurately describe the effects of the flow field on optical beam propagation in more than just a time-averaged sense. Thus, more emphasis is beginning to be placed on characterizing the structure of the turbulence and determining which characteristic parts of this structure, often referred to as "coherent structure", creates the most significant degradation. It is clear that such an effort is required to develop solutions more accurate than the widely published time averaged solutions, to ultimately compensate or correct for the degrading effects of turbulent flow fields on optical beam propagation through such flows. As noted in Gilbert [2] numerous applications exist, such

as airborne observatories, airborne laser platforms and other imaging operations.

METHODOLOGY

Jumper [1] conducted a proof-of-principle project in which an objective was to construct a conceptual model of a turbulent boundary layer in a channel flow across a heated flat plate. The model was then used to produce a simulated instantaneous temperature field in the boundary layer. A scalar index of refraction field which was allowed to convect past the optical beam was obtained from the temperature field. Using a ray tracing technique the single optical beam was passed through the thermal boundary layer and lateral beam deflection was computed.

To expand on this idea, an attempt was made to expand the scalar temperature field so that two beams could be passed through the scalar field at a distance of one boundary thickness apart. While this part of the program appeared to work fine, countless attempts to debug the program never resulted in good dual beam deflection data. Figure 1 shows light beam deflections for .015 seconds which were obtained from the program developed by Jumper and Hugo [1] for propagation of a single light beam. As can be seen, the signal in Figure 1 is highly fluctuating and looks somewhat like experimental results obtained by Wissler and Roshko [3]. The experiments conducted by Wissler and Roshko [3] used a lateral

effect detector to dynamically track the deflection of a He-Ne laser beam which was passed through a turbulent mixing layer.

Preliminary design calculations and drawings were made for a channel flow. The channel flow in Figure 3 is designed to produce a turbulent flow with a fully developed thermal profile in the test section with a Reynolds number of 3300 ($Re=hu/v$, where h =half height of channel, u =mean velocity and v =kinematic viscosity), provided entrance length requirements are satisfied. A fully developed turbulent thermal profile is developed in the test section as the flow passes over heated flat plates positioned just upstream of the two laser beams. A similar computational experiment was conducted by Truman [4] using a passive scalar field generated from data obtained from the data base of direct numerical simulation at the NASA-Ames/Stanford Center for Turbulent Research. The experiment studied the effect of organized turbulent structure on the propagation of an optical beam in a turbulent channel shear flow. Instantaneous index-of refraction fluctuations which were generated from the passive scalar by direct numerical simulation, induced a phase error in the coherent optical beam being passed through the flow. From this numerical experiment it was concluded that the phase distortion induced in the optical beam propagating through the homogeneous shear flow is sensitive to the direction of propagation which indicates that the turbulence is highly anisotropic. Further numerical experiments by Truman [5] studied the relative influence of large-scale and small-scale turbulent

structure on the propagation of an optical beam through the turbulent flow field. The spatial distribution and magnitude of the phase error was studied. Figure 2 from Truman [5] shows the phase error obtained from the channel flow with a hot lower surface and a cold upper surface. Results of the numerical experiment showed that phase errors induced in a coherent optical beam were largely dependent on the large-scale turbulent structure. Using temperature as the scalar, a laboratory experiment could be constructed in which the top wall of a channel flow could be held at room temperature and the bottom wall heated to produce a similar flow field. Figure 3 shows the design concept to be utilized in constructing such a channel flow.

Using the method described in Pope and Harper [6] to calculate the pressure drop across the entire wind tunnel, the pressure drop across the channel flow in Figure 3 is 0.566 inches of water. This indicates the blower supplying the air flow must be able to maintain the desired flow rate while operating at this static pressure. It is believed that the value is actually high since the inlet flow will be variably restricted to vary the flow rate in the test section. Therefore, a blower capable of operating at higher static pressures will be used. A flow velocity of 1.4 meters per second is required to obtain the desired Reynolds number in the test section. Furthermore, based on a desired Reynolds number of 3300 and a half height of 0.04 meters, an entrance length to channel width ratio of 17 (however it is thought that this ratio

could be as high as 50:1) is required for the turbulent flow to be fully developed in the test section. This requires that the first laser not be placed less than 0.7 meters (2 meters if the ratio is 50:1) from the entrance to the channel.

The optical system consists of a single 5 mW He-Ne laser which will have its beam split into two separate beams which will each be passed through the test section at two separate locations. Optical flats of controlled flatness will be used at both locations and likewise at both the top and the bottom of the test section so that the optical beam will pass through the test section unaffected by the test section structure itself. Up to four lateral effect detectors will be used to measure the deflection of the beam. For a thin beam the one dimensional lateral deflection is given by

$$\theta_x = d\phi/dx$$

If the direction of beam propagation is along the y-axis then the phase error is defined as

$$\phi(x; t) = k \int_0^L n(x; t) dy$$

where n is the index of refraction, L is the path length and k is the wave number given by

$$k = 2\pi/\lambda$$

Other notable characteristics of the wind tunnel are the bellows, the expansion section, the honeycomb section, the screens and the

plenum leading into the channel test section. The bellows are placed between the blower and the expansion section to isolate the blower from the rest of the wind tunnel to reduce vibrations induced into the test section by the blower. A maximum expansion angle of seven degrees is required in the expansion section to avoid separation. The next section of the wind tunnel is the honeycomb section which acts to straighten the flow and reduce the turbulence in the flow. The screens which are placed after the honeycomb section reduce the large scale turbulence in the flow by breaking the large scale turbulence down into smaller scale turbulence which decays much more rapidly. A natural contraction will form in the plenum chamber at the entrance to the test section as part of the flow is allowed to escape through the end of the plenum while the remaining flow passes through the test section.

CONCLUSION:

This paper summarizes some of the work that has been done in the field of aero-optics as it relates to channel flows. The works summarized were all of the numerical nature and provide a possible comparison for future experiments to be conducted in the channel flow which is to be built based on the preliminary drawings and calculations presented.

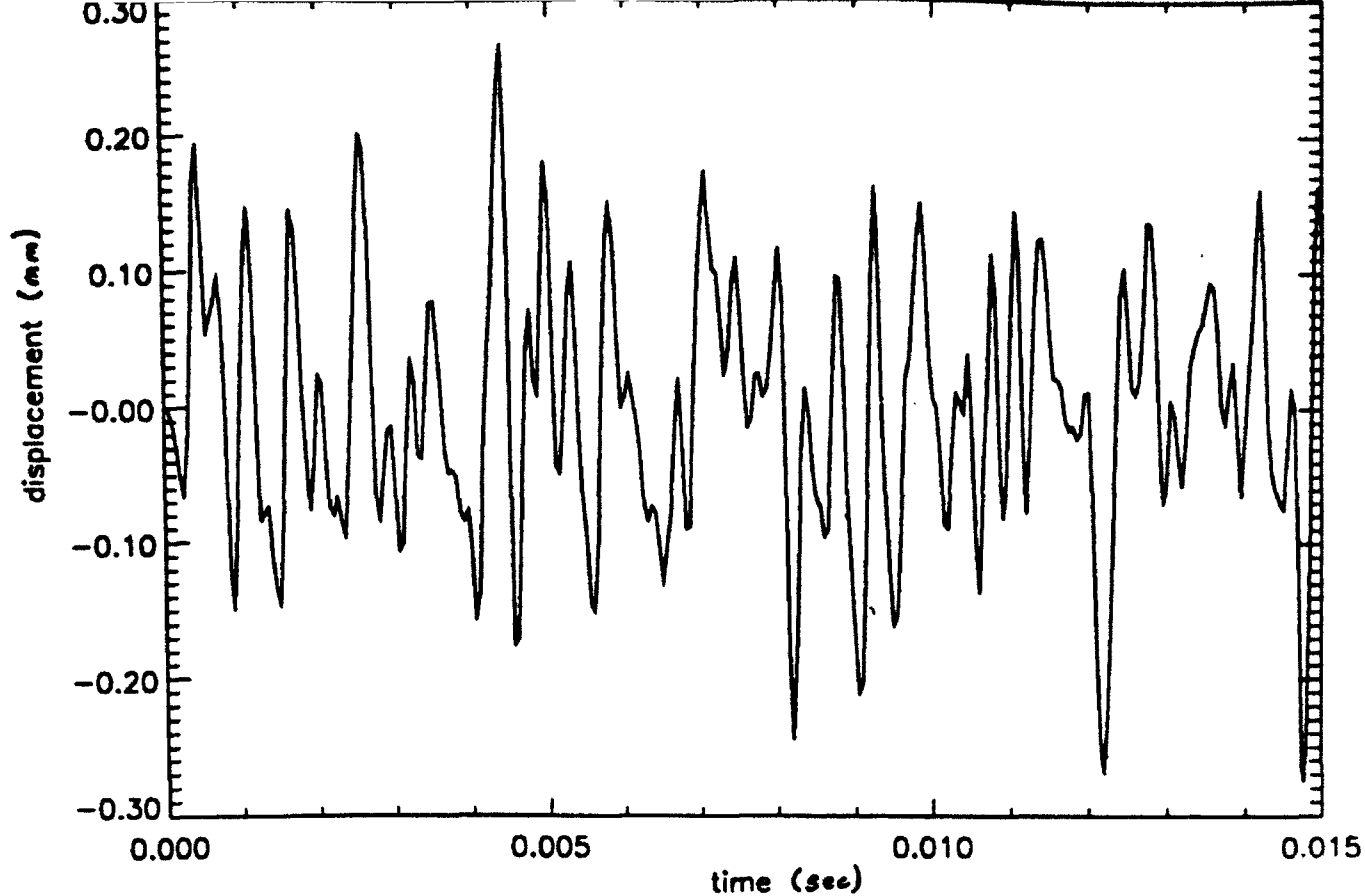


FIGURE 1
BEAM DEFLECTION
 (from Jumper and Hugo [1] computer program)

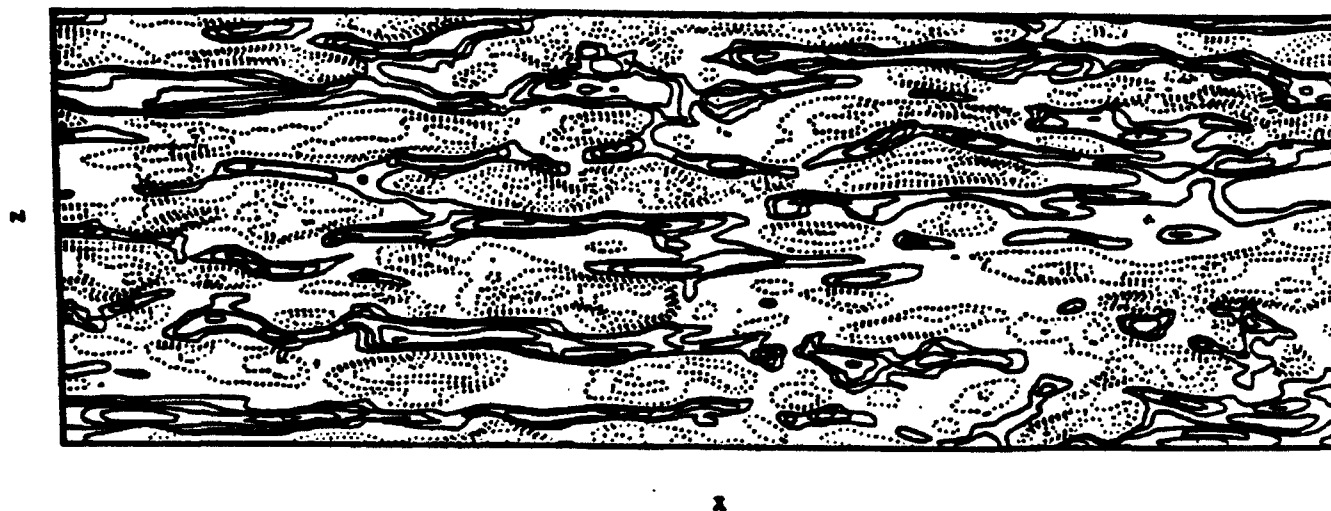


FIGURE 2
PHASE ERROR
 Contours of constant phase error in xz-plane for the
 propagation through the near wall region of a turbulent
 channel flow in the normal (y) direction

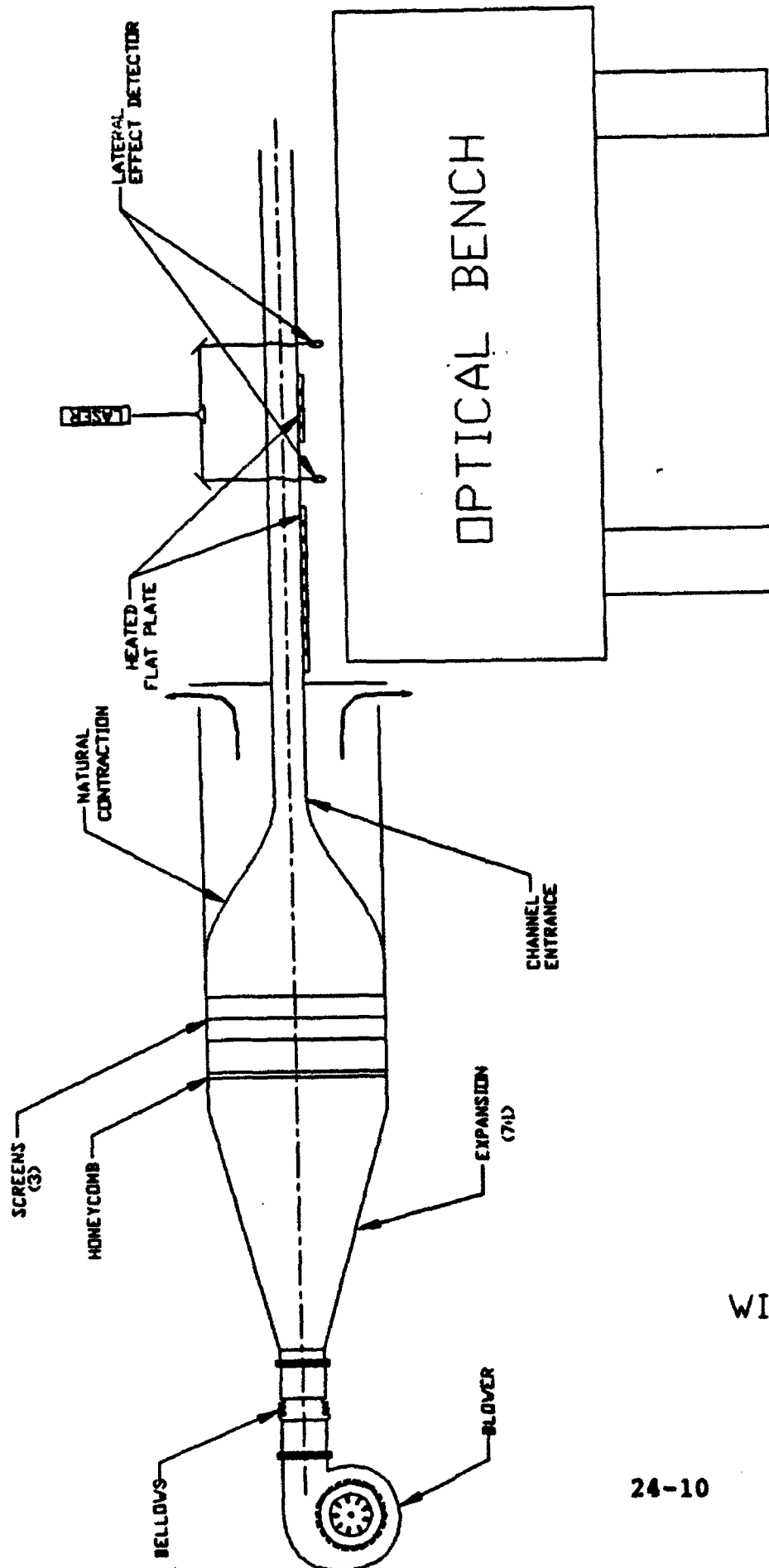


FIGURE 3
WIND TUNNEL DESIGN

REFERENCES

1. Jumper, E.J. and Hugo, R.J., "Optical Phase Distortion Due to Turbulent-Fluid Density Fields: Quantification Using the Small-Aperture Beam Technique," AIAA Paper 92-3020, July 1992.
2. Gilbert, K.G. and Otten, L.J. (editors), Aero-Optic Phenomena, Progress in Astronautics and Aeronautics, Vol 80, American Institute of Aeronautics and Astronautics, 1982.
3. Wissler, John B. and Roshko, Anatol, "Transmission of Thin Light Beams Through Turbulent Mixing Layers," AIAA Paper 92-0658, January 1992.
4. Truman, C.Randall, "Effects of Organized Turbulence Structures on the Phase Distortion in a Coherent Optical Beam Propagating Through a Turbulent Shear Flow," Physics of Fluids A, Vol. 2, 1990, pp. 851-857.
5. Truman, C. Randall, "The Influence of Turbulent Structure on Optical Phase Distortion Through Shear Flows," AIAA Paper 92-2817, May 1992.
6. Pope, Alan and Harper, John J., 1966, Low-Speed Wind Tunnel Testing, Wiley & Sons, New York, PP. 36-82.

THIS PAGE INTENTIONALLY LEFT BLANK

A BRIEF STUDY OF PASSIVE VISCOUS DAMPING FOR THE SPICE BULKHEAD STRUCTURE

Thomas J. Thompson
Graduate Research Assistant
Department of Mechanical Engineering

Joseph R. Baumgarten
Professor
Department of Mechanical Engineering

Iowa State University
2024 H. M. Black Engineering Building
Ames, Iowa 50013

Final Report for:
Summer Research Program
Phillips Laboratory

Sponsored by:
Air Force Office of Scientific Research
Bolling Air Force Base, Washington DC

September 1992

A BRIEF STUDY OF PASSIVE VISCOUS DAMPING
FOR THE BULKHEAD STRUCTURE

Thomas J. Thompson
Graduate Research Assistant

Joseph R. Baumgarten
Professor

Department of Mechanical Engineering
Iowa State University

ABSTRACT

The SPICE Testbed at Phillips Laboratory is being used to evaluate the effects of structural vibration on line-of-sight error for this strut built structure. A design incorporating active control and passive damping techniques is suggested to reduce the optical path distortion created in the vibrating structure. The passive viscous damping applied to the structure serves to aid the active control system stability in the cross-over and spill-over frequency range by producing a specified magnitude of damping in specified critical modes. This magnitude of damping is to be achieved by replacing the standard filament wound undamped struts with optimally placed D-struts which contain series and parallel combinations of springs and viscous dampers and produce damped vibration response from in-line strut deflection. This D-strut must replace standard struts in a tear-down of the bulkhead. The present study proposes to provide the requisite damping by adding on viscous damping at diagonal nodal locations in the bulkhead, circumventing the need to disassemble the SPICE bulkhead. The study shows specific increase in loss factor and improved damping ratio provided by the diagonal dampers when compared to in-line D-struts for specific modes and frequencies.

**VIBRATION AND COMPRESSION TESTING
OF COMPOSITE ISOGRID PANELS**

**Sean A. Webb
Graduate Student**

**Dr. Christopher A. Rotz
Associate Professor
Department of Manufacturing Engineering and Engineering Technology**

**Brigham Young University
435 CTB
Provo, Utah 84602**

**Final Report for:
AFOSR Summer Research Program
Phillips Laboratory**

**Sponsored by:
Air Force Office of Scientific Research
Edwards Air Force Base, California**

September 1992

VIBRATION AND COMPRESSION TESTING OF COMPOSITE ISOGRID PANELS

Sean A. Webb
Graduate Student

Dr. Christopher A. Rotz
Associate Professor
Department of Manufacturing Engineering and Engineering Technology
Brigham Young University

Abstract

Experimental vibration and compression tests of a composite isogrid panel have been successfully carried out. The first four natural frequencies and mode shapes were successfully identified. A simple analytical model developed in the study provided good estimates of the natural frequencies of the bending modes. Bending and torsional modes were analyzed with a simple finite element model. The predicted mode shapes agreed very well with those observed experimentally. Failure loads in the compression test were lower than predicted. This may have been caused by problems with the fixtures used to hold the specimen. Predicted strains were in good agreement with the average values measured in the test. The strains varied more with location on the panel than anticipated in the model, resulting in some strains being higher and others lower than predicted.